Interactions between an Incident Bore and a Free-Standing Coastal Structure

Halldór Árnason

A dissertation submitted in partial fulfillment

of the requirements for the degree of

Doctor of Philosophy

University of Washington

2005

Program Authorized to Offer Degree:

Department of Civil and Environmental Engineering

University of Washington

Graduate School

This is to certify that I have examined this copy of a doctoral dissertation by

Halldór Árnason

and have found that it is complete and satisfactory in all respects,
and that any and all revisions required by the final
examining committee have been made.

Chair of Supervisory Committee:

____

Catherine M. Petroff

Reading Committee:

____

Catherine M. Petroff

____

Harry H. Yeh

____

Peter B. Rhines

Date: ______________________

University of Washington

Abstract

Interactions between an Incident Bore and a Free-Standing Coastal Structure

by Halldór Árnason

Chair of Supervisory Committee:

Affiliate Assistant Professor Catherine M. Petroff
Department of Civil and Environmental Engineering

This dissertation describes experiments carried out to examine the problem of tsunami impact on coastal structures. Using a 16.6 m long and 0.61 m wide tank situated in the Harris Hydraulics Laboratory at the University of Washington, bores were generated using a lift gate and made to impinge on structures of simple geometry.

Measurements were made of water level using wave gauges and a laser profiler. Flow velocities were obtained at single points with a laser doppler velocimeter and a two dimensional flow field was constructed using particle image velocimetry. A six degree of freedom load cell recorded forces on the structures.

The energy and momentum in the flow was analyzed. The contribution of the potential energy was found to be approximately equal to that of the kinetic energy. The turbulence in the bore and the wake of the structure was also analyzed. Turbulent kinetic energy was found to be negligible. The dynamics of the bore interaction with the structures and tank side walls yielded highly unsteady momentum flux in the region of the structures.

The forces on the structures were examined and related to the Froude number, bore height, tank width and structure geometry. Resistance coefficients in the range of 1–2 were observed. The resistance decreased with increasing Froude number and relative bore height.

The variation of the resistance coefficients with bore height was more pronounced for circular columns than for square columns. Resistance coefficients increased with decrease in the ratio between flow depth and column width owing to more redirection of the flow.

TABLE OF CONTENTS

List of Figures

List of Tables

List of Symbols

Roman letters

A	Area
A_{p}	Area of projection
B	Tank width
C	Chézy coefficient
C_{D}	Drag coefficient
C_{R}	Resistance coefficient
D	Diameter
E	Energy
$\mathscr{E}$	Energy flux
F	Force
F_{I}	Impact force
F'_{I}	Force immediately after impact
F_{R}	Resistance force
F_{f}	Friction force
F_{h}	Hydrostatic force
F_x	Force in the x-direction
F_y	Force in the y-direction
Fr	Froude number
Fr'	Froude number in a moving coordinate system
H	Head (energy per unit weight)

H_k	Kinetic head
H_p	Potential head
H_t	Turbulent head
K	Integration constant
L	Distance from gate to object
M	Moment
M_x	Moment around the x-axis
M_y	Moment around the y-axis
M_z	Moment around the z-axis
P	Pressure
Re	Reynolds number
Re_b	Object Reynolds number
Re_h	Flow Reynolds number
S	Slope
T	Temperature
V	Volume
a	Acceleration
$\boldsymbol{a}$	Three dimensional acceleration vector
b	Object width
c	Celerity
f_f	Frequency of video frame acquisitions
f_N	Natural frequency
g	Acceleration of gravity
h	Water depth
h_0	Initial water depth downstream of gate

h_1	Impoundment behind the gate
i	$\sqrt{-1}$
i, j, k	Indices
m	Mass
$\boldsymbol{n}$	Normal vector
p	Momentum
p_s	Specific momentum
q	Discharge per unit width
t	Time
t_0	Bore arrival time
t^*	Upper time limit on bore conditions
t_f	Time between video frame acquisitions
u	Velocity in the x-direction
$\boldsymbol{u}$	Three dimensional velocity vecteor
$\overline{u}$	Mean velocity in the x-direction
$\overline{\boldsymbol{u}}$	Three dimensional mean velocity vector
u'	Deviation from the mean velocity in the x-direction
$\boldsymbol{u}'$	Three dimensional velocity deviation vector
u_*	Friction velocity
u_b	Base velocity in the x-direction
$\boldsymbol{u}_\mathbf{b}$	Three dimensional base velocity vector
v	Velocity in the y-direction
v'	Deviation from the mean velocity in the y-direction
v_b	Base velocity in the y-direction
w	Velocity in the z-direction
w'	Deviation from the mean velocity in the z-direction

x	The horizontal flow-wise direction
y	The horizontal span-wise direction
z	Vertical direction

Greek letters

α	Calibration coefficient
γ	Specific weight
ζ	Relative depth $\frac{z}{h}$
θ	Angle
κ	Von Kármán constant
μ	Dynamic viscosity
ν	Kinematic viscosity
ξ	Position of bore front
$\dot{\xi}$	Propagation speed of bore
ξ'	Position of reflected bore front
$\dot{\xi}'$	Propagation speed of the reflected bore
π	The ratio between circumference and diameter of a circle
ρ	Density
ϕ, φ	Voltage
ω	Angular frequency

ACKNOWLEDGMENTS

The author extends special thanks to Tony McKay for his helpful assistance and laboratory expertise, and to Andrew L. Moore for all his help. The author also thanks Chase Barton, Todd Prince, and Trevin Roletto for their assistance on the project.

The author thanks Sherrill L. Lingel, Þórhildur Guðmundsdóttir, Ólöf Rós Káradóttir, Sigurður M. Garðarsson, Guðmundur Freyr Úlfarsson, and Þórarinn Sveinn Arnarson for their help and friendship.

The author thanks the committee members Harry H. Yeh and Peter B. Rhines for their assistance, suggestions and helpful critique. The author gratefully thanks his advisor, Catherine M. Petroff, for her advice and continued support during this research.

In Memoriam

Árni Guðjónsson

1928–2003

Chapter 1

INTRODUCTION

A tsunami is a wave or a series of waves produced by an abrupt submarine earth motion. This motion may be caused by landslides, volcanic activity, explosions, meteor impact or more commonly by fault motion during a seismic event. The term *tsunami* is from Japanese and means *great wave in harbor* (Dudley and Lee, 1988). Throughout history, tsunamis have caused tremendous damage and loss of life in many coastal areas around the world. The deadliest and also most recent was triggered by a large earthquake on December 26, 2004 off the west coast of Sumatra. The preliminary estimate of its moment magnitude is 9.3. According to news reports, almost 300 000 people, in 12 countries around the Indian Ocean, lost their lives. Another very destructive tsunami in relation to loss of life was generated by the eruption of volcano Krakatoa in Indonesia on August 27, 1883 (Warton and Evans, 1888). A 30 m high tsunami was generated which killed approximately 36 000 people. One of the most dramatic documented cases of tsunami runup occurred in Lituya Bay, Alaska in 1958 where a landslide-generated tsunami levelled trees up to 525 m above the original water level and produced a 50 m high wave in the bay (Miller, 1960).

During sudden vertical changes in the seafloor, such as those caused by seismic motion occurring beneath the sea or by large underwater failures, a large volume of water is displaced from its equilibrium position and a rise or depression is formed. This disturbance then propagates outwards from the source region in the form of a long wave or a tsunami. Unlike wind generated waves, which have their energy contained primarily near the surface, the kinetic energy of a tsunami is evenly distributed throughout the entire water depth. The wave length of a tsunami can be of the order of several hundred kilometers, making it behave as a shallow water wave even in the “deep” ocean. This means that when tsunamis approach shore, their wavelengths decrease due to shoaling, leading to an increase in wave height. In many cases, tsunamis reach the shore as non-breaking waves, i.e. a tsunami which acts as a rapidly rising tide. In some cases they can arrive as very large breaking waves; as large as 30 m or even greater in extreme cases. These broken waves cannot be characterized by cyclic wave action impinging on the shoreline, but are more aptly modelled as a strong turbulent bore. Bores can pass the shoreline and continue onshore as high-speed surges propagating over a dry bed with celerities on the order of tens of meters per second and wave heights on the order of several to tens of meters. The form of the wave at the shoreline depends on the incident tsunami as well as the local bathymetry and the tidal level. Local bathymetry can cause effects like wave resonance in near shore regions or harbors and wave focussing on headlands and in gradually narrowing estuaries with steep sidewalls.

Swift tsunami flow effects were clearly observed in many video recordings of the 2004 Sumatra tsunami event. Some of the structural failures from tsunamis suggest the damage was caused by the force of flow itself as opposed to the impacts of floating debris. Eaton et al. (1961) report observations from Hilo, Hawai‘i during the tsunami caused by the 1960 Chilean earthquake, that a bore travelled from the breakwater to the shore of Hilo (about 2100 m) within 2.5 to 3 minutes. The speed of the bore for that stretch would then have been between 12 and 14 m/s. This velocity corresponds to a Froude number close to one.

The forces from a tsunami runup can be of different types: buoyant and hydrostatic forces result from partial or total submergence in the surging water, impact forces are caused by the leading edge of the bore impinging on a structure. The high flow velocity exerts drag forces on structures and debris picked up by the tsunamis can add additional impact forces.

As far as tsunami-structure interactions and mitigation of tsunami damage are concerned, an accurate understanding of local tsunami flow effects around structures is critical for accurate force and scour predictions. This knowledge can be combined with runup height predictions to devise measures for limiting exposure to tsunami damage.

The work described in this dissertation focused on physical modelling of free-standing structures of simple shapes, subjected to a passing of a tsunami modelled by a turbulent bore. Measurements were made of surface levels and velocity of the passing water as well as the forces acting on each structure. The goal is to further our understanding of the interaction between the bore and the structure, i.e. the structure's effect on the bore as well as the bore's effect on the structure, and to predict the magnitude of the hydrodynamic force on a structure during impact and passage of a tsunami.

Chapter 2

LITERATURE REVIEW

2.1 Dam Break Problem

This study uses bores formed by the fast removal of a gate with water impounded on one side, i.e. a *dam break*. Ritter (1892) introduced a theoretical description of the two-dimensional dam break problem for an inviscid fluid for a dry bed by solving the non-linear shallow-water equations. The solution gives a parabolic water surface profile which is concave upward. The front travels downstream with the wave celerity $c = 2\sqrt{gh_1}$ where g is acceleration due to gravity and h_1 is the initial quiescent water depth behind the dam. Upstream of the dam a negative wave travels upstream with $c = \sqrt{gh_1}$ which corresponds to the shallow water wave celerity.

In the shallow front region of the flow, neglecting resistance from bed friction is not realistic. It has considerable influence on the propagation speed. Dressler (1952) adds a Chézy resistance term of the form $C(\frac{u}{c})^2$ to the momentum equation and obtains a first order approximation of the location of the water front as a function of time.

Whitham (1955) argued that near the surge front the effect of friction is to pile up the fluid so the water surface slope is steep, where the depth becomes small. Noting that the acceleration terms would remain finite, Whitham (1955) reasoned that the friction and the pressure gradient terms in the horizontal momentum equation should balance each other as they become large near the tip of the surge. Neglecting the acceleration terms in the equation of motion, while using a friction model, which is quadratic in the flow velocity, results in a parabolic water surface profile for the surge tip which is concave downward. This profile asymptotically approaches a vertical face near the tip of the surge and tends to a very mild slope far behind the front of the surge. Whitham (1955) compared the tip speed from both his study and that of Dressler (1952) and found both approaching the Ritter (1892) solution for short times.

Cross (1967) performed experiments on a bore propagating onto a dry bed. He derived an expression for the profile of a surge tip

$$\xi - x = \frac{h}{\beta} - \frac{u^2}{C^2\beta^2}\log\left(1 + \frac{C^2\beta}{u^2}h\right) \tag{2.1}$$

where

$$\beta = \frac{1}{g}\frac{\mathrm{d}u}{\mathrm{d}t} - S, \tag{2.2}$$

$x = \xi$ is the location of the tip, C is the Chézy coefficient and S is the bottom slope. He concluded that the shape of the tip of a surge advancing over a dry bed in his experiments was described fairly well by Equation 2.1, especially close to the tip, but further back the theory tended to overestimate the water depth. When the acceleration and the slope are both zero or their effects cancel each other, his solution reduces to the profile presented by Whitham (1955).

Wang and Ansari (1986) present a model for the flow in a surge where the velocity field was approximated with a power law. They computed the pressure field with a finite element solution of Poisson's equation where an eddy viscosity turbulence model and an experimentally determined head loss distribution along the water surface were used to obtain a closed solution.

Fujima and Shuto (1990) produced a stationary surge front using a flume with a bottom made up of inclined moving belts. They used laser doppler velocimetry (LDV) to measure the mean velocity field and the Reynolds stress. They found that the energy loss in the boundary layer near the tip of a surge on a dry bed, can be modelled by the friction law for uniform flow over a flat plate (Schlichting, 1979).

2.2 Bores and jumps

Often bores are considered to act similarly to hydraulic jumps taken in a moving reference frame. Bradley and Peterka (1957) classify hydraulic jumps in horizontal rectangular channels into five categories based on the approach Froude number. Froude numbers in the range 1.7–2.5 fall into the category of *weak jump*, characterized with a series of surface rollers developing on the surface of the hydraulic jump and a smooth surface downstream of the jump. Froude numbers in the range 2.5–4.5 fall into the category of *oscillating jump*. There the incoming jet oscillates in a random manner between the bed and the surface producing surface waves that persist a considerable distance downstream. Jumps with approaching Froude numbers in the range 4.5–9.0 are *steady jumps*. The jump is well stabilized. The downstream extremity of the surface roller and the point at which the high velocity jet tends to leave the floor occur in practically in the same vertical plane. The other two categories are *undular jump* ($1 < Fr < 1.7$) and *strong jump* ($9.0 < Fr$).

Afzal and Bushra (2002) presented calculations for flow structure in hydraulic jumps in a channel of arbitrary shape. Their results, together with those of previous models and experiments show a marked variation of relative jump length for Froude numbers between 1 and 5.

2.3 Tsunami impact effects

In order to approximate the impact of a tsunami, Cumberbatch (1960) presented a solution for the impact of a two-dimensional fluid wedge on a flat surface. He assumed a constant wedge angle before impact, an inviscid fluid and irrotational flow where the velocities throughout the wedge before impact are equal to the constant approach velocity. He used a no-flux boundary condition at the wall and fully nonlinear free surface boundary conditions. Since gravity was neglected in the problem formulation, the theory was intended to model the dynamics soon after impact, before the gravitational acceleration begins to affect the flow along the wall. Water surface profiles and pressure distributions along the wall were presented for wedge angles of 22.2 degrees and 45 degrees. Cumberbatch (1960) defined a force coefficient which relates the force on the wall to the momentum flux which would occur at the wall location if the wall were not present, as follows

$$F = C_F \rho b h c^2, \tag{2.3}$$

where C_F is the force coefficient which was shown to be a function of only the incident wedge angle θ, ρ is the density of the fluid, b is the width of the wall, h is the water level at the wall location and c is the celerity.

As mentioned before, Cross (1967) studied the properties of surges. His work included a study on their impact forces on vertical walls. He used the same approach as Cumberbatch (1960), but added gravity forces

$$\frac{F}{b} = \frac{1}{2}\gamma h^2 + C_F \rho u^2 h. \tag{2.4}$$

Fukui et al. (1963a) measured the pressures generated on walls due to the reflections of bores. The bores propagate on to a slope varying from 34° to 90° and the bore heights were varied so

$$0.5 \leq \frac{h - h_0}{h_0} \leq 3.0, \tag{2.5}$$

where h is the water level in the bore and h_0 is the still water depth it propagates onto. The experiments were made in a 152 mm wide, 460 mm deep and 6.9 m long glass walled channel.

Fukui et al. (1963a) differentiated between what they called the *impulsive* pressure which is obtained soon after the bore strikes the wall and the *continuous* pressure which corresponds to the hydrostatic pressure at the wall once the reflected bore has propagated away from the wall. Using linear regression they concluded that the impulsive pressure was proportional to the fourth power of the celerity.

Nakamura and Tsuchiya (1973) study the shock pressure of a tsunami bore on a composite structure. The bores were generated by the dam break mechanism using impoundment of 300, 400 and 500 mm. Large pressure heads of relatively short duration just after

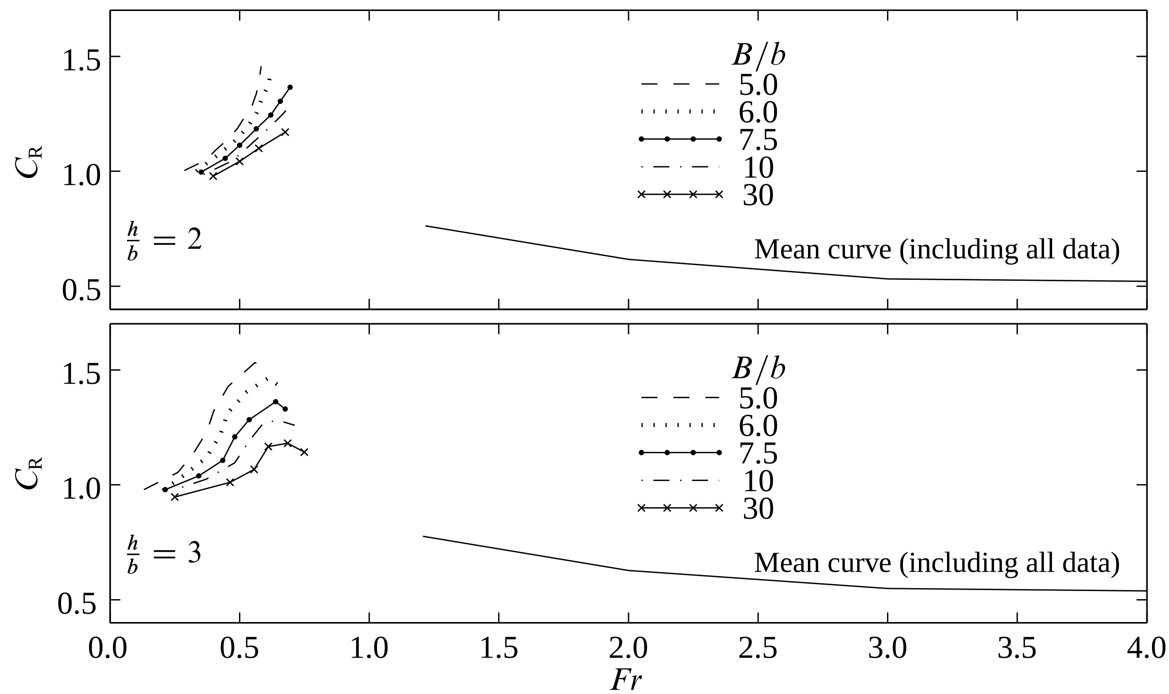

Figure 2.1: Examples of data from Gupta and Goyal (1975), where h is the flow depth, b is the column diameter, B is the column spacing center to center and Fr is the Froude number

the impact were measured. This was followed by a nearly constant hydrostatic pressure from the height of the reflected bore. They found the maximum pressure to be about 50 % of the following hydrostatic pressure. Velocity measurements however showed higher velocities than predicted by Dressler (1952) and Whitham (1955), in some cases as high as triple the theoretical values.

Ramsden (1993) investigated the interaction of tsunamis with a vertical wall. He used a physical model to look at bores and surges propagating on dry bed as well as solitary waves. His measurement included both force and runup measurements. He found that the force computed from the maximum measured runup, assuming hydrostatic condition, exceeded the maximum measured force. He also found that the model of Cross (1967) underpredicted the measured forces due to bore on dry bed by 30–50 %.

Davletshin and Lappo (1986) investigated tsunami forces exerted on a vertical cylindrical barrier. They looked at three cases, first a long unbroken shallow water wave; second, a transformed solitary wave and third, a surge resulting from breaking of large waves. They use a formulation from Fukui et al. (1963b) and conclude that a load on a vertical circular cylinder is

$$F = \rho b h u^2, \tag{2.6}$$

which corresponds to the linear momentum flux.

Gupta and Goyal (1975) use laboratory studies (no scale given in their paper) to analyze aspects of three-dimensional flow around bridge piers. They relate the coefficient of resistance, C_R, defined as

$$C_R = \frac{F}{\frac{1}{2}\rho g A_p u}, \tag{2.7}$$

to the Froude number, Fr, relative spacing of the piers and the relative depth. They found the C_R to peak around or above $Fr = 0.5$, while the value of C_R around the peak was dependent on both the relative spacing of the piers with regard to pier width and relative flow depth with regard to pier width. For Froude number above 1, that dependence was less pronounced. Figure 2.1 shows some of their data. For supercritical flow ($Fr > 1$), the depth of flow does not have a pronounced effect on C_R nor does the blockage. On the other hand, for subcritical flow C_R increases with increase in blockage (decrease in B/b). The value of C_R reaches a very definite maximum around $F_R = 0.5$. Because the value of C_R reflects both the wave and form drags, the sharpness of the curves at relatively small depths of the oncoming flow indicates that the wave drag is then important to the total resistance, but as the depth increases, the relative importance of the form drag increases resulting in a flatter curve.

2.4 Cylinders in steady and unsteady flow

For information about the flow around cylinders in free surface flows, the reader is referred to the work of Sumer and Fredsøe (1997) who have compiled a comprehensive overview of hydrodynamics around cylindrical structures. During the onrush of a tsunami bore, an important consideration is the initial interaction of the bore and structure during impact Wang and Chwang (1984) look at nonlinear impulsive force on a vertical cylinder. They also look at flow around an impulsive starting vertical cylinder (Wang and Chwang, 1986) and free-surface flow produced by accelerating a vertical cylinder (Wang and Chwang, 1989). They found good agreement between measurements and the non-linear potential flow theory.

Chapter 3

THEORETICAL CONSIDERATIONS

3.1 Shallow water wave equation

Conservation of mass or continuity for incompressible fluid in 2 dimensions (x, z) states that

$$\nabla \cdot \boldsymbol{u} = \frac{\partial u}{\partial x} + \frac{\partial w}{\partial z} = 0. \tag{3.1}$$

A fluid domain with a flat nonporous bottom yields a no-flow condition at $z = 0$ or

$$w|_{z=0} = 0. \tag{3.2}$$

At a free surface at $z = h(x, t)$ the kinematic condition is

$$w|_{z=h} = \frac{\mathrm{D}h}{\mathrm{D}t} = \frac{\partial h}{\partial t} + u|_{z=h} \frac{\partial h}{\partial x} \tag{3.3}$$

and the dynamic condition is

$$P|_{z=h} = 0, \tag{3.4}$$

where P represents pressure. Integrating Equation 3.1 with respect to z and making use of Equations 3.2 and 3.3 yields

$$\int_0^h \frac{\partial u}{\partial x} \, \mathrm{d}z + \frac{\partial h}{\partial t} + u|_{z=h} \frac{\partial h}{\partial x} = \frac{\partial h}{\partial t} + \frac{\partial}{\partial x} \int_0^h u \, \mathrm{d}z = 0. \tag{3.5}$$

So far, no use has been made of the assumption that the flow is shallow. Shallow water theory assumes that the fluid acceleration in the z-direction has a negligible effect on the pressure P, which means that the pressure is hydrostatic

$$P = \rho g(h - z), \tag{3.6}$$

where ρ is the fluid density and g is the acceleration of gravity. Note that

$$\frac{\partial P}{\partial x} = \rho g \frac{\partial h}{\partial x} \tag{3.7}$$

is independent of z. Therefore the x-component of the fluid acceleration is also independent of z and if at any time u is independent of z it will be so at any time. Equation 3.5 can then be written as

$$\frac{\partial h}{\partial t} + \frac{\partial (uh)}{\partial x} = \frac{\partial h}{\partial t} + h\frac{\partial u}{\partial x} + u\frac{\partial h}{\partial x} = 0. \tag{3.8}$$

The momentum principle or Newton's second law of motion states the total force on a fluid particle equals its mass times its acceleration. Assuming the significant forces are pressure and gravity, i.e. ignoring both turbulent and viscous shear, this can be written as

$$\rho\frac{\mathrm{D}\boldsymbol{u}}{\mathrm{D}t} = \rho\left(\frac{\partial \boldsymbol{u}}{\partial t} + (\boldsymbol{u}\cdot\nabla)\boldsymbol{u}\right) = -\nabla(P + \rho g z) = -\nabla(\rho g h). \tag{3.9}$$

The x component, divided by ρ is then

$$\frac{\partial u}{\partial t} + u\frac{\partial u}{\partial x} + w\frac{\partial u}{\partial z} = -g\frac{\partial h}{\partial x} \tag{3.10}$$

and the shallow water assumption leaves

$$\frac{\partial u}{\partial t} + u\frac{\partial u}{\partial x} + g\frac{\partial h}{\partial x} = 0. \tag{3.11}$$

Now, with the introduction of the propagation speed

$$c = \sqrt{gh}, \tag{3.12}$$

Equations 3.8 and 3.11 can be rewritten in terms of u and c rather than u and h, yielding

$$2\frac{\partial c}{\partial t} + c\frac{\partial u}{\partial x} + 2u\frac{\partial c}{\partial x} = 0 \tag{3.13}$$

and

$$\frac{\partial u}{\partial t} + u\frac{\partial u}{\partial x} + 2c\frac{\partial c}{\partial x} = 0. \tag{3.14}$$

3.2 Method of characteristics

3.2.1 Introduction

Equations 3.13 and 3.14 are partial differential equations that can be solved using the method of characteristics. In solving them here, a discussion in Stoker (1948) is followed and applied to the tank used in this study. Adding the aforementioned equations together yields

$$\left\{\frac{\partial}{\partial t} + (u + c)\frac{\partial}{\partial x}\right\}(u + 2c) = 0 \tag{3.15}$$

and subtracting them

$$\left\{\frac{\partial}{\partial t} + (u - c)\frac{\partial}{\partial x}\right\}(u - 2c) = 0. \tag{3.16}$$

Equation 3.15 states that the function $(u + 2c)$ is a constant on a curve defined by the ordinary differential equation

$$\frac{\mathrm{d}x}{\mathrm{d}t} = u + c \tag{3.17}$$

and similarly, Equation 3.16 states that $(u - 2c)$ is a constant on a curve defined by

$$\frac{\mathrm{d}x}{\mathrm{d}t} = u - c. \tag{3.18}$$

These curves are called characteristic lines.

3.2.2 Infinite tank

Now consider the flow resulting from a instantaneous removal of a wall at $x = 0$ causing a discontinuity in water level there with

$$h = \begin{cases} h_0 & \text{for} \quad x > 0 \\ h_1 & \text{for} \quad x < 0 \end{cases} \tag{3.19}$$

and

$$u = 0 \tag{3.20}$$

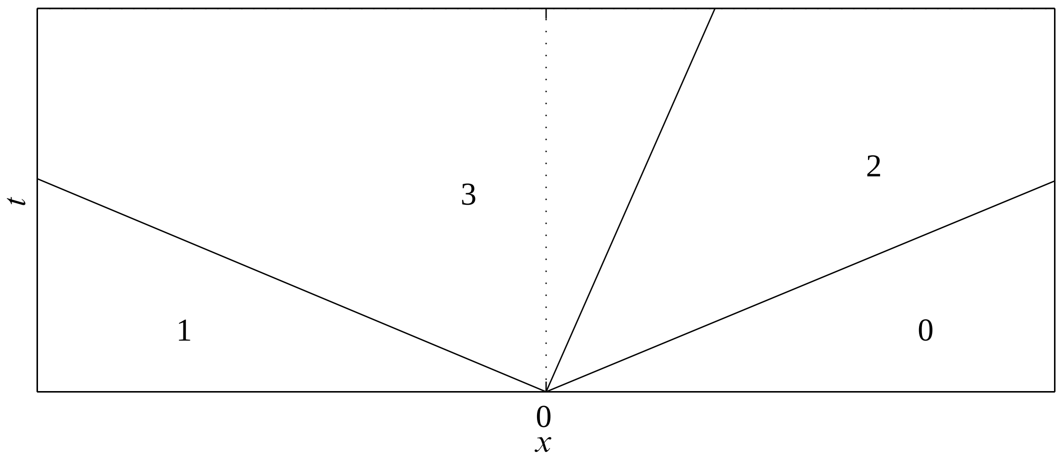

Figure 3.1: Characteristic lines for the dam break problem, 0,1: undisturbed, 2: propagating disturbance and 3: simple wave

everywhere at $t = 0$.

Four different zones can be identified in the fluid at any time t (see Figure 3.1). Zone 0 is the quiet downstream region which is terminated on the upstream by the shock wave, zone 1 is the undisturbed upstream region, zone 2 is a zone of constant state in which the water is not at a rest and zone 3 is a centered simple wave which connects zones 2 and 1.

The shock conditions between zones 0 and 2 are

$$-\dot{\xi}(u_2 - \dot{\xi}) = \frac{1}{2}(c_0^2 + c_2^2) \tag{3.21}$$

and

$$c_2^2(u_2 - \dot{\xi}) = -c_0^2\dot{\xi} \tag{3.22}$$

where $\dot{\xi}$ is propagation speed of the shock wave. By solving them together for u_2 we get

$$\frac{u_2}{c_0} = \frac{\dot{\xi}}{c_0} - \frac{c_0}{4\dot{\xi}}\left(1 + \sqrt{1 + 8\left(\frac{\dot{\xi}}{c_0}\right)^2}\right). \tag{3.23}$$

Doing the same for c_2 we get

$$\frac{c_2}{c_0} = \sqrt{\frac{1}{2}\left(\sqrt{1+8\left(\frac{\dot{\xi}}{c_0}\right)^2}-1\right)}. \tag{3.24}$$

The straight characteristics in zone 3 have slope of $u - c$ so the characteristics that delimit zone 3 are $x = -c_1 t$ on the left hand side and $x = (u_2 - c_2)t$ on the right hand side. On the curved characteristic in zone 3 the quantity $u + 2c$ is a constant. Therefore on one hand

$$u_3 + 2c_3 = 2c_1 \tag{3.25}$$

and the other

$$u_3 + 2c_3 = u_2 + 2c_2. \tag{3.26}$$

This means that

$$\frac{u_2}{c_0} + 2\frac{c_2}{c_0} = 2\frac{c_1}{c_0}. \tag{3.27}$$

Substituting Equations 3.23 and 3.24 into Equation 3.27 gives the following:

$$\frac{\dot{\xi}}{c_0} - \frac{c_0}{4\dot{\xi}}\left(1+\sqrt{1+8\left(\frac{\dot{\xi}}{c_0}\right)^2}\right) + 2\sqrt{\frac{1}{2}\left(\sqrt{1+8\left(\frac{\dot{\xi}}{c_0}\right)^2}-1\right)} = 2\frac{c_1}{c_0}. \tag{3.28}$$

The values of c_0 and c_1 are known so this yields a value for $\dot{\xi}$ when solved numerically. Having found the value of $\dot{\xi}$ the values of u_2 and c_2 can be drawn directly from Equations 3.23 and 3.24 respectively. Then the water depth in zone 2 can be found by

$$h_2 = \frac{c_2^2}{g}. \tag{3.29}$$

In zone 3 we have, along with the straight characteristics in this zone, the relations

$$\frac{\mathrm{d}x}{\mathrm{d}t} = \frac{x}{t} = u_3 - c_3 = 2c_1 - 3c_3 = \frac{3}{2}u_3 - c_1 \tag{3.30}$$

from which we get

$$c_3^2 = \frac{1}{9}\left(2c_1 - \frac{x}{t}\right)^2 \tag{3.31}$$

and

$$u_3 = \frac{2}{3}\left(c_1 + \frac{x}{t}\right). \tag{3.32}$$

Thus the water surface in zone 3 is curved in the form of a parabola in all cases. At the junctions with both zones 1 and 2 the parabola does not have a horizontal tangent, so that the slope of the water surface is discontinuous at these points.

The t-axis, i.e. the line $x = 0$ is a characteristic belonging to zone 3. We then observe from Equations 3.31 and 3.32, which are then valid on the t-axis, that c and u are both independent of t at $x = 0$, which means that the depth of the water and its velocity u are both independent of t at this point, i.e. the original location of the gate, and hence that the volume $\mathrm{d}q/\mathrm{d}t = uh$ of water crossing that site per unit of time is independent of time although the motion as a whole is not steady. In fact, $h = \frac{4}{9}h_1$ and $u = \frac{2}{3}c_1$ for all times t at this point. In addition, u and c and thus also $\mathrm{d}q/\mathrm{d}t$ are not only independent of t but also independent of the undisturbed depth h_0 on the lower side, if h_1 is held fixed, as long as

$$\frac{h_0}{h_1} < \frac{4}{9}. \tag{3.33}$$

This condition holds for every case in this study.

3.2.3 Effects of end walls

As the bore travels downstream it will hit the downstream wall and a bore will reflect back forming zone 4 as can be seen in Figure 3.2. The bore will hit the wall at $t_4 = x_{\max}\dot{\xi}$. Looking at how it reflects from the wall, Stoker (1948) is used again. The shock conditions give us the propagation speed of the reflected bore from

$$-\dot{\xi}(u_2 - \dot{\xi}') = \frac{gh_2}{2}\left(1 - \frac{u_2 - \dot{\xi}'}{\dot{\xi}'}\right). \tag{3.34}$$

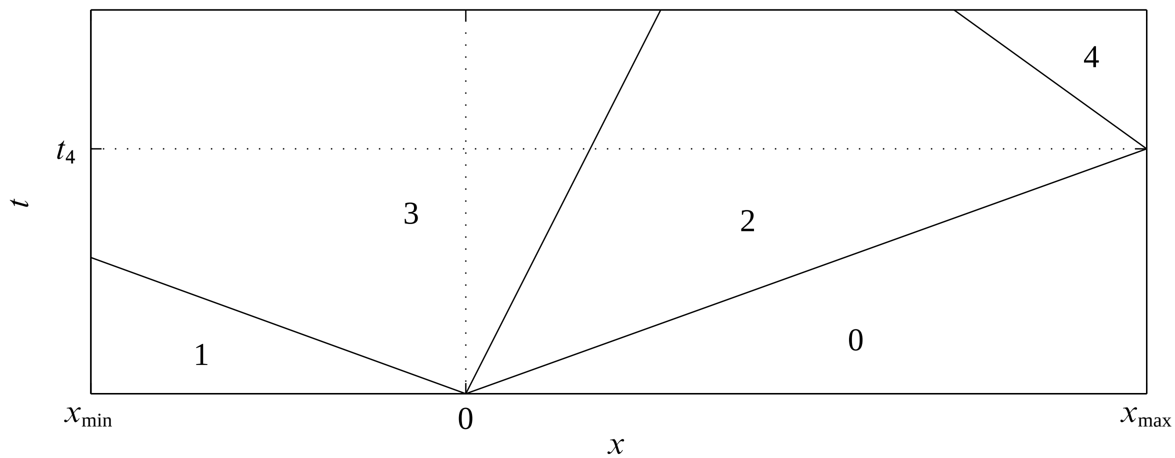

Figure 3.2: Characteristic lines for the dam break problem, with reflection from the downstream end-wall

The largest root corresponds to $\dot{\xi}$, while the smallest is the speed of the reflected bore $\dot{\xi}'$. The height of the reflected bore h_4 is found by solving

$$(u_2 - \dot{\xi}')h_2 = -\dot{\xi}' h_4 \tag{3.35}$$

or

$$h_4 = \frac{u_2 - \dot{\xi}'}{\dot{\xi}'} h_2. \tag{3.36}$$

The characteristic line between zones 2 and 4 is then

$$x = x_{\max} + \dot{\xi}'(t - t_4). \tag{3.37}$$

The limit of undisturbed area behind the gate (zone 1) moves back with the speed $-c_1$ and therefore reaches the upstream wall at

$$t_1 = -\frac{x_{\min}}{c_1}. \tag{3.38}$$

This forms a zone 5 (see Figure 3.3) in which h and c are affected by the upstream wall ($x = x_{\min}$). To estimate the time before those effects reach a location downstream, we need

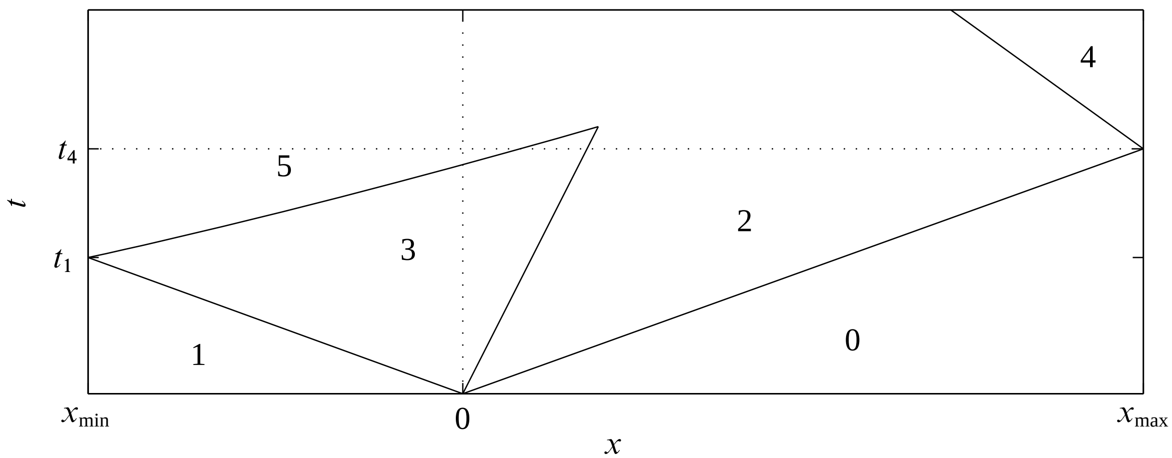

Figure 3.3: Characteristic lines for the dam break problem, with reflection from the end-walls

the characteristic line originating in $(t_1, x_{\min})$. Using the values of h and c in zone 3, the coordinates of any point on that characteristic line (t, x) fulfill the following differential equation

$$\frac{\mathrm{d}x}{\mathrm{d}t} = \frac{1}{3}\left(4c_1 - \frac{x}{t}\right). \tag{3.39}$$

Its solution for the given initial condition is

$$x = 2x_{\min}\left(\frac{t_1}{t}\right)^{\frac{1}{3}} + c_1 t. \tag{3.40}$$

This line intersects the line between zones 2 and 3 where the condition

$$2x_{\min}\left(\frac{t_1}{t}\right)^{\frac{1}{3}} + c_1 t = (u_2 - c_2)t \tag{3.41}$$

holds, or at

$$t_{25} = \left(\frac{2x_{\min}t_1^{\frac{1}{3}}}{u_2 - c_2 - c_1}\right)^{\frac{3}{4}}, \tag{3.42}$$

where the subscript 25 refers to the time and location at which the characteristic from t_1 affects zone 2.

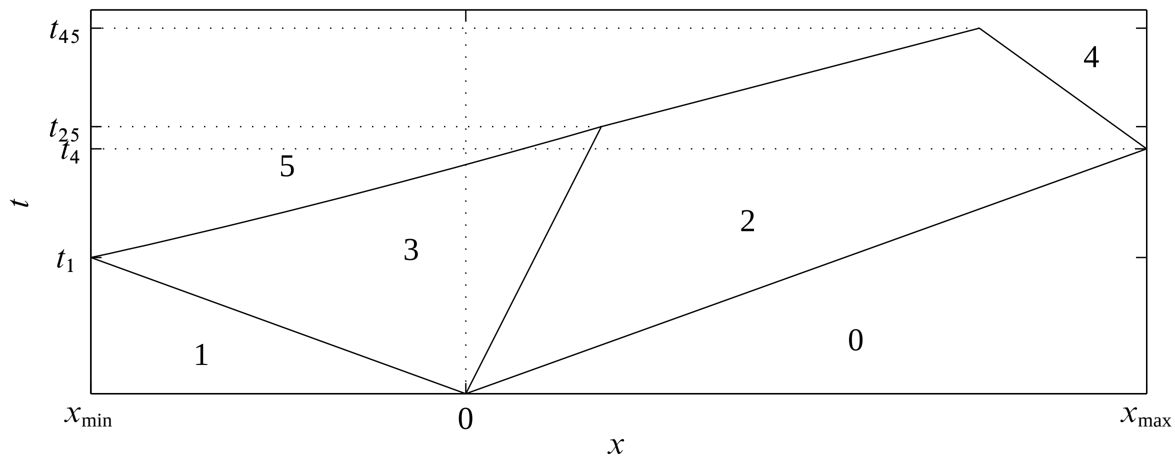

Figure 3.4: Characteristic lines for the dam break problem, with reflection from the end-walls

Now we need to find the characteristic line starting in (x_{25}, t_{25}). We do that in the same way except now we use h and c from zone 2 rather than 3. The constant water level gives us the straight characteristic

$$x = (u_2 + c_2)t. \tag{3.43}$$

We have then fully enclosed the area in the x-t plane representing the bore condition, i.e. zone 2 as can be seen in Figure 3.4.

3.2.4 Calculations

Calculations were carried out for the 16.62 m long tank used in this study for physical modelling (See §4.1 for the layout of the tank) and the various values of impoundment h_1. The resulting values of h_2, $\dot{\xi}$ and u_2 can be seen in Table 3.1 along with values of t_0 and t^*, which represent arrival times of the bore front and the effects of the back wall respectively, at $x = 5.2$ m, which is the location of the columns in the flow. The locus of the characteristic lines for each case can also be seen in Figures 3.5 through 3.13. For every case the initial downstream depth is $h_0 = 20$ mm.

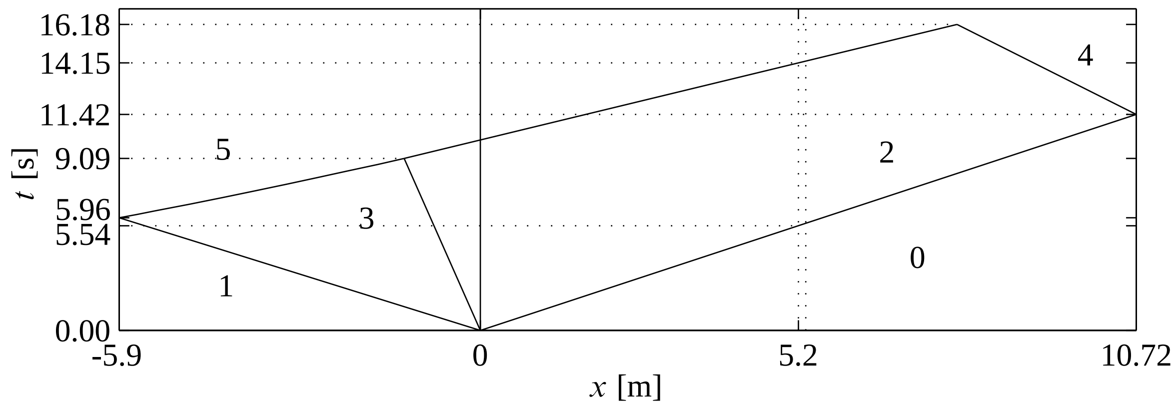

Figure 3.5: Characteristic lines bounding the bore for impoundment $h_1 = 100$ mm

Table 3.1: Bore heights h_2, propagation speeds $\dot{\xi}$, flow velocities u_2 and arrival times at $x = 5.2$ m of the bore t_0 and any effects of the back wall t^* for different impoundments h_1.

h_1	h_2	$\dot{\xi}$	u_2	t_0	t^*	Fr'
[mm]	[mm]	[m/s]	[m/s]	[s]	[s]	—
100	50.8	0.94	0.57	5.54	14.15	2.12
125	58.5	1.06	0.70	4.90	12.54	2.39
150	65.8	1.18	0.82	4.42	11.39	2.66
175	72.7	1.29	0.93	4.05	10.51	2.91
200	79.2	1.39	1.04	3.74	9.82	3.14
225	85.5	1.49	1.14	3.50	9.26	3.36
250	91.5	1.58	1.24	3.29	8.79	3.57
275	97.4	1.67	1.33	3.11	8.39	3.77
300	103	1.76	1.42	2.95	8.05	3.97

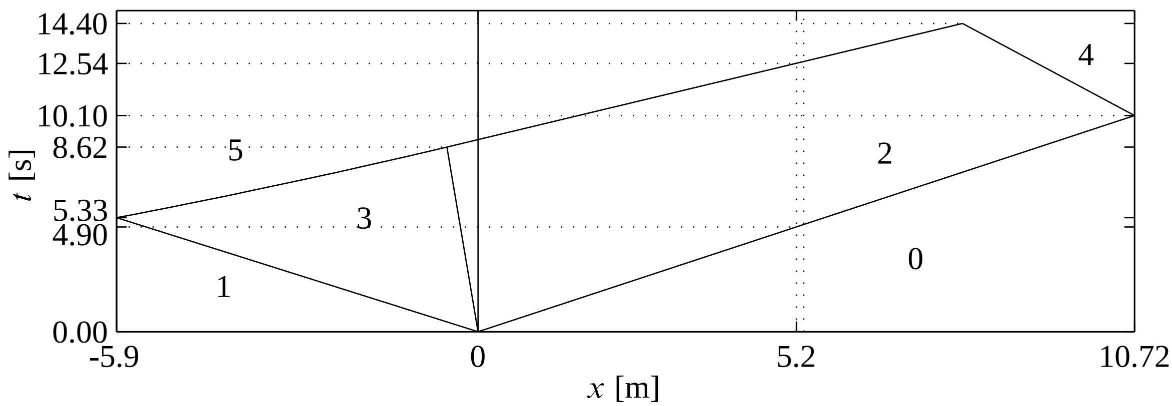

Figure 3.6: Characteristic lines bounding the bore for impoundment $h_1 = 125$ mm

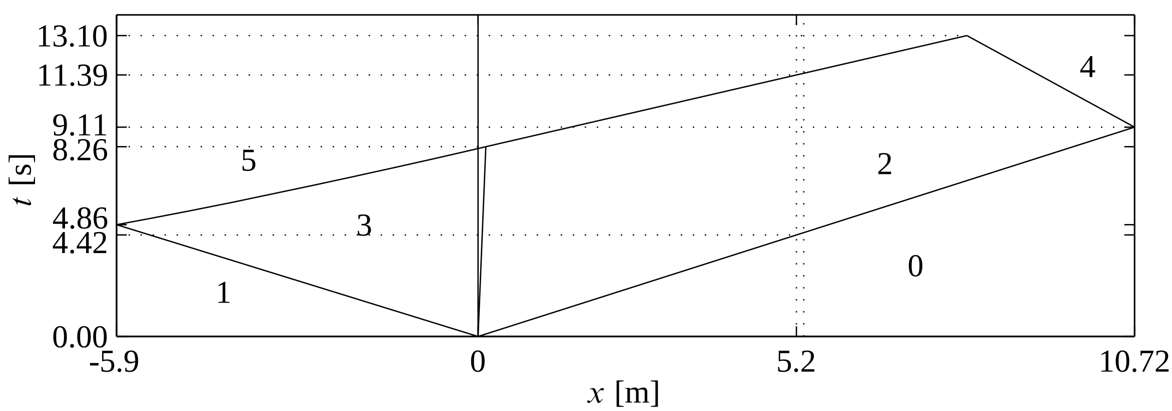

Figure 3.7: Characteristic lines bounding the bore for impoundment $h_1 = 150$ mm

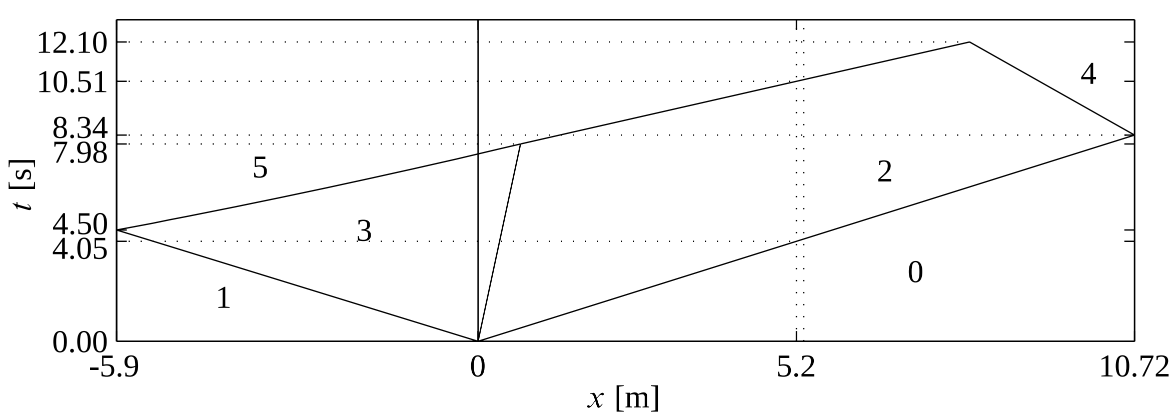

Figure 3.8: Characteristic lines bounding the bore for impoundment $h_1 = 175$ mm

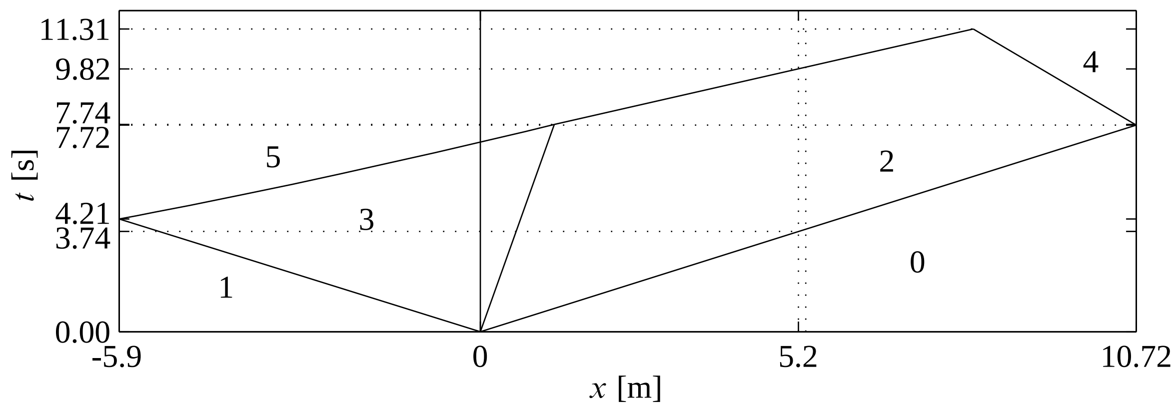

Figure 3.9: Characteristic lines bounding the bore for impoundment $h_1 = 200$ mm

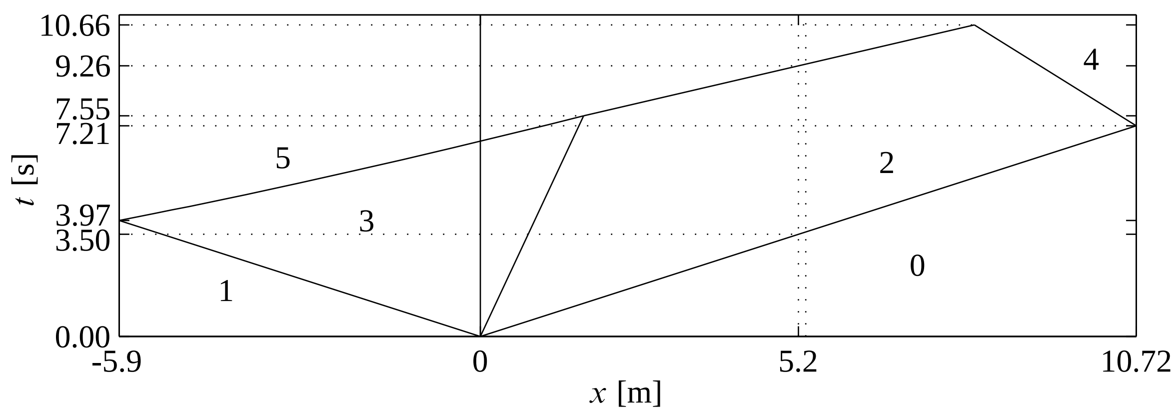

Figure 3.10: Characteristic lines bounding the bore for impoundment $h_1 = 225$ mm

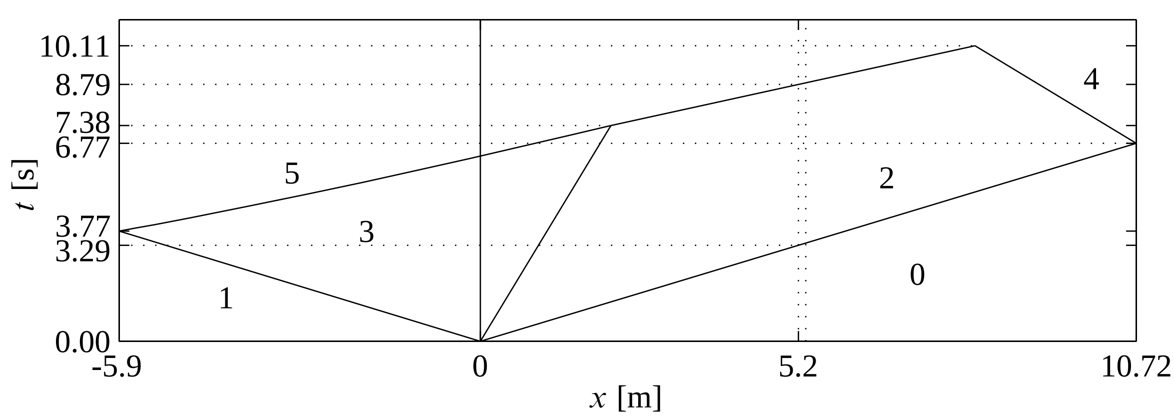

Figure 3.11: Characteristic lines bounding the bore for impoundment $h_1 = 250$ mm

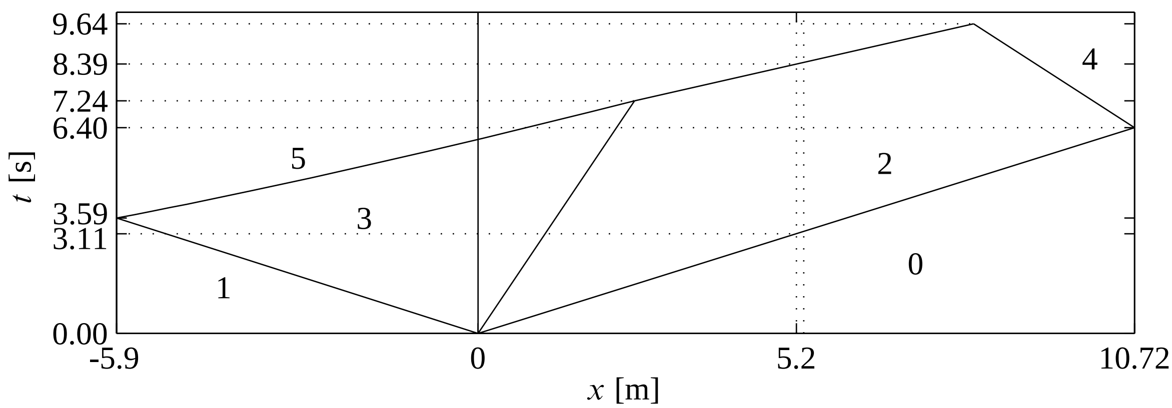

Figure 3.12: Characteristic lines bounding the bore for impoundment $h_1 = 275$ mm

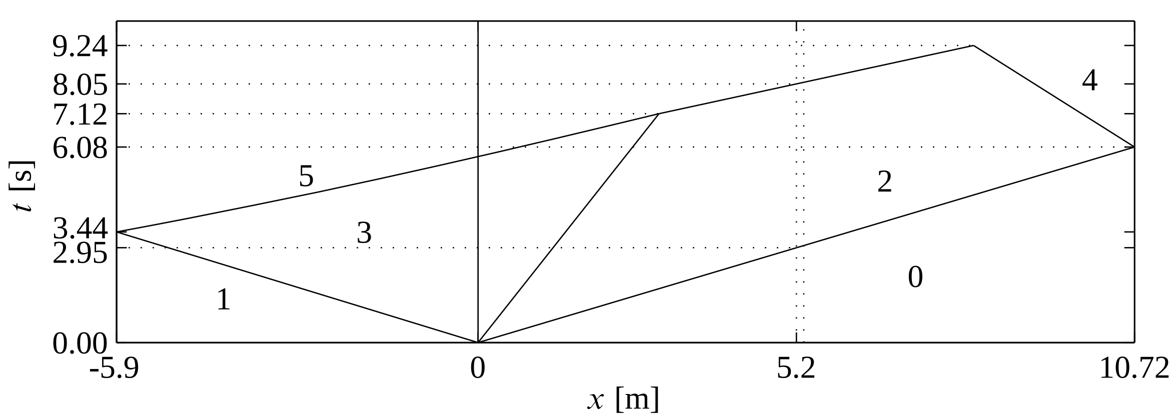

Figure 3.13: Characteristic lines bounding the bore for impoundment $h_1 = 300$ mm

Chapter 4

EXPERIMENTAL FACILITIES AND PROCEDURES

4.1 Location

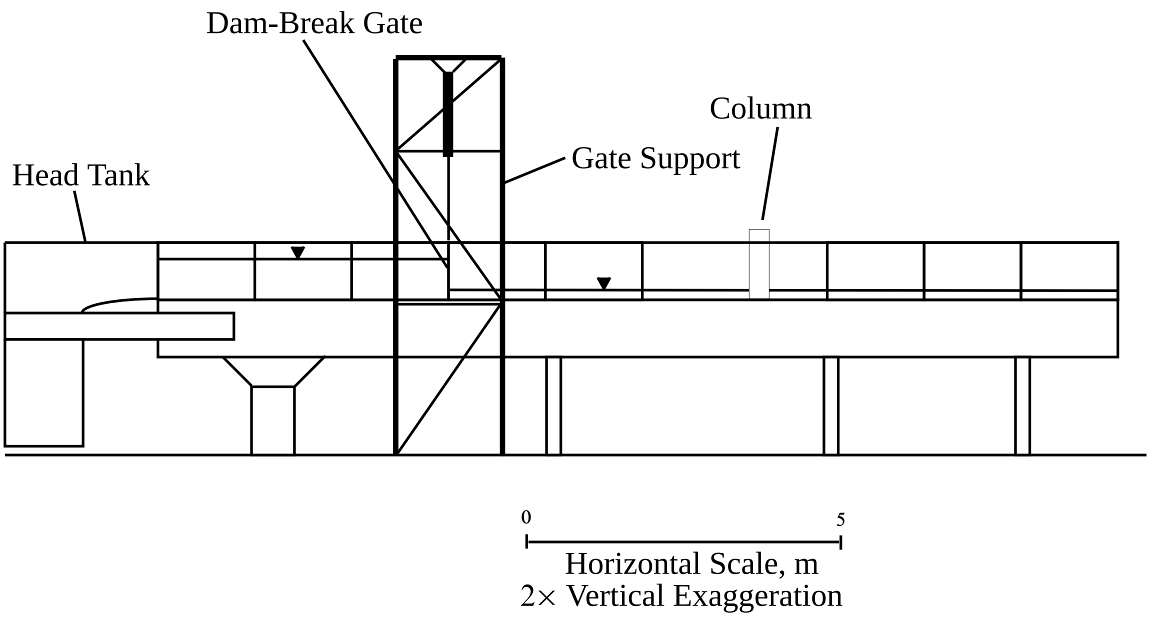

Figure 4.1: A diagram of the tank (adapted from Moore (1999))

Physical experiments were carried out in a wave tank (see Figure 4.1) at the Charles W. Harris Hydraulics Laboratory of the University of Washington. The tank is 16.62 m long, 0.61 m wide and 0.45 m deep. The tank walls are 13 mm thick plate glass. The tank is equipped with a pneumatically activated gate 5.9 m from the head tank (see Figure 4.2). The lift gate is made of 6.4 mm thick stainless steel and rides in an ultra-high molecular weight plastic track fitted into the walls of the tank. The gate is lifted by a 64 mm diameter pneumatic piston driven by 0.5 MPa air pressure. The piston can lift the gate at the average

Figure 4.2: The gate

speed of 2 m/s allowing the gate to reach the top of the tank in 0.2 s. The time it takes to clear the water surface depends on the impoundment. Figure 4.3 shows that for $h_1 =$ 250 mm, the gate has cleared the surface in 0.13 s.

Since the sides of the tank are made from glass, the flow can be viewed from the side. The bottom is primarily made from stainless steel, except for a 1.5 m long plexiglas window 5 m downstream of the gate. Over this window, an obstacle can be placed. The window enables a view from below or for a laser light shining from below to aid flow visualization.

4.2 Obstacles

The obstacles used in this study are three circular columns of varying diameters and a square column. The diameters of the three circular columns are 140 mm, 60.6 mm and 29 mm. They will hereafter be referred to as *large*, *intermediate* and *small* respectively. The square column is 120 mm × 120 mm. It can be set up in two different configurations. In one, referred to as *square*, it has two sides parallel to the tank side walls and consequently

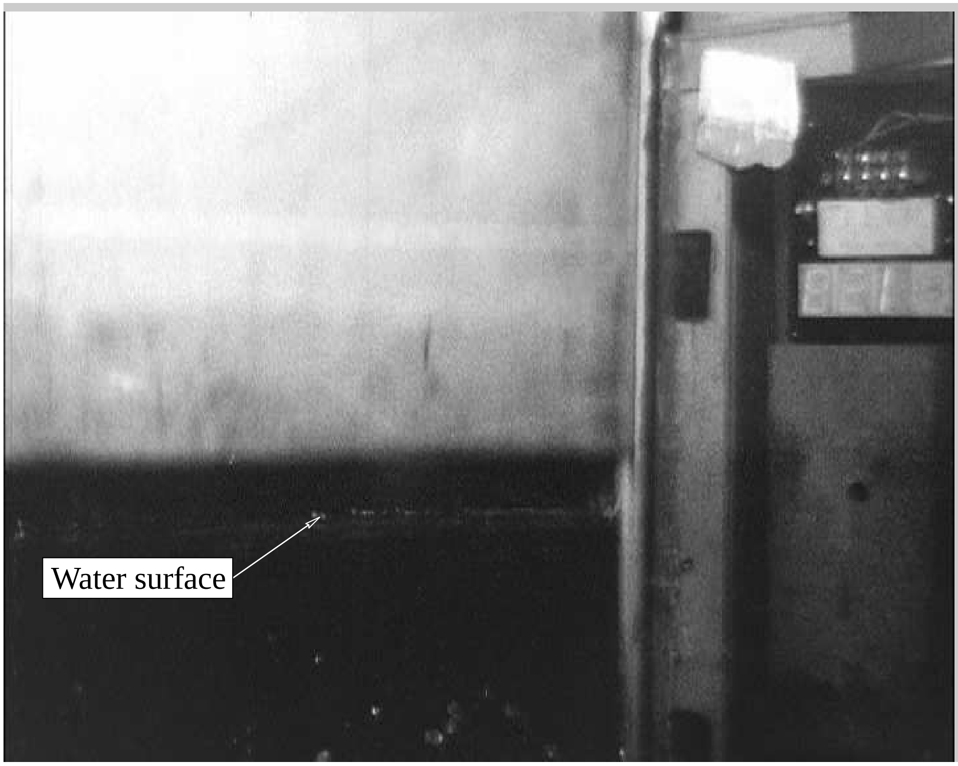

Figure 4.3: The gate has cleared the water surface at $t = 0.13$ s for $h_1 = 250$ mm

the other two perpendicular. In the other configuration, referred to as *diamond*, the column is rotated by 45°, so that one corner is facing the flow. The square and the large circular columns are made of acrylic. The material of the intermediate column is steel and the small one is aluminum.

4.3 Supporting structure

The obstacle is supported from above by a mount attached to the tank sidewalls. The support is set up so that all the hydrodynamic load impinges on the load cell (see §4.6). The acrylic columns are fastened to the load cell so that the cell is inside the column. This is optimal for the experiment since the force on the column is at about the centerline of the load cell and moments are minimized The load cell is then connected to a rigid vertical aluminum

Figure 4.4: View over the tank, the cylinder above the plexiglas window can be seen in the center of the picture

beam. The vertical aluminum beam is connected to a thick horizontal aluminum beam that lies across the tank and rests on instrument rails mounted on top of the tank's sides (see Figure 4.4). The medium and small circular columns are too small for the load cell to fit within them. In those cases the load cell is fastened to the cross beam and the columns then to the load cell. The connection for the medium column can be seen in Figure 4.6.

Since the column is not attached to the floor of the tank, it is important that it be stiff enough that the bottom of the column does not swing with the flow, bend considerably or touch the tank floor. To answer the question of whether the supporting structure is stiff enough, the following tests were performed. The structure was stiffened in successive steps so that its natural frequency of oscillation changed, then the forces on the square obstacle were measured (see §4.6). These measurements were performed in a shortened tank with 300 mm of water impoundment behind the gate.

The results of taking one of the force time series for the highest frequency of 28.5 Hz as a base time series and then finding the root-mean-square (rms) of the difference between

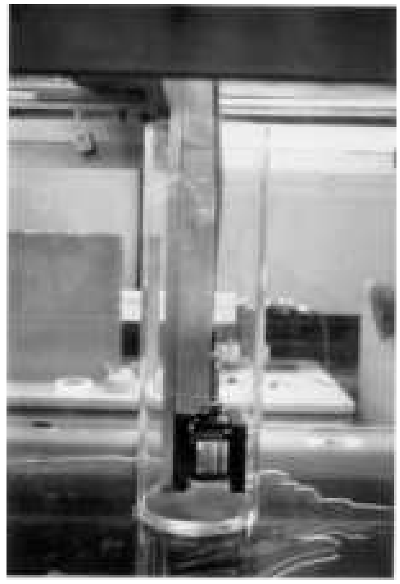

Figure 4.5: The cylindrical column

it and the other series, for a duration of 6 seconds from the time of impact, can be seen in Table 4.1. Where there was more than one time series for the same frequency the table shows the mean of the rms, i.e. the rms for each series was calculated and then the results were averaged. For $f_{\mathrm{N}} = 28.5$ Hz the base series was, of course, excluded from the average.

Looking at Figure 4.7, the time series at 22.5 and 24.0 Hz do not differ substantially from the series at 28.5 Hz. From this the conclusion can be inferred, that when the natural frequency of the structure has risen up to about 22 Hz, it has become stiff enough to not have a noticeable effect on the results. The natural frequency of 28.5 Hz is therefore high enough and the support structure is deemed stiff enough to be used in the following experiments.

4.4 Water level measurements

4.4.1 Surface profiles

To obtain a time history of the spatial variation of the water surface, laser induced image processing was used. This method is laid out in Gardarsson (1997). A two-dimensional

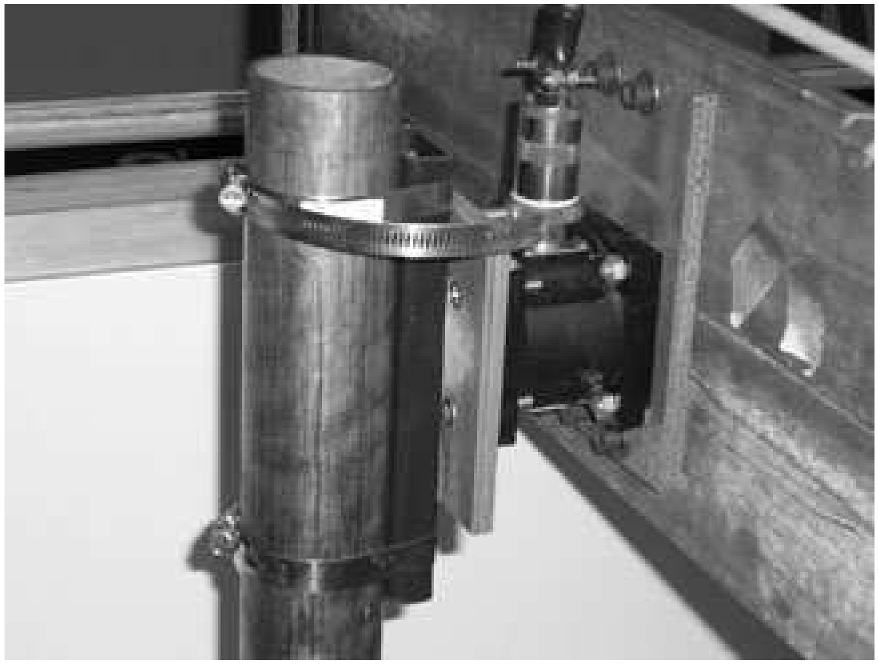

Figure 4.6: The connection of the column, load cell and the supporting beam

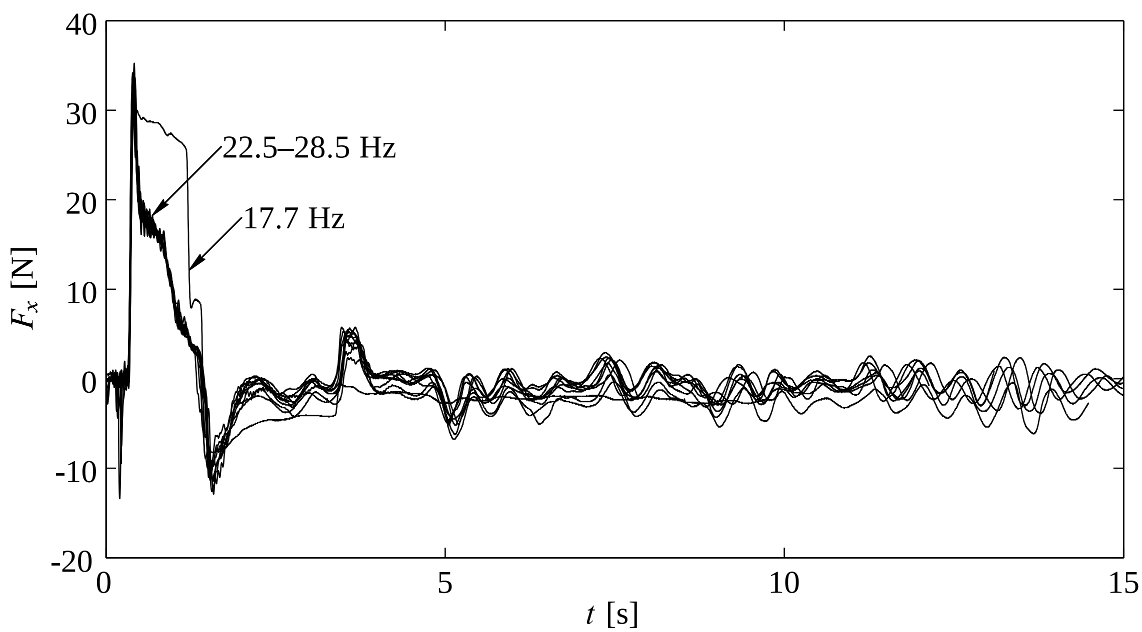

Figure 4.7: Force history for several runs using different configurations of the supporting structure

Table 4.1: Root-mean-square difference in force time history on the square column for different natural frequencies of the supporting structure

f_N [Hz]	Run 1 [N]	Run 2 [N]	Run 3 [N]	Run 4 [N]
17.7	6.03	6.03	5.90	6.05
22.5	1.41	1.46	1.01	1.49
24.0	0.91	1.46	1.21	1.57
28.5	1.45	1.61	1.35	1.65

vertical plane is illuminated by a laser and recorded on videotape during the experiment.

A 4 W Argon-ion laser (*Spectra Physics, Stability 2017*) is used to generate a laser beam. Next the beam is sent through a manipulator (*Dantec 60X24*) to align it to a fiber optic cable (*Dantec 60X0302*). The cable transports the beam to an oscillating mirror (*General Scannings, 6214*) which produces a laser sheet, used to illuminate a section of the flow in the tank. The mirror is driven by a scanner drive (*General Scannings, AX-200*) which controls the scanning amplitude, location of the sheet and the oscillating frequency. A uniform intensity is achieved by a skewed saw-toothed signal from a function generator. Unlike the DPIV (see §4.5.1), shining the laser from above is actually preferable in this case as it delineates a sharp surface interface. The intersection of the laser sheet with the water surface identifies the water surface profile. A video camera is used to capture the illuminated water surface. An image-processing software package called *Optimas* is used to digitize the images frame by frame from the video tape. *Optimas* is further used to trace and extract the coordinates of the water surface. The image processing is as follows:

Optimas 6.0, running on a *Gateway 2000, P5-200*, computer which drives the VCR (*Panasonic Desktop Editor, RS-232C*) is used to advance the video tape frame by frame. For each frame, *Optimas* uses a frame grabber (*Imaging Technology Visionplus-AT, OFG*

47-G30001-01) on the computer to acquire and digitize a relevant portion of the frame and place it in a digitized form in a file on the hard drive. An example of such a frame can be seen in Figure 4.8a. It is for $h_1 = 250$ mm and the square column.

The images on the video tape are slightly distorted because the camera records through the wall of the tank and at a small angle. To correct for this distortion and to calibrate the images, a calibration board is placed at the location of the laser sheet. At the start of each digitization the coordinates on the calibration board are entered into the *Optimas* database. These coordinates are then used to calibrate the images and correct for distortion.

Now, depending on the light intensity in the frame, a threshold value is chosen. The user has to choose the light intensity value that best conforms to the water surface. This traces not only the water surface but can delineate other phenomena such as reflections of the tank walls, droplets and other things. The coordinates of points on all the traced lines are written to a file (see Figure 4.8b).

To distinguish the water surface from all the other lines, scripts were developed in *Matlab*. First, all lines that fall outside the physical range of interest, indicated by dotted lines in Figure 4.8c, are removed. On one side, this range is usually limited by the location of the obstacle. Then, utilizing user input, the script goes systematically through the remaining lines piece by piece and determines whether they are a part of the water surface profile or not. This leaves the surface profile (thick line in Figure 4.8c). Figure 4.8d then shows the resulting surface profile. Figure 4.9 shows a number of such profiles for an impoundment $h_1 = 250$ mm impinging on the square column compiled on one plot. Each profile represents the water surface at $1/30$ of a second before or after the one next to it. The evolution of the surface can be seen from an advancing bore to the runup and splashup on the structure and the reflecting flow and disturbance of the water after the impact. The time is measured from the raising of the gate, the x coordinate is measured from the face of the obstacle and z is measured from the bottom of the tank.

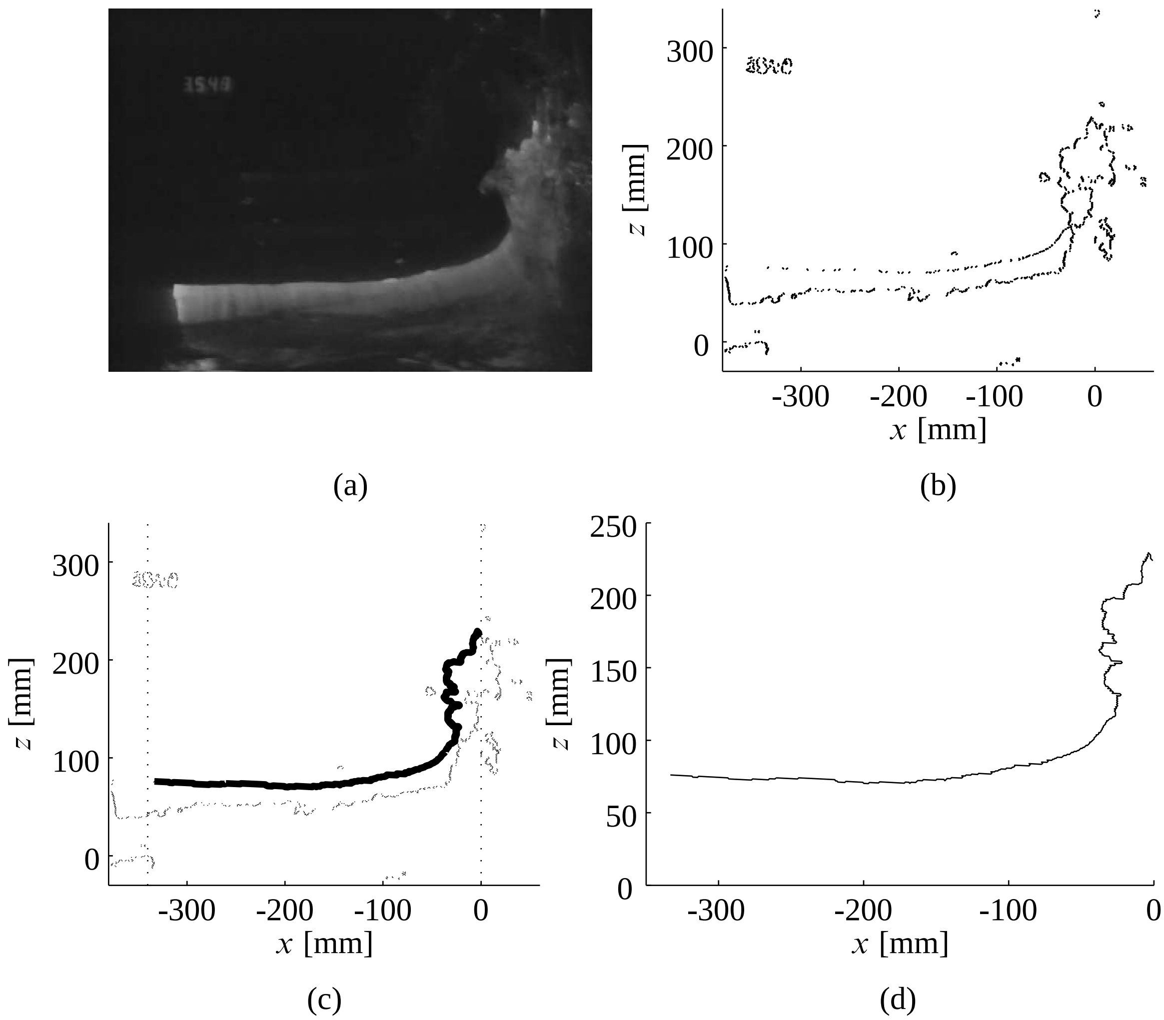

Figure 4.8: Water surface profile processing from a video capture. (a) A capture from a video. (b) Coordinates of isoluminous curves with spatial distortion corrected. (c) Range of interest defined (dotted lines) and the surface identified (thick line). (d) The resulting surface profile.

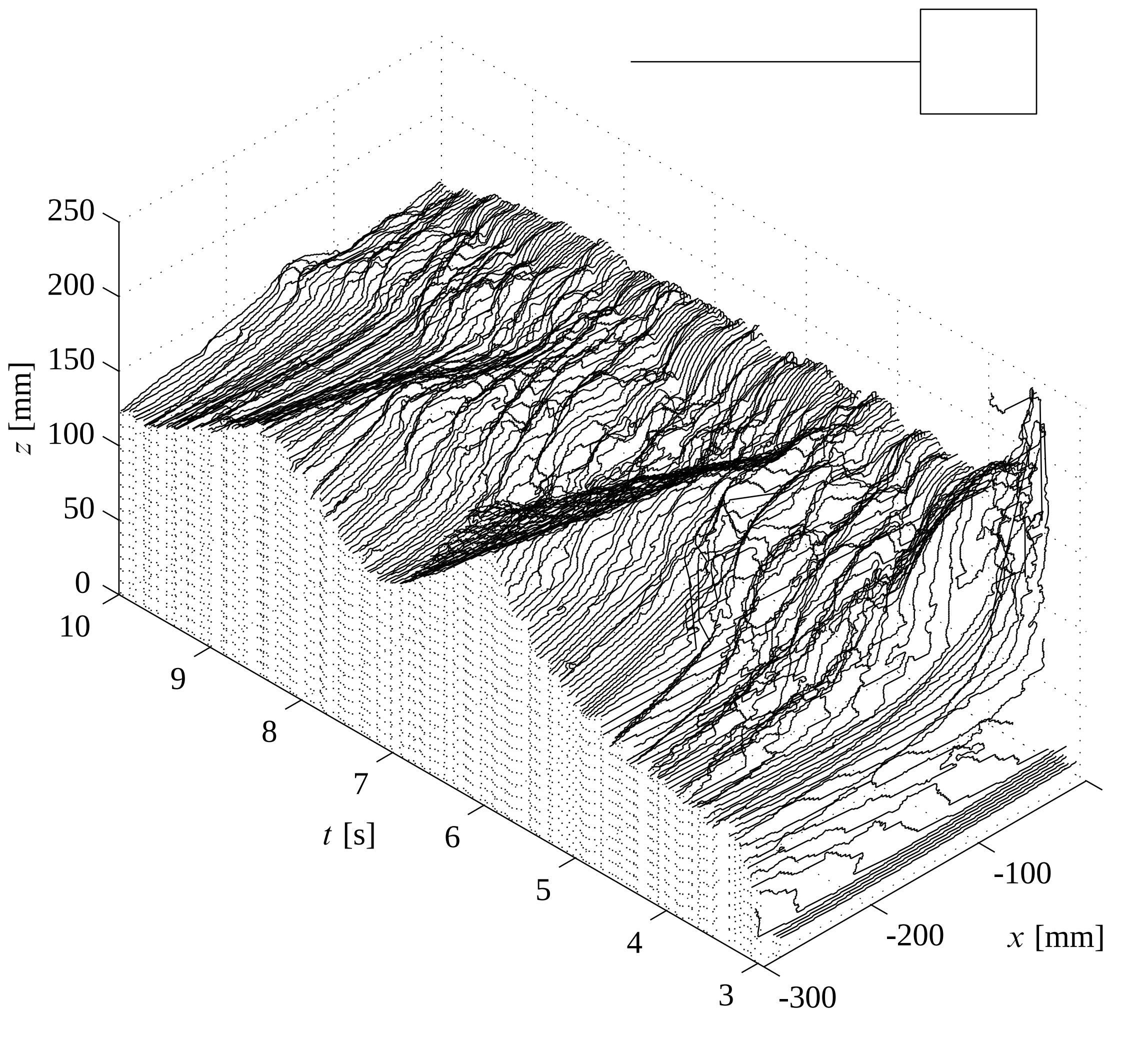

Figure 4.9: The evolution of the water surface profile

4.4.2 Film

No measurements were made in the wake close to the obstacle. However high speed films were used to get estimates of the water level on the downstream sides of the columns for the case of $h_1 = 250$ mm. The screws on the supporting structure can be seen on the films. Their location is known and therefore they can be used for calibration. Figure 4.10 shows each column with the supporting structure. The distance of the centers of each row of load cell screws to the bottom of the aluminum beam is 7.9 mm and 68.3 mm. The bottom of the larger screws are 107.5 mm and 184.9 mm above the bottom of the beam. For the square column the bottom of that beam is 15.5 mm above the tank floor, while it is 36.5 mm above the floor for the large circular beam. Those heights can then be calibrated with the pixel line numbers on a digitized frame from the film using a linear relation, as can be seen in Figure 4.11. For the square column a least square regression gives the relation as

$$z = -1.10 \text{ mm} \times N_\text{l} + 246 \text{ mm}, \tag{4.1}$$

where N_l represents the pixel line number. The linear relation indicates that any distortion is not a problem in the z-direction. For the circular column the corresponding relation is

$$z = -0.98 \text{ mm} \times N_\text{l} + 200 \text{ mm}. \tag{4.2}$$

The aforementioned beam and the screws are inside the columns and therefore never come in contact with the water. In the case of the square column it is 17 mm from the outside of the wall and 29 mm in the case of the circular one. This means that the water level at the outside of the column is higher than at the screw pattern would indicate. The height difference was calculated as

$$\Delta z = \Delta x \sin\theta \tag{4.3}$$

where Δx is the distance of the aluminum beam from the outside of the column and θ is the angle of view of the camera from horizontal. Effects of refraction are negligible.

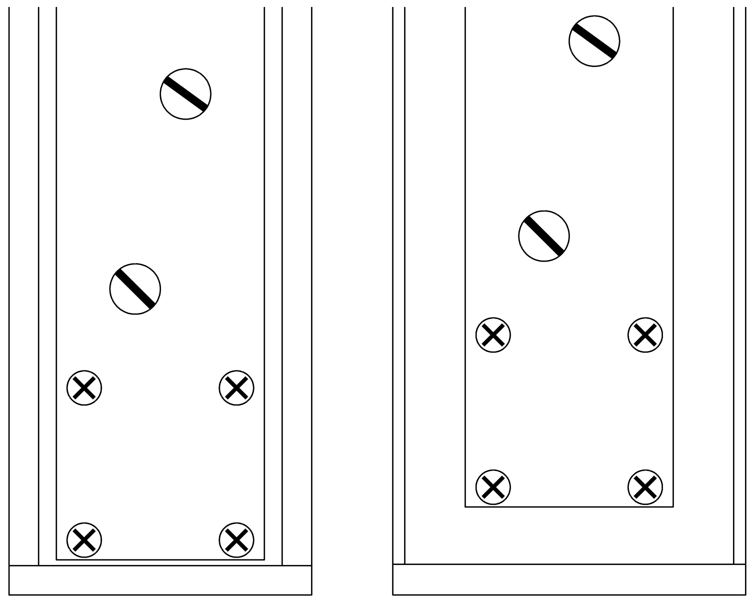

Figure 4.10: Views of the square and circular column from downstream (scale 1:3)

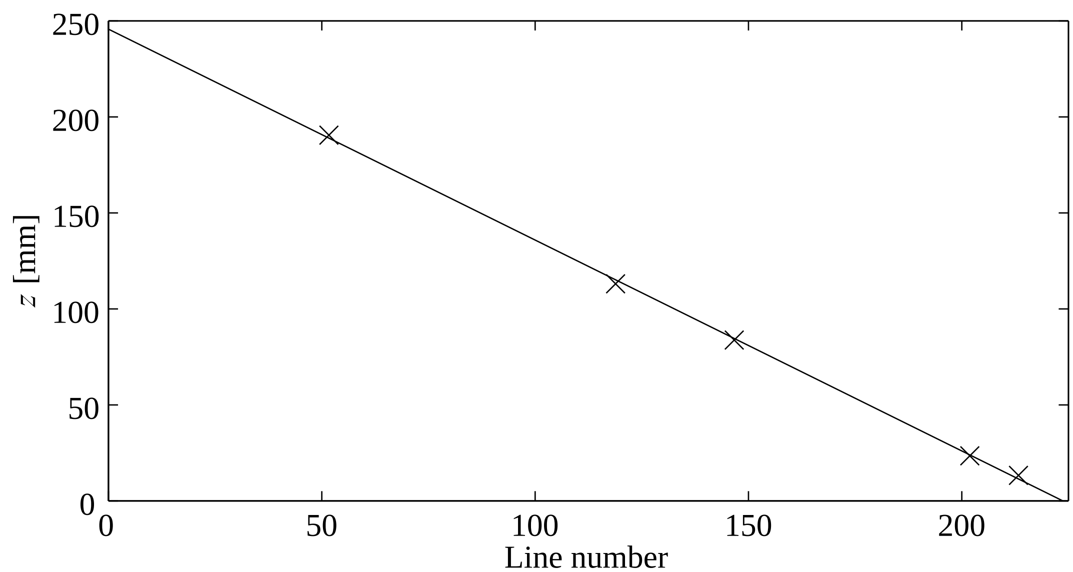

Figure 4.11: Typical calibration of the vertical coordinates for the square column

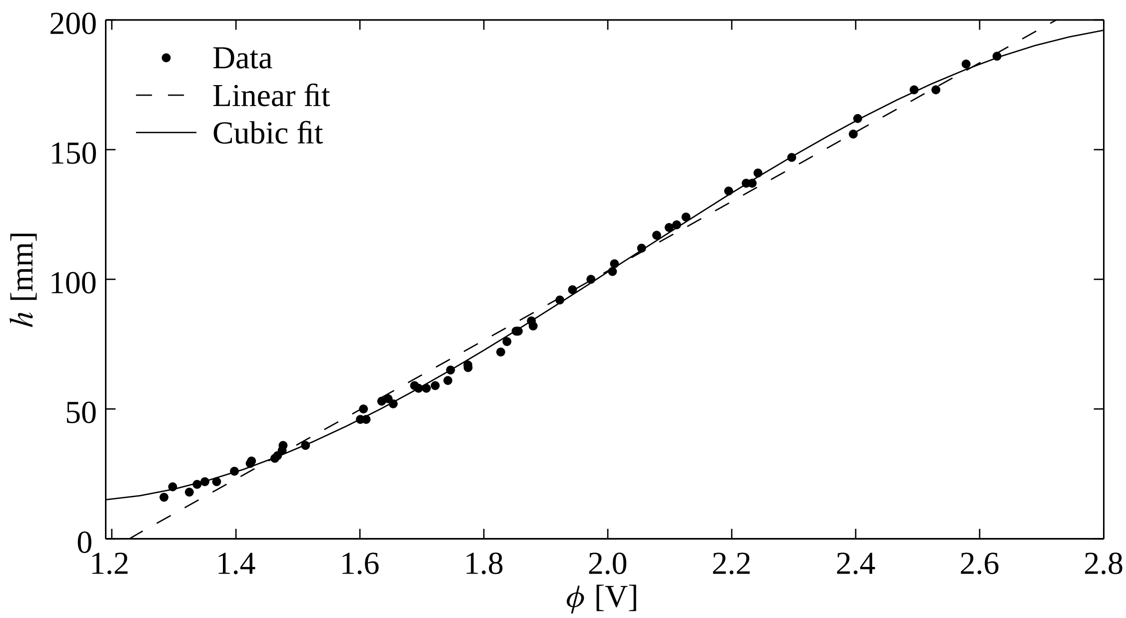

Figure 4.12: Calibration curve for the wave gauge

4.4.3 Wave gauge

In some instances the water surface was recorded with a capacitance wave gauge consisting of a steel rod with a diameter of 3.1 mm, with plastic tubing and sealed at the bottom with a plastic plug. The analog voltage output of the gauge is then transferred to a personal computer using a data acquisition system from *Computer Boards Inc.* The same system is also used to acquire data from the load cell (see §4.6). The gauge is calibrated by taking measurements in standing water of varying known depths. A typical calibration curve is shown in Figure 4.12. Calibrating the voltage ϕ with the water level by means of a least square regression gives a cubic calibration formula in the form of

$$h = -64.50\ \mathrm{mm/V^3} \times \phi^3 + 391.4\ \mathrm{mm/V^2} \times \phi^2 - 637.4\ \mathrm{mm/V} \times \phi + 391.4\ \mathrm{mm}. \quad (4.4)$$

4.5 Velocity measurements

4.5.1 Digital particle image velocimetry

Measurements of velocities were done with a digital particle image velocimeter (DPIV) from *TSI Inc* (see Figure 4.13). It can measure the flow velocity in a two dimensional plane. It measures the velocity components in that plane.

A dual-head *Continuum Nd:YAg* laser is used to generate a pulsating laser beam. The beam is passed through a cylindrical lens to form a sheet. Each head pulsates at the same frequency f_{f}, but with an offset Δt. The timing of the video camera is synchronized with the lasers so one pulse occurs at the end of the first exposure period and then the other at the start of the second exposure period (see Figure 4.14). This allows short time intervals between pulses so that high velocity flows can be measured. The maximum acquisition rate is then half of the frame rate of the camera as two image frames are required for each measurement. For our 30 Hz camera the maximum flow sampling rate is 15 Hz. The values used in these experiments were $f_{\mathrm{f}} = 14$ Hz and $\Delta t = 0.4$ ms.

A digital 30 Hz video camera is used to take pictures of the illuminated area and the images downloaded to a personal computer (*Micron Millenia Pro2*). The computer has a 267 MB internal memory. A large internal memory is necessary so that a sequence of video captures does not have to be written to disk while capturing is taking place, as that would be too time consuming. A software package called *Insight* is then used to compute the velocity at several points by looking at the cross-correlation of the location of particles in the water between consecutive frames. Two-frame cross-correlation uses two image frames with one pulse of light on each frame. The flow velocity is found by measuring the distance the particles have travelled from one frame to the next.

For the best results, a camera that can capture a picture and then move the image into memory and start integrating the next image frame quickly is desired. The movement of charge between the photosensitive pixels and memory must be very fast for high-speed two-frame cross-correlation. The time it takes from the end of one exposure period to the start

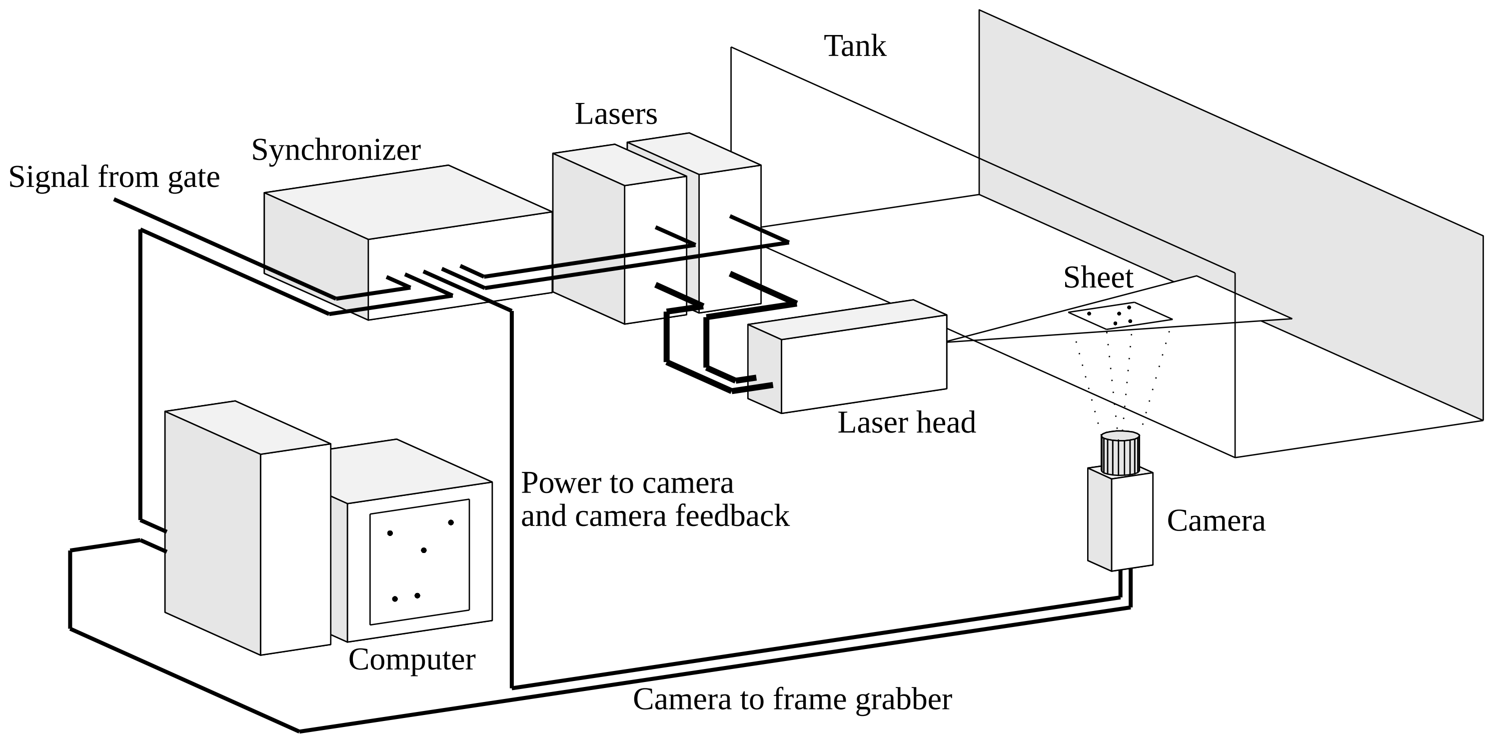

Figure 4.13: Schematic of digital particle image velocimetry setup

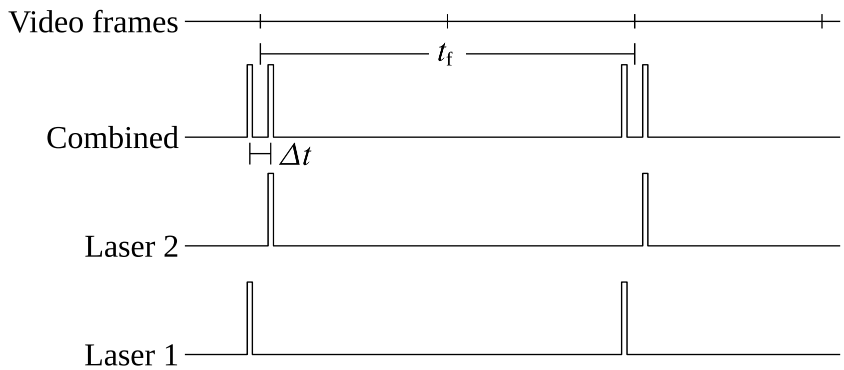

Figure 4.14: Timing of laser pulses for DPIV measurements

of the next exposure period determines the maximum flow velocity that can be measured. The time it takes to read out the image from the CCD to the computer determines the frame rate or how frequently the flow can be sampled.

The cross-correlation function is computed using Fast Fourier Transforms (FFT). The power spectrum is computed from the sum of the squares of the real and imaginary components. The square root of the computed power spectrum should be used to get the same scaling factors for the peak intensities to compare the direction correlation techniques with FFT correlation. Calculating the square root of the computed power spectrum is skipped to save processing time. It does not affect which peak is selected as the displacement peak, but it does change the relative peak intensities and the signal-to-noise ratio numbers.

For there to be enough particles in the water for the laser light to reflect off and be visible on the video, the water needs to be seeded with reflective particles. Therefore 8–12 μm hollow glass spheres are added to the water. The density of the spheres is in the range of 1050–1150 kg/m^3. The fall velocity for the particles would then be 2–12 μm/s, meaning it would take a particle about 100–500 s to fall 1 mm. The particles can therefore be considered neutrally buoyant for the purpose of these measurements.

4.5.2 Laser doppler velocimeter

Another velocity measuring device available at the time at Harris Laboratory is a non-intrusive two-component back-scattering Laser Doppler Velocimeter (LDV) system from Dantec Electronics Inc. It can offer more frequent measurements than the DPIV, but can only measure velocity at one point at a time. It measures two-dimensional velocity components in a plane perpendicular to the laser beam.

The LDV system used in this study consists of the optics, the fiberflow system and the processor and a 4 W argon-ion *Coherent Innova 70* laser. After coming out of the laser, the laser beam is split into three separated beams (blue, green and cyan) as it passes through the beam splitters of the optics. Both the green beam and the blue beam are shifted by the Bragg cell inside the optics (the shifted frequency for the the LDV system is 40 MHz). The three laser beams are directed by the fiberflow system. The fiberflow system has three manipulators which direct the three laser beams through a probe distribution box into the fiber probe. Then the laser beams shoot out through the fiber probe which is placed on a levelled positioning system with three degrees of freedom. The laser beams focus at a focal point (inside the fluid) in front of the fiber probe. The focal lengths used for this LDV system are either 160 or 600 mm by changing the optical head. Small particles in the measurement fluid will scatter the laser light. The scattered light is collected by a spherical lens (the same lens as the transmitting lens) and converted into an electrical signal by a high speed photodetector. The frequency of the electrical signal, which is proportional to the particle velocity, is then measured with an electrical device.

The processor receives signals from three detectors (located at different and well specified scattering angles) to estimate the Doppler frequency from which the two-dimensional velocity of the particle is calculated. The signal from the photodetector is bandpass filtered and amplified. The signal is then fed to a delay line that delays the signal by a time t and to a phase splitter that produces two outputs with a phase difference of $\frac{\pi}{2}$. The function of the phase splitter is to transform the signal from the real form $\cos \omega t$ into the complex form

$\cos \omega t + \mathrm{i} \sin \omega t$. Each output from the phase splitter is now multiplied by the delayed signal and integrated to form both the real and the imaginary part of the auto-covariance function. The two integrators are gated by a signal generated by the burst detector. The detected burst envelope signal does not depend on the Doppler frequency, provided that it is within the passband of the input filters. Also the signal to noise ratio is very low, since the delay t has been chosen to assure that the correlation between the noise of the two input signals to each of the multipliers is negligible. The resolution of the LDV system is 1.56 mm/s. The sideways-looking setup of these experiments means that the location of the measurements goes from being in air to fluid, as the bore front passes, with a lot of bubbles in between. This also means that the system can not make any measurements until the bore passes the measurement location.

4.6 Force measurements

The load on the column is measured by a multi-component force transducer (*Advanced Mechanical Technology Inc., MC3A-6-100*), referred to as load cell in this dissertation. It can measure the force in three dimensions and moment around three axes. The load cell incorporates strain gauges and a precision cylindrical element to isolate and measure applied forces and moments. Bridge excitation and signal amplification are required. The amplifiers process the signals from a transducer and provide analog outputs.

In the same way as for the wave gauge (see §4.4.3), the analog output of the transducer is then transferred to a personal computer using a data acquisition system from *Computer Boards Inc.* The acquisition board can handle 8 analog to digital input channels. The *Computer Boards' DAS Wizard* is a macro package for use within *Microsoft Excel,* so the data is gathered into a *Excel worksheet.*

The load cell is calibrated using a *Sheppo—Digital load gauge.* The gauge is pressed against the column, and the peak force is recorded and compared with the peak voltage from the load cell. A calibration curve is then made by fitting a curve to the data using

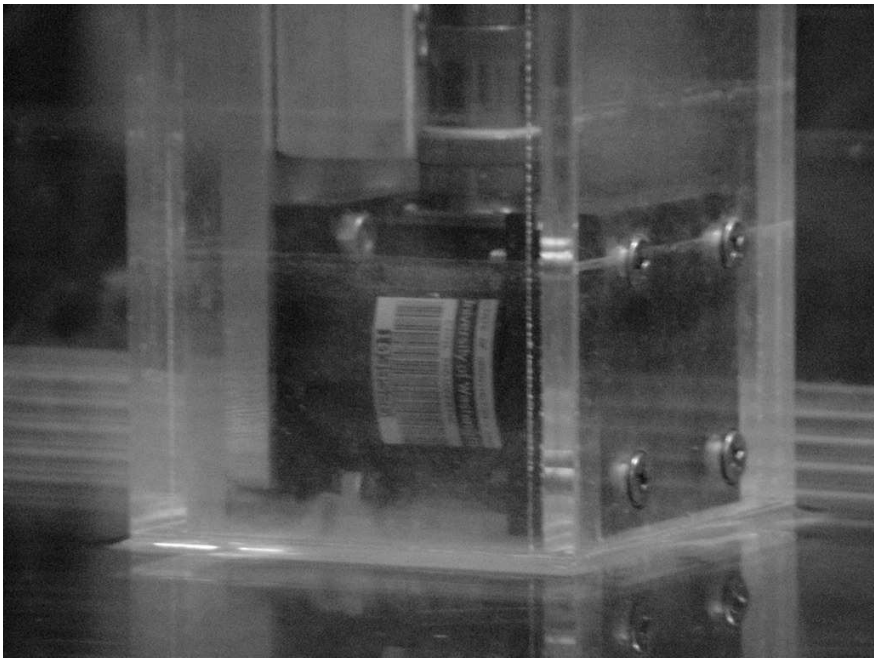

Figure 4.15: The load cell inside the square column

least squares regression. For the large columns, where hydrodynamic forces act directly on the load cell, the data can be fit to a straight line and furthermore this line has the same slope for both the circular and square column, so $F_x = 20.0\ \mathrm{N/V} \times \phi_x$, where ϕ_x is the voltage from the load cell corresponding to the force in the x-direction. However when the load cell is mounted above the water surface, some of the force in the x-direction translates into vertical forces and moment in the x-z plane, before going through the load cell. This makes it necessary to include into the calibration formula for F_x, the voltage from the load cell corresponding to F_z and M_y. An example of a single push with the calibrating gauge, for the medium circular column is shown in Figure 4.16. The voltage deviation from the baseline for channels corresponding to F_x, F_z and M_y are represented by ϕ_x, ϕ_z and φ_y respectively. The baseline for the vertical force lies at the maximum capacity of the load cell, so we can not trust that this is the actual baseline, i.e. for some non-zero values of F_z we can still record $\phi_z = 0$. Therefore it is necessary to include a constant term. Including

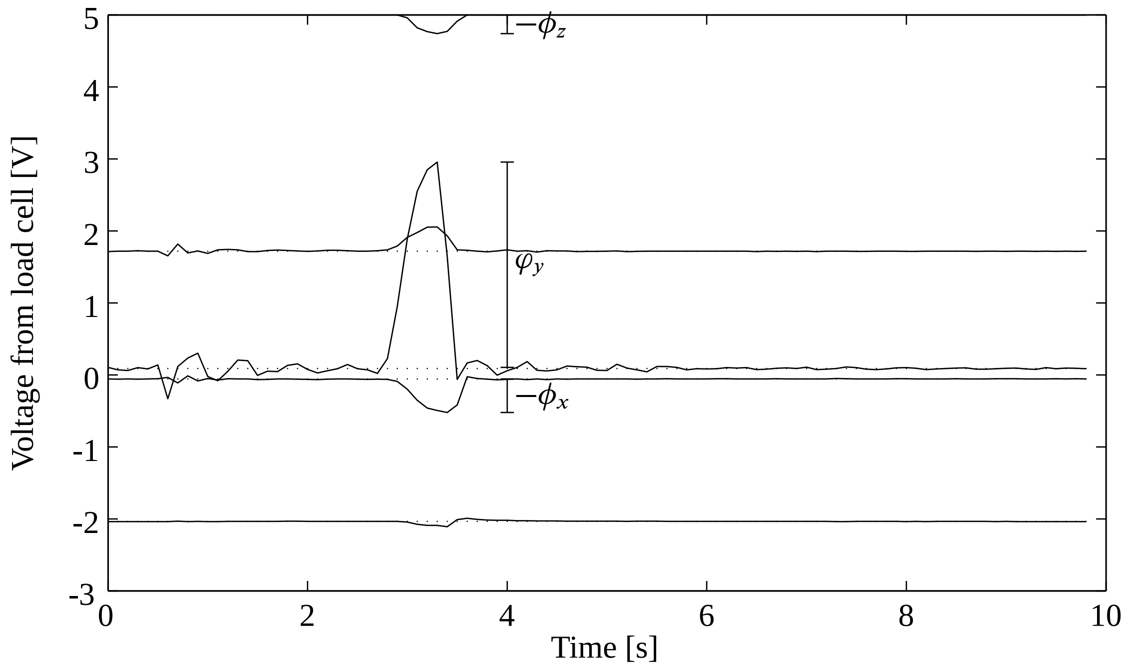

Figure 4.16: An example of load cell data from one push with the force meter on the intermediate circular column

the second order terms, the form of calibration curve is then

$$F_x = \alpha_1\phi_x + \alpha_2\phi_x^2 + \alpha_3\phi_z + \alpha_4\phi_z^2 + \alpha_5\varphi_y + \alpha_6\varphi_y^2 + \alpha_7. \tag{4.5}$$

and a least square regression gives the following values for α_i, $\alpha_1 = -30.37$ N/V, $\alpha_2 = 16.59$ N/V^2, $\alpha_3 = -19.32$ N/V, $\alpha_4 = -25.14$ N/V^2, $\alpha_5 = -1.388$ N/V, $\alpha_6 = -0.1484$ N/V^2 and $\alpha_7 = -0.4775$ N.The small circular column was calibrated similarily.

4.7 Synchronization

To use all the measurements together it is important to be able to know what is going on at specific times for each measurement device. A trigger system was set up so that when the gate was released, a precise clock started in view of video for the visual surface data. The

Table 4.2: Surface profiles

h_1	Circular				Square			Diamond		
	Centerline	Along side	60 mm off side	Centerline downstr.	Centerline	Along side	60 mm off side	Centerline	70 mm off centerline	180 mm from wall
100 mm			•		•	•	•	•	•	
125 mm					•			•		
150 mm					•			•	•	
175 mm					•			•		
200 mm	•	•		•	•	•	•	•	•	
225 mm					•			•		
250 mm	•	•	•	•	•	•	•	•	•	
275 mm					•			•		
300 mm	•	•			•	•	•	•	•	•

trigger also sends an indication of the gate release to the data gathering system for both the force and velocity and time is set to zero.

4.8 Experiments

4.8.1 Surface profiles

Surface profiles using a laser light sheet were taken for the cases shown in Table 4.2. There, the vertically oriented text refers to the position of the vertical laser sheet and therefore the surface profile. *Centerline* refers to the upstream centerline of the column in the direction of the flow. The sheets marked *Along side* are one radius (for the circular column) or half a side length (for the square) from the centerline sheets in the same direction. The sheets marked 60 mm *off side* are then parallel to the *Along side* profiles but 60 mm further away. The left-most column h_1 refers to the impoundment behind the gate.

4.8.2 Velocity measurements using DPIV

The DPIV was used to measure flow fields for the cases shown in Table 4.3. In it the left most column, refers to the impoundment behind the gate. The second column is the position of the lasersheet, *upstream* refers to a camera view of one of the upstream corners of the column in question and *downstream*, then refers to a similar view, only of a downstream corner. The camera views for the circular column are shown in Figure 4.17, marked ‘u’ and ‘d’.

The columns in Table 4.3 under the word *No obstacle* refer to measurements made without any column in the tank. The second line of vertically oriented text in the table refers to the height of the sheet above the tank floor.

DPIV-measurements for all regions shown in Figure 4.17 were made for the circular column at 15 mm above the tank floor for impoundments of 250 mm and 300 mm and at 35 mm above the floor for an impoundment of 250 mm.

4.8.3 Velocity measurements using LDV

4.8.3.1 The bore

The LDV was used to acquire a velocity profile in bores of different sizes. The measurements were first made without any obstacles in the flow. They were made at varying heights above the floor on the centerline 5200 mm downstream of the gate. This location corresponds to the obstacles’ most upstream points. Table 4.4 shows the heights, z, at which measurements were made for each impoundment, h_1. In each case the two horizontal velocity components were measured.

Table 4.3: The DPIV measurement matrix

		Circular					Square									No obstacle		
		Large				Small	Straight				Oblique						
		15 mm off floor	35 mm off floor	75 mm off floor	115 mm off floor	35 mm off floor	15 mm off floor	35 mm off floor	75 mm off floor	115 mm off floor	15 mm off floor	35 mm off floor	75 mm off floor	115 mm off floor	15 mm off floor	35 mm off floor	75 mm off floor
100 mm	upstream	•	•			•	•	•			•					•	
	downstream	•				•	•	•			•						
125 mm	upstream	•	•				•	•			•					•	
	downstream	•															
150 mm	upstream	•	•	•			•	•			•					•	
	downstream	•	•														
175 mm	upstream	•	•	•			•	•			•					•	
	downstream	•	•														
200 mm	upstream	•	•	•	•	•	•	•	•		•	•	•			•	
	downstream	•	•			•	•	•			•	•					
225 mm	upstream	•	•	•	•		•	•			•					•	
	downstream	•	•														
250 mm	upstream	•	•	•	•	•	•	•	•	•	•	•	•		•	•	•
	downstream	•	•			•	•	•			•	•					
275 mm	upstream	•	•	•	•		•	•			•					•	
	downstream	•	•														
300 mm	upstream	•	•	•	•	•	•	•	•	•	•	•	•	•	•	•	•
	downstream	•	•			•	•	•			•	•					
400 mm	upstream		•													•	
	downstream		•														

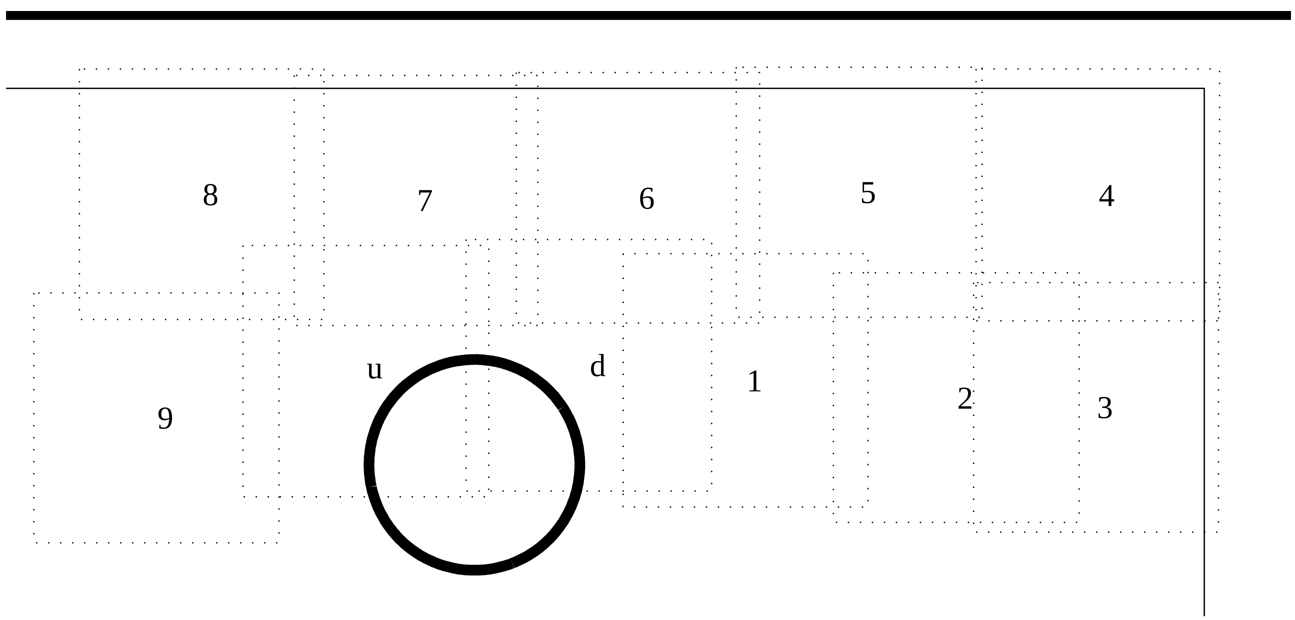

Figure 4.17: Regions of DPIV measurements

Table 4.4: LDV measurements of (u, v) without any obstacle in the flow 5.2 m downstream of the gate

h_1	z [mm]								
[mm]	8	14	19	30	36	46	56	82	89
100	•	•	•						
125	•	•	•	•	•	•			
150	•	•	•	•	•	•			
175	•	•	•	•	•	•			
200	•	•	•	•	•	•	•		
225		•	•		•	•	•	•	
250	•	•	•	•	•	•	•	•	•
275	•	•			•	•	•	•	•
300	•	•	•	•	•	•	•	•	•

Table 4.5: LDV measurements of (u, w) with no obstacle, $h_1 = 300$ mm

x	y	z
−1200 mm	0 mm	30 mm
−1200 mm	0 mm	50 mm
−1200 mm	0 mm	70 mm
−1200 mm	0 mm	90 mm
−1200 mm	0 mm	110 mm
−1200 mm	100 mm	50 mm
−1200 mm	200 mm	50 mm
−1200 mm	260 mm	50 mm

For a single boreheight $h_1 = 300$ mm, u and w, i.e. the velocity components in the x-z plane, were measured further upstream. The coordinates of the measurement points can be found in Table 4.5.

4.8.3.2 The wake

The horizontal velocity components were measured with LDV at several points downstream of the circular column. The plan layout of the points can be seen in Figure 5.48. For each position, measurements were made at 15 mm and 35 mm off the floor. These measurements were made with $h_1 = 250$ mm.

4.8.3.3 Upstream of the circular column

As in the wake, the horizontal velocity components were measured for $h_1 = 250$ mm. Those measurements were made at points forming a 3×3 matrix with $y = 0$ mm, 70 mm and 130 mm measured from the centerline and $z = 8$ mm, 24 mm and 60 mm measured from the tank floor. This cross-section was set at $x = -300$ mm, i.e. 300 mm upstream of the obstacles extreme upstream point or 4900 mm downstream of the upstream edge of the gate. For $h_1 = 300$ mm, u and w were measured at larger distances upstream of the circular column. The coordinates of the measurement points can be found in Table 4.6.

4.8.3.4 Around the square column

Using $h_1 = 250$ mm the two horizontal velocity components were measured at a few points around the square column. The coordinates of the measurement points can be found in Table 4.7. There x is the downtank direction, y is crosstank, z is up and $(x, y, z) = (0, 0, 0)$ at the center of the upstream face of the column at floor level. The upstream face of the gate is at $x = -5200$ mm.

Table 4.6: LDV measurements of (u, w) upstream of the circular column, $h_1 = 300$ mm

x	y	z
−1200 mm	0 mm	30 mm
−1200 mm	0 mm	50 mm
−1200 mm	0 mm	70 mm
−1200 mm	0 mm	90 mm
−1200 mm	0 mm	110 mm
−1200 mm	−100 mm	50 mm
−1200 mm	−200 mm	50 mm
−1200 mm	−260 mm	50 mm
−2400 mm	0 mm	40 mm
−3200 mm	0 mm	50 mm
−3200 mm	0 mm	70 mm
−3200 mm	0 mm	90 mm
−3200 mm	0 mm	110 mm
−3200 mm	−100 mm	70 mm
−4200 mm	0 mm	50 mm
−4200 mm	−140 mm	50 mm

Table 4.7: LDV measurements around the square column, $h_1 = 250$ mm

x	y	z
-60 mm	0 mm	30 mm
-60 mm	-60 mm	30 mm
-60 mm	-120 mm	30 mm
-120 mm	0 mm	30 mm
180 mm	0 mm	30 mm
180 mm	-60 mm	30 mm
180 mm	-120 mm	30 mm
240 mm	0 mm	30 mm

4.8.4 Force measurements

Force measurements using the larger obstacles, i.e. both orientations of the square and the large circular, were made for impoundments h_1 of 100 mm, 125 mm, 150 mm, 175 mm, 200 mm, 225 mm, 250 mm, 275 mm and 300 mm. For the small and intermediate circular columns, force was measured for h_1 of 100 mm, 150 mm, 200 mm, 250 mm and 300 mm.

Chapter 5

RESULTS AND DISCUSSIONS

5.1 Qualitative analysis of the flow structure

5.1.1 Introduction

The goal in this section is to represent a few qualitative observations about the flow around the obstacles and describe the main features of the flow structure. For that purpose both velocity and surface data are used in combinations with video footage. The main focus is the bore generated using $h_1 = 250$ mm, where h_1 is the initial water impoundment depth behind the gate.

5.1.2 Large circular column

Figure 5.1 shows 8 photographs, captured from a high speed film taken at 100 frames per second, of the upstream side of the large circular column for $h_1 = 250$ mm. Each capture is marked with the time that has passed since the raising of the gate. Figure 5.1a shows the splashup on the upstream side of the column just after the bore has arrived. After the water falls back there is a buildup of water right upstream of the column caused by the flow blockage (Figure 5.1b), which then flattens out both in the upstream direction and towards the sides of the tank (Figure 5.1c). When the wave coming off the column reaches the side-walls (Figure 5.1d), a wave forms over the whole width at the upstream edge of the column (Figure 5.1e) which then starts to propagate upstream (Figures 5.1f–h). Smaller waves can also be seen moving at an angle from the sidewalls. This behavior can also be seen in Figure 5.2. It shows the evolution of the water surface upstream of the large circular column for impoundment $h_1 = 250$ mm. It shows the bore propagating towards the column and then

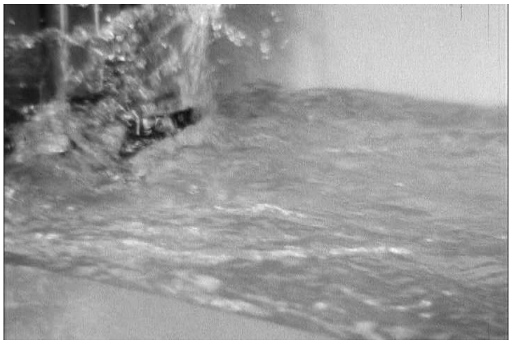

(a) $t = 3.29$ s

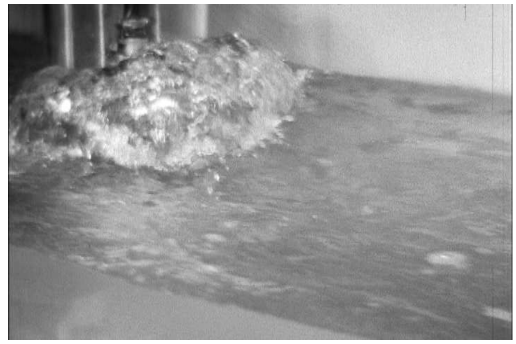

(b) $t = 3.63$ s

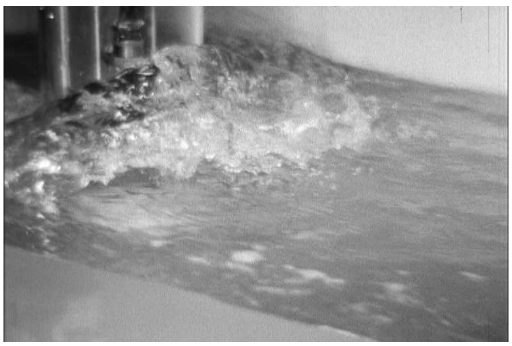

(c) $t = 3.91$ s

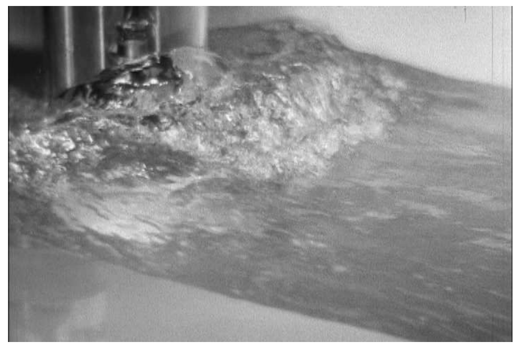

(d) $t = 4.24$ s

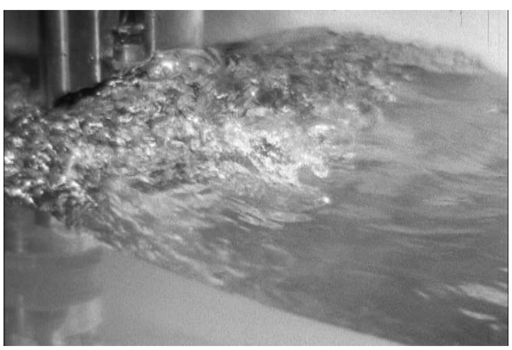

(e) $t = 4.82$ s

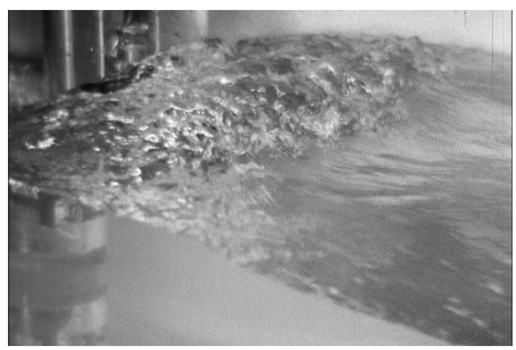

(f) $t = 5.36$ s

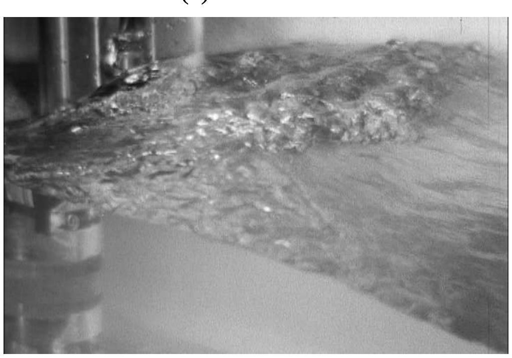

(g) $t = 5.77$ s

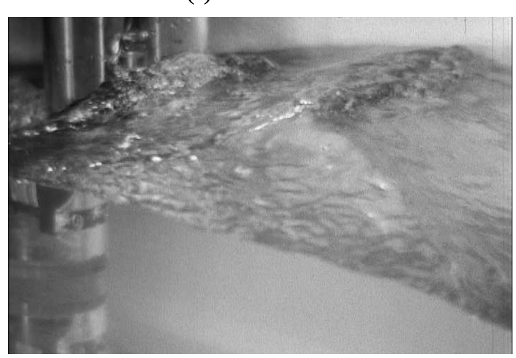

(h) $t = 6.38$ s

Figure 5.1: Views of the flow around the large circular column from upstream for $h_1 = 250$ mm

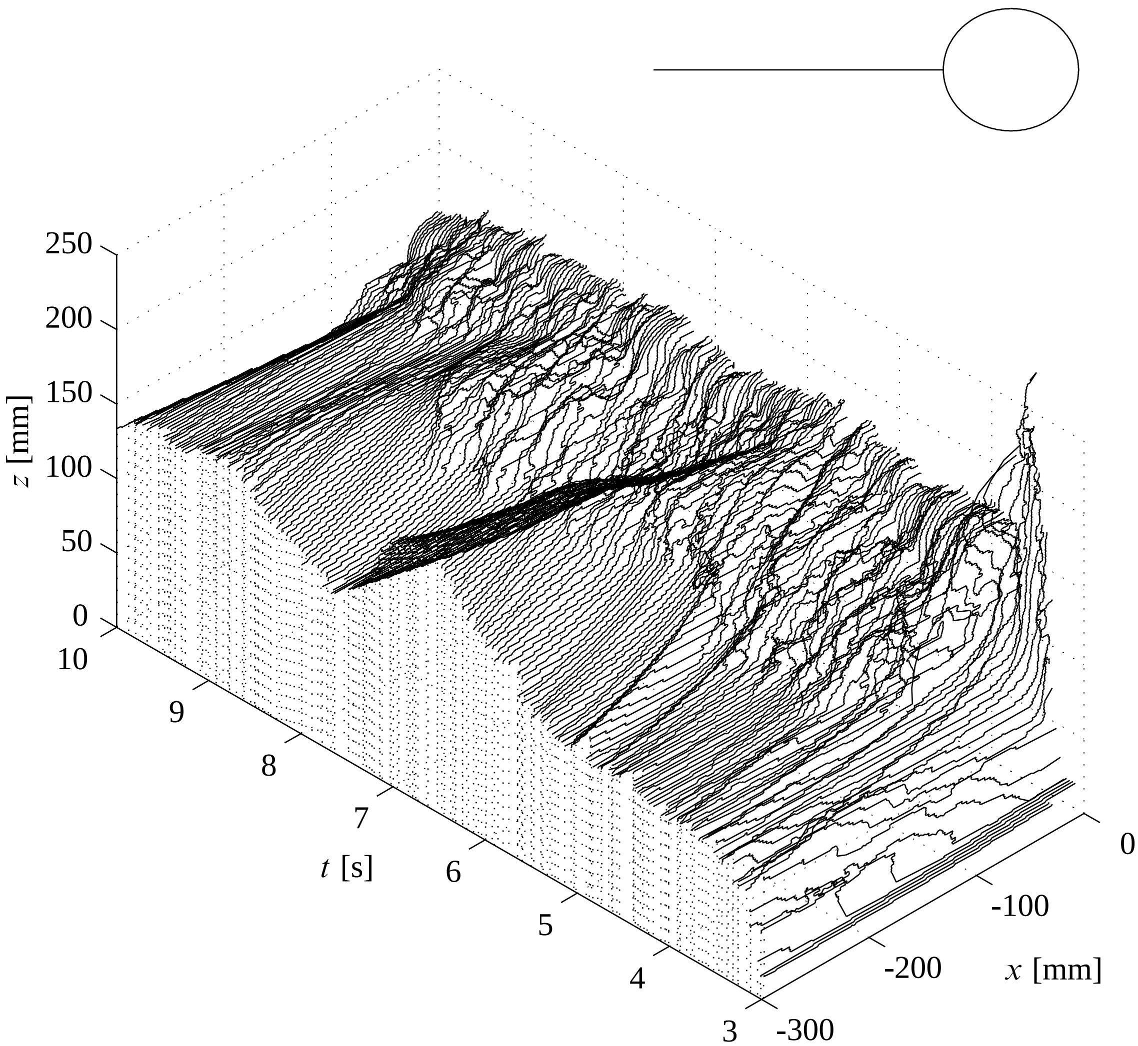

Figure 5.2: Evolution of the water surface profile in the vertical plane at the centerline upstream of the large circular column for $h_1 = 250$ mm

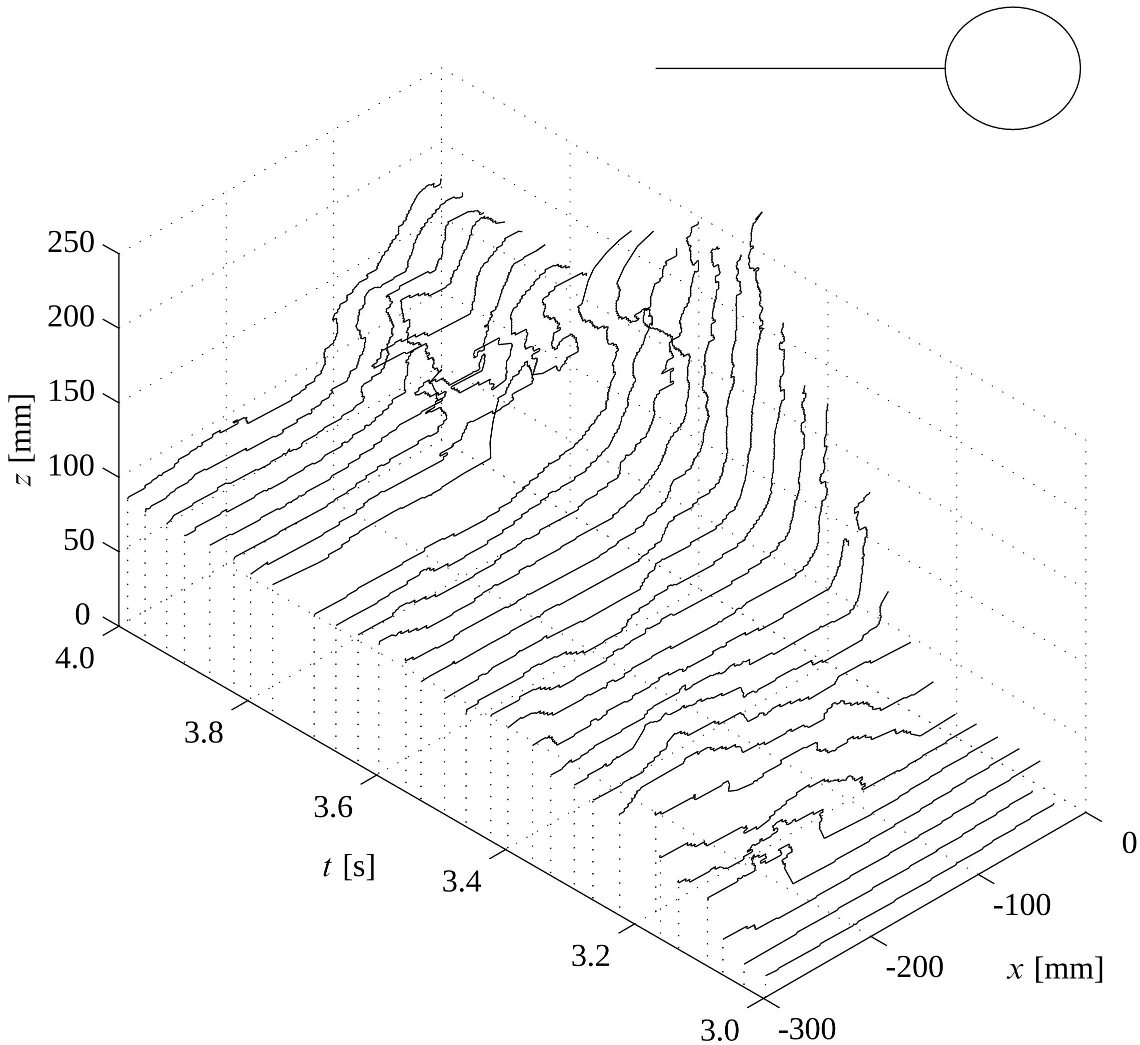

Figure 5.3: Evolution of the water surface profile in the vertical plane at the centerline upstream of the large circular column for $h_1 = 250$ mm. Expanded view near initial impact.

running up onto it. In this graph the front edge of the column is at $x = 0$, z is measured from the bottom of the tank and $t = 0$ when the gate starts to raise. Flow-disturbance due to impingement is confined to an area extending about 100 mm upstream of the column but evens out at a lower level further upstream. After the initial splashup the water level at the upstream edge of the column is at approximately 170 mm. The undisturbed height away from the impinging disturbance is about 90 mm. Figure 5.2 also shows that the wave seen in Figures 5.1f–h is in fact only the first one of two prominent waves propagating upstream. These waves start at the upstream face of the column at approximately 6 and 8 s after gate opening and can be seen clearly at $x = -300$ mm near $t = 7$ and $t = 9$ s. The wave propagates upstream at about 0.17 m/s. As Figure 5.2, Figure 5.3 shows the evolution of the water surface upstream of the large circular column for impoundment $h_1 = 250$ mm, but with expanded detail near the time of initial impingement of the bore on the structure. In Figure 5.3 the surface is initially still at a level of 20 mm. At $t = 3.0$ s the arriving bore is first seen. The raised bore surface at the toe is quite irregular as can be expected from the overturning and air entrainment at the bore face. At $t = 3.4$ s the water hits the structure and begins to climb up the front face. As the bore continues to impinge on the column, both the water level on the column and the depth of flow upstream increase. The flow is being set up at this stage and the flow blockage caused by the column is affecting the upstream depth. The water surface on the column itself can not maintain its steep slope. It reaches a maximum of 270 mm at $t = 3.5$ s and begins to break, sending the broken volume of water back upstream. This reflected wave reaches $x = -100$ mm at $t = 3.8$ s before being swept back onto the column. It is useful to look at Figure 5.2 at this point. It can be seen there that the process of buildup on the column front face occurs several times during the experiment.

In Figure 5.2, as in all the water surface time histories, coordinated wave motions or reflection appear as areas of convergence of the lines of the water surface. There are a number of small reflections during the initial runup on the column, but the biggest reflections are seen from $t = 6.0$ s to $t = 7.0$ s and again $t = 8.0$ s to $t = 9.0$ s. These correspond to the reflections of a travelling wave from both side walls as seen in the video. The water surface on the upstream side of the column rises to 170 mm and the wave propagates upstream with a speed of 1.7 m/s. The first of the two large waves visible in Figure 5.2 is much more distinct. Its peak is clearly seen at $x = -300$ mm at $t = 6.6$ s. The second wave is more gradual and can be seen at $x = -300$ mm at $t = 7.9$ s. The second wave appears to be affected by additional reflections occurring in the tank.

Figure 5.4 shows 8 captures from the high speed film of the wake of the large circular column for $h_1 = 250$ mm. As before, each capture is marked with the time that has passed since the gate was lifted. In Figure 5.4a the front of the bore has passed the column. Most of the water shoots straight downstream, whereas only a small portion bends around the column and moves towards the centerline (Figure 5.4b). The front has travelled about two diameters downstream before the two sides meet in the wake (Figure 5.4c). Figure 5.4d shows the wake during the impact of the two swerving fronts. They originally flow past each other (Figure 5.4e) but soon a so called rooster tail forms at the junction of the opposite flows as can be seen in Figure 5.4f. The rooster tail is unsteady and oscillates around the centerline (Figures 5.4g and h).

Figures 5.5 through 5.8 show examples of the combined velocity fields using DPIV around the large circular column for $h_1 = 250$ mm measured at $z = 15$ mm above the floor. As for every case, the initial water level downstream of the gate, h_0 is 20 mm. The whole set of DPIV measurements for this case can be seen in Appendix A.2. Figure 5.5 shows the velocity field at $t = 3.243$ s. The bore has just reached the obstacle and the span-wise velocity v is close to zero everywhere. The water that the obstacle has prevented from continuing downstream has run up the obstacle rather than gone around. Figure 5.6 shows the velocity field 0.215 s, or 3 frames, later. The water is now flowing past the obstacle, but its effects have not reached the side wall. This corresponds to the flows shown in Figures 5.4a and b. Figure 5.7 shows the velocity field at $t = 3.886$ s. Some positive velocity v (towards the side wall) can be seen between the column and the wall. The direction of v is negative further downstream, showing the effects of the wall. Where positive and negative values of v converge, the water surface is forced up forming what is termed a rooster

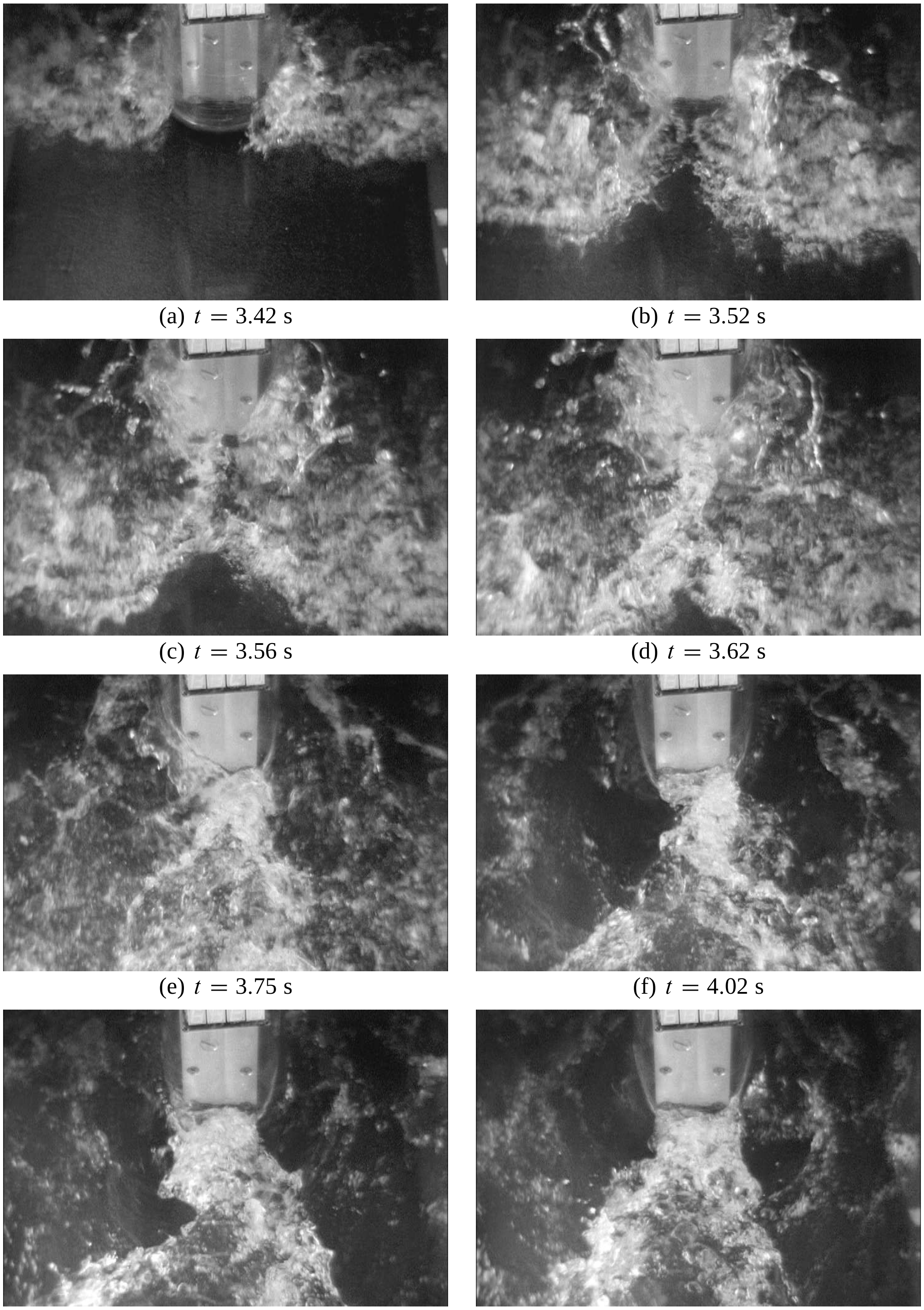

(a) $t = 3.42$ s
(b) $t = 3.52$ s
(c) $t = 3.56$ s
(d) $t = 3.62$ s
(e) $t = 3.75$ s
(f) $t = 4.02$ s
(g) $t = 4.34$ s
(h) $t = 4.47$ s

Figure 5.4: View of flow around the large circular column from downstream for $h_1 = 250$ mm

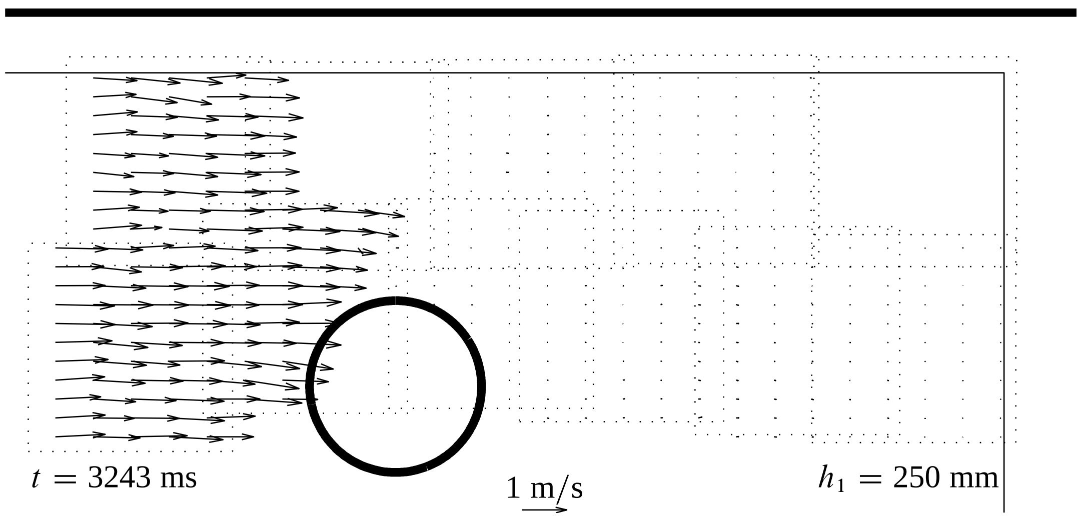

Figure 5.5: Horizontal velocity field around the large circular column at $t = 3243$ ms, with $h_1 = 250$ mm and $z = 15$ mm

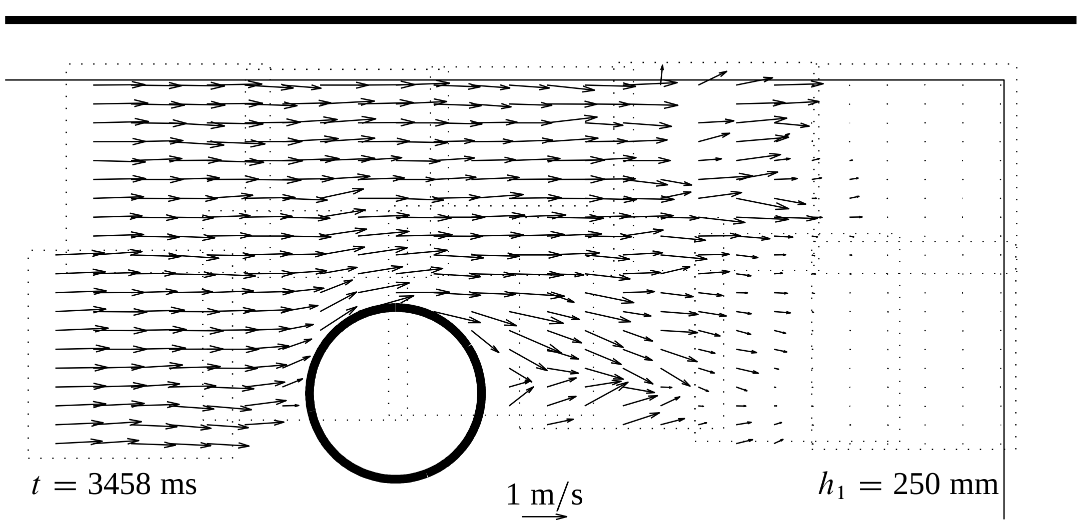

Figure 5.6: Horizontal velocity field around the large circular column at $t = 3458$ ms, with $h_1 = 250$ mm and $z = 15$ mm

tail because of its arcing narrow shape. The rooster tail is forming in the wake and is now a little to the left of the centerline. Figure 5.8 shows the velocity field at $t = 4.600$ s. The rooster tail is now fully formed. The velocity close to the side wall is close to being parallel to the wall, i.e. $v \approx 0$. Figure 5.9 shows the velocity field at the same time as Figure 5.7, but 20 mm higher in the flow, i.e. $z = 35$ mm above the floor. The full set of the measurements for $z = 35$ mm can be seen in Appendix A.3. The three-dimensional character of the wake is evident when this figure is compared to Figure 5.7. At different elevations in the flow, the velocity deviations from the downstream direction are significantly different at points with the same relative location with respect to the column. At the upstream side near the cylinder, the horizontal velocity is higher closer to the bottom. At the higher elevation, more of the fluid is swaying upwards as part of the buildup upstream of the column. Downstream of the column, the width of the separation area is greater higher up in the flow than near the bottom. Figure 5.10 shows the velocity field for a larger bore, i.e. $h_1 = 300$ mm at $t = 3.158$ s. The full set of flow fields can be seen in Appendix A.4. Using the time scale described in §5.3.1 this time should correspond closely to 3.886 s for the bore with $h_1 = 250$ mm shown in Figures 5.7 and 5.9. The effects of the side walls are not quite as prominent for this larger bore while the deviations from the mean flow directions upstream are a bit larger.

Figures 5.11 and 5.12 show the evolution of the water surface profiles at two different cross-sections in the wake of the large circular column for $h_1 = 250$ mm. The centerline of the tank is at $y = 0$ and the side wall at $y = -305$ mm The waterlevel is highest near the centerline. This rise represents the rooster tail that forms in the wake. It oscillates around the centerline ($y = 0$), with an oscillation period of about 1.0–1.5 s. Between $x = 350$ mm and $x = 470$ mm the rooster tail becomes lower and wider. At $x = 350$ mm, the waterlevel at the sidewall rises to 107 mm right after the bore first passes, but establishes at about (76 ± 3) mm, so that is an overshoot of about 40 %. The same kind of behavior can still be seen at $x = 470$ mm, where the initial peak is 93 mm but the flow stays at about (60 ± 3) mm after that. Here the overshoot is 55 %.

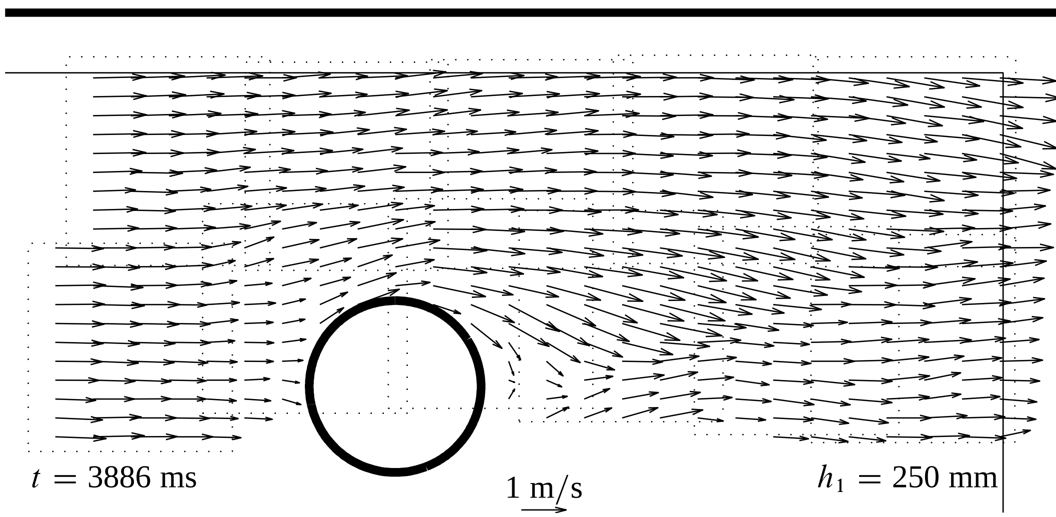

Figure 5.7: Horizontal velocity field around the large circular column at $t = 3886$ ms, with $h_1 = 250$ mm and $z = 15$ mm

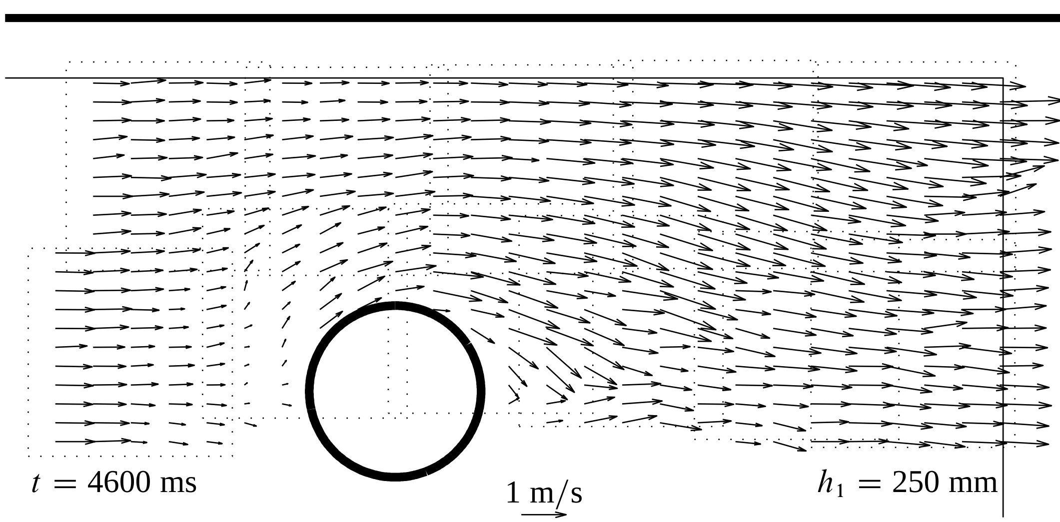

Figure 5.8: Horizontal velocity field around the large circular column at $t = 4600$ ms, with $h_1 = 250$ mm and $z = 15$ mm

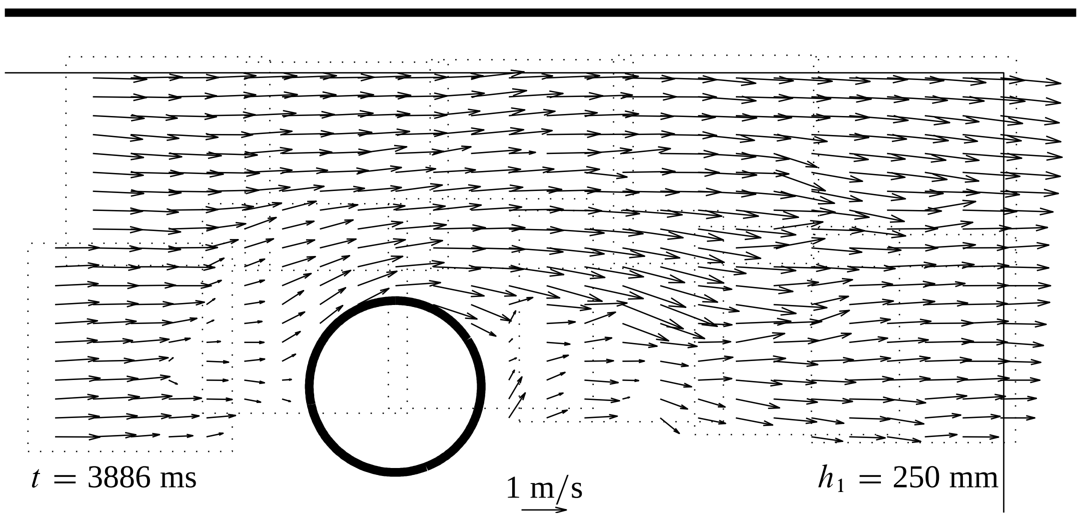

Figure 5.9: Horizontal velocity field around the large circular column at $t = 3886$ ms, with $h_1 = 250$ mm and $z = 35$ mm

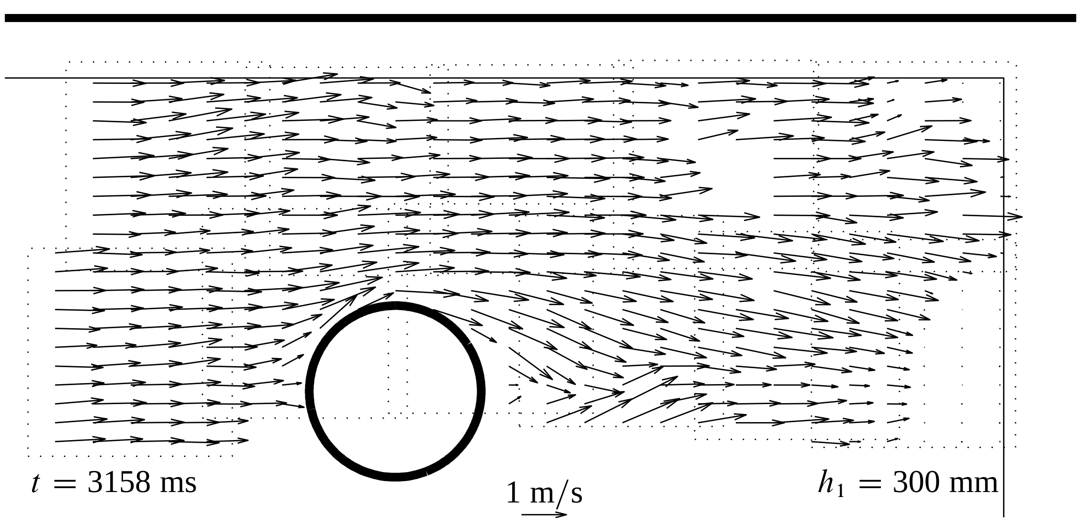

Figure 5.10: Horizontal velocity field around the large circular column at $t = 3158$ ms, with $h_1 = 300$ mm and $z = 15$ mm

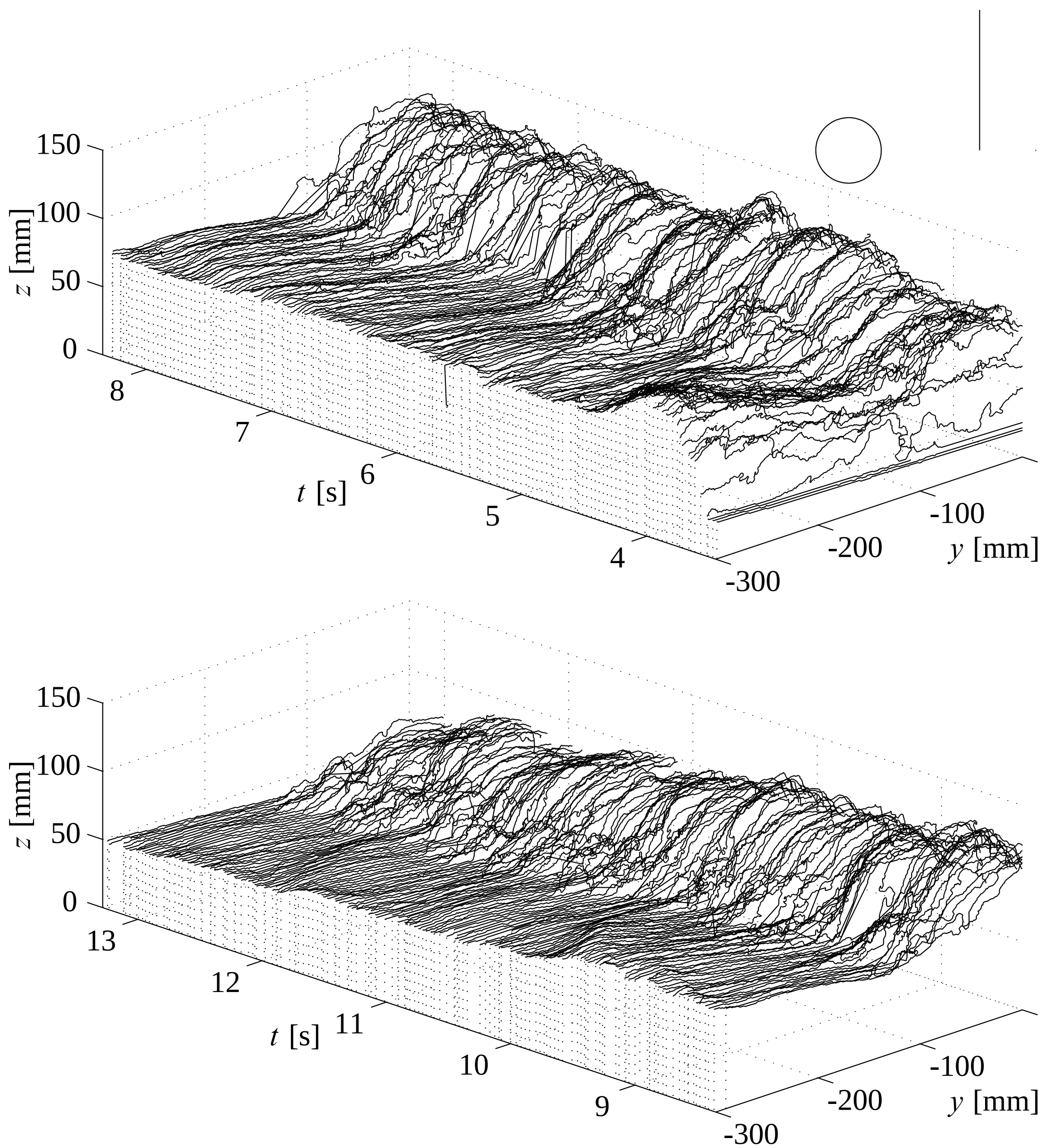

Figure 5.11: Time history of surface data in the wake of the circular column at $x = 350$ mm for $h_1 = 250$ mm

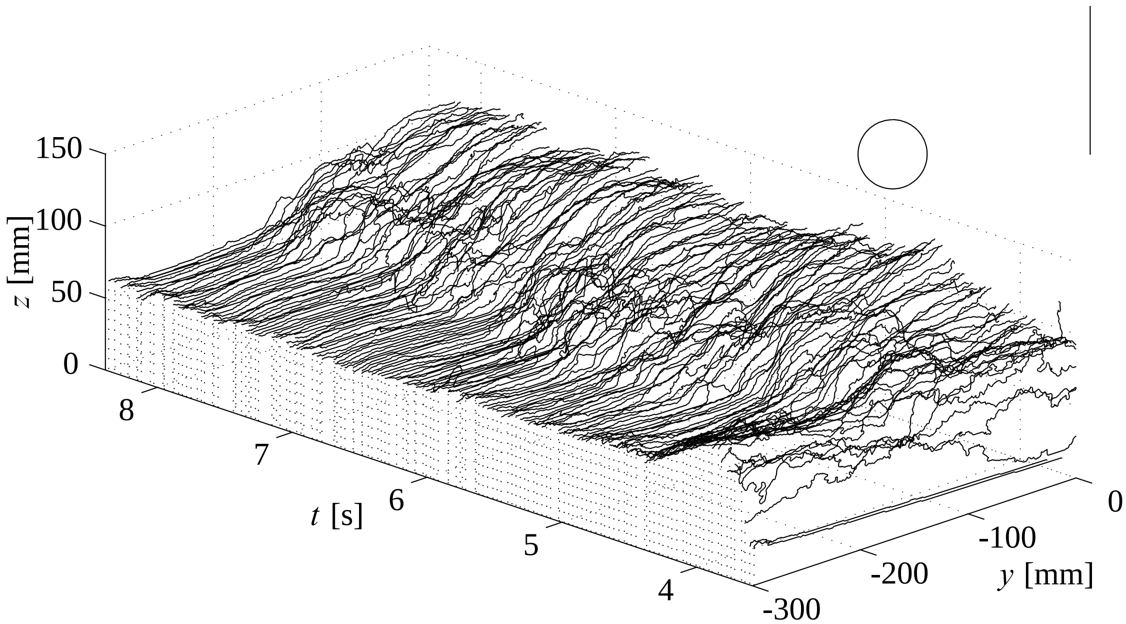

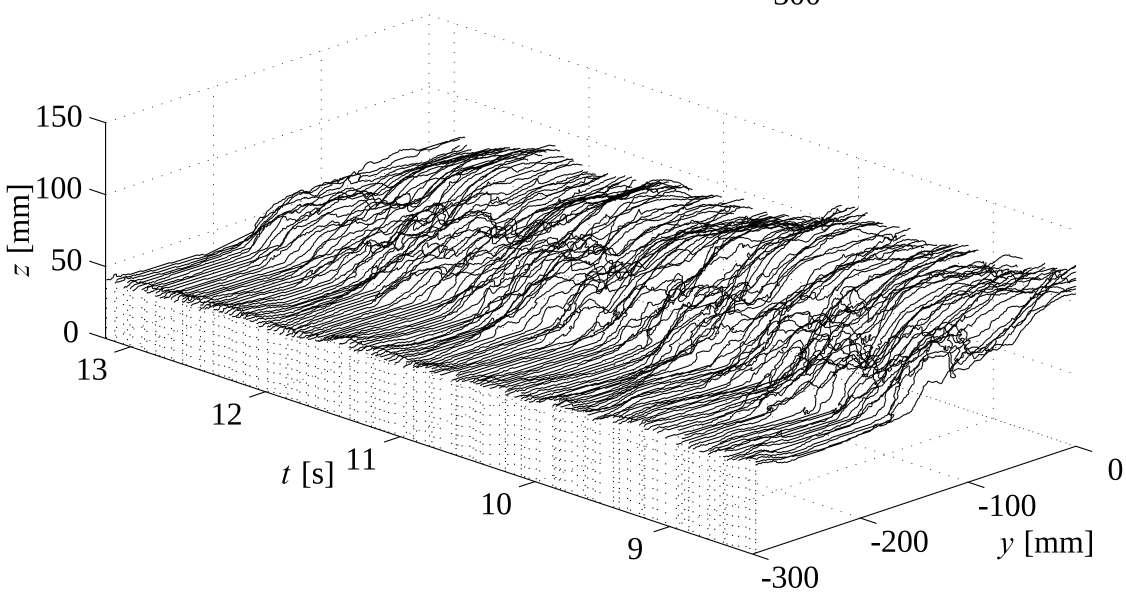

Figure 5.12: Time history of surface data in the wake of the circular column at $x = 470$ mm for $h_1 = 250$ mm

5.1.3 Small and intermediate circular column

Figure 5.13 shows a side view of a bore with $h_1 = 250$ mm passing the small circular column. The effects of the column on the water surface level are minimal. There is only a small runup directly on the cylinder but only minor signs of it affecting the surface further away. That would indicate minimal effects of blockage for this setup. A small wake effect can be observed in the slightly raised surface behind the cylinder. Figure 5.14 has the same kind of side view for the intermediate column. The obstacle now affects the water surface all the way across the tank, but while there is a difference between the water level upstream and downstream it is small compared to what is seen for the large column (Figures 5.1 and 5.4).

5.1.4 Square column

Figure 5.15 shows 8 captures from the high speed video of the wake of the square column for $h_1 = 250$ mm. Each capture is marked with the time passed from the gate being raised. The main characteristics of the flow are similar to that of the large circular column. The shape of the flow around the column is obviously different as it conforms to the shape of the column and is affected by the sharp corners of the square. The flows from either side meet in the wake at $t = 3.6$ s (Figure 5.15d), which corresponds well with the time for the circular column (Figure 5.4d). As in the case of the circular column, the wake oscillates from side to side, but the two trailing edges of the square column also appear to generate separate wake structures that then interact downstream (Figures 5.15e–h), whereas the circular column does not have such clearly defined flow separation.

Figure 5.16 shows captures of 8 consecutive video frames, showing the runup onto the square column for $h_1 = 250$ m and as always $h_0 = 20$ mm. As soon as the bore front arrives at the column, a thin tongue of water travels up the column wall (Figure 5.16b–d) and when it has reached its final height it falls back over itself (Figure 5.16f–h). After this initial splashup the water surface elevation at the column face is approximately 170–

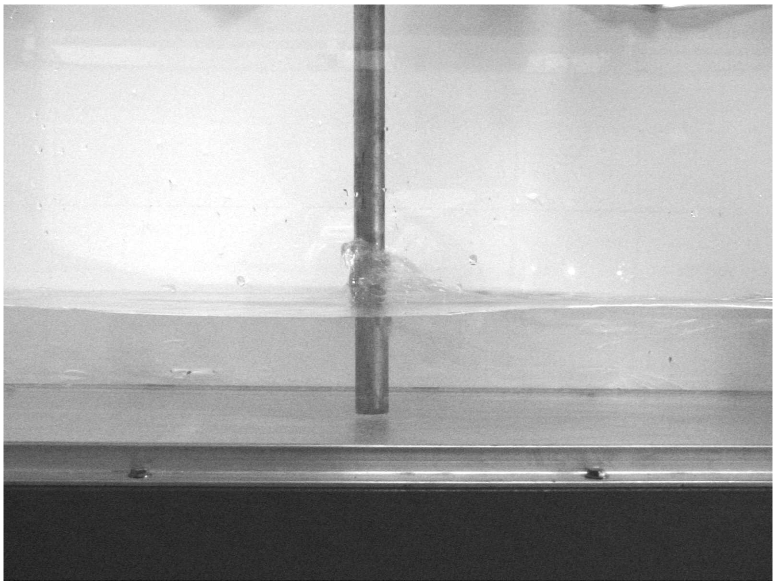

Figure 5.13: A typical side view of the small circular column, $h_1 = 250$ mm

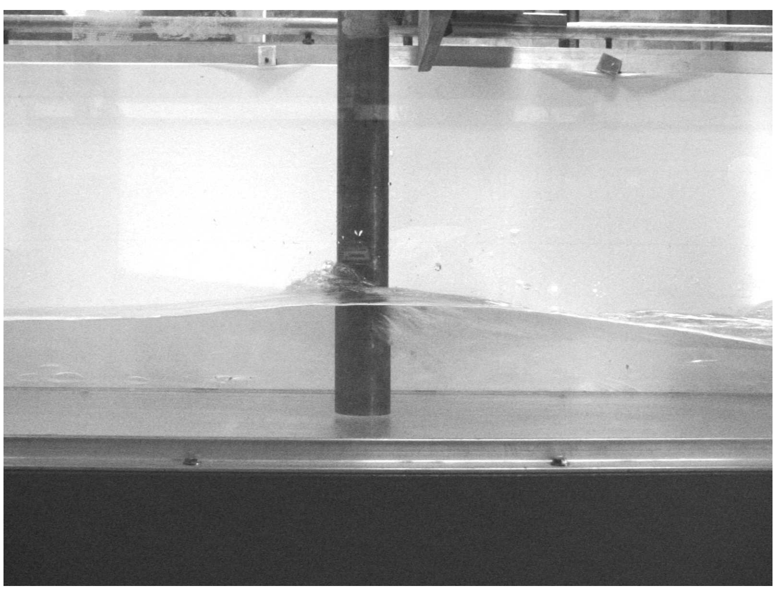

Figure 5.14: A typical side view of the intermediate circular column, $h_1 = 250$ mm

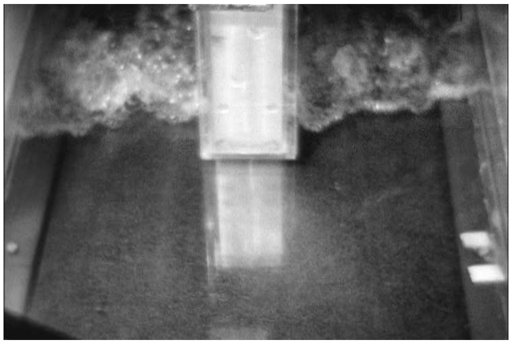

(a) $t = 3.30$ s

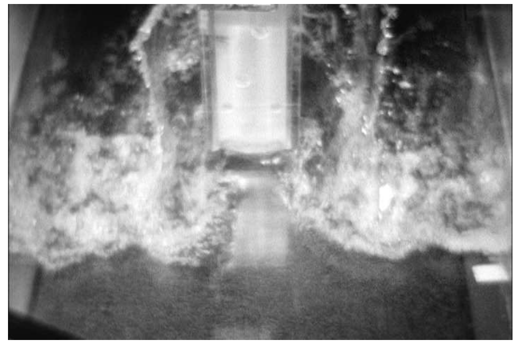

(b) $t = 3.48$ s

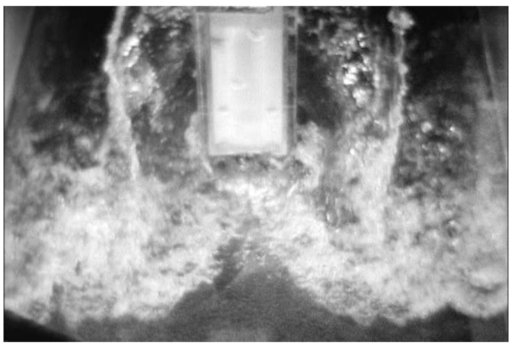

(c) $t = 3.54$ s

(d) $t = 3.61$ s

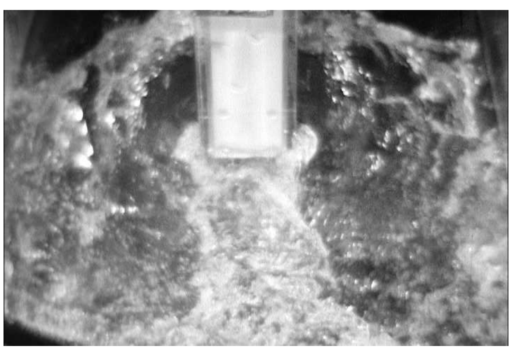

(e) $t = 3.72$ s

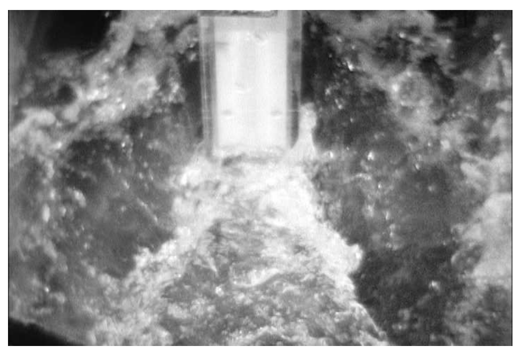

(f) $t = 3.88$ s

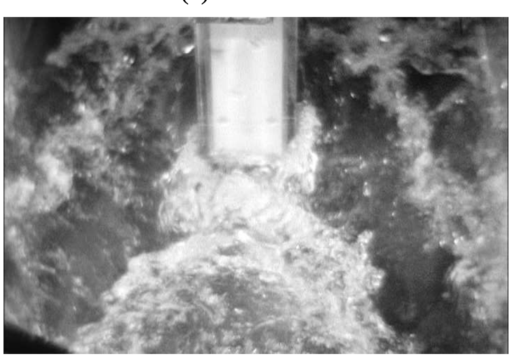

(g) $t = 3.99$ s

(h) $t = 4.22$ s

Figure 5.15: View of flow around the square column from downstream for $h_1 = 250$ mm

(a) $t = 3.21$ s

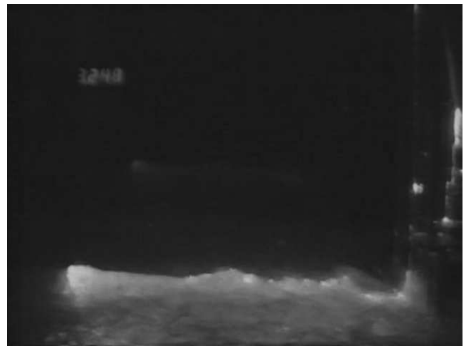

(b) $t = 3.24$ s

(c) $t = 3.27$ s

(d) $t = 3.31$ s

(e) $t = 3.34$ s

(f) $t = 3.37$ s

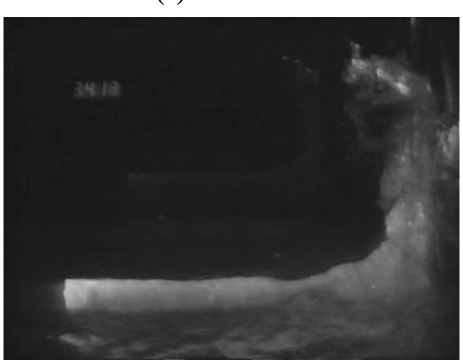

(g) $t = 3.41$ s

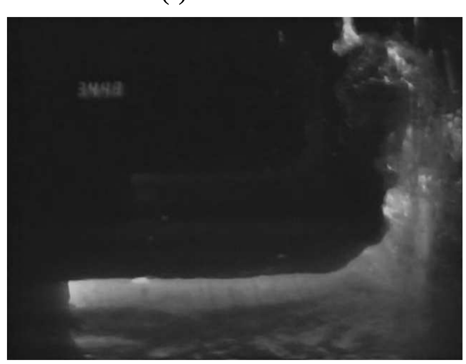

(h) $t = 3.44$ s

Figure 5.16: The water surface upstream of the square column for $h_1 = 250$ mm

175 mm, slightly higher than for the circular column. This can be seen in Figures 5.17 and 5.18. They show the evolution of the water surface on the centerline at the upstream side of the square column for the bore formed by a 250 mm impoundment. Figure 5.17 covers a 7 s interval while Figure 5.18 focuses on a 1 s interval around the bore front arrival and the initial splashup. The main features here are also similar to those of the circular column. The straight side facing the flow causes a larger splashup than the round features of the circular column. As with the circular column, there are the two reflected waves travelling upstream. The speed is similar to that of the circular column but the waves appear to be generated a little bit earlier, most likely because of the abrupt front face of the column. Figures 5.19 and 5.20 also show the evolution of the water surface elevation upstream of the square column using the same two intervals, though in this case the column is oriented with one corner facing the flow. For this case the original splashup is considerably smaller than for the other cases. However the water level after the splashup is about the same for either orientation of the square column and even the circular one as well, or about 170 mm. The pair of waves also propagate upstream for this case though the second one is less prominent. The reflected waves appear to depend more on bore size than obstacle shape, given a similar blockage coefficient.

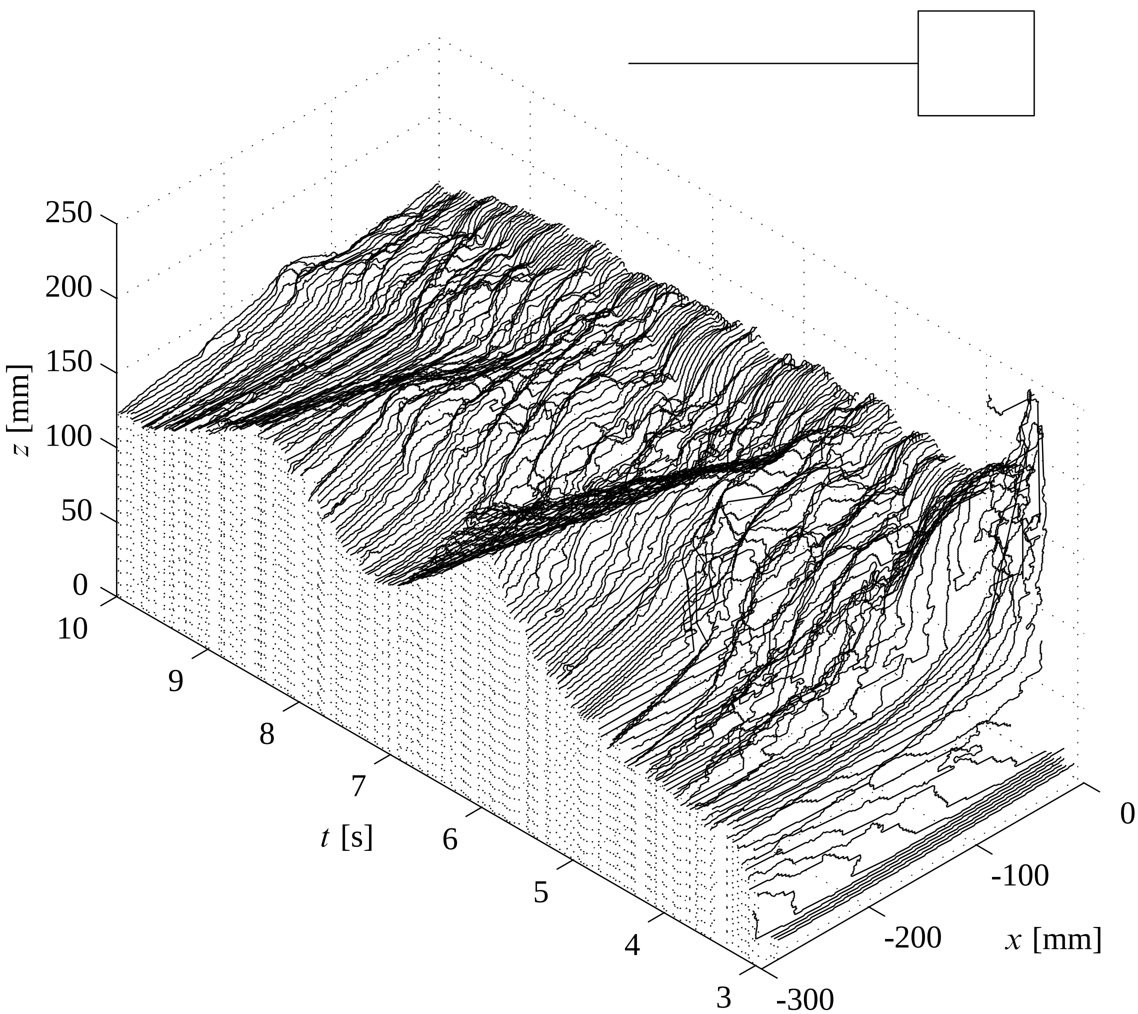

Figure 5.17: Evolution of the water surface profile in the vertical plane at the centerline upstream of the square column with one side facing the flow for $h_1 = 250$ mm

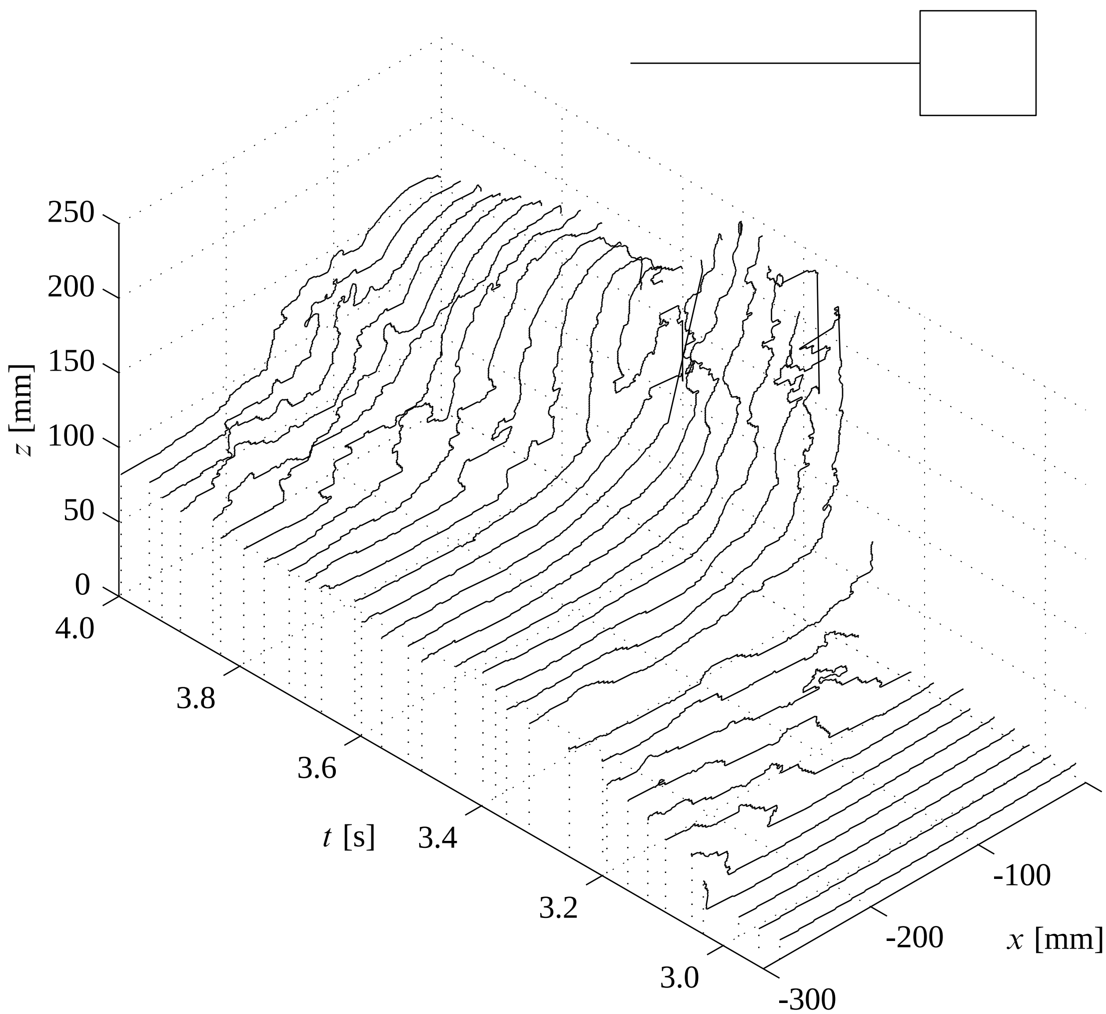

Figure 5.18: Evolution of the water surface profile in the vertical plane at the centerline upstream of the square column with one side facing the flow for $h_1 = 250$ mm, expanded view near initial impact

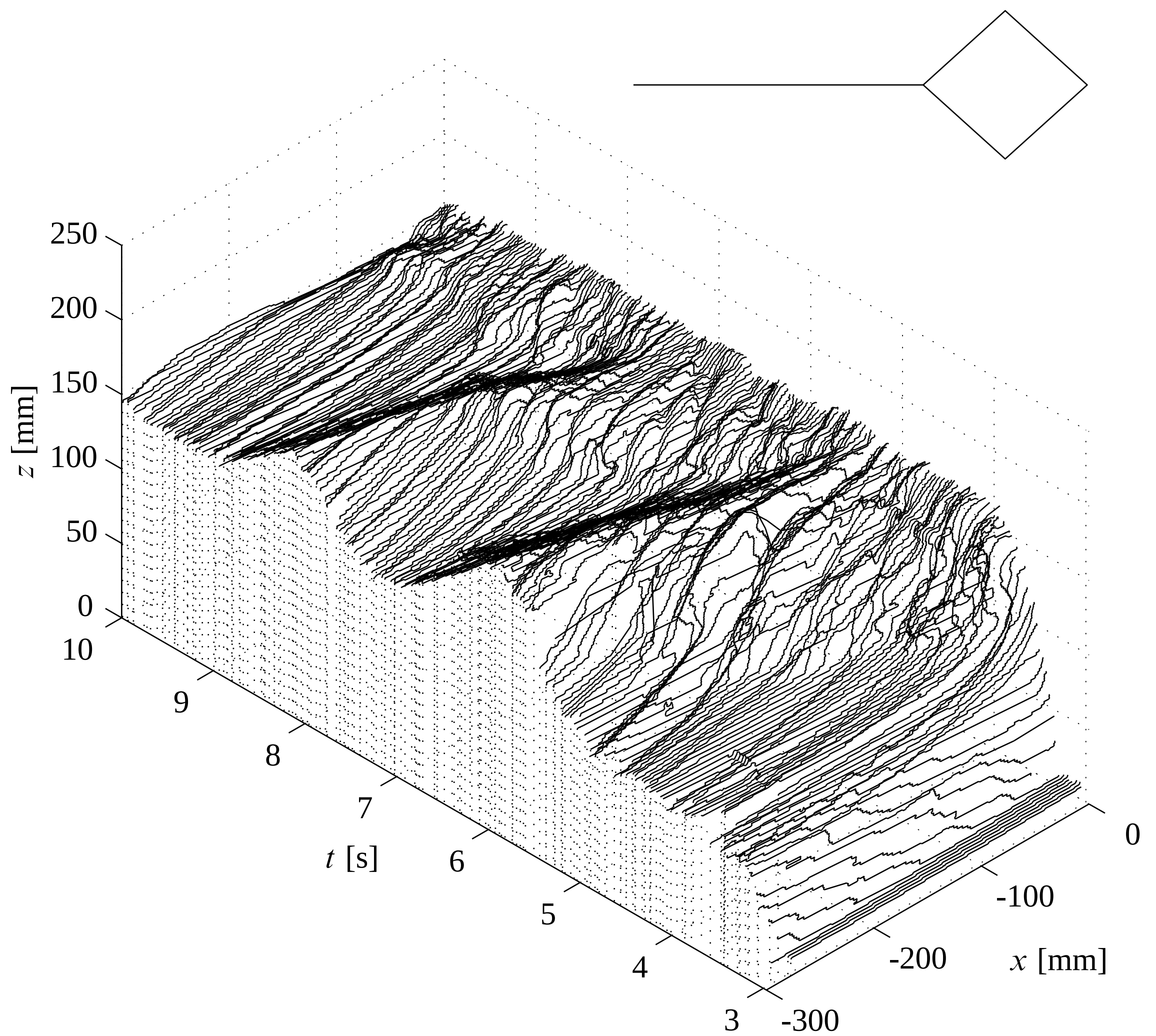

Figure 5.19: Evolution of the water surface profile in the vertical plane at the centerline upstream of the square column with its diagonal aligned with the flow for $h_1 = 250$ mm

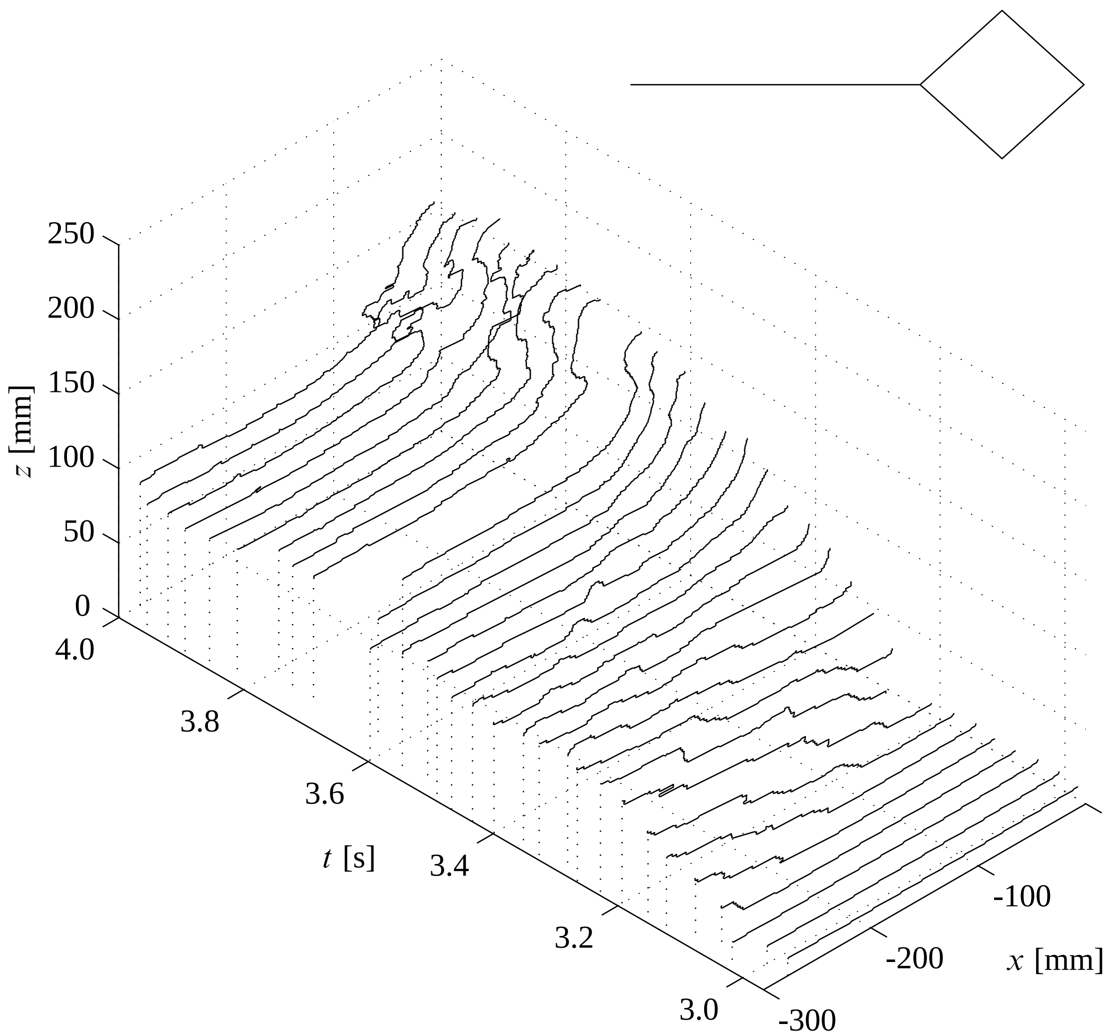

Figure 5.20: Evolution of the water surface profile in the vertical plane at the centerline upstream of the square column with its diagonal aligned with the flow for $h_1 = 250$ mm, expanded view near initial impact

5.2 Quantitative analysis of the flow structure

5.2.1 Introduction

The goal in this section is to examine the effects of the structure on the total energy of the flow and its components, the specific momentum of the flow and the structure of the velocity field. In order to examine the energy and specific momentum, it is necessary to decompose the flow velocity to mean and fluctuating components.

5.2.2 Comparison with wave gauge data

Figures 5.21 through 5.29 show how the calculated water level histories from §3.2 compare with wave gauge measurements at $x = 5.2$ m. The time of arrival, and therefore the propagation speed $\dot{\xi}$ are in good agreement. So is the agreement with water level, though an increase in depth can be seen in the measured data, whereas the theory indicates a constant depth while in zone 2, i.e. during bore conditions. The timing of a decrease in the water level data corresponds reasonably well with the calculated time of the upstream wall effects arriving at this location (marked with * in the figures).

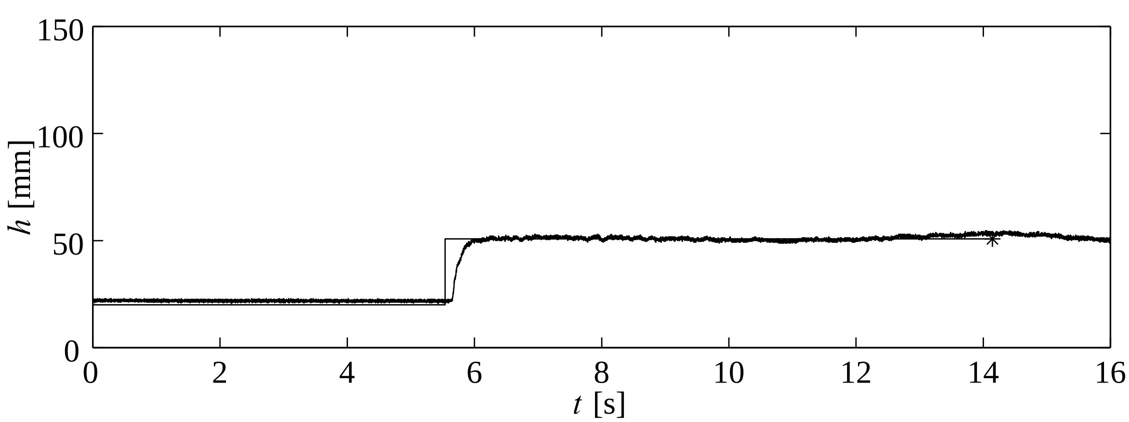

Figure 5.21: Comparison of measured water level with theory for $h_1 = 100$ mm

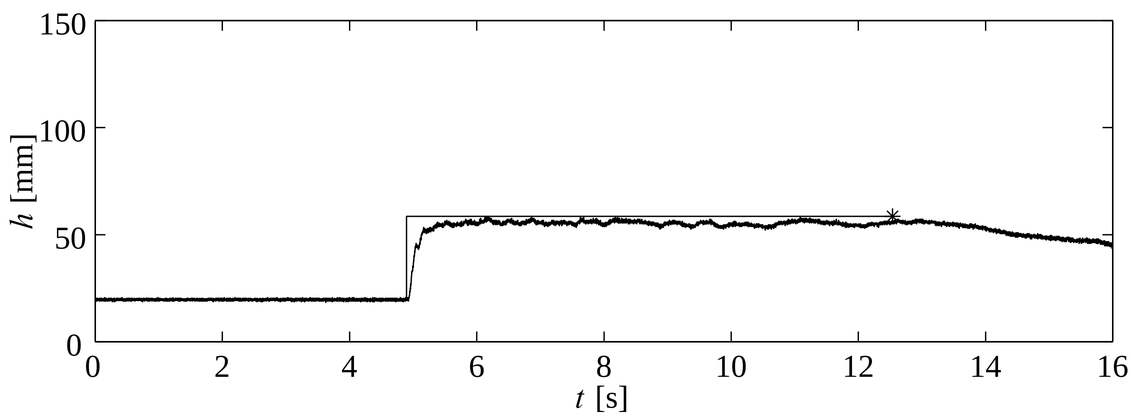

Figure 5.22: Comparison of measured water level with theory for $h_1 = 125$ mm

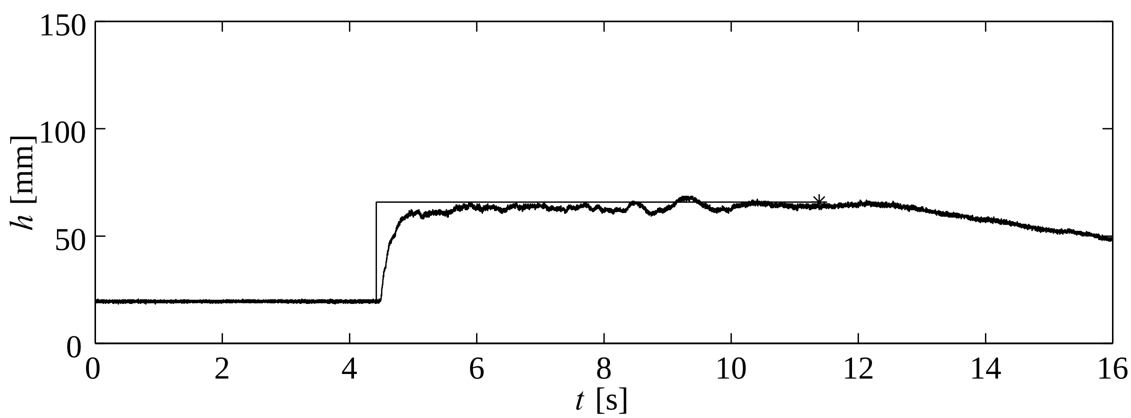

Figure 5.23: Comparison of measured water level with theory for $h_1 = 150$ mm

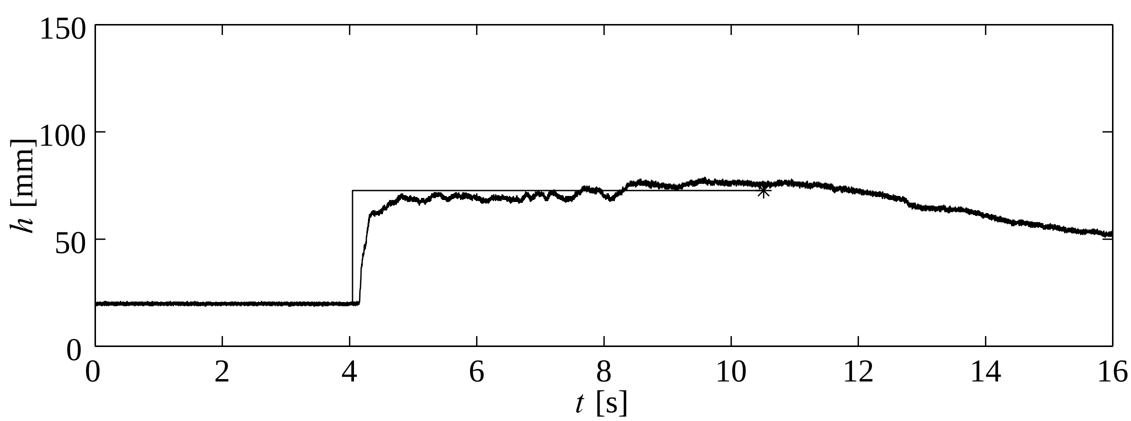

Figure 5.24: Comparison of measured water level with theory for $h_1 = 175$ mm

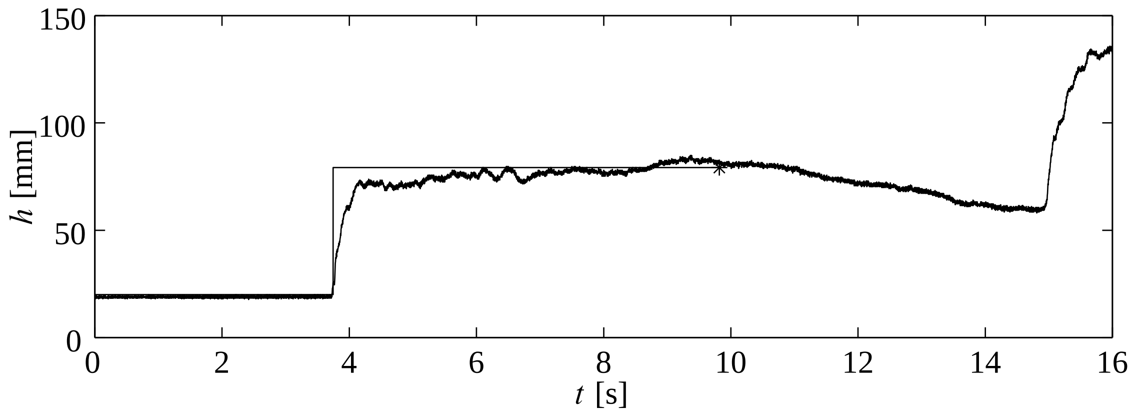

Figure 5.25: Comparison of measured water level with theory for $h_1 = 200$ mm

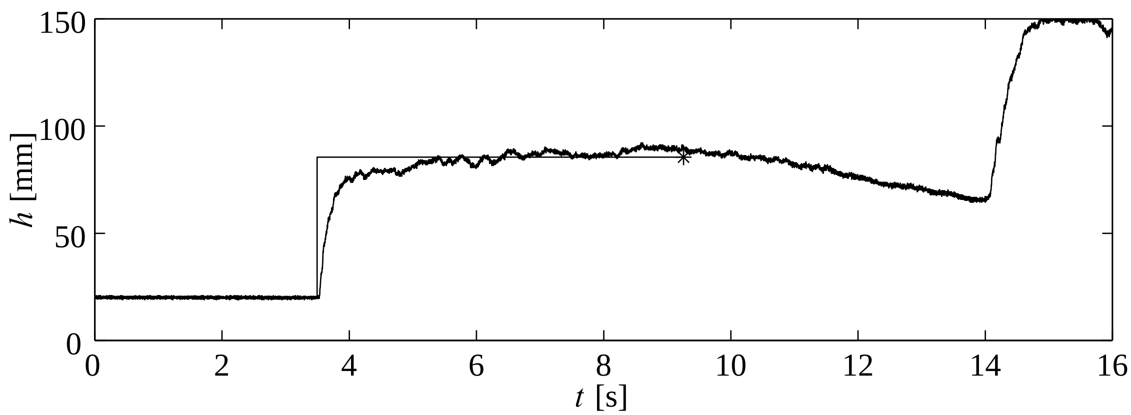

Figure 5.26: Comparison of measured water level with theory for $h_1 = 225$ mm

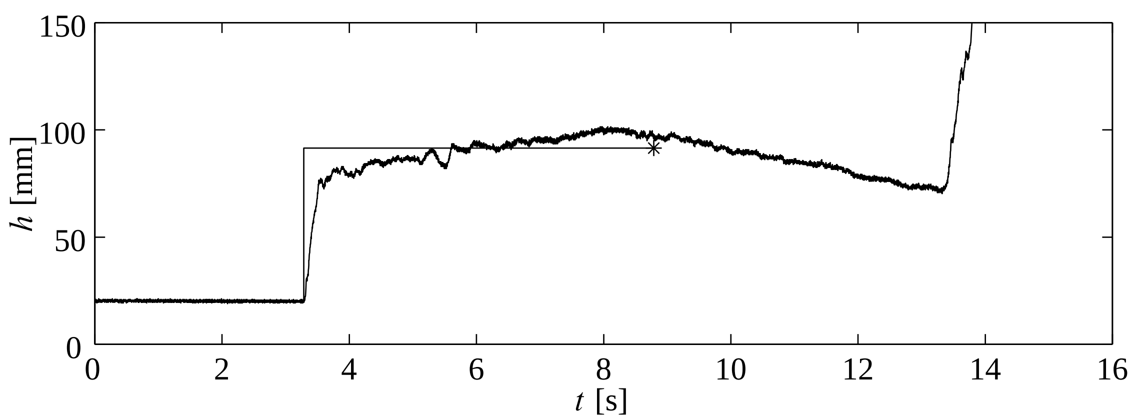

Figure 5.27: Comparison of measured water level with theory for $h_1 = 250$ mm

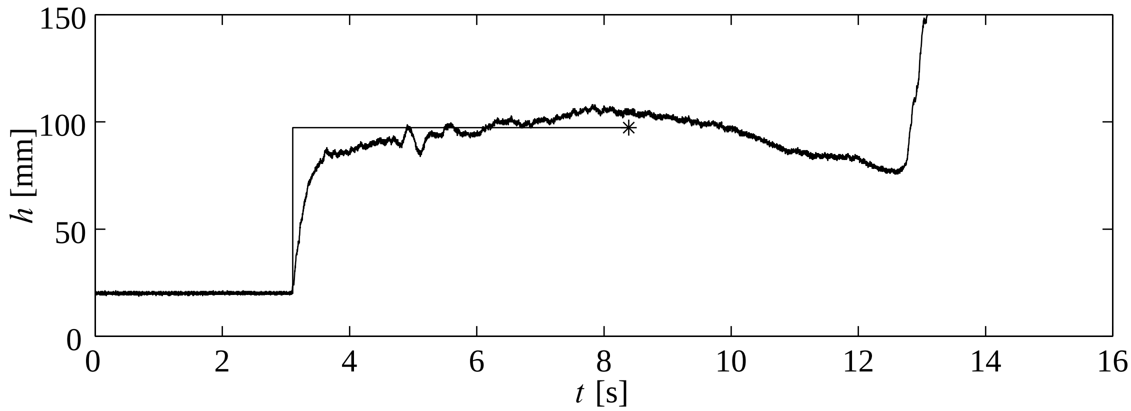

Figure 5.28: Comparison of measured water level with theory for $h_1 = 275$ mm

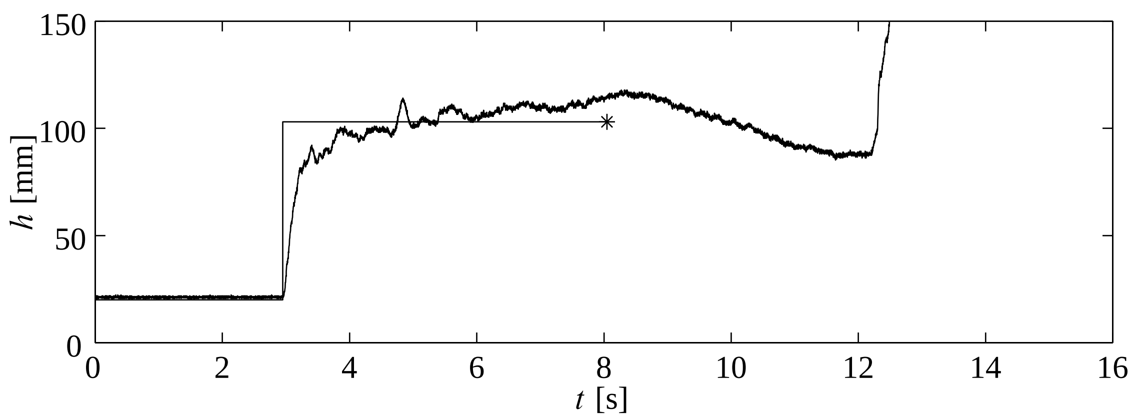

Figure 5.29: Comparison of measured water level with theory for $h_1 = 300$ mm

5.2.3 Comparison with velocity data

Figures 5.30 through 5.38 show how our calculated velocity histories compare with velocity measurements, both using LDV and DPIV, at $x = 5.2$ m. In each figure, the dots represent the DPIV and the solid line the LDV measurements. The straight solid line segments are the results of the calculations from §3.2. As in the water level comparisons, the arrival of the upstream wall effects are marked with an asterisk (*). As with the water level,

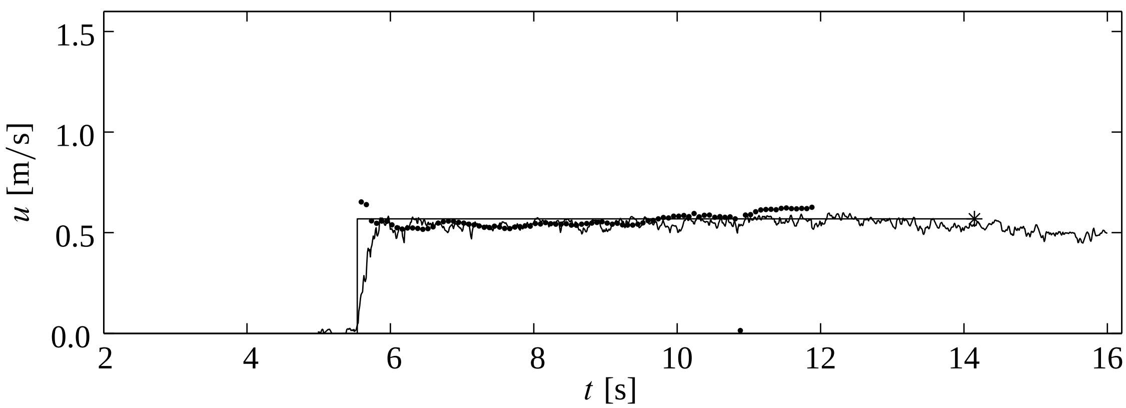

Figure 5.30: Comparison of measured velocity with theory for $h_1 = 100$ mm

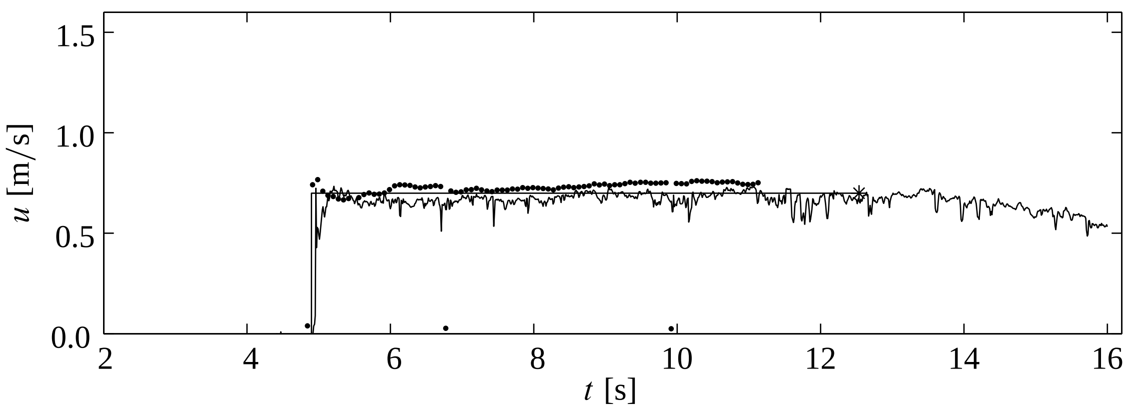

Figure 5.31: Comparison of measured velocity with theory for $h_1 = 125$ mm

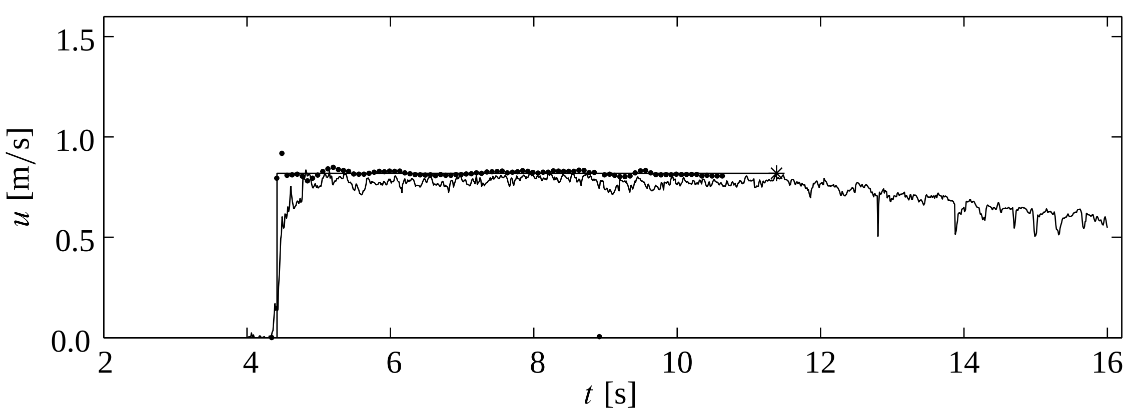

Figure 5.32: Comparison of measured velocity with theory for $h_1 = 150$ mm

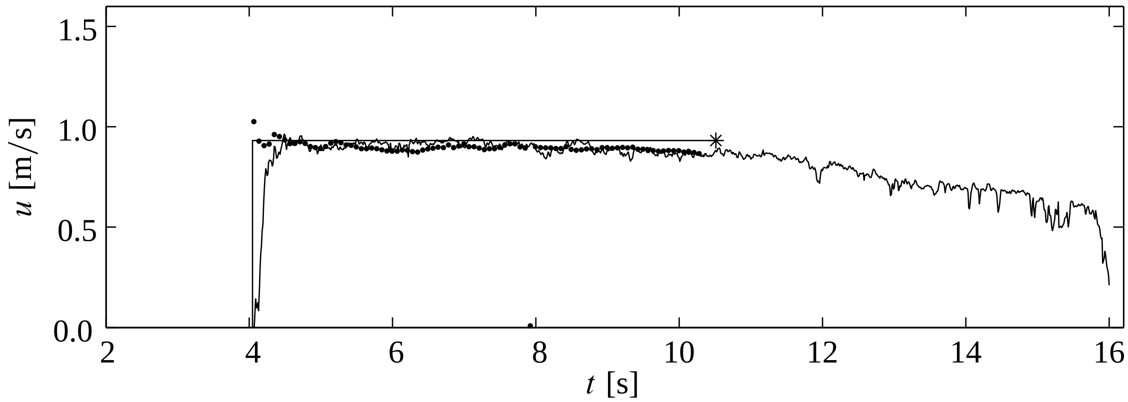

Figure 5.33: Comparison of measured velocity with theory for $h_1 = 175$ mm

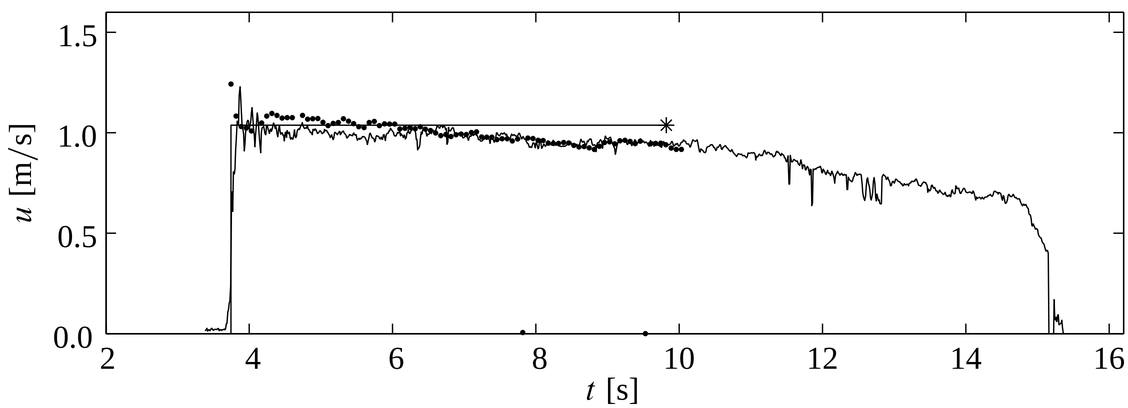

Figure 5.34: Comparison of measured velocity with theory for $h_1 = 200$ mm

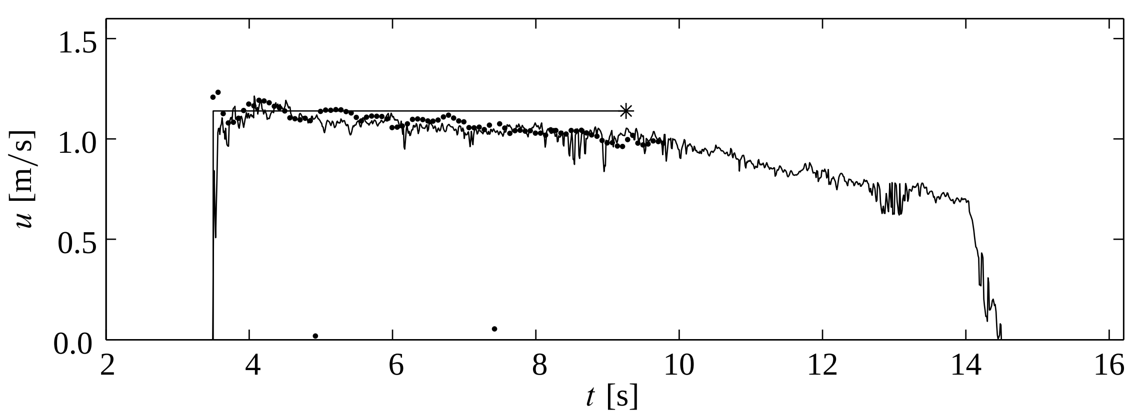

Figure 5.35: Comparison of measured velocity with theory for $h_1 = 225$ mm

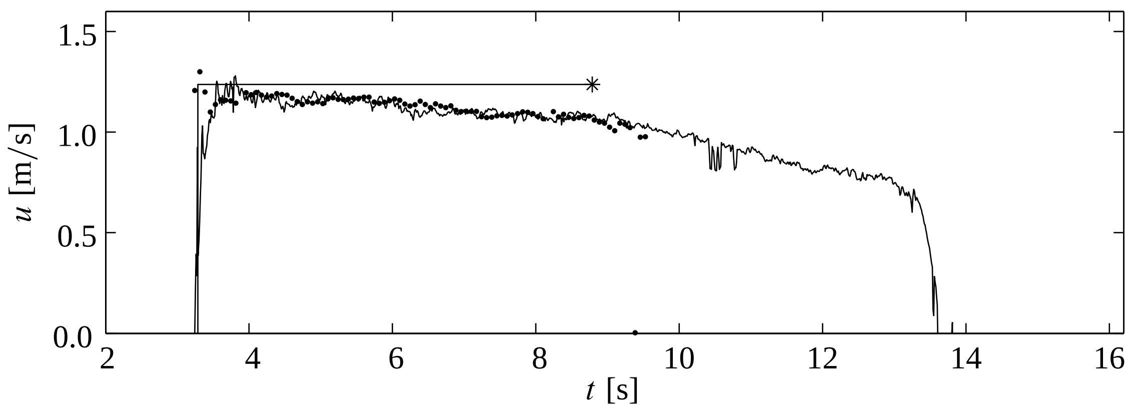

Figure 5.36: Comparison of measured velocity with theory for $h_1 = 250$ mm

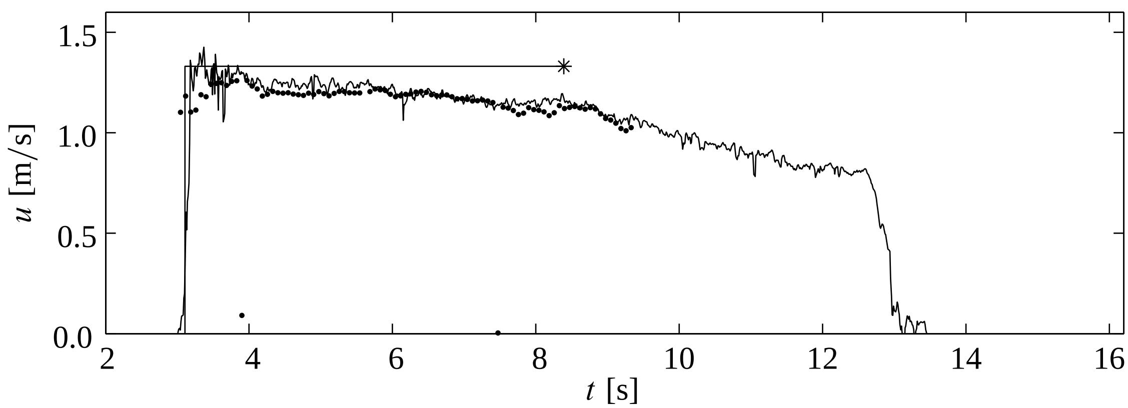

Figure 5.37: Comparison of measured velocity with theory for $h_1 = 275$ mm

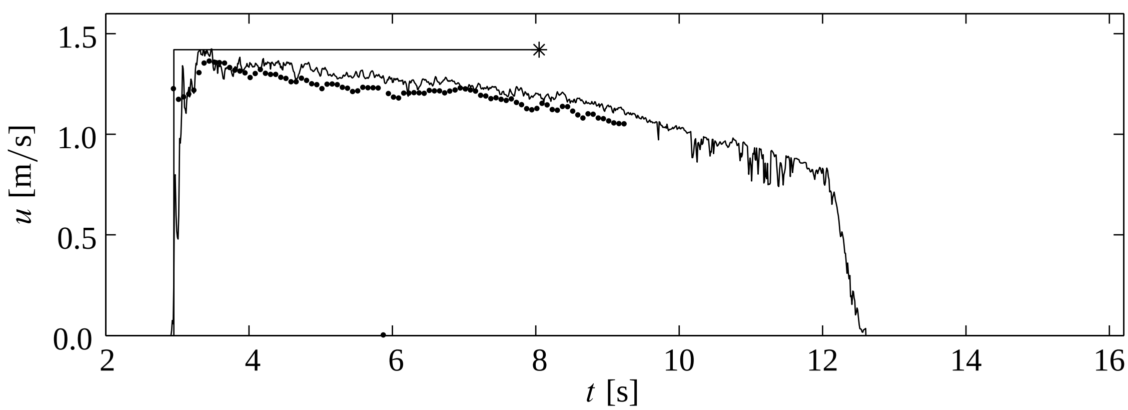

Figure 5.38: Comparison of measured velocity with theory for $h_1 = 300$ mm

the agreement is quite good. The velocity does however decrease during the passing of the bore, and the calculations overestimate the velocity for the larger bores. This is consistent with the results for the depth.

The shape of the larger bores is different from calculated theory. The theoretical assumptions are those of a irrotational, incompressible, inviscid and hydrostatic flow. As the bore becomes larger, these assumptions start to break down near the bore front, the incompressibility because of air entrainment. Other weaknesses in the assumptions relate to the tank. The removal of the gate is not instantaneous but takes a finite time. Friction effects from the gate might affect the initial shape and vorticity of the flow. A small stretch at the upstream end of the tank (see Figure 4.1) is actually deeper than the rest of the tank, while the calculations assume a constant depth. This should not significantly affect the bore because any influence of this extra depth would arrive at the measurement point at about the same time as the upstream end wall effects, and not influence the bore in any way before that.

Applying the classification of Bradley and Peterka (1957) (see §2.2) to the Froude numbers calculated in a coordinate system moving with the bore

$$Fr' = \frac{\dot{\xi}}{\sqrt{gh_0}}, \tag{5.1}$$

as seen in Table 3.1, we see that the smallest bores fall into the category of a weak jump while the others would be characterized as oscillating jumps. For the largest bore ($h_1 = 300$ mm) $Fr' = 4.0$, which is close to the upper limit of the oscillating category so some characteristics of a steady jump might be expected to appear. The water surface profiles of both oscillating and steady jumps rise with distance away from the jump in the downstream direction. The downstream direction in the moving coordinate system corresponds to evolution in time at a fixed location in the fixed coordinate system.

For $Fr' = 4$ the length of a hydraulic jump should be about $5.5h_2 = 570$ mm, which corresponds to about 0.32 s.

5.2.4 Filtering of data

The velocity data acquired using the LDV has several fairly sharp spikes. An example can be seen in Figure 5.39. The 3 small frames within the figure show selected peaks with the t-axis stretched by a factor of 50 while the u-axis is compressed by a factor of 2. Each spike is composed of several data points and is therefore not just a single outlier. A filtering process was implemented to remove the sharpest spikes from the data. The premise is that a very sudden change in velocity represents an outlier. Any interval between 2 consecutive data points, where the change in velocity, either acceleration or deceleration, exceeds a given value a_{max} is identified and both endpoints flagged, i.e. when

$$\left|\frac{u_{i+1}-u_i}{t_{i+1}-t_i}\right| > a_{\mathrm{max}} \tag{5.2}$$

both points i and $i+1$ are flagged. Any outlier should form a cluster of at least three flagged points, more in most cases. Flagged points are considered to form a single cluster if no consecutive non-flagged points are among them. Now if

$$\left|\frac{u_j-u_i}{t_j-t_i}\right| < a_{\mathrm{max}}, \tag{5.3}$$

where i and j represent the endpoints of a cluster, any point k where $i<k<j$ is removed from the data set. If, however, the absolute acceleration between points i and j still exceeds a_{max}, the cluster is considered to be a real velocity change and all data points within it are retained.

To assist in deciding on the value of the maximum allowable acceleration or deceleration a_{max}, the value of $\Delta u/\Delta t$ for each data point was calculated and the 1st and 99th percentile was determined for each data set in the wake. The results can be seen in Table 5.1. The same value of $a_{\mathrm{max}} = 40\ \mathrm{m/s^2}$ was used for each location.

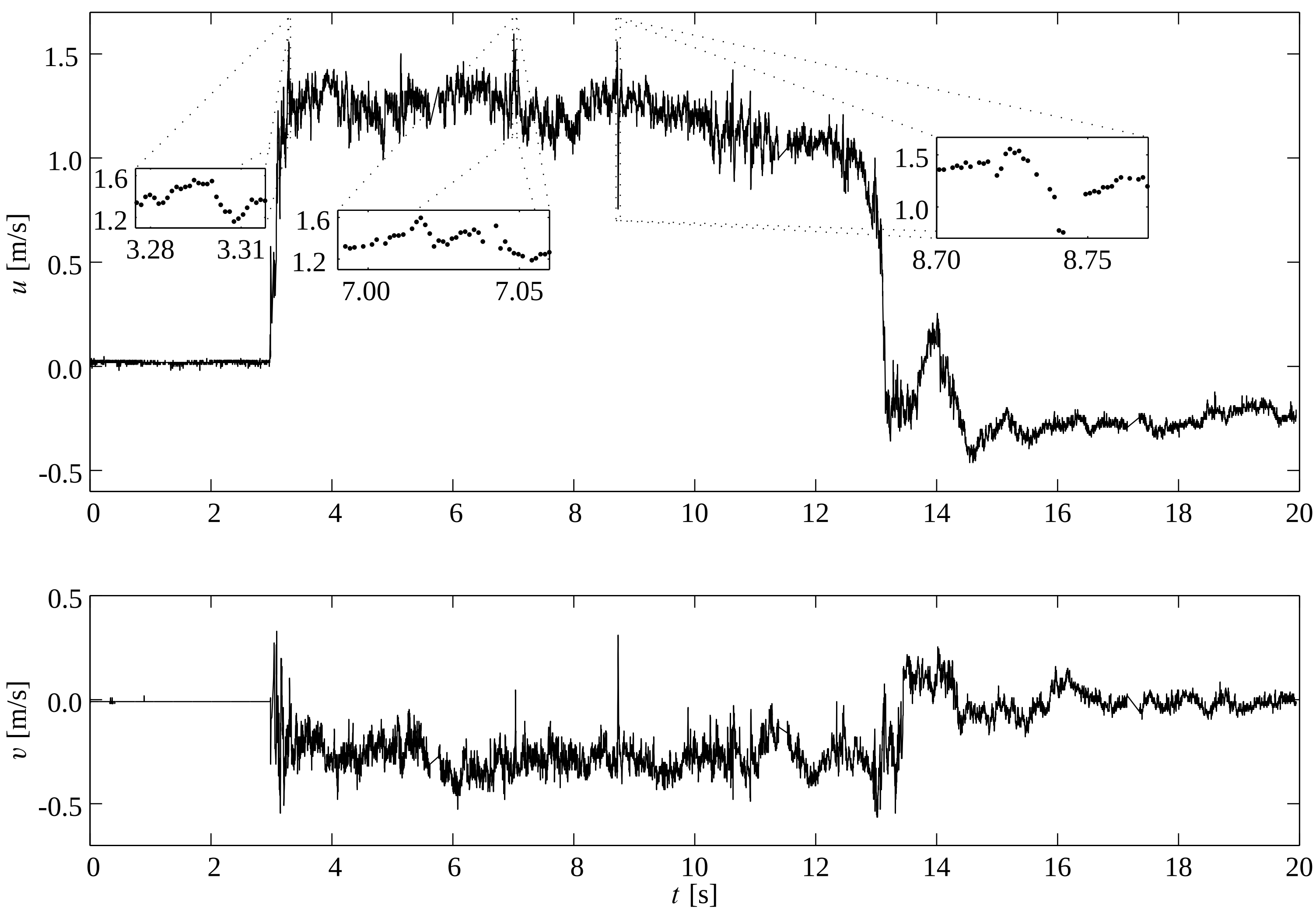

Figure 5.39: Spikes in velocity measurements in the wake of the circular column, $h_1 = 250$ mm, $(x, y, z) = (350, 70, 15)$ mm

Table 5.1: Values of the 1st and 99th percentile of $\Delta u/\Delta t$ for different data sets

x	y	z	$a_{0.01}$	$a_{0.99}$
350 mm	0 mm	15 mm	-70 m/s^2	75 m/s^2
		35 mm	-68 m/s^2	78 m/s^2
	70 mm	15 mm	-36 m/s^2	36 m/s^2
		35 mm	-48 m/s^2	48 m/s^2
	140 mm	15 mm	-32 m/s^2	32 m/s^2
		35 mm	-34 m/s^2	32 m/s^2
	210 mm	15 mm	-29 m/s^2	29 m/s^2
		35 mm	-32 m/s^2	29 m/s^2
470 mm	0 mm	15 mm	-49 m/s^2	54 m/s^2
		35 mm	-53 m/s^2	54 m/s^2
	70 mm	15 mm	-42 m/s^2	42 m/s^2
		35 mm	-55 m/s^2	50 m/s^2
	140 mm	15 mm	-32 m/s^2	32 m/s^2
		35 mm	-36 m/s^2	36 m/s^2
	210 mm	15 mm	-32 m/s^2	34 m/s^2
		35 mm	-32 m/s^2	32 m/s^2

5.2.5 Base velocity

In order to estimate the turbulent kinetic energy, values for velocity deviations are needed. These can be expressed as

$$\boldsymbol{u}' = \boldsymbol{u} - \boldsymbol{u}_{\mathbf{b}} \tag{5.4}$$

where $\boldsymbol{u}$ is a velocity vector and $\boldsymbol{u}_{\mathbf{b}}$ is a base velocity. As the bore passes the obstacle, there are large changes in the flow structure, and therefore in the velocity. These changes represent changes in the base flow and are not related to turbulence in the flow. Therefore defining $\boldsymbol{u}_{\mathbf{b}}$ as the time averaged velocity is not applicable, rather, a type of moving average is needed. However calculating a moving average, $\overline{\boldsymbol{u}}$, using

$$\overline{\boldsymbol{u}}(t) = \frac{1}{\Delta t} \int_{t-\frac{1}{2}\Delta t}^{t+\frac{1}{2}\Delta t} \boldsymbol{u}(\tau)\,\mathrm{d}\tau, \tag{5.5}$$

where t is time and Δt represents the length of the time interval the velocity is averaged over, does not solve the problem, as the changes in the flow are very abrupt, especially at the time of bore impact. A single averaging interval Δt provides too much averaging in some portions of the velocity time history and does not provide enough averaging in others. A different definition of a base velocity $\boldsymbol{u}_{\mathbf{b}}$ is then needed. First the time of bore arrival, t_0, needs to be identified from the velocity time history. Before that the water is still so

$$\boldsymbol{u}_{\mathbf{b}}(t < t_0) = (0, 0, 0). \tag{5.6}$$

After the bore has arrived the base velocity is calculated using repeated moving average calculations.

$$\boldsymbol{u}_{i+1}(t) = \begin{cases} \dfrac{1}{t - t_0 + \Delta t} \displaystyle\int_{t_0}^{t+\Delta t} \boldsymbol{u}_i(\tau)\,\mathrm{d}\tau & \text{if} \quad t_0 < t < t_0 + \Delta t, \\ \dfrac{1}{2\Delta t} \displaystyle\int_{t-\Delta t}^{t+\Delta t} \boldsymbol{u}_i(\tau)\,\mathrm{d}\tau & \text{if} \quad t_0 + \Delta t < t, \end{cases} \tag{5.7}$$

where i is the step number in the repetition and $\boldsymbol{u}_0 = \boldsymbol{u}$. Four repetitions are used so $\boldsymbol{u}_{\mathrm{b}} = \boldsymbol{u}_4$. The value of the half-interval Δt is set to 0.1 s. Figures 5.40 and 5.41 show examples of these calculations at different locations in the wake of the large circular column. The broken vertical line indicate the interval used in the calculations in §5.2.6.

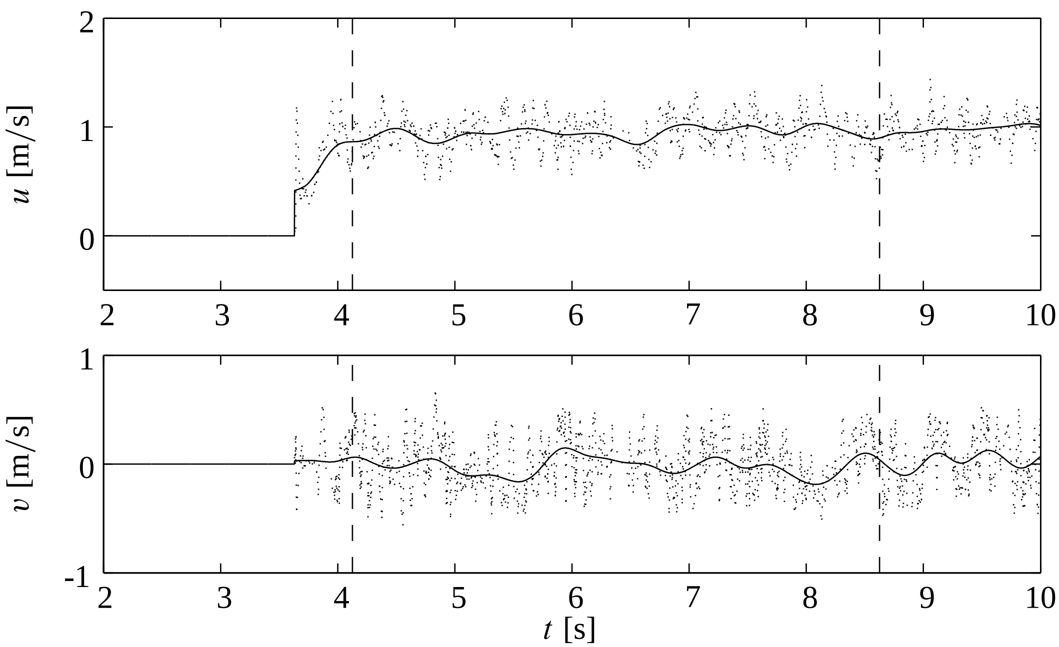

Figure 5.40: Velocity data and base velocity in the wake of the large circular column at $x = 350$ mm, $y = 0$ mm and $z = 15$ mm for $h_1 = 250$ mm

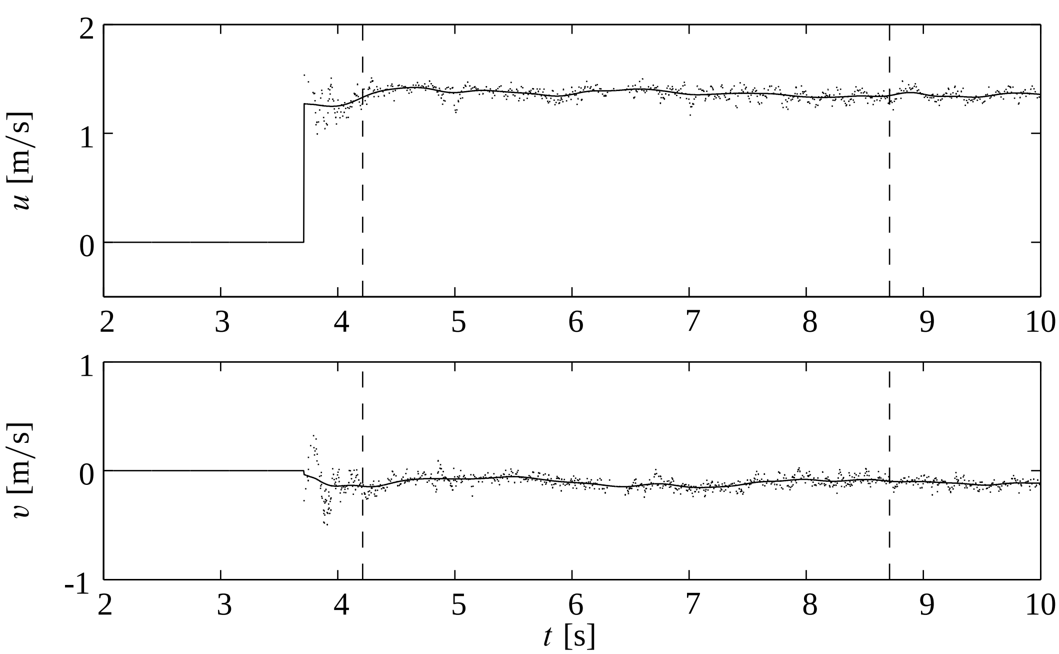

Figure 5.41: Velocity data and base velocity in the wake of the large circular column at $x = 470$ mm, $y = 210$ mm and $z = 35$ mm for $h_1 = 250$ mm

5.2.6 Turbulence intensity

Restating the definition of turbulent velocity:

$$\boldsymbol{u}' = \boldsymbol{u} - \boldsymbol{u}_{\mathrm{b}}. \tag{5.8}$$

The turbulence intensity is then calculated as the root-mean-square average of the velocity deviations or

$$\mathrm{rms}(u') = \sqrt{\overline{u}'^2} \tag{5.9}$$

where the averaging interval is 20 times that used for the base velocity calculations or $20\varDelta t = 2$ s. Figures 5.42 through 5.43 show results of such calculations for a 5.5 s long interval starting 0.5 s after the bore arrival. Away from the centerline there is a clear decrease in turbulence intensity in time, in both the x and y-directions. The magnitudes of u'_{rms} and v'_{rms} are about the same away from the centerline, while $v'_{\mathrm{rms}} > u'_{\mathrm{rms}}$ near the centerline. Using root mean square values over the interval described above, and calculating $u'_{\mathrm{rms}}/\,|\overline{\boldsymbol{u}}|$, where

$$|\overline{\boldsymbol{u}}| = \sqrt{\overline{u}^2 + \overline{v}^2}, \tag{5.10}$$

yields values of 0.04–0.06 away from the centerline, 0.18 on the centerline at $x = 350$ mm and 0.11 at $x = 470$ mm. For all values see Table 5.2. Generally the turbulence in the x-direction is greater at the lower elevation, but that does not hold for the y-direction. There the turbulence is greater at the lower elevation on the centerline, but varies outside of it. On the centerline the turbulence intensity in the y-direction is considerably higher than that in the x-direction, while the magnitude is similar in either direction away from the centerline. The turbulence intensity in either direction is much higher on the centerline than away from it. Figures 5.44 and 5.45 show how the ratio varies with the downstream distance and Figures 5.46 and 5.47 show how it varies across the tank.

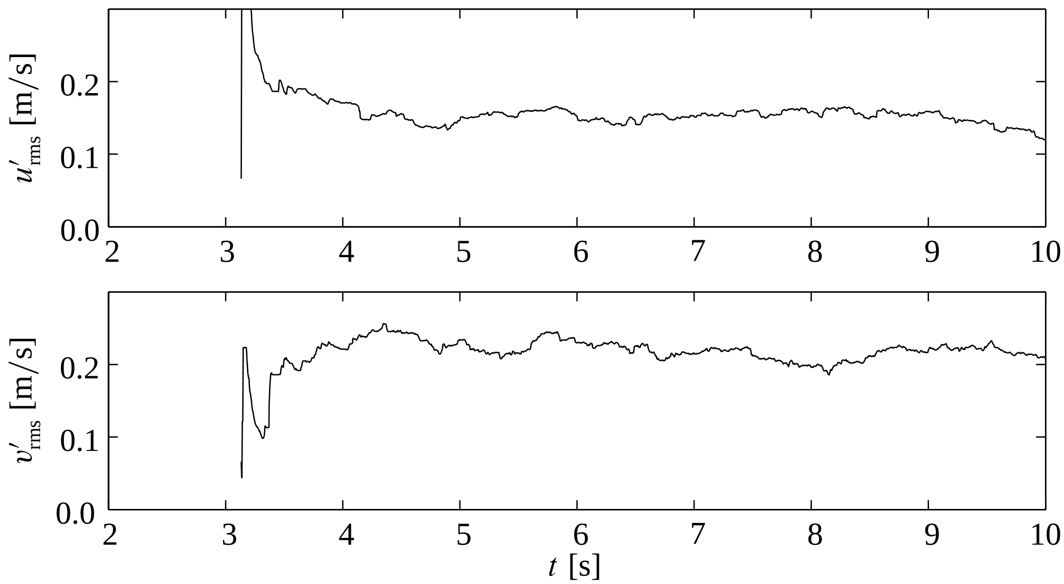

Figure 5.42: Root-mean-square average of velocity deviations in the wake of the large circular column at $x = 350$ mm, $y = 0$ mm and $z = 15$ mm for $h_1 = 250$ mm

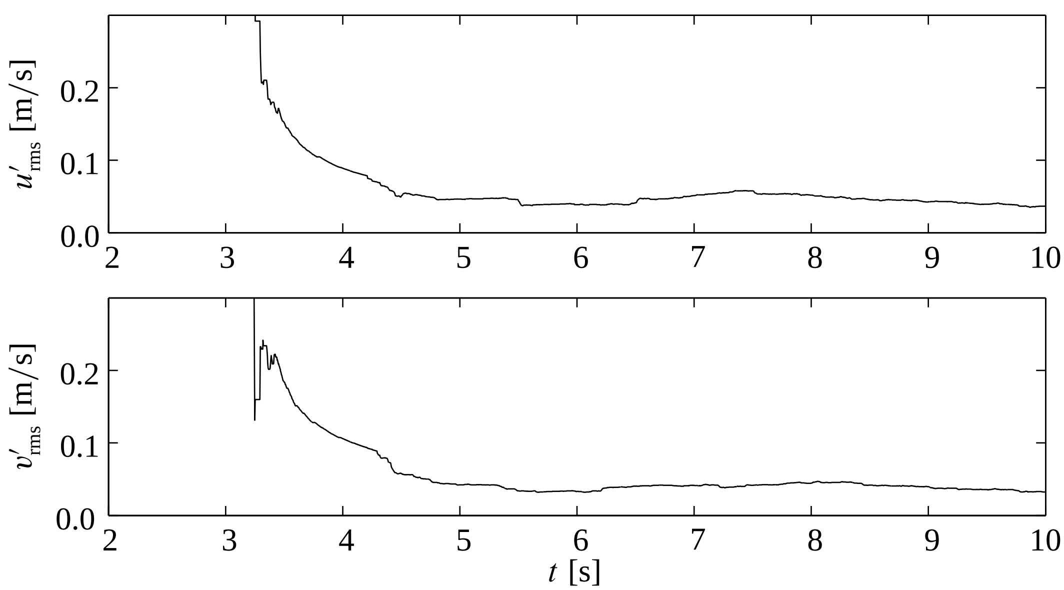

Figure 5.43: Root-mean-square average of velocity deviations in the wake of the large circular column at $x = 470$ mm, $y = 210$ mm and $z = 35$ mm for $h_1 = 250$ mm

Table 5.2: Velocity deviation as a ratio of the mean velocity in the wake of the circular column for $h_1 = 250$ mm

x	y	z	$u'_{\mathrm{rms}}/\lvert\overline{\boldsymbol{u}}\rvert$	$v'_{\mathrm{rms}}/\lvert\overline{\boldsymbol{u}}\rvert$
210 mm	0 mm	15 mm	0.1762	0.2581
		35 mm	0.1399	0.3044
	70 mm	15 mm	0.0374	0.0325
		35 mm	0.0363	0.0295
	140 mm	15 mm	0.0468	0.0456
		35 mm	0.0362	0.0394
	210 mm	15 mm	0.0618	0.0636
		35 mm	0.0501	0.0487
350 mm	0 mm	15 mm	0.1621	0.2335
		35 mm	0.1597	0.2315
	70 mm	15 mm	0.0460	0.0407
		35 mm	0.0444	0.0417
	140 mm	15 mm	0.0464	0.0394
		35 mm	0.0307	0.0281
	210 mm	15 mm	0.0418	0.0402
		35 mm	0.0366	0.0354
470 mm	0 mm	15 mm	0.1093	0.1489
		35 mm	0.0955	0.1740
	70 mm	15 mm	0.0598	0.0595
		35 mm	0.0604	0.0597
	140 mm	15 mm	0.0417	0.0394
		35 mm	0.0433	0.0439
	210 mm	15 mm	0.0376	0.0364
		35 mm	0.0332	0.0311

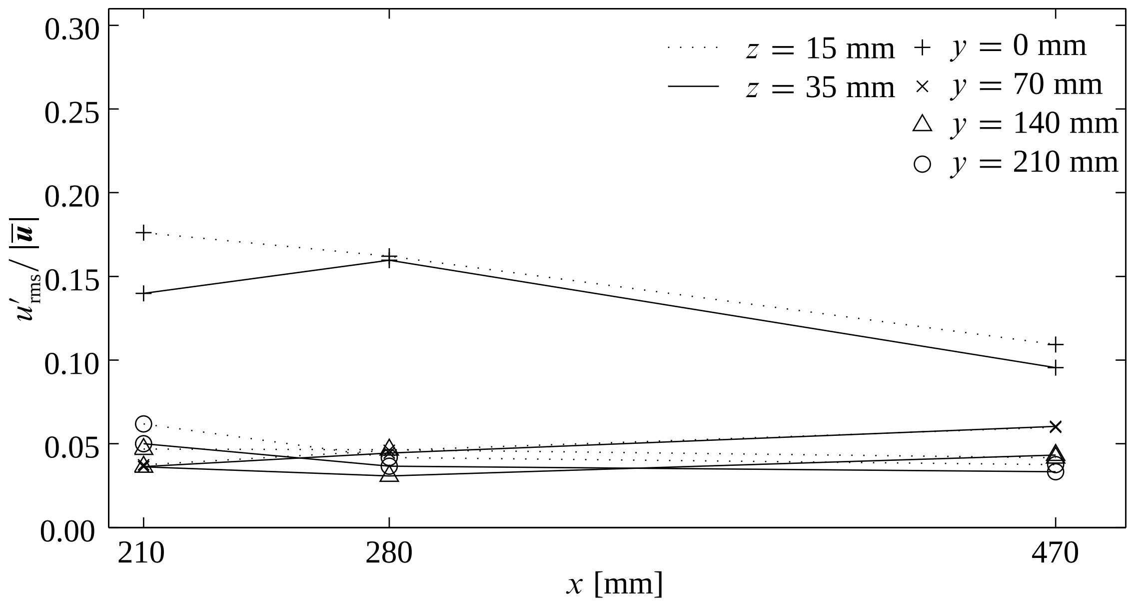

Figure 5.44: The flow-wise variations in relative flow-wise turbulence intensity

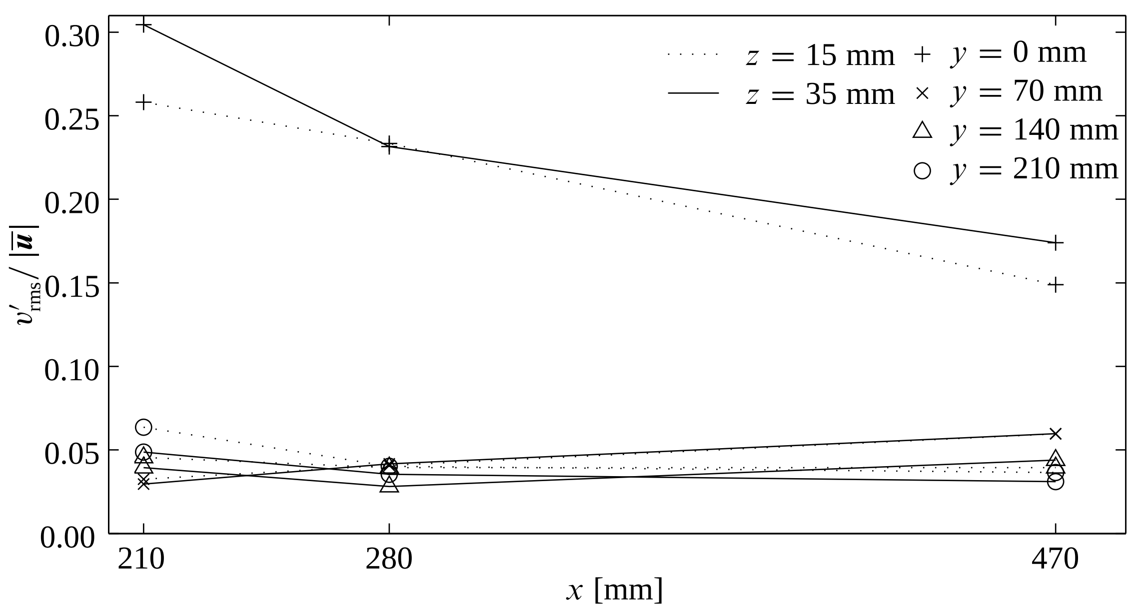

Figure 5.45: The flow-wise variations in relative span-wise turbulence intensity

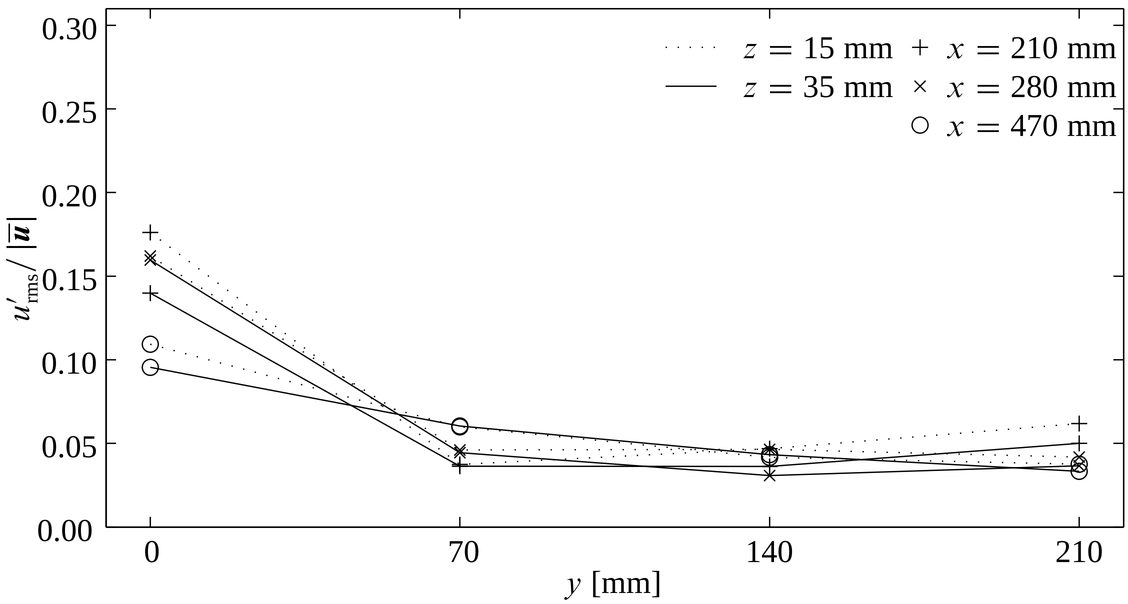

Figure 5.46: The span-wise variations in relative flow-wise turbulence intensity

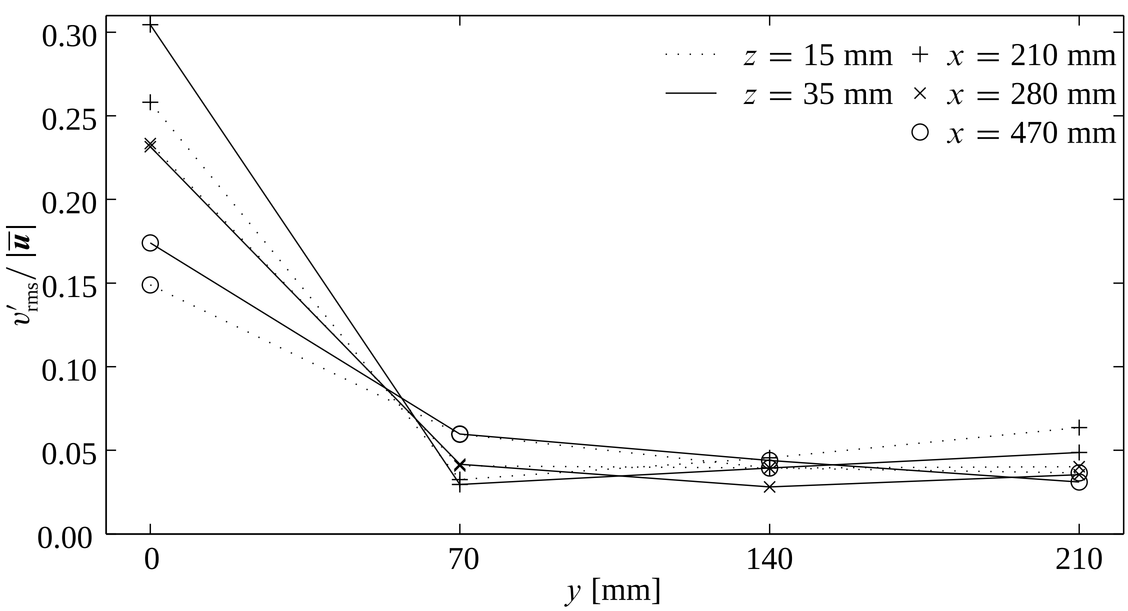

Figure 5.47: The span-wise variations in relative span-wise turbulence intensity

5.2.7 Energy budget in the wake

Using H to denote head or energy divided by weight, we have at a cross-section x, three energy components, potential energy H_{p}, mean flow kinetic energy H_{k} and turbulent kinetic energy H_{t}. For a level bottom the potential energy is equivalent to the depth, so

$$H_{\mathrm{p}}(x, y, t) = h(x, y, t), \tag{5.11}$$

$$H_{\mathrm{k}}(x, y, z, t) = \frac{\overline{\boldsymbol{u}}^2(x, y, z, t)}{2g} = \frac{1}{2g}\left(\overline{u}^2 + \overline{v}^2 + \overline{w}^2\right) \tag{5.12}$$

and

$$H_{\mathrm{t}} = \frac{1}{A}\iint \frac{\boldsymbol{u}'^2}{2g}\,\mathrm{d}A = \frac{1}{Bhg}\int_0^{\frac{B}{2}}\int_0^{h(x,y)} \left(u'^2 + v'^2 + w'^2\right)\mathrm{d}z\,\mathrm{d}y. \tag{5.13}$$

For $\overline{u}$, the base velocity calculations, as described in §5.2.5, are used. The total energy flux $\mathscr{E}$ through a cross-section at x is

$$\begin{aligned}\mathscr{E}(x, t) &= \iint_A H(x, y, z, t)\gamma u\,\mathrm{d}A \\ &= 2\gamma \int_0^{\frac{B}{2}}\int_0^{h(x,y,t)} \left(H_{\mathrm{p}}(x, y, t) + H_{\mathrm{k}}(x, y, z, t) + H_{\mathrm{t}}(x, y, z, t)\right) \\ &\qquad\qquad \times u(x, y, z, t)\,\mathrm{d}z\,\mathrm{d}y\end{aligned} \tag{5.14}$$

where $\frac{B}{2}$ is the distance from the obstacle's centerline to the side wall of the tank.

To estimate the kinetic turbulent head, H_{t}, the values of u'_{rms}, v'_{rms} and w'_{rms} are required. For the cases of bore impact on an obstacle, the LDV measurements provide the first two values, but not w'_{rms}. Therefore it must be estimated from the other two turbulent velocity components. It can be expected to be of the same order of magnitude as u' and v'. The assumption is therefore made that

$$w'_{\mathrm{rms}} = \frac{1}{2}\left(u'_{\mathrm{rms}} + v'_{\mathrm{rms}}\right) \tag{5.15}$$

or

$$\left(u'_{\mathrm{rms}} + v'_{\mathrm{rms}} + w'_{\mathrm{rms}}\right) = \frac{3}{2}\left(u'_{\mathrm{rms}} + v'_{\mathrm{rms}}\right) \tag{5.16}$$

so H_{t} is estimated to be

$$H_{\mathrm{t}} = \frac{1}{2g}\overline{\boldsymbol{u}'^2} = \frac{1}{2g}\left(\overline{u'^2} + \overline{v'^2} + \overline{w'^2}\right) = \frac{3}{4g}\left(u'^2_{\mathrm{rms}} + v'^2_{\mathrm{rms}}\right). \tag{5.17}$$

In the wake of the large circular column for an impoundment of 250 mm, water surface data is available at $x = 350$ mm and 470 mm for $0 \leq y \leq \frac{B}{2}$. The data are a time sequence of snapshots of the surface, taken every $\frac{1}{30}$ of a second (see Figures 5.11 and 5.12). Each snapshot is composed of a sequence of points $(y, h(y))$, where y is not at a regular interval because of the image processing of the water surface described in §4.4.1.

A velocity time history for u and v is available at 24 points on a three-dimensional rectangular grid at $x = 210$ mm, 350 mm and 470 mm, $y = 0$ mm, 70 mm, 140 mm and 210 mm, and $z = 15$ mm and 35 mm (see Figure 5.48). No data is available for the vertical velocity component w, but w' is estimated from u' and v' as described in §5.2.6.

Using discrete data, the integrals in Equation 5.14 become sums. The velocity at each measurement point is taken to represent the velocity over a section of the cross-section as seen in Figure 5.49, i.e. at any given point in the cross-section the velocity is taken to be the same as at the closest measurement point. The components of total energy then become

$$\mathscr{E}_{\mathrm{p}} = \gamma \sum_{i=1}^{8} u_i \overline{h}_i A_i, \tag{5.18}$$

$$\mathscr{E}_{\mathrm{k}} = \frac{\rho}{2} \sum_{i=1}^{8} u_i \left(u_{\mathrm{b}}^2 + v_{\mathrm{b}}^2\right)_i A_i \tag{5.19}$$

and

$$\mathscr{E}_{\mathrm{t}} = \frac{3\rho}{4} \sum_{i=1}^{8} u_i \left(u'^2_{\mathrm{rms}} + v'^2_{\mathrm{rms}}\right)_i A_i \tag{5.20}$$

where A_i represents the area closest to point i. For $1 \leq i \leq 4$ (the lower points) it is a constant whereas for $5 \leq i \leq 8$ (the upper points) it evolves with h. The horizontal velocity deviations (u', v') are calculated as

$$u'_{\mathrm{rms}} = \left(\frac{1}{n} \sum_{t-\Delta t < t_i < t+\Delta t} u'^2\right)^{\frac{1}{2}}. \tag{5.21}$$

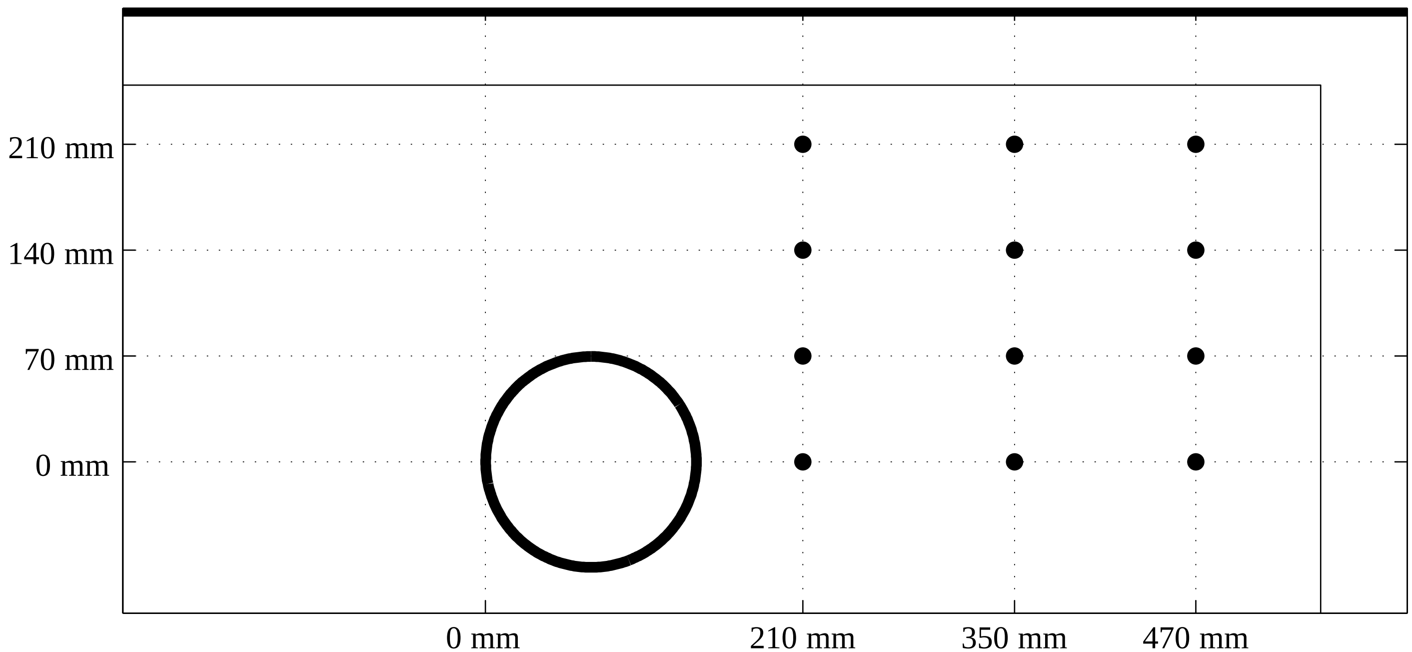

Figure 5.48: Location of LDV measurements in the wake of the large circular column

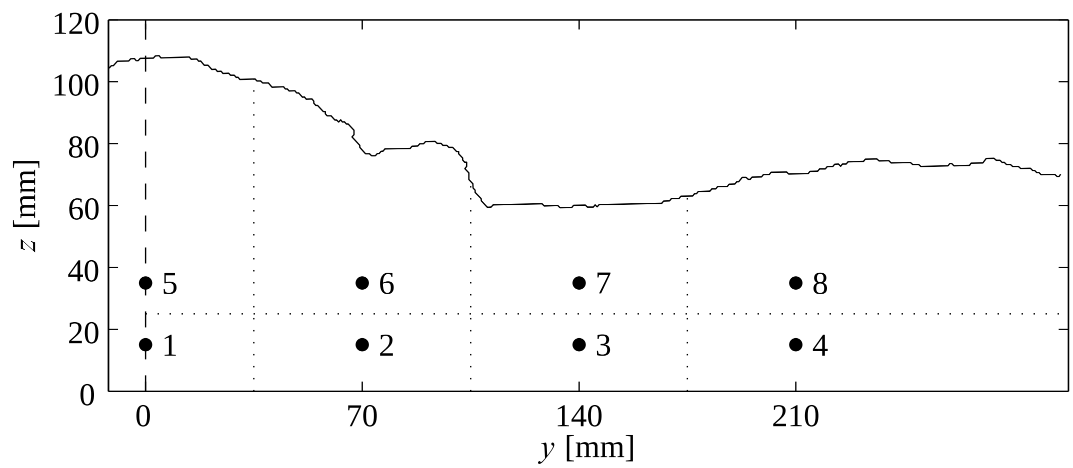

Figure 5.49: An example of a cross-section, showing the water surface and location of the velocity measurement points used in the summation of the energy flux, $x = 350$ mm and $h_1 = 250$ mm

Figures 5.50 through 5.52 show the calculations for each of the 8 segments, for the $x = 350$ mm cross-section.

Results for a cross-section at $x = 470$ mm can be seen in Figure 5.53. It shows the time history of the total energy flux, as well as the three components, i.e. the flux of potential, mean kinetic and turbulent kinetic energy. The magnitude of the turbulent kinetic energy flux is just under 2 % of the mean kinetic energy flux, averaged over the whole cross-section. The mean kinetic and the potential energy flux through the cross-section are about the same, never more than about 10 % from each other during the passage of the bore. So during the passing of the bore, both the potential and kinetic energy flux is in the range (50 ± 5) %, while the turbulent kinetic energy is a little over 1 %.

Figure 5.54 shows the energy flux through a cross-section closer to the cylinder, at $x = 350$ mm. The numbers there are very similar, though the turbulent kinetic energy is closer to 3 % of the mean kinetic energy. So there is more turbulent energy closer to the cylinder, while still not a significant portion of the total energy.

Points with available velocity data upstream of the obstacle for the same impoundment,

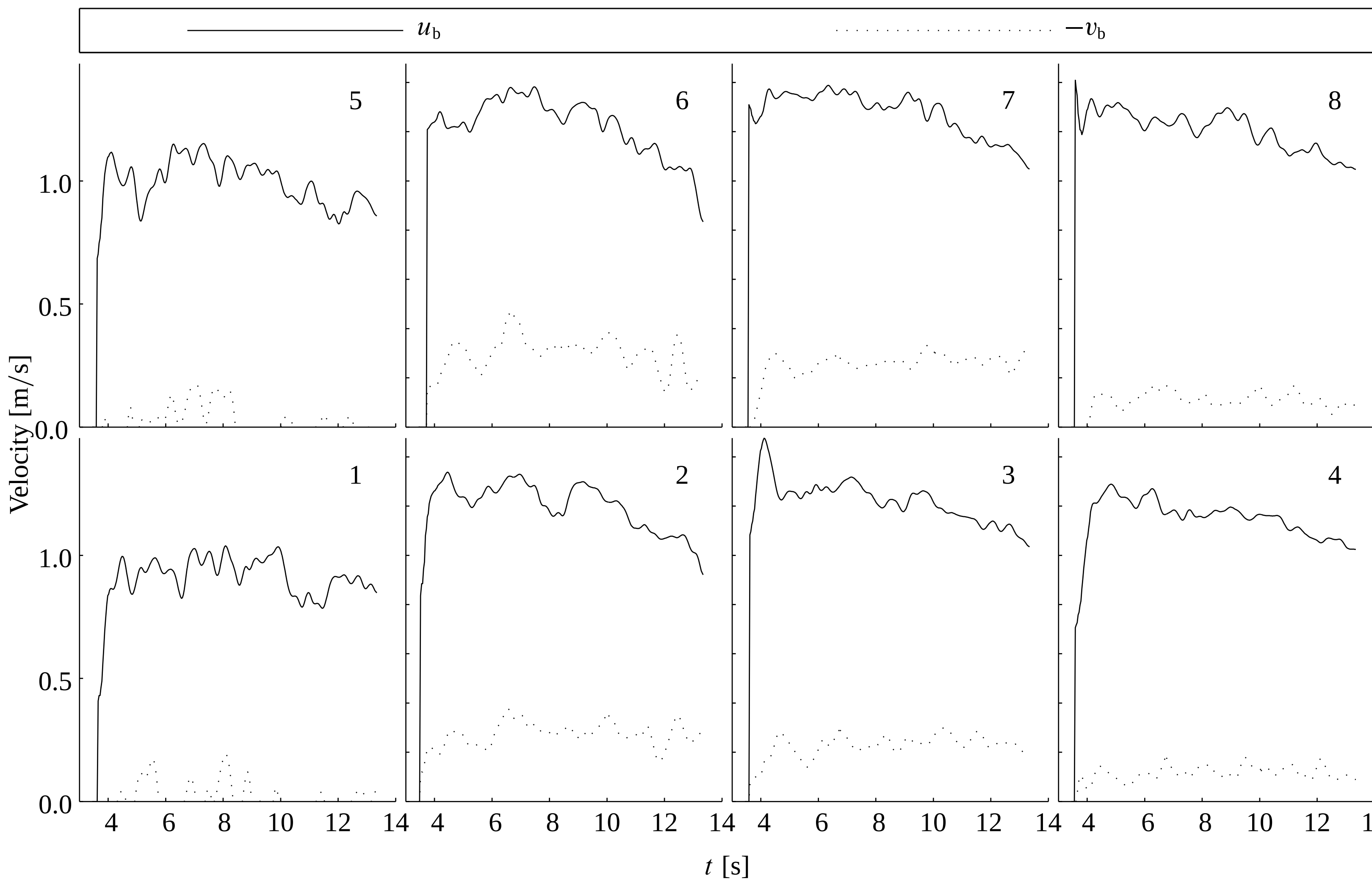

Figure 5.50: The mean velocity history for each segment at $x = 350$ mm and $h_1 = 250$ mm

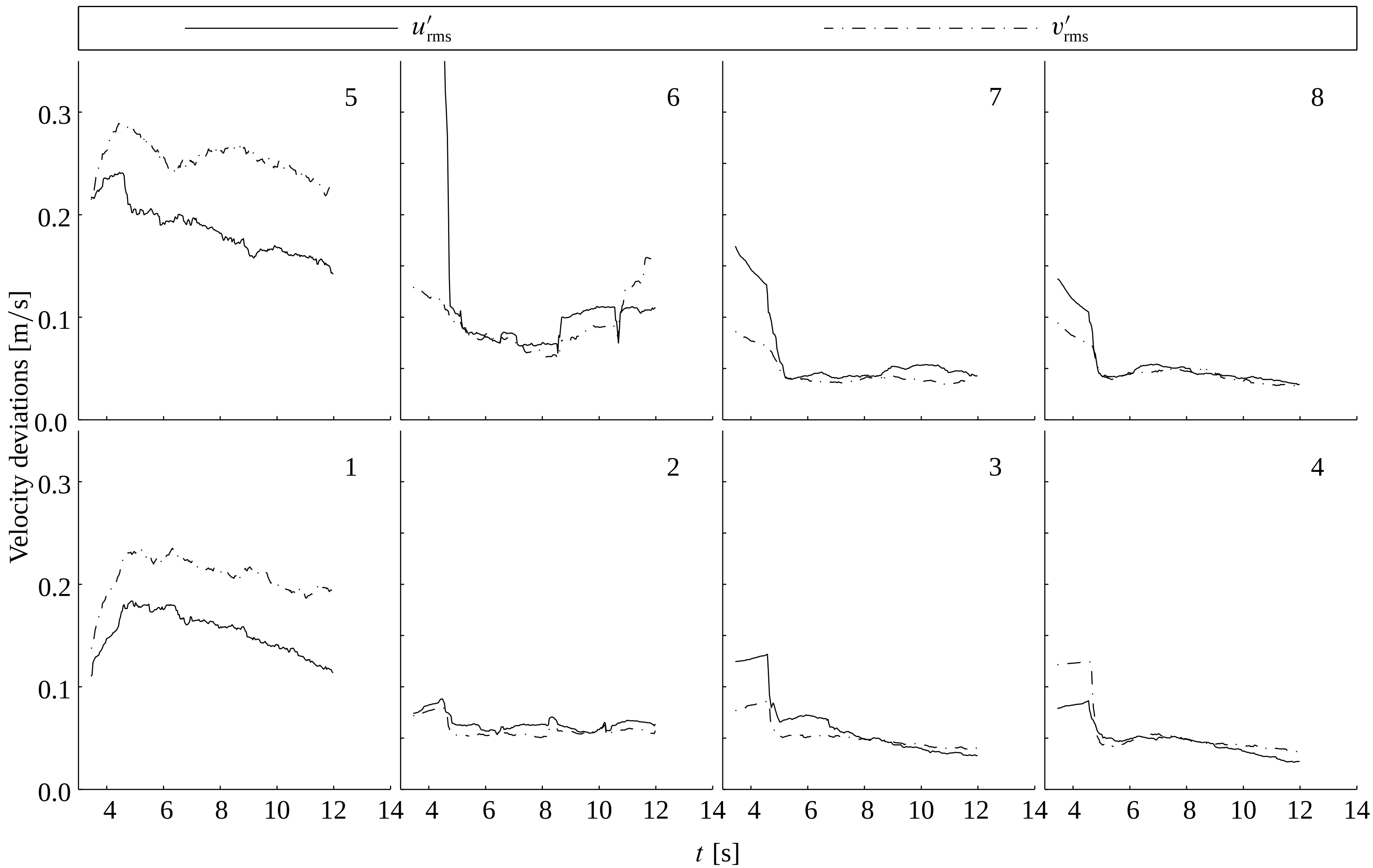

Figure 5.51: The velocity deviation history for each segment at $x = 350$ mm and $h_1 = 250$ mm

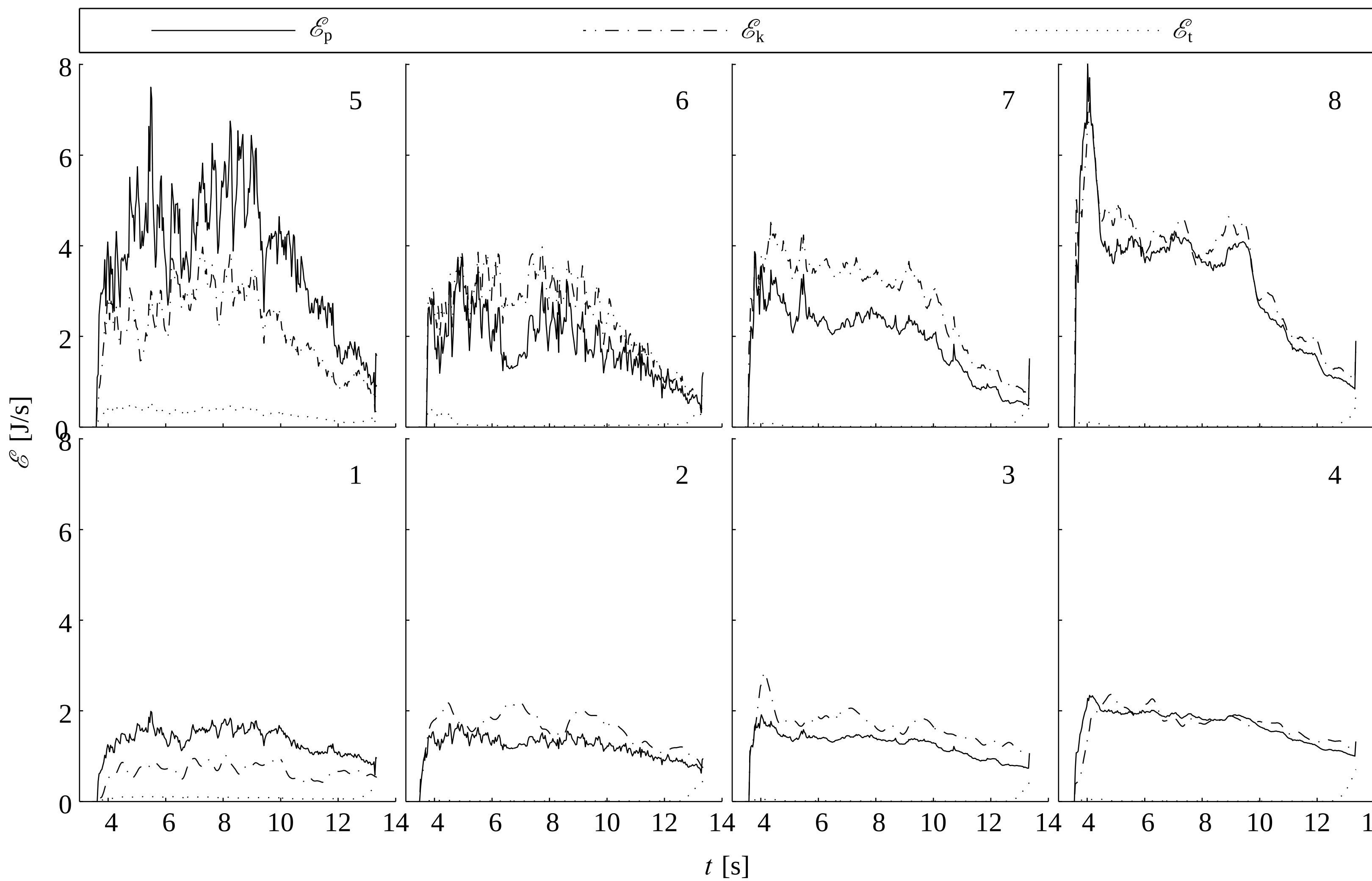

Figure 5.52: The energy flux history for each segment at $x = 350$ mm and $h_1 = 250$ mm

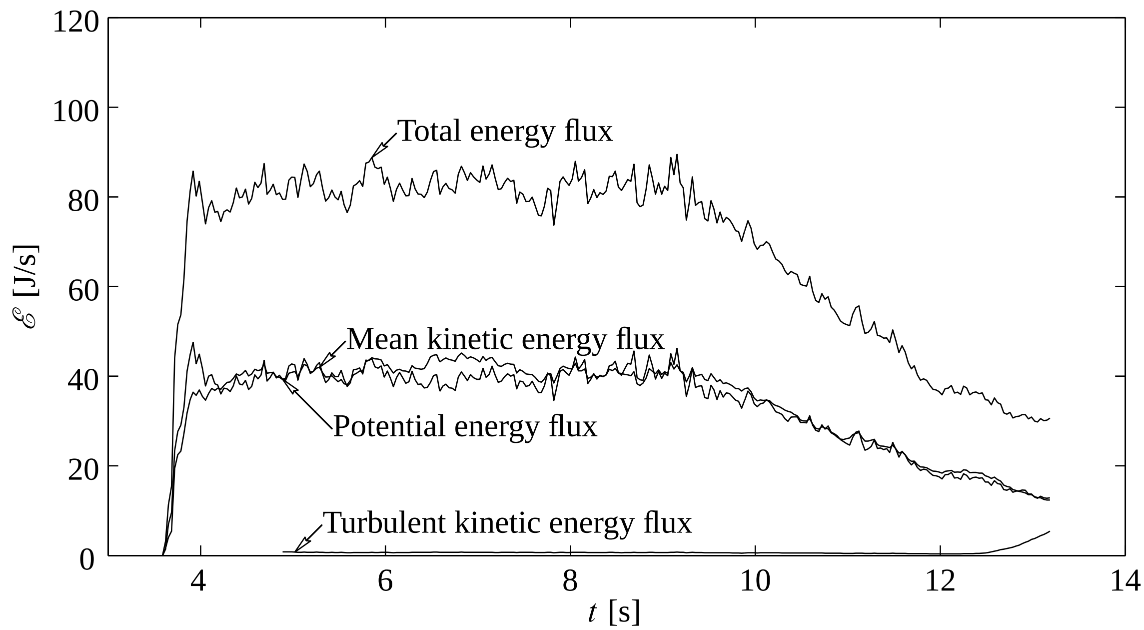

Figure 5.53: Energy flux through a cross-section at $x = 470$ mm in the wake of the large circular column for $h_1 = 250$ mm

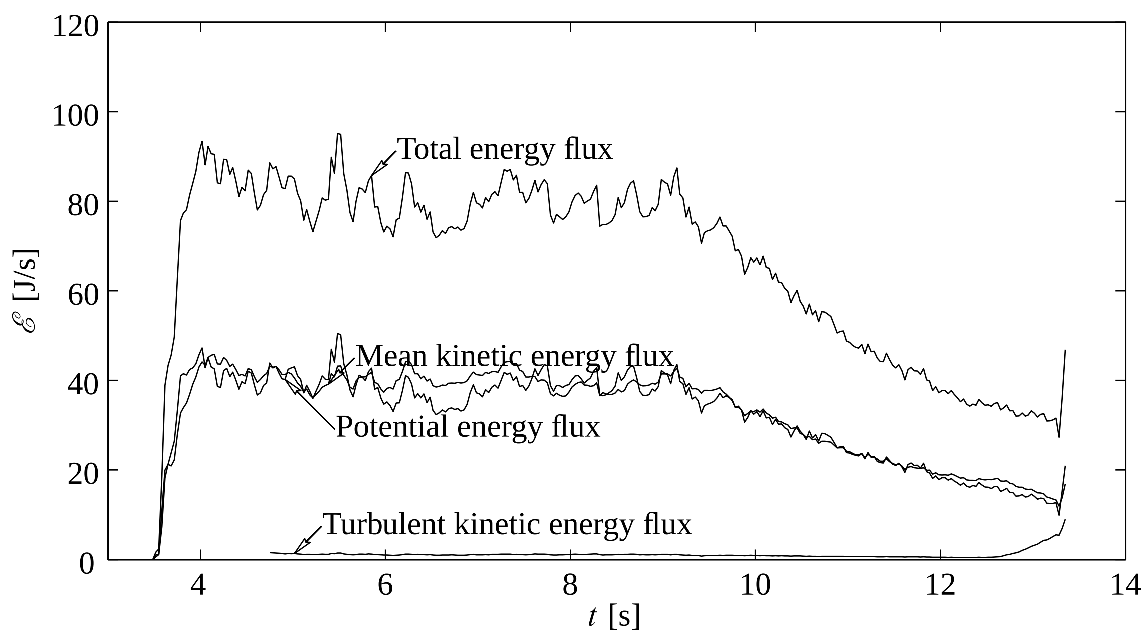

Figure 5.54: Energy flux through a cross-section at $x = 350$ mm in the wake of the large circular column for $h_1 = 250$ mm

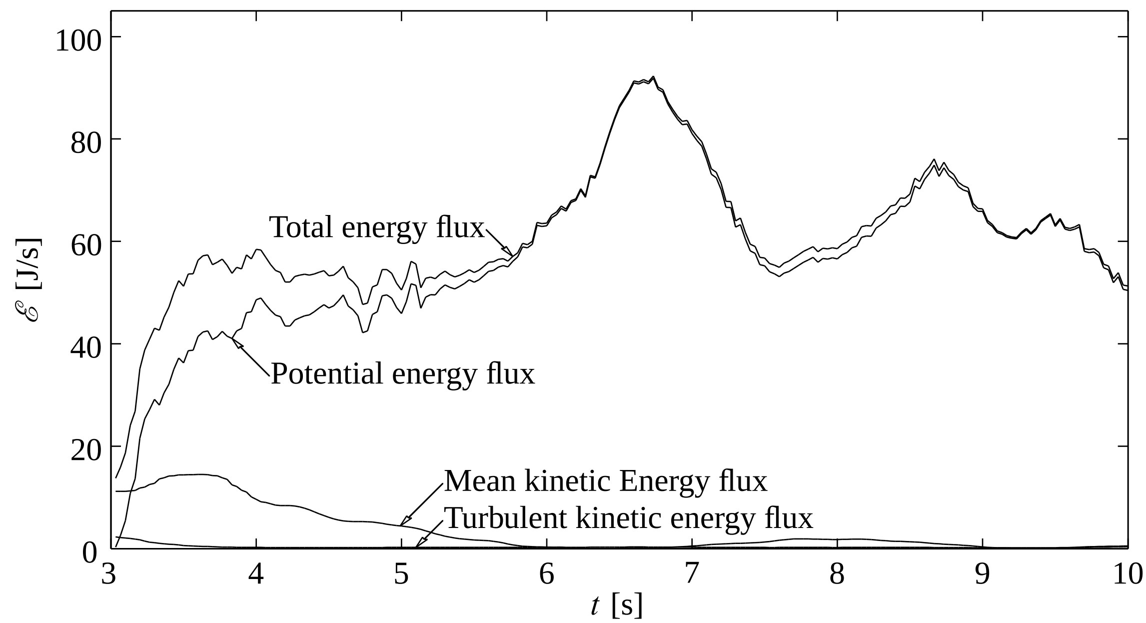

Figure 5.55: Energy flux through a cross-section at $x = -300$ mm for $h_1 = 250$ mm

form a 3×3 matrix with $y = 0$ mm, 70 mm and 130 mm measured from the centerline and $z = 8$ mm, 24 mm and 60 mm measured from the tank floor. This cross-section is at $x = -300$ mm, i.e. 300 mm upstream of the obstacle's extreme upstream point. There is no surface profile at $x = -300$ mm, but there are profiles at all three y-values, crossing the section. It is therefore possible to obtain a water level time history $h(x = -300 \text{ mm}, y, t)$, where as before $y = 0$ mm, 70 mm or 130 mm and t ranges from 3–10 s. Now the energy flux through this cross-section can be calculated with the same methods as for the downstream cross-sections, with the exception that no numerical integration of the water surface level over the cross-section takes place, but each segment uses the depth from the single measurement point within it. As the span-wise variations in the water surface level are much smaller upstream of the obstacle than they are in the wake this should not cause any discrepancy. Figure 5.55 shows each component of the energy flux through this upstream cross-section. Unlike in the cross-sections in the wake, the potential energy dominates here. As the bore front passes, the kinetic energy represents about 20 % of the total energy, but

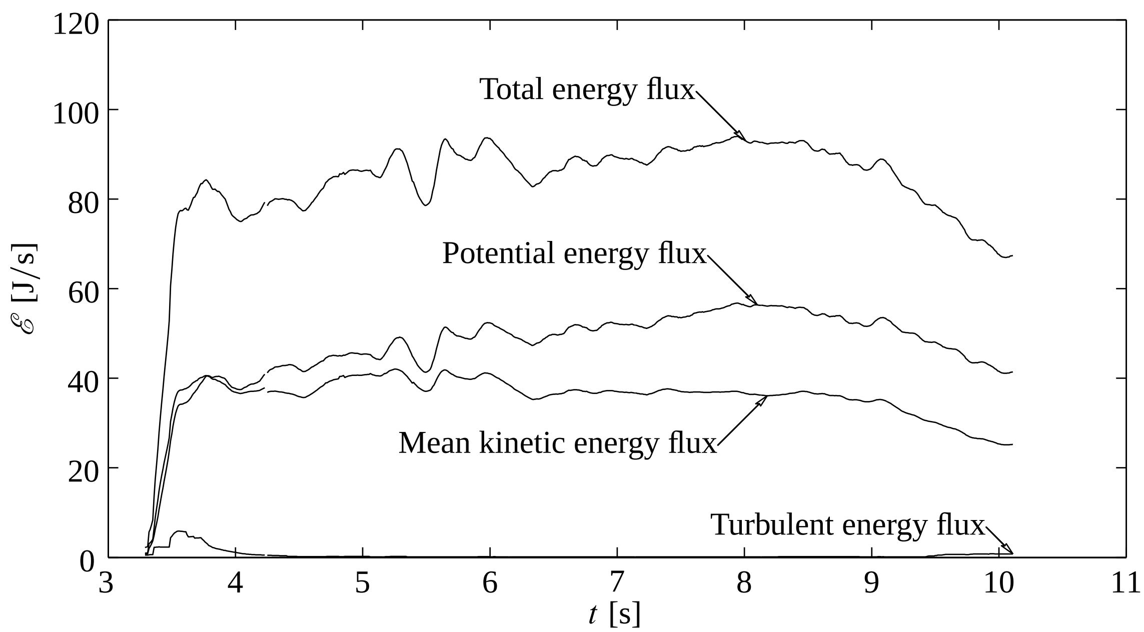

Figure 5.56: Energy flux in the bore with no obstacle at $x = 0$ and $h_1 = 250$ mm

decreases quickly and is within 1 % after about 2.5 s. During the passing of the first reflected wave from the obstacle the kinetic energy flux is less than 0.1 % of the total energy flux and just under 0.2 % for the second and only rises to about 1.5 % in the trough.

Figure 5.56 shows the results of calculating the energy flux through a cross-section of the undisturbed bore, i.e. without any obstacle in it. The impoundment was 250 mm and the velocity data are all from the centerline but at varying depths (see Table 4.4). The waterlevel data comes from wavegauge measurements (see Figure 5.57) The magnitude of the turbulent kinetic energy is about 0.5 % of that of the mean kinetic energy. The mean kinetic energy is about 60 % of the magnitude of the potential energy flux just behind the bore front, but that ratio gradually decreases during the passing of the bore. At approximately $t = 8.5$ s the decreases and the ratio hold at 33–35 %. The timing of this behavior change corresponds reasonably to expected time of the effects of flow depletion form the tank's upstream boundary, which according to Table 3.1 should be at 8.79 s.

Figure 5.58 compares the time history of the energy flux through the downstream cross-

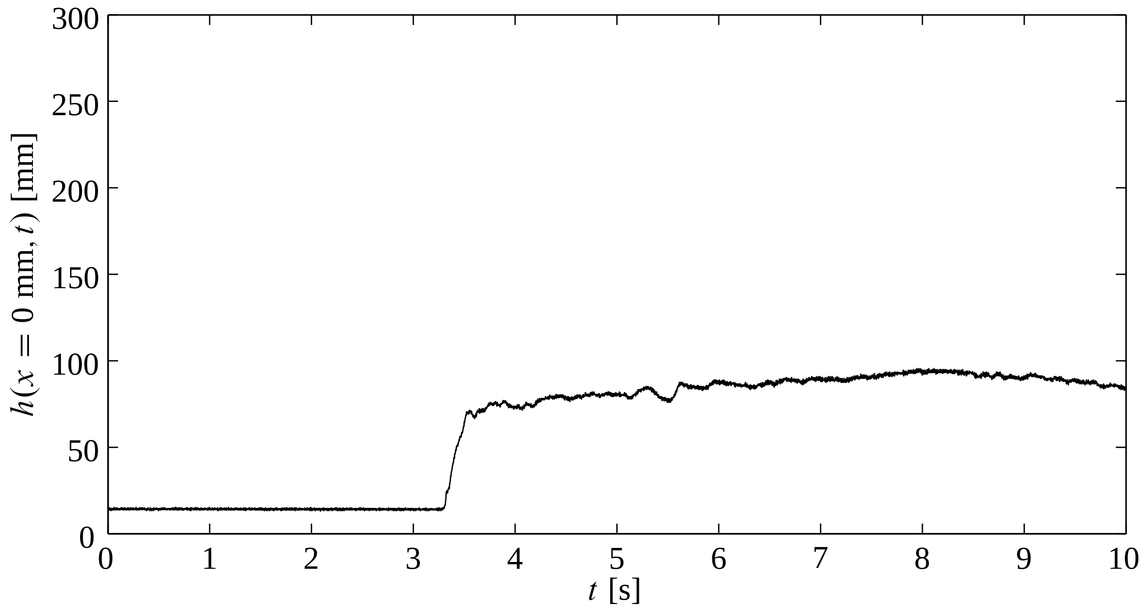

Figure 5.57: The water surface profile on the centerline without any obstacle in the flow at $x = 0$ for $h_1 = 250$ mm

sections with that of the flow without any obstacle. It shows how the placing of an obstacle in the flow affects the energy flux. Figure 5.59 shows time history of the amount of energy that has been transported through the cross-sections calculated as

$$E(t) = \int_0^t \mathscr{E}(\tau)\,\mathrm{d}\tau. \tag{5.22}$$

The difference in slope indicates the energy loss of approximately 7 %.

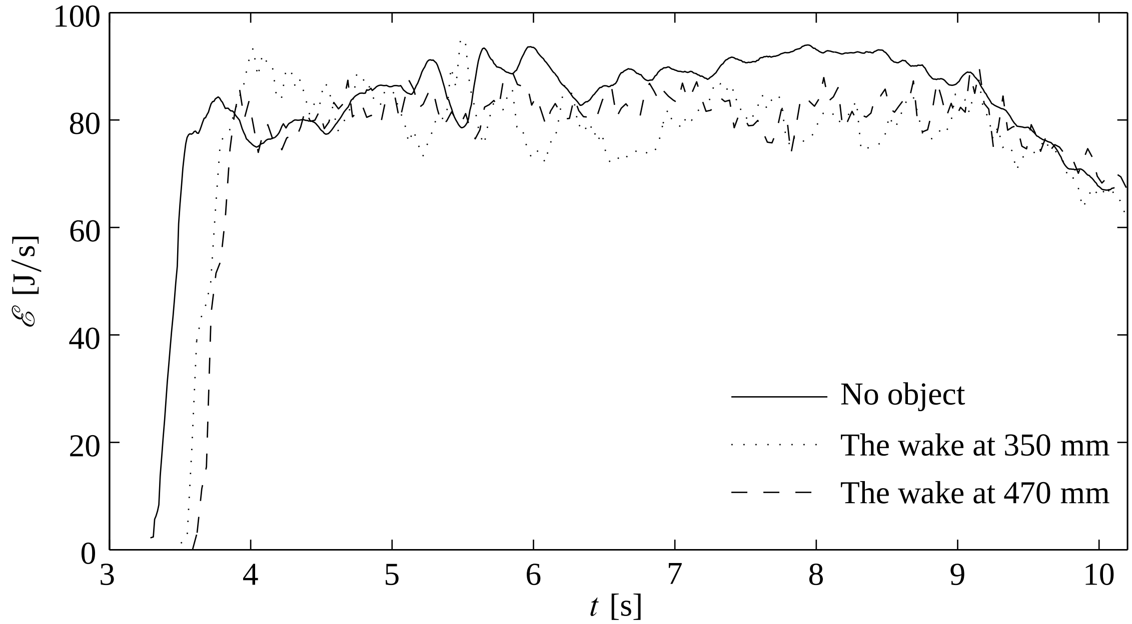

Figure 5.58: Total energy flux with and without an obstacle for $h_1 = 250$ mm

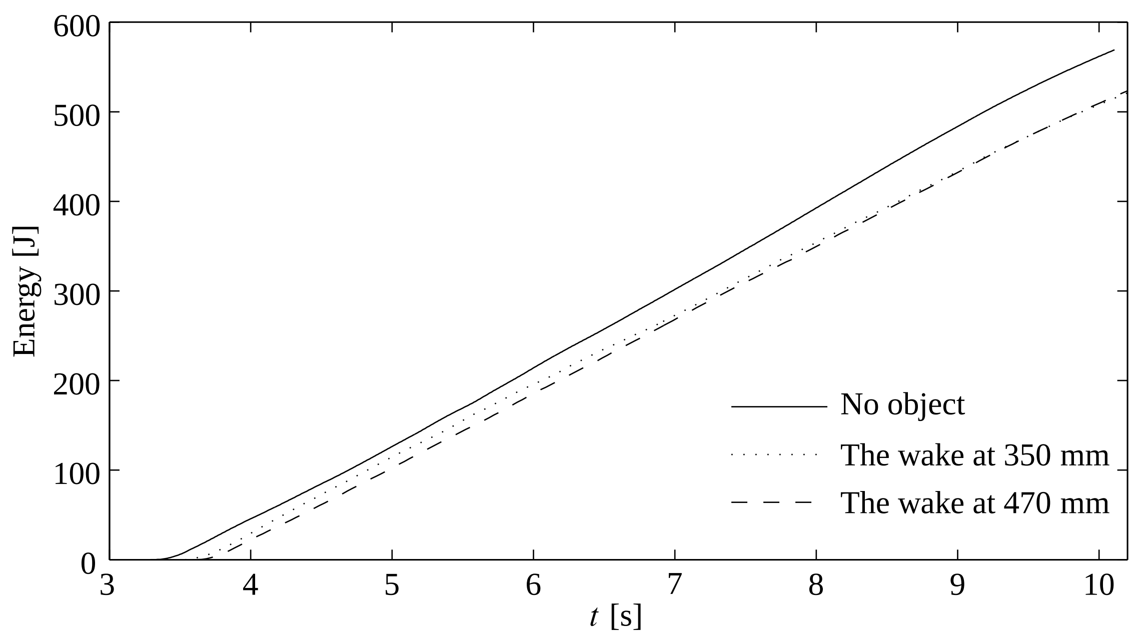

Figure 5.59: Total energy that has passed through the cross-section as a function of time for $h_1 = 250$ mm

5.2.8 Specific momentum

Using V_c and A_c to denote a control volume and its surface respectively, the momentum equation can be written as

$$\sum \boldsymbol{F} = m\boldsymbol{a} = \frac{\mathrm{d}}{\mathrm{d}t}\iiint_{V_\mathrm{c}} \rho\boldsymbol{u}\,\mathrm{d}V + \iint_{A_\mathrm{c}} \rho\boldsymbol{u}(\boldsymbol{u}\cdot\boldsymbol{n})\,\mathrm{d}A \tag{5.23}$$

where $\boldsymbol{F}$ represents the forces acting on the control volume, m is mass, $\boldsymbol{a}$ is the three-dimensional acceleration and $\boldsymbol{n}$ is the normal vector, i.e. vector of unit length normal to the surface. The first part of the right hand side of Equation 5.23 represents the rate of change of linear momentum inside the control volume over time and the second part represents the net momentum flux out of the control volume.

For a control volume limited by the tank walls and floor between two cross-sections normal to the x axis in the tank, there is only flow through the cross-sections and

$$(\boldsymbol{u}\cdot\boldsymbol{n}) = \begin{cases} u & \text{at the downstream cross-section,} \\ -u & \text{at the upstream cross-section,} \\ 0 & \text{elsewhere.} \end{cases} \tag{5.24}$$

The x direction component of the surface integral then becomes

$$\iint_{A_\mathrm{c}} \rho u(\boldsymbol{u}\cdot\boldsymbol{n})\,\mathrm{d}A = \iint_{A_\mathrm{d}} \rho u^2\,\mathrm{d}A - \iint_{A_\mathrm{u}} \rho u^2\,\mathrm{d}A \tag{5.25}$$

where A_d and A_u refer to the downstream and up stream cross-sections respectively.

The forces included in $\sum \boldsymbol{F}$ in Equation 5.23 can be divided into three separate forces. First the pressure forces acting on the upstream and downstream faces of the control volume, second friction forces from the tank walls and bottom and third, resistance and shear forces from the obstacle in the flow, i.e.

$$\sum F = F_\mathrm{h} + F_\mathrm{f} + F_x \tag{5.26}$$

Assuming a hydrostatic pressure the force from the fluid we have

$$P(y,z,t) = \gamma(h(y,t) - z) \tag{5.27}$$

where P is the pressure and γ is the specific weight of the fluid. The hydrostatic forces on the cross-sections then become

$$F_\mathrm{h} = \iint_{A_\mathrm{d}} P\,\mathrm{d}A - \iint_{A_\mathrm{u}} P\,\mathrm{d}A = \iint_{A_\mathrm{d}} \gamma(h-z)\,\mathrm{d}A - \iint_{A_\mathrm{u}} \gamma(h-z)\,\mathrm{d}A. \qquad (5.28)$$

Assuming a relatively short control volume

$$F_\mathrm{f} \approx 0 \qquad (5.29)$$

can be assumed. Adding the hydrostatic forces and momentum flux associated with each cross-section together yields

$$p_\mathrm{s}(x,t) = \iint_A \left(\rho u^2 + \gamma(h-z)\right)\mathrm{d}A \qquad (5.30)$$

where p_s will be referred to as specific momentum. The x direction component of Equation 5.23 for the control volume can now be rewritten as

$$F_x = \frac{\mathrm{d}p}{\mathrm{d}t} + p_{\mathrm{s_d}} - p_{\mathrm{s_u}} \qquad (5.31)$$

whereF_x is the reaction force of the obstacle on the control volume., p is the momentum integrated over the volume and $p_{\mathrm{s_d}}$ and $p_{\mathrm{s_u}}$ are the specific momentum at each cross-section. Therefore, by evaluating the right hand side of Equation 5.31 F_x can be estimated and compared with measured values, provided the the assumptions about V_c hold.

Using the same data as for the energy calculations (§5.2.7) for the single cross-section upstream and the two cross-sections downstream, the specific momentum is calculatedfor each section. Figure 5.60, shows the result for each of the 8 sections of the cross-section at $x = 350$ mm. Figure 5.61 shows the specific momentum at a cross-section at $x = 470$ mm and Figure 5.62 shows the same thing at $x = 350$ mm. Figure 5.63 shows the specific momentum upstream of the obstacle at $x = -300$ mm and Figure 5.64 shows what the specific momentum looks like at $x = 0$ without any obstacle in the channel.

As can be seen in Figure 5.65, the reaction force estimated by Equation 5.31 does not fit well with the measured force record (see §5.3.1). It is therefore clear that the assumption of

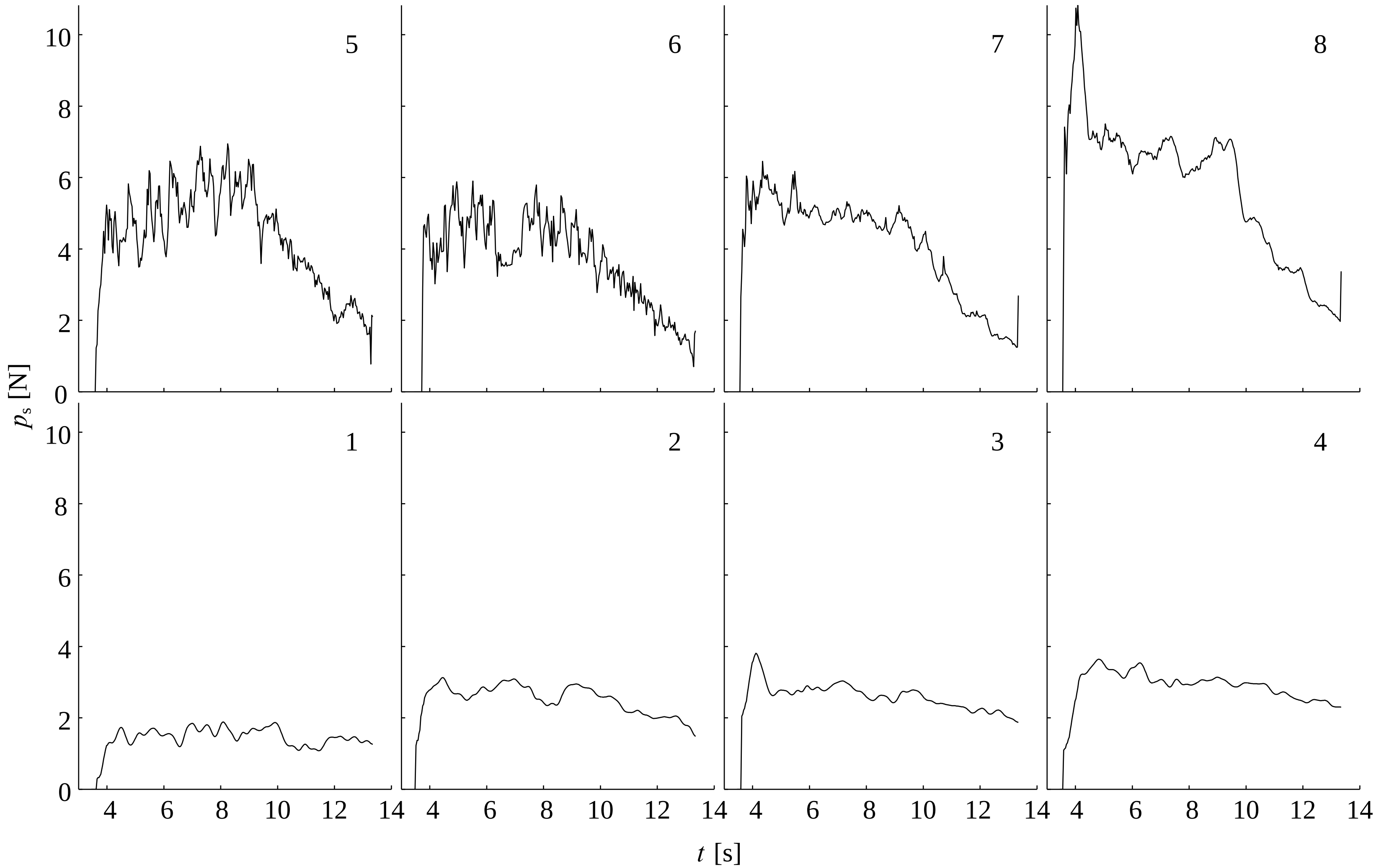

Figure 5.60: The specific momentum history for each segment at $x = 350$ mm in the wake of the large circular column for $h_1 = 250$ mm

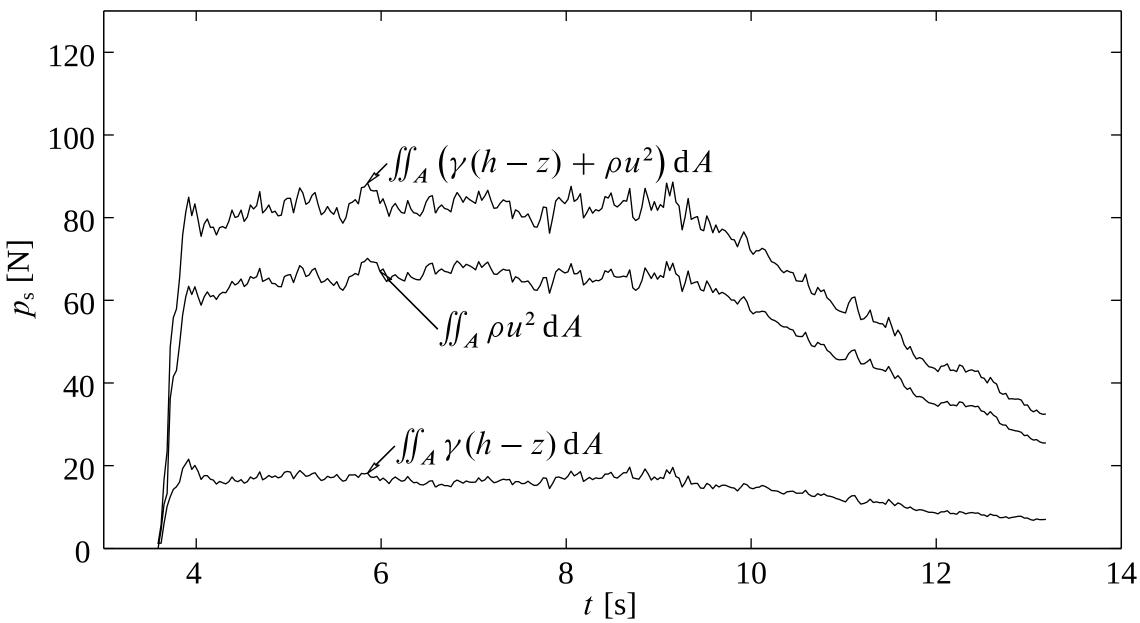

Figure 5.61: Specific momentum at a cross-section at $x = 470$ mm in the wake of the large circular column for $h_1 = 250$ mm

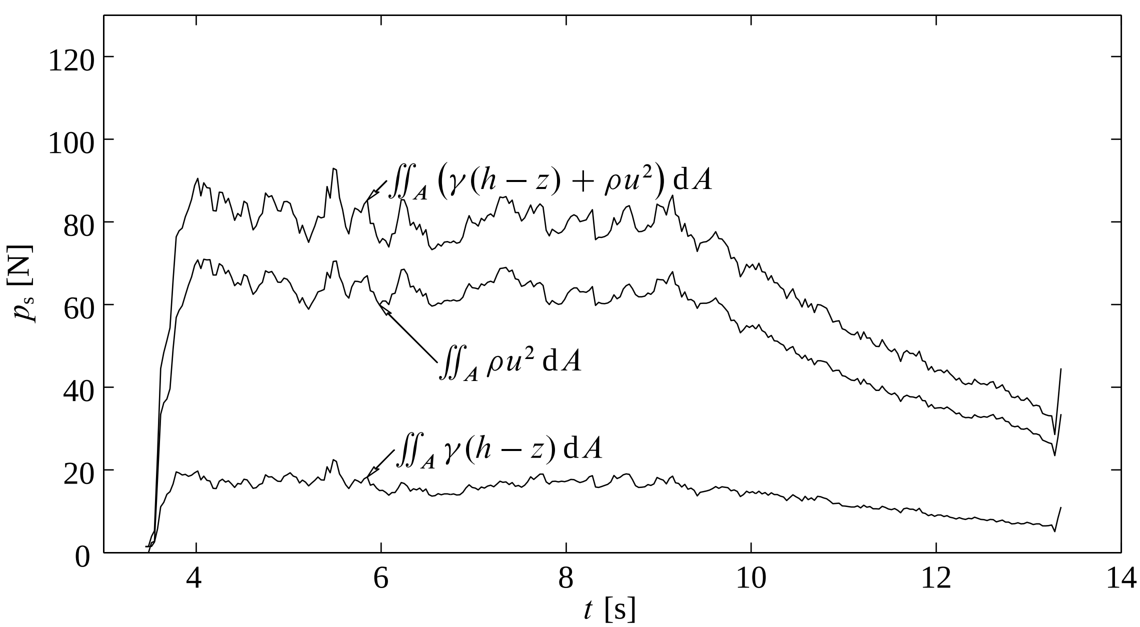

Figure 5.62: Specific momentum at a cross-section at $x = 350$ mm in the wake of the large circular column for $h_1 = 250$ mm

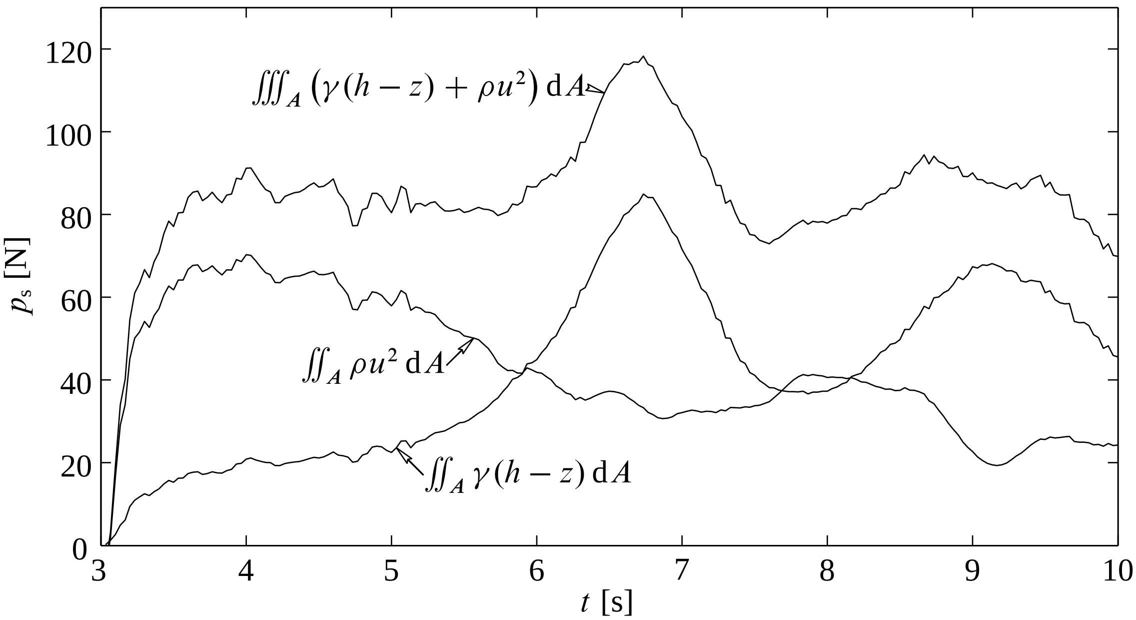

Figure 5.63: Specific momentum at a cross-section $x = -300$ mm upstream of the large circular column for $h_1 = 250$ mm

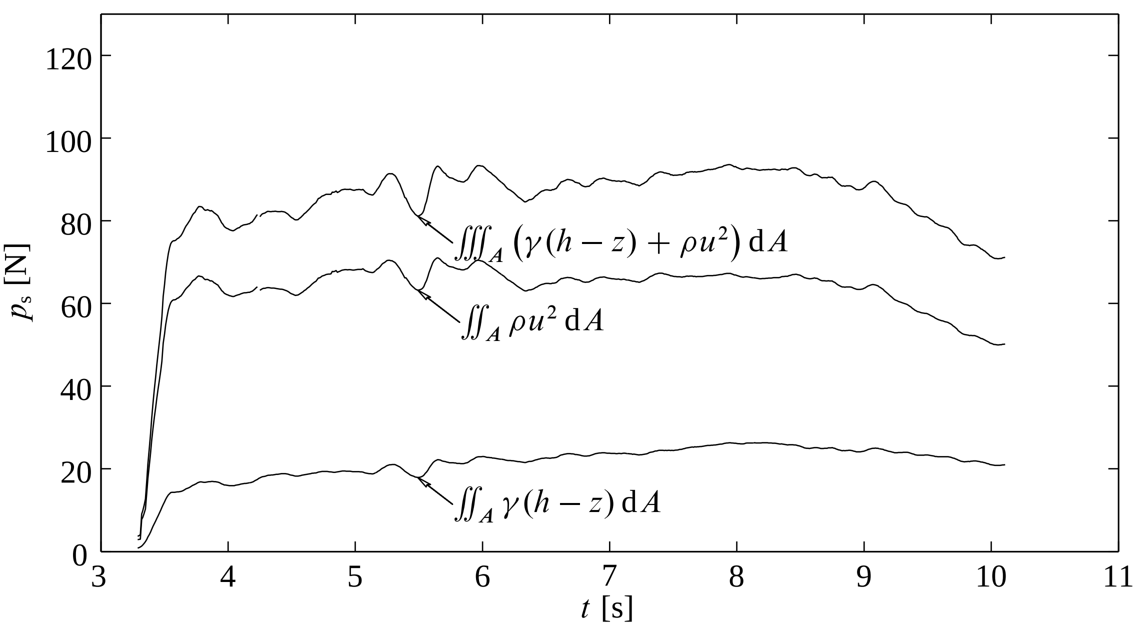

Figure 5.64: Specific momentum in the bore without any obstacles at $x = 0$ for $h_1 = 250$ mm

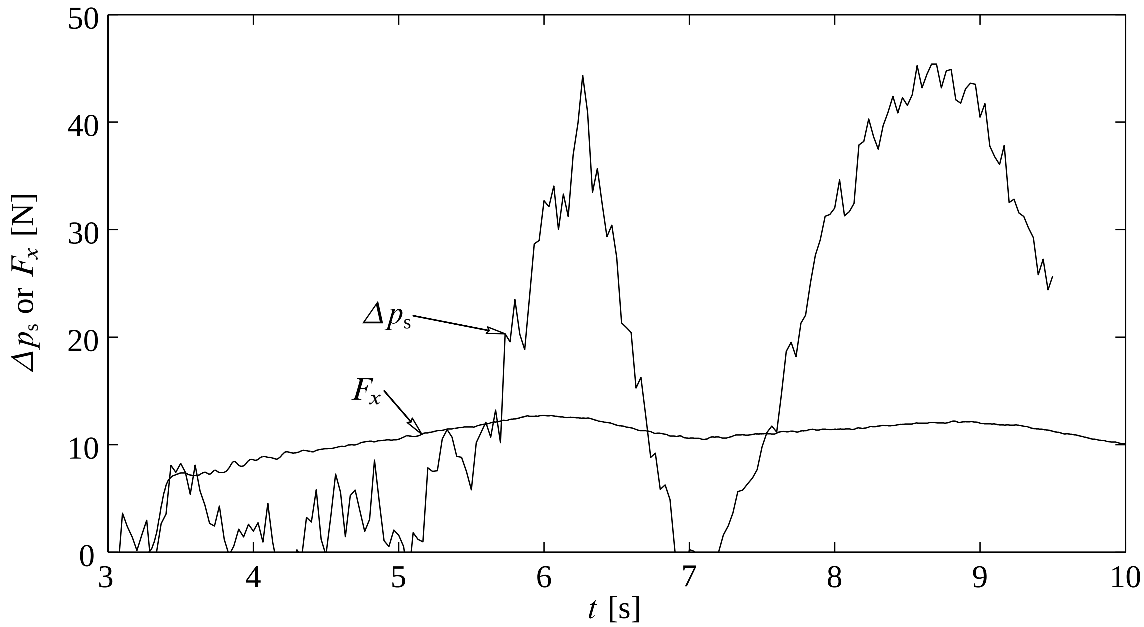

Figure 5.65: Comparison of measured force record, F_x, and force estimate by specific momentum calculations, Δp_s

a steady flow, i.e. no accelerations, does not hold and the control volume approach will not give a reliable estimate in this case. The two waves travelling upstream from the obstacle (see §5.1.2) give two very prominent peaks in the momentum estimate. The force record does have local maxima at the corresponding times, but with much smaller values.

5.3 Forces

5.3.1 Resistance

Time histories of the stream wise load F_x on the columns from bores of several different heights were recorded using the load cell. Figures 5.66 through 5.70 show the time histories for both orientations of the square column and all three circular ones. In most cases the curves have similar shapes indicating that they could be normalized to collapse into a single curve. As the evolution of the load must be in step with that of the bore, it makes sense to use

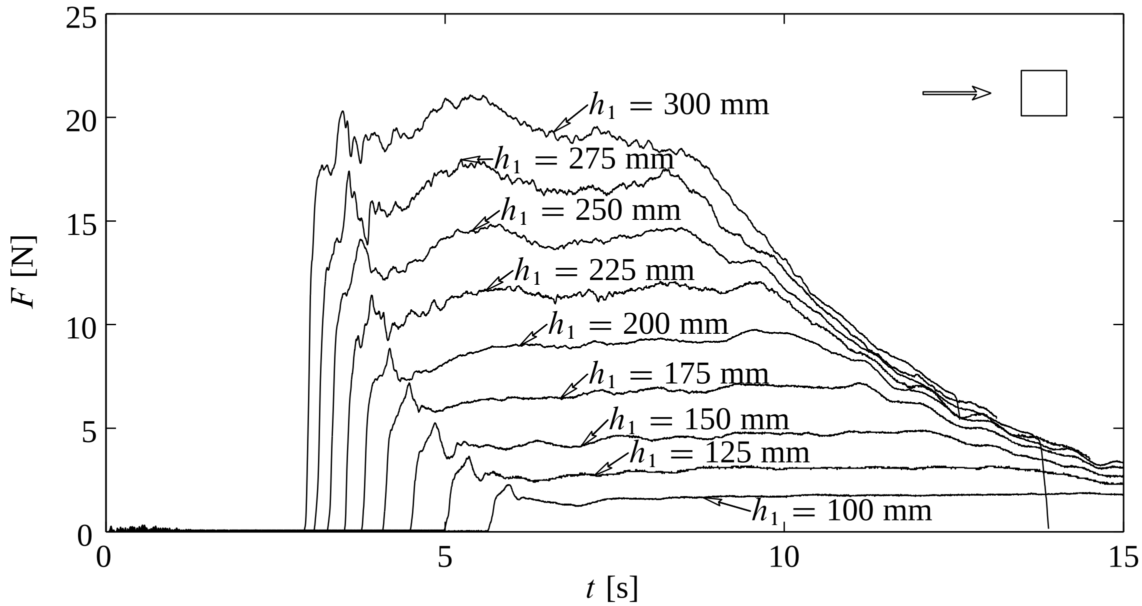

Figure 5.66: Force histories for the square column with one side facing the flow

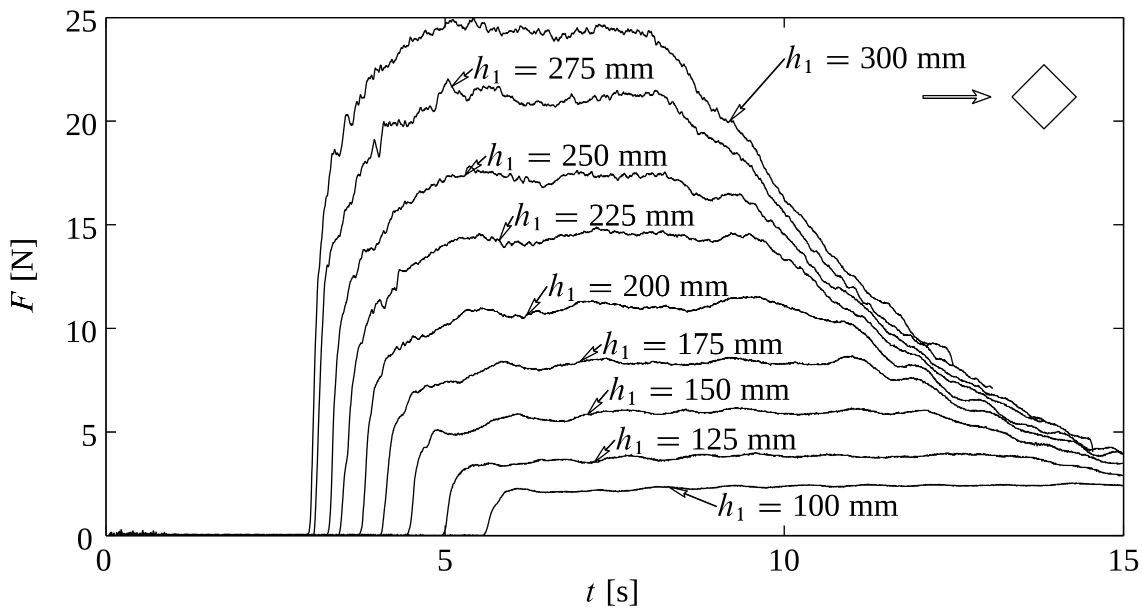

Figure 5.67: Force histories for the square column with one corner facing the flow

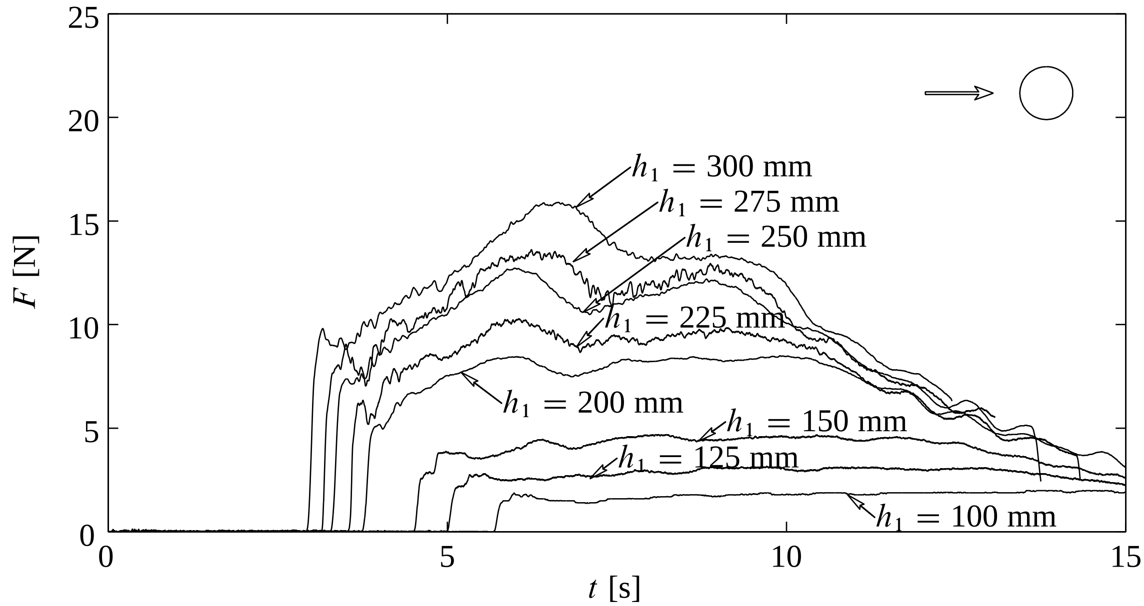

Figure 5.68: Force histories for the large circular column

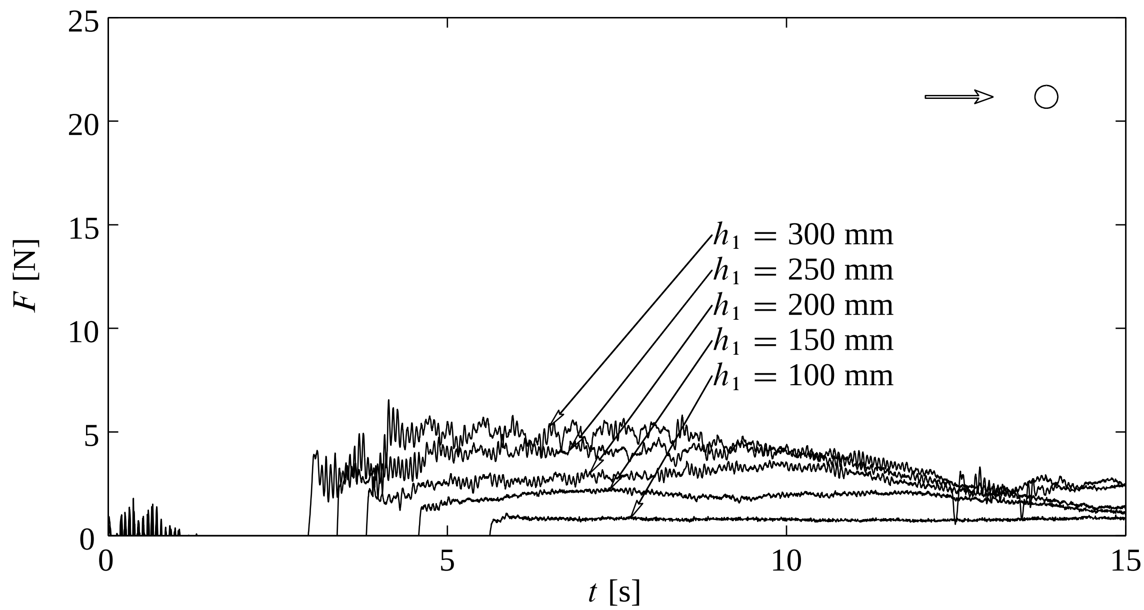

Figure 5.69: Force histories for the intermediate circular column

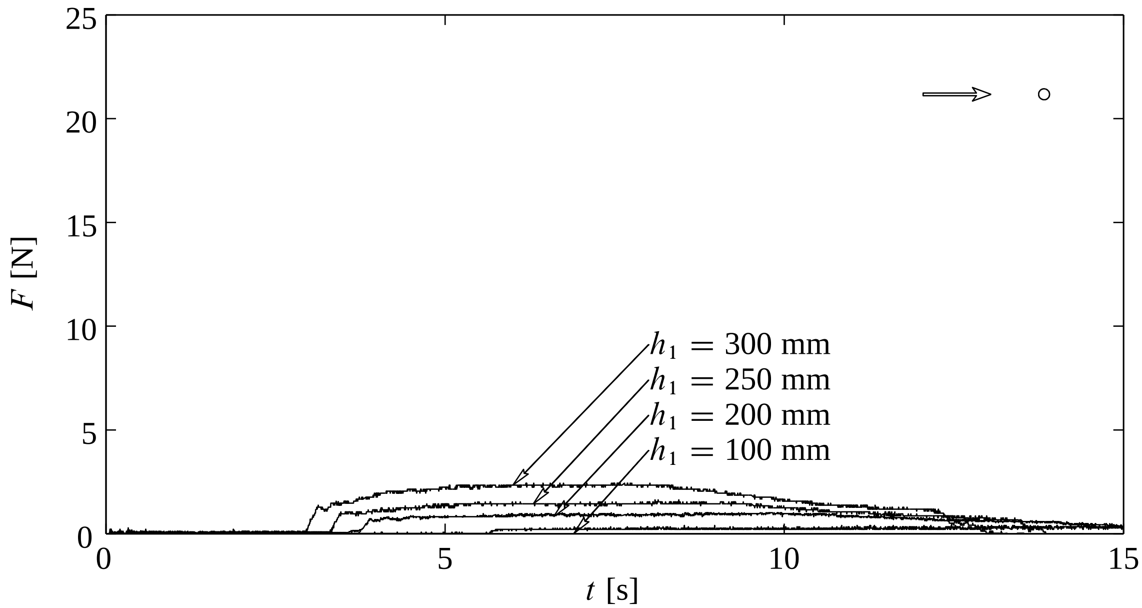

Figure 5.70: Force histories for the small circular column

the propagation speed $\dot{\xi}$ to normalize the time or more directly the arrival time of the bore at the object t_0. The force record can be normalized with $\frac{1}{2}\rho h b u^2$, where $\rho = 998$ kg/m^3 is the density of the water during the runs, h is the water depth, b is the width of the object perpendicular to the flow and u is the flow velocity. Values of both h and u are taken from free flow conditions, i.e. flow without any objects.

This formulation also corresponds to the drag coefficient C_{D}, but as hydrostatic pressure difference between the back and the front of the obstacle may contribute a portion of the force, referring to this value solely as a drag coefficient is not appropriate so the term coefficient of resistance C_{R} will be used instead. This is similar to the resistance coefficient reported by Gupta and Goyal (1975) for steady flows around bridge piers.

$$C_{\mathrm{R}} = \frac{F_x}{\frac{1}{2}\rho A_{\mathrm{p}} u^2} = \frac{2F_x}{\rho h b u^2}, \tag{5.32}$$

with the exception of C_{R} being a time history rather than a constant. The results of this normalization are shown in Figures 5.71 through 5.75. The results for either orientation of

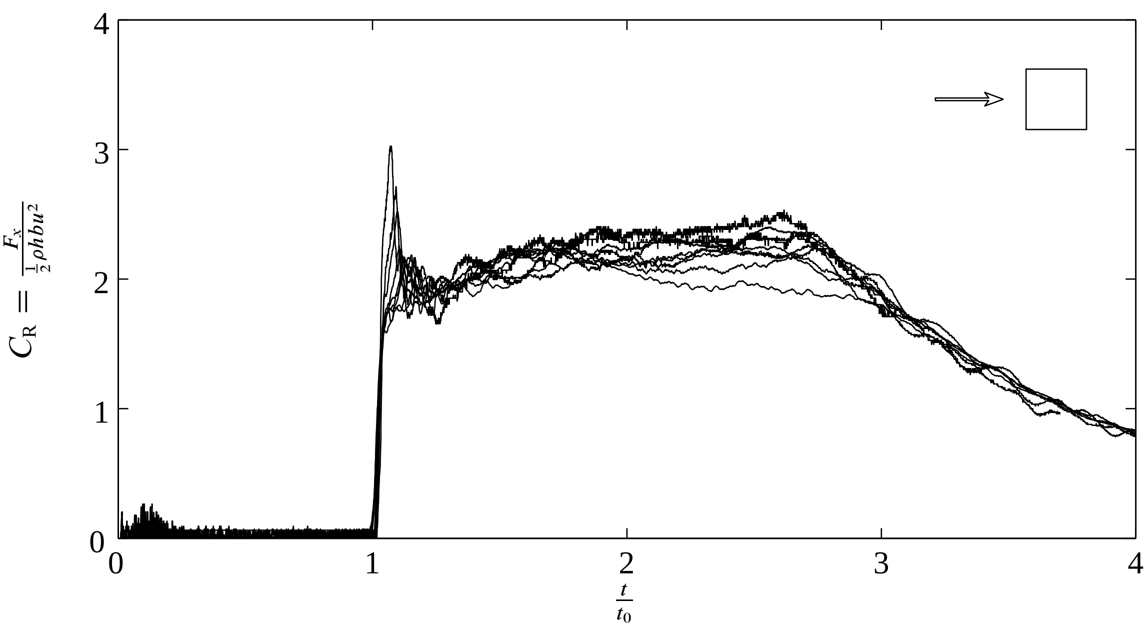

Figure 5.71: Non-dimensionalized force histories for the square column with one side facing the flow

the square column are reasonable (Figures 5.71 and 5.72) and the same can be said about the small cylinder (Figure 5.75) for three of the four curves. The fourth curve corresponds to the smallest bore ($h_1 = 100$ mm) and there the lack of resolution of the force measurements for such a small force is evident. However, the larger cylinders (Figures 5.73 and 5.74) behave quite differently.

Defining the mean resistance coefficient as

$$\overline{C}_{\mathrm{R}} = \frac{1}{t^* - 1.2t_0} \int_{1.2t_0}^{t^*} C_{\mathrm{R}} \, \mathrm{d}t, \tag{5.33}$$

where t^* is the time when the effects of the flow depletion from the tank's upstream boundary are expected to arrive (see §3.2 for calculations). Henceforth, the symbol C_{R} will be used to refer to the average coefficient of resistance $\overline{C}_{\mathrm{R}}$. The results for different obstacles and impoundments are tabulated in Table 5.3. In standard hydraulics texts (see for example Roberson and Crowe (1995) and Daugherty et al. (1985)) the drag coefficient for cylinders

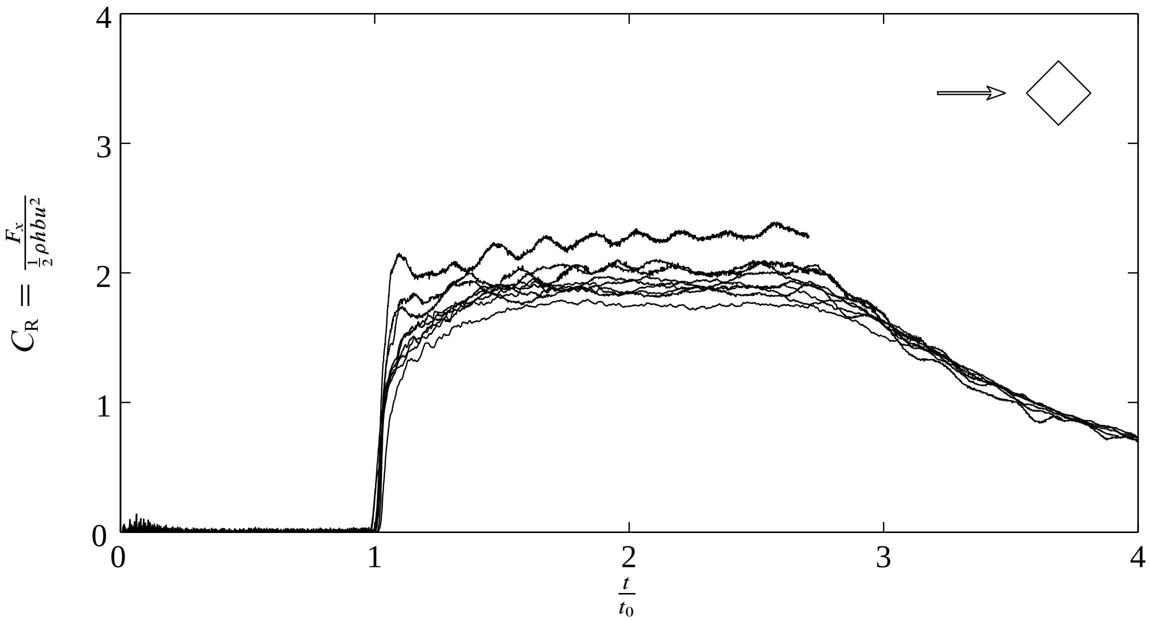

Figure 5.72: Non-dimensionalized force histories for the square column with one corner facing the flow

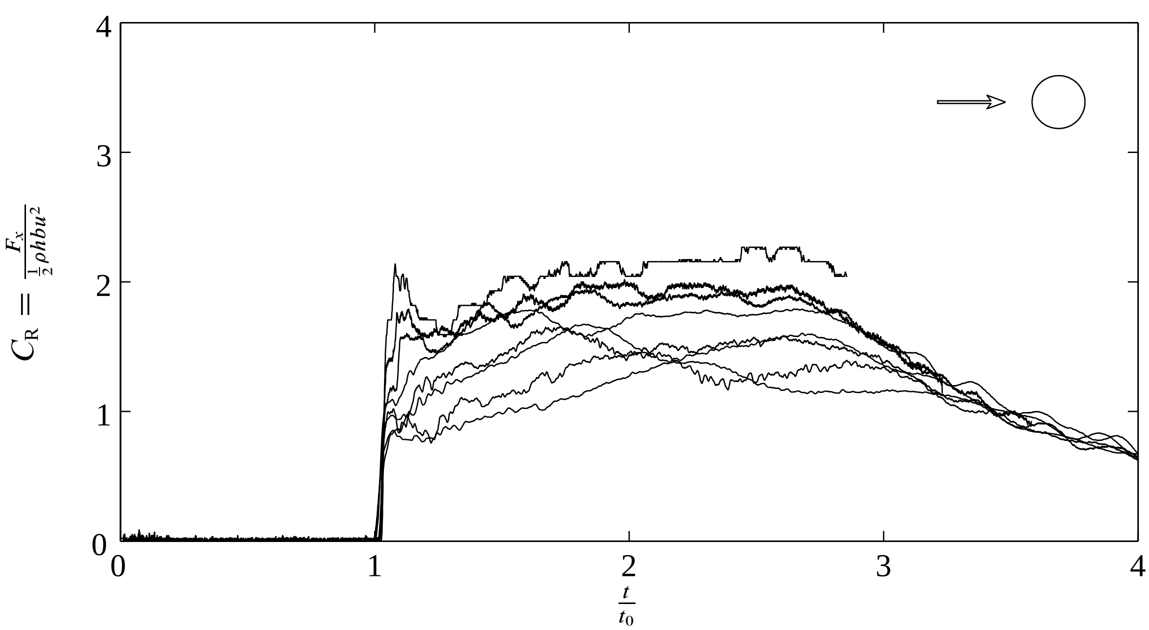

Figure 5.73: Non-dimensionalized force histories for the large circular column

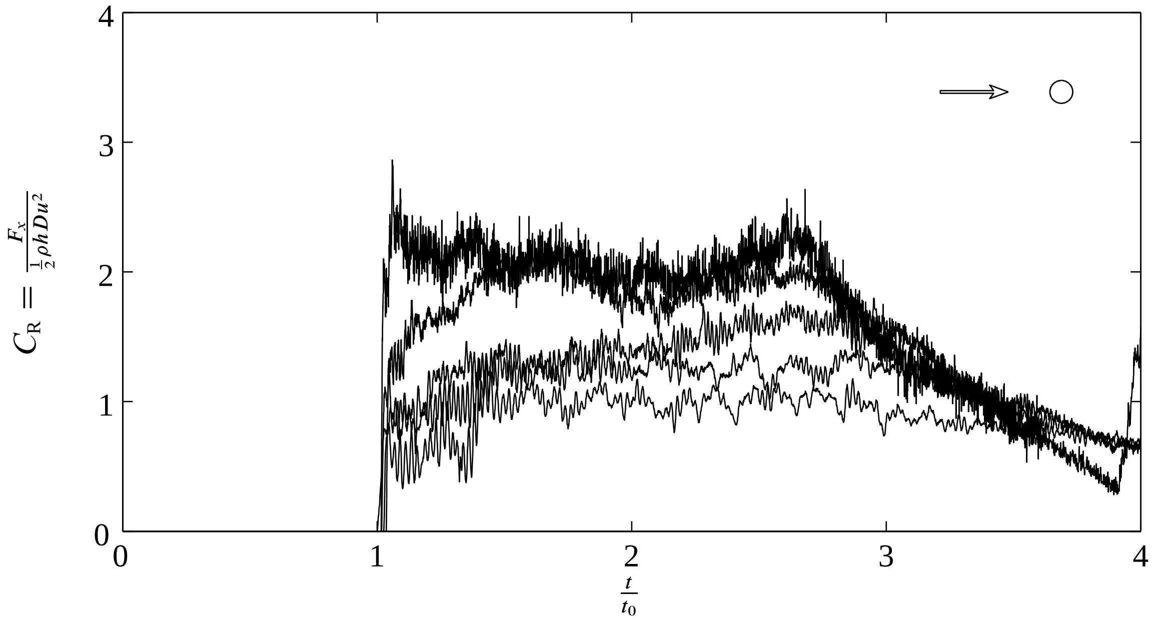

Figure 5.74: Non-dimensionalized force histories for the intermediate circular column

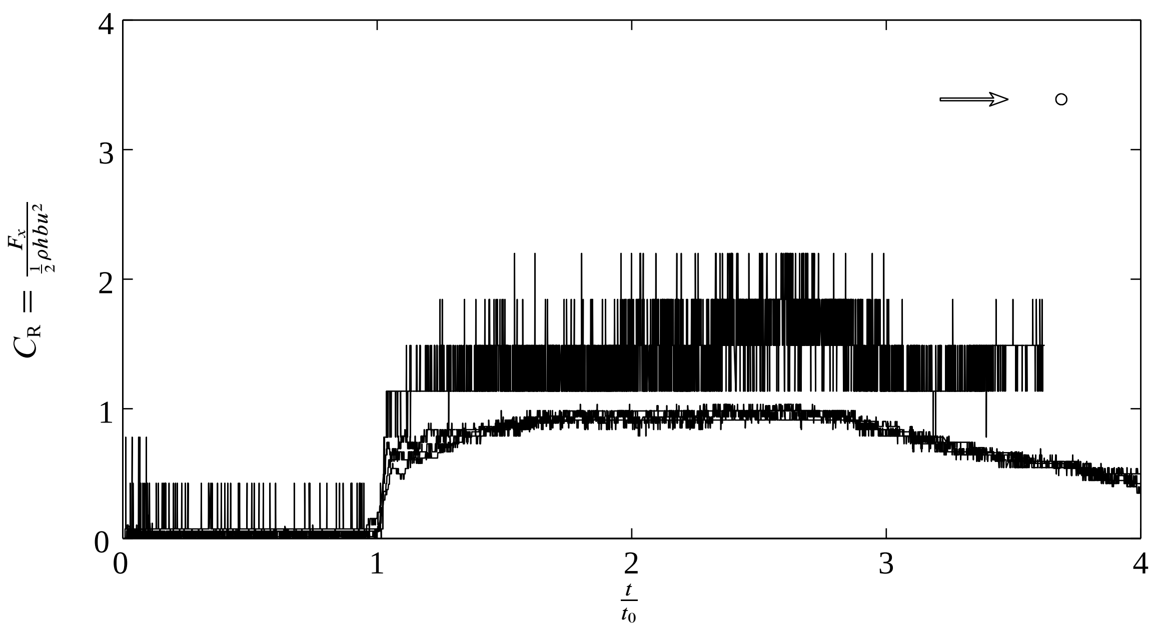

Figure 5.75: Non-dimensionalized force histories for the small circular column

Table 5.3: C_R values for different impoundments and column configurations

h_1	C_R				
	◯	○	∘	□	◇
100 mm	2.05	2.06	1.39	2.26	2.22
125 mm	1.86			2.20	1.99
150 mm	1.80	1.90		2.17	2.00
175 mm				2.09	1.82
200 mm	1.70	1.40	0.92	2.21	1.90
225 mm	1.49			2.15	1.89
250 mm	1.47	1.21	0.89	2.15	1.85
275 mm	1.26			2.10	1.85
300 mm	1.15	0.97	0.93	1.99	1.72

is found to be about 1.2 for $2 \times 10^4 < Re_b < 2 \times 10^5$, which is the range observed in this study. The coefficients in this study are of the same order, while a bit higher, especially for the smaller bores. The main trend for each column here is that the value of C_R decreases with increased bore height. It's also evident that C_R increases with increased diameter of the circular columns, owing to more redirection of the flow. This would indicate that both bore height and column size, or blockage, affects the value of C_R. In the next few figures the relationships between C_R and a few non-dimensional groupings are investigated.

Figure 5.76 shows how C_R, for all five shapes, varies with the flow Reynolds number Re_h calculated as

$$Re_h = \frac{uh}{\nu}, \tag{5.34}$$

where ν is the kinematic viscosity of the fluid. The resistance coefficient C_R appears mostly independent of Re_h for the square column of either configuration, while it is uniformly decreasing with increasing Re_h for the circular columns. Figure 5.77 shows how C_R varies

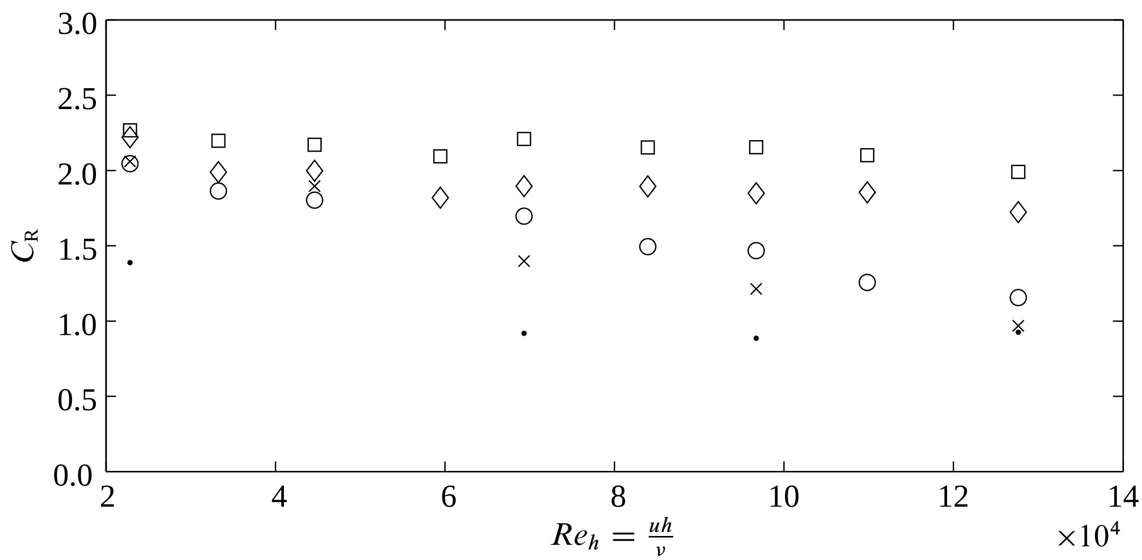

Figure 5.76: Resistance coefficients vs. flow Reynolds number, □ and ◇ represent data from the square column with a side and corner facing the flow respectively, ○ represents data from the large cylinder, × from the intermediate one and · from the small one.

with the object Reynolds number,

$$Re_b = \frac{ub}{\nu}. \tag{5.35}$$

Similar to the results for Re_h, while C_R seems to be independent of Re_b for the square column, it is uniformly decreasing with increasing Re_b for the circular columns. In neither the case of Re_h (Figure 5.76) nor that of Re_b (Figure 5.77) can the values for the three circular cylinders be considered to belong to a mutual function. The same can be said about the Froude number

$$Fr = \frac{u}{\sqrt{gh}}, \tag{5.36}$$

as can be seen in Figure 5.78. Again, there is no apparent dependence on Fr for the square column, but C_R decreses with increase in Fr for each circular column. Figure 5.79 shows the variations of C_R with the ratio of water depth to the object width, h/b and Figure 5.80

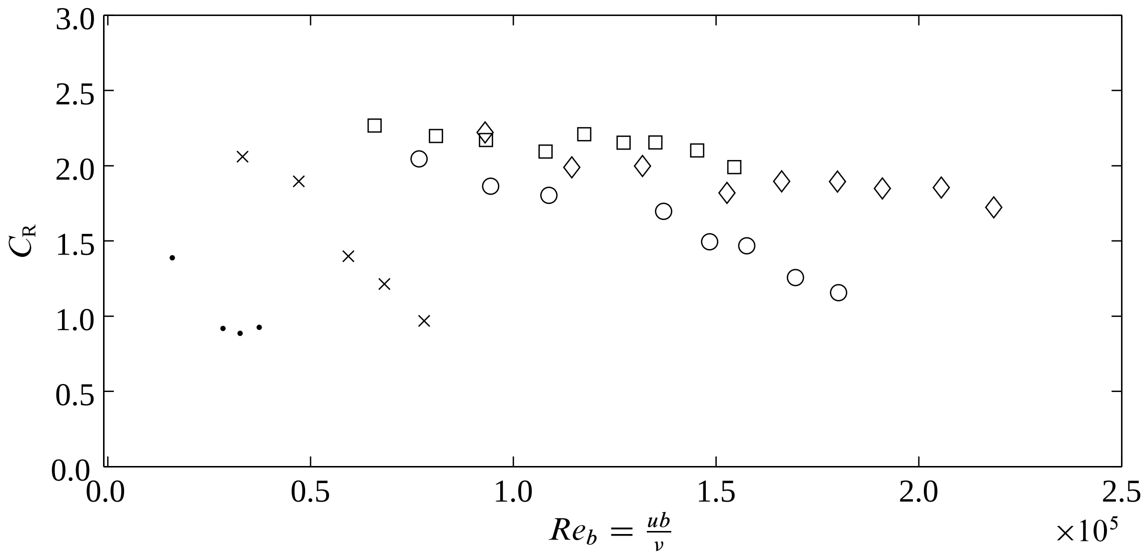

Figure 5.77: Resistance coefficients vs. object Reynolds number, □ and ◇ represent data from the square column with a side and corner facing the flow respectively, ○ represents data from the large cylinder, × from the intermediate one and · from the small one.

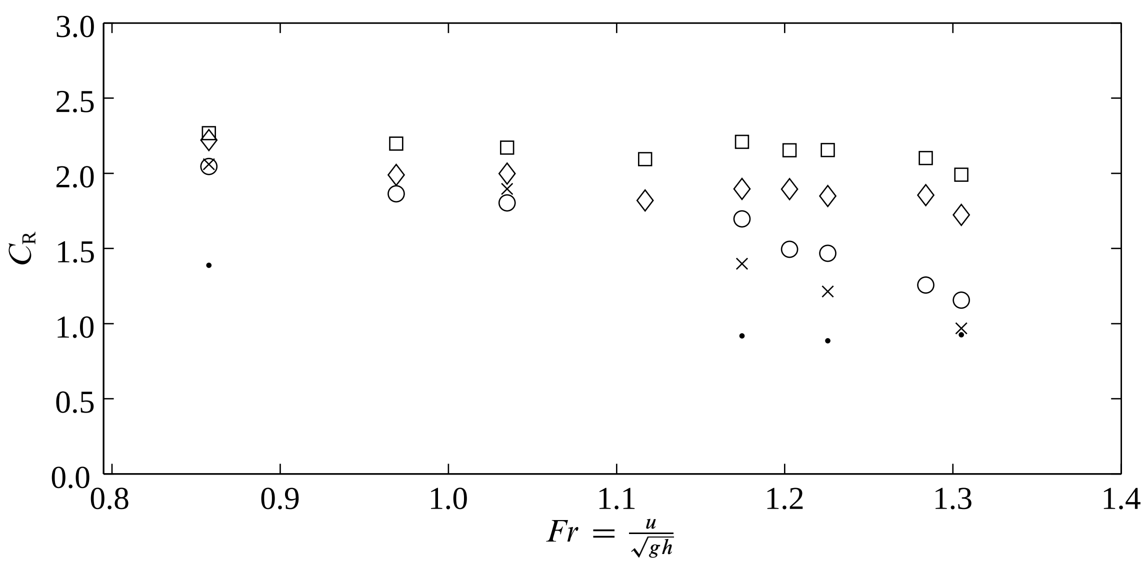

Figure 5.78: Resistance coefficients vs. the Froude number, □ and ◇ represent data from the square column with a side and corner facing the flow respectively, ○ represents data from the large cylinder, × from the intermediate one and · from the small one.

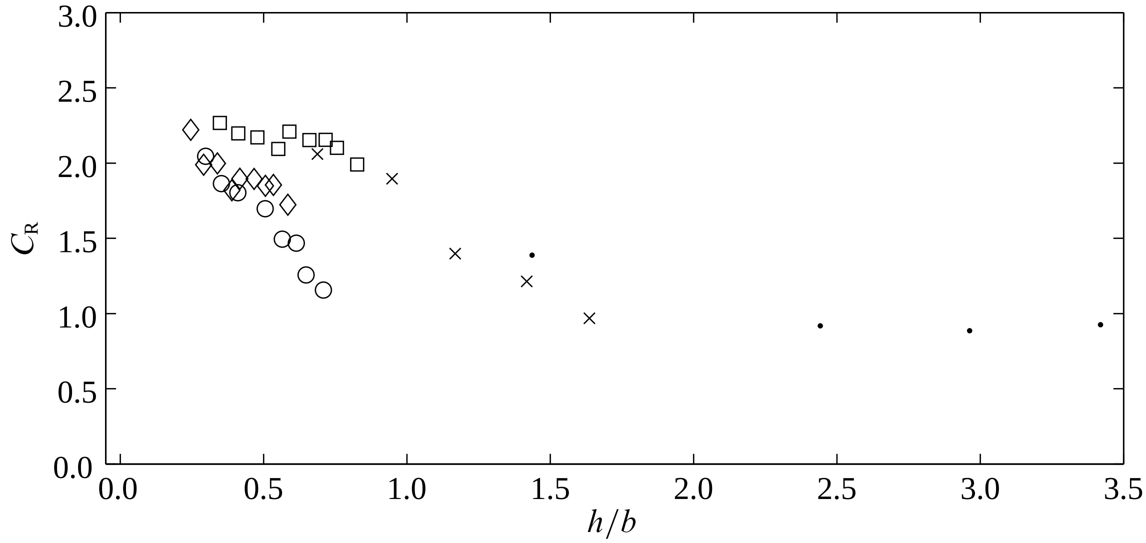

Figure 5.79: Resistance coefficients vs. the ratio of flow depth to object width, □ and ◇ represent data from the square column with a side and corner facing the flow respectively, ○ represents data from the large cylinder, × from the intermediate one and · from the small one.

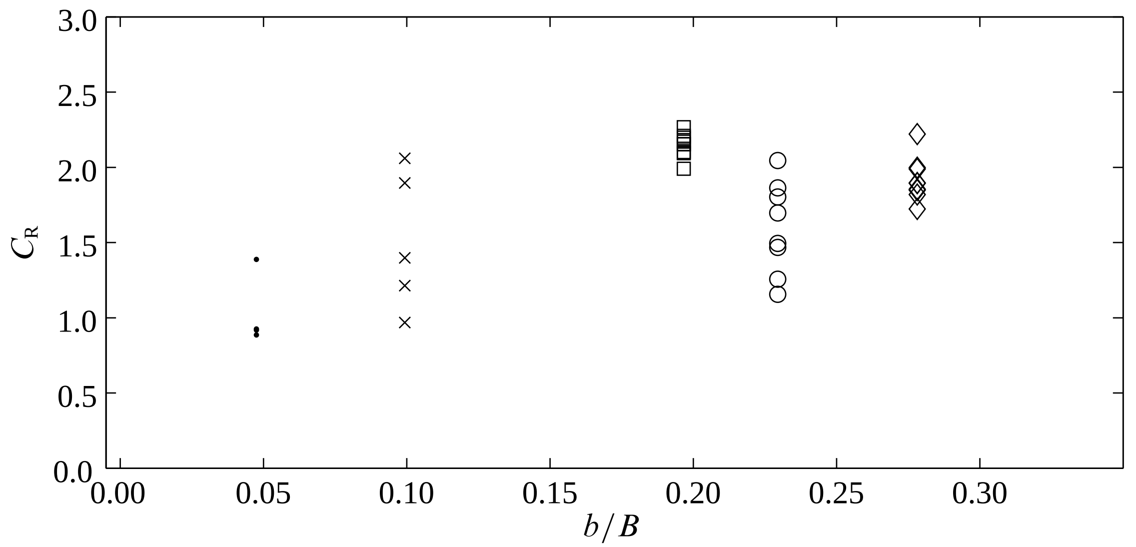

Figure 5.80: Resistance coefficients vs. the ratio of object width to tank width, □ and ◇ represent data from the square column with a side and corner facing the flow respectively, ○ represents data from the large cylinder, × from the intermediate one and · from the small one.

shows the variation with the blockage coefficient, i.e. what portion of the tank width B is blocked by the width of the column b/B.

Figures 5.76 through 5.80 indicate that C_R can not be considered to be a function of any single one of these non-dimensional groupings. That however doesn't mean that it isn't a function of some combination of them. The biggest contributing factors to the variations in C_R seem to be the flow velocity u, bore height h, object width b and tank width B. It would then be reasonable to deduce that there exists such a function f that

$$C_\mathrm{R} = f\left(Fr, \frac{b}{B}, \frac{h}{b}\right). \tag{5.37}$$

The largest differences between the conditions in this study and the standard conditions that yield $C_\mathrm{D} = 1.2$, are twofold. First is the free surface condition and the second is the blockage the column causes in the narrow channel. In general, for a given column, the smaller the bore the more of an impact the column has on the free surface because a larger proportion of the flow must be redirected around the column. For a given bore height, the larger the column the larger the blockage effect. As an example, for a large proportional blockage, like for the large column, the free surface is greatly raised upstream and the load on the column becomes larger. The small cylinder causes a much smaller blockage and is consequently closer to the free flow drag condition.

Data from Gupta and Goyal (1975) suggests that for $Fr < 1$, C_R is a function of Fr, $\frac{B}{b}$ and $\frac{h}{b}$. The data from the current research falls on a similar shape, but it is difficult to do a direct comparison of values as the range of the independent variables, especially h/b, is quite different. The only real overlap is for the small cylinder at $h_1 = 100$ mm, which is the case with the least precise measurement (see Figure 5.75). For that single point, however, the agreement is good.

5.3.2 Hydrostatic forces

Figures 5.81 through 5.83 show the measured force on the three large columns for $h_1 = 250$ mm and the water level at the upstream side of the column as well as 10, 20, 30, 40

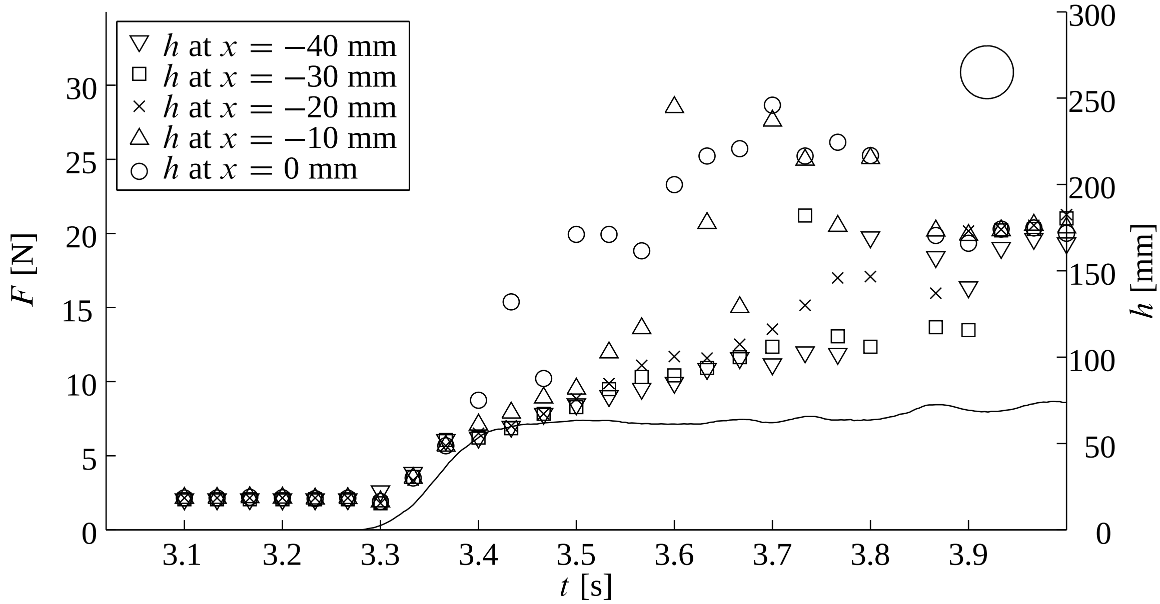

Figure 5.81: Time history of the force (solid line) on the circular column and the waterlevel at the upstream side

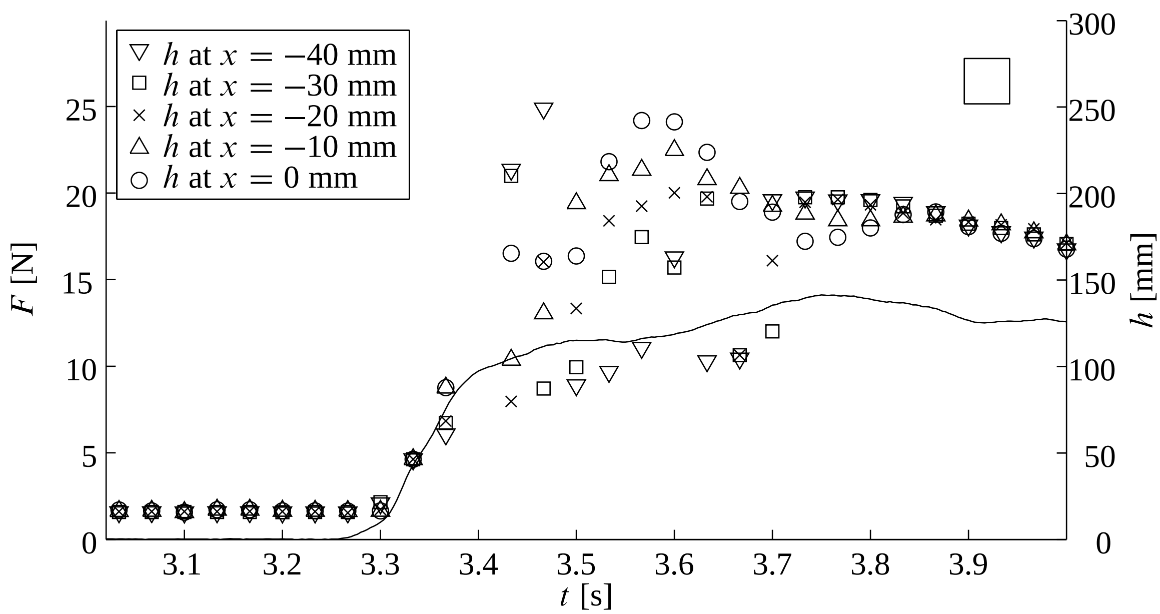

Figure 5.82: Time history of the force (solid line) on the square column with one side facing the flow and the waterlevel at the upstream side

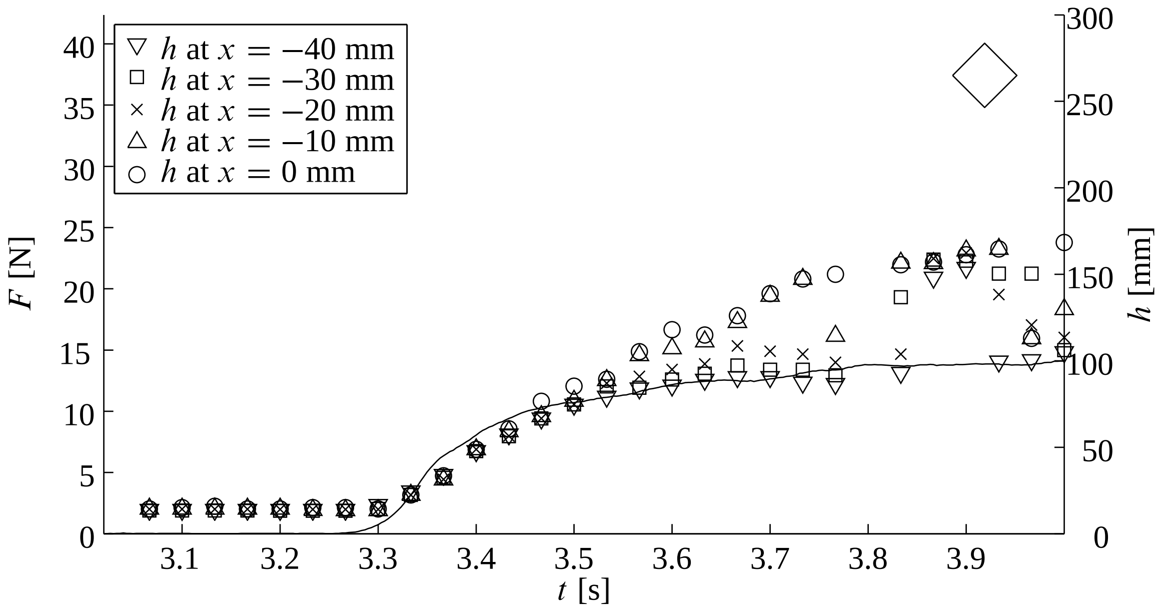

Figure 5.83: Time history of the force (solid line) on the square column with one corner facing the flow and the waterlevel at the upstream side

and 50 mm upstream of it for 1.0 s around the bore impact. It can be deduced from them, that the water level just off the upstream edge may be a better indicator of the force acting on the column than the water level right at it. These figures do not include information for the the water surface in the wake of the columns.

During the bore passing, the water level on the upstream side of an obstacle is higher than that of the downstream side. The hydrostatic force from water of depth h on one side of a column of a width b is

$$F_h = \int_0^h (h - z)\gamma b \, \mathrm{d}z = \tfrac{1}{2}\gamma b h^2. \tag{5.38}$$

The net hydrostatic force in the x-direction should then be the difference between this force on the upstream and downstream side or

$$\Delta F_h = \tfrac{1}{2}\gamma b \left(h_{\mathrm{u}}^2 - h_{\mathrm{d}}^2\right) \tag{5.39}$$

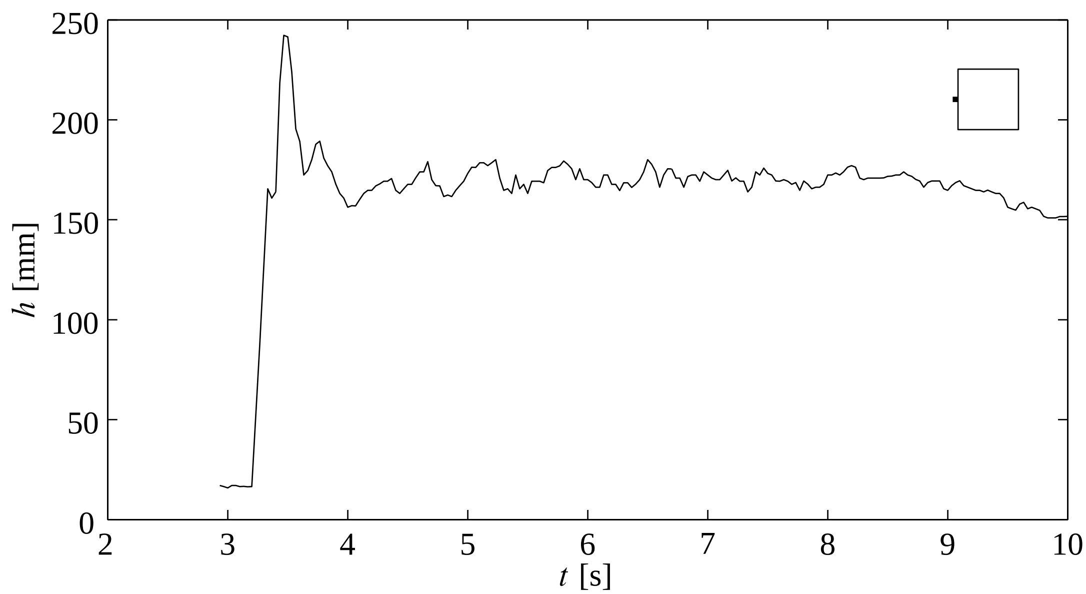

Figure 5.84: Water level time history at $x = 0$ mm for $h_1 = 250$ mm and the square column

where h_u and h_d represent the water level on the upstream and downstream side, respectively. Figure 5.84, shows the water level at the upstream side ($x = 0$) of the large square column for impoundment of $h_1 = 250$ mm. Figure 5.85 also shows the water level upstream of the column, but it uses an average water level over an interval starting at the upstream side and extending 100 mm upstream, rather than just the value right at the column. Figure 5.86 shows the water level on the centerline at the upstream side of the large circular column while Figure 5.87 shows the water level history on the upstream side of the large circular column, using an average over an interval extending 100 mm upstream from the column. The upstream water level data for both columns is acquired from video (see §4.4.1). Figure 5.88 shows the time history of the estimates of the water level at the downstream wall of the square column and Figure 5.89 shows the same for the circular column. The downstream water level data comes from the high speed film (see §4.4.2). The two lines in each figure represent the possible range of the camera position, i.e. a camera angle in the range of $20° < \theta < 35°$. Figures 5.90 through 5.93 show the net force from

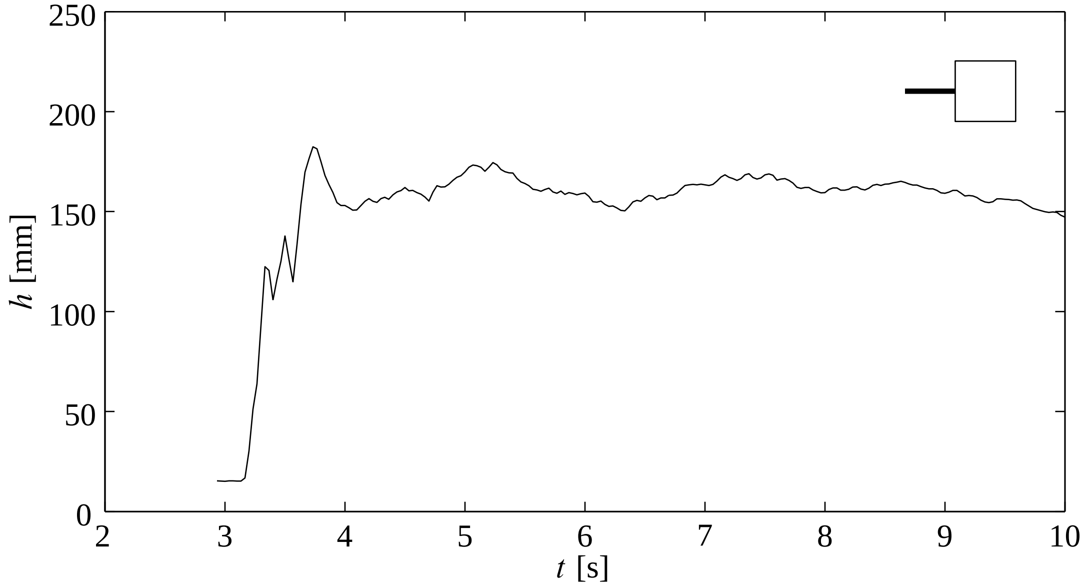

Figure 5.85: Water level time history averaged over the interval -100 mm $< x < 0$ mm for $h_1 = 250$ mm and the square column

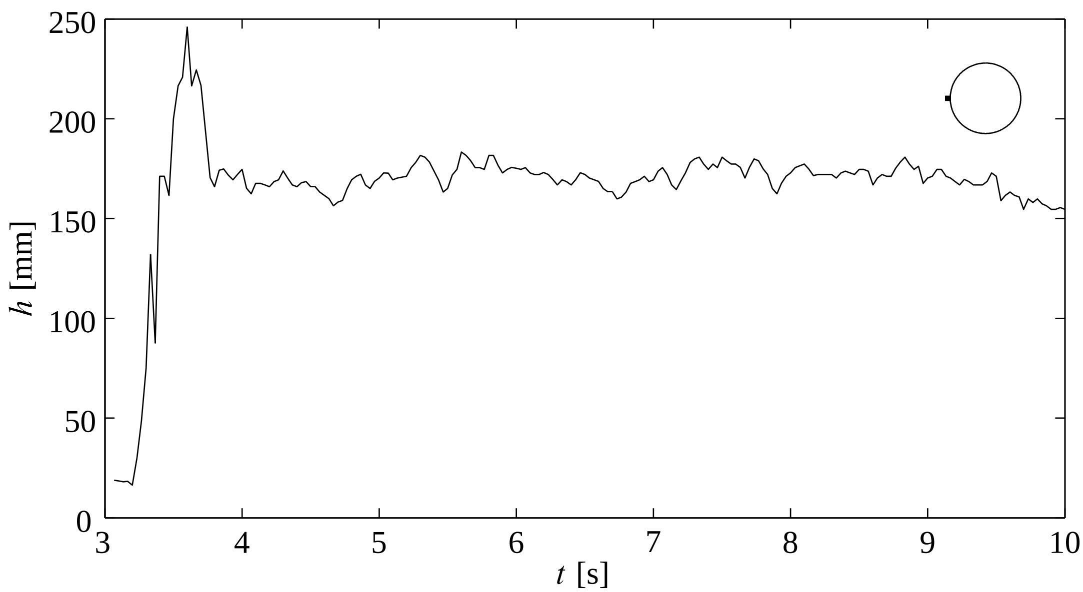

Figure 5.86: The water level history at the upstream side ($x = 0$) of the large circular column for $h_1 = 250$ mm

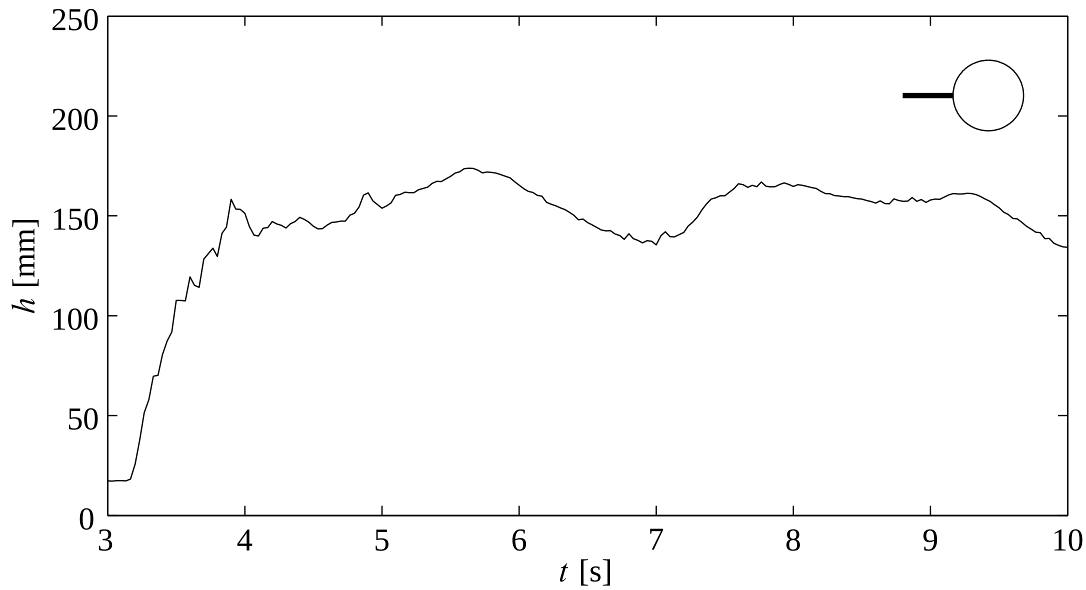

Figure 5.87: Water level time history averaged over the interval -100 mm $< x <$ 0 mm for $h_1 = 250$ mm and the large circular column

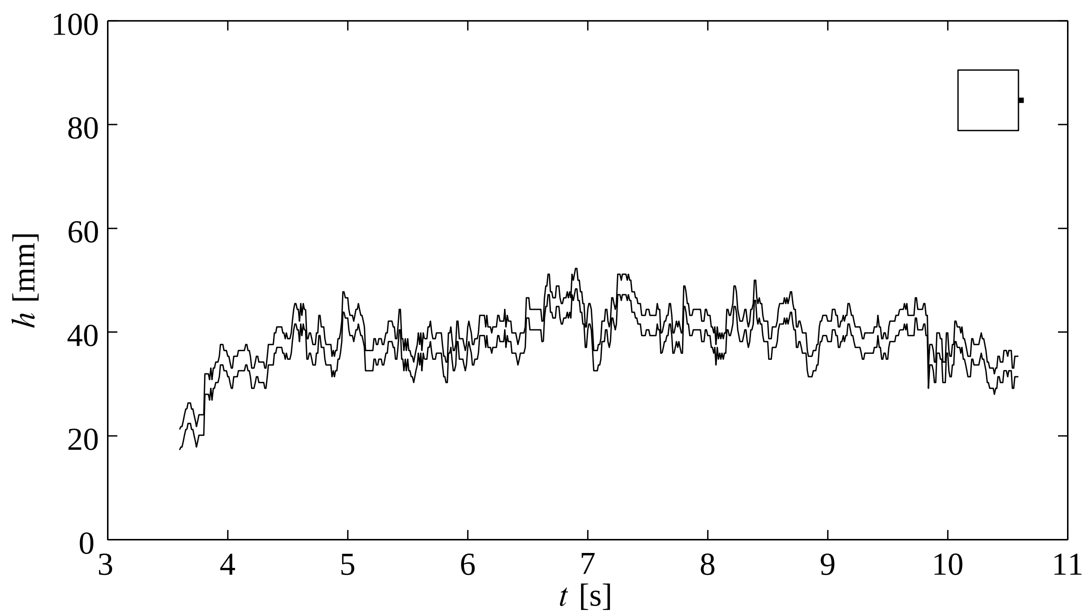

Figure 5.88: Water level at the downstream side of the square column for $h_1 = 250$ mm

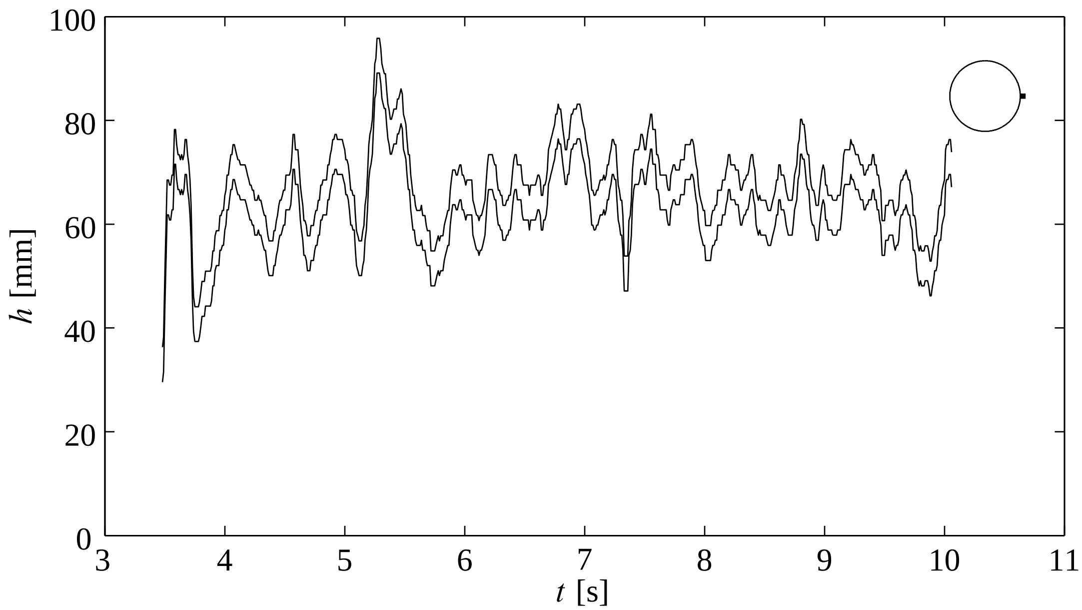

Figure 5.89: Water level at the downstream side of the circular column for $h_1 = 250$ mm

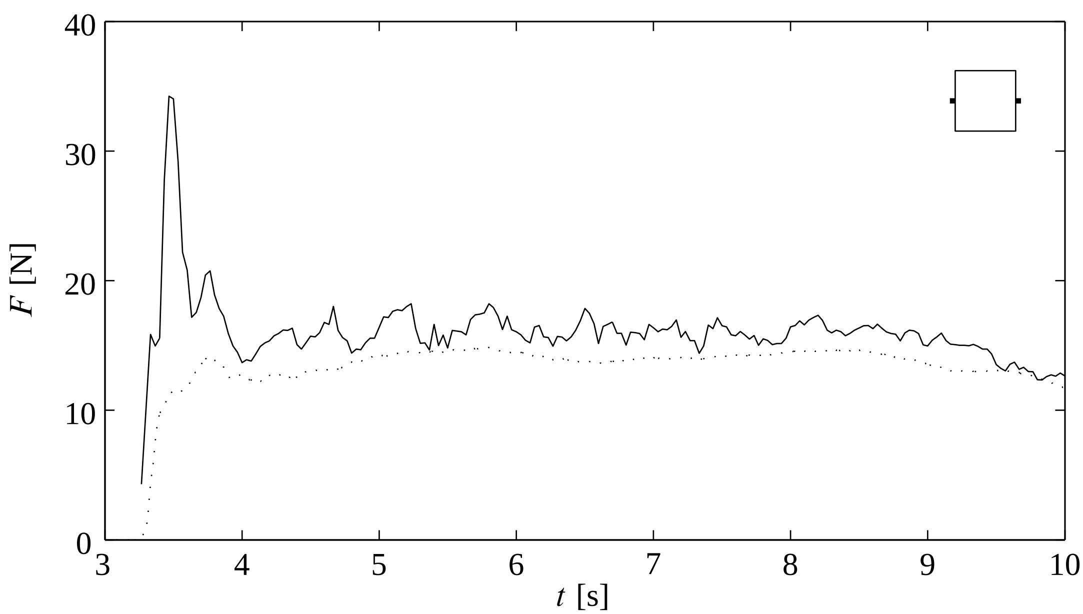

Figure 5.90: Hydrostatic force (solid lines) using the water level at the upstream ($x = 0$ mm) and downstream ($x = 120$ mm) sides of the square column compared to the measured force (dotted line) for $h_1 = 250$ mm

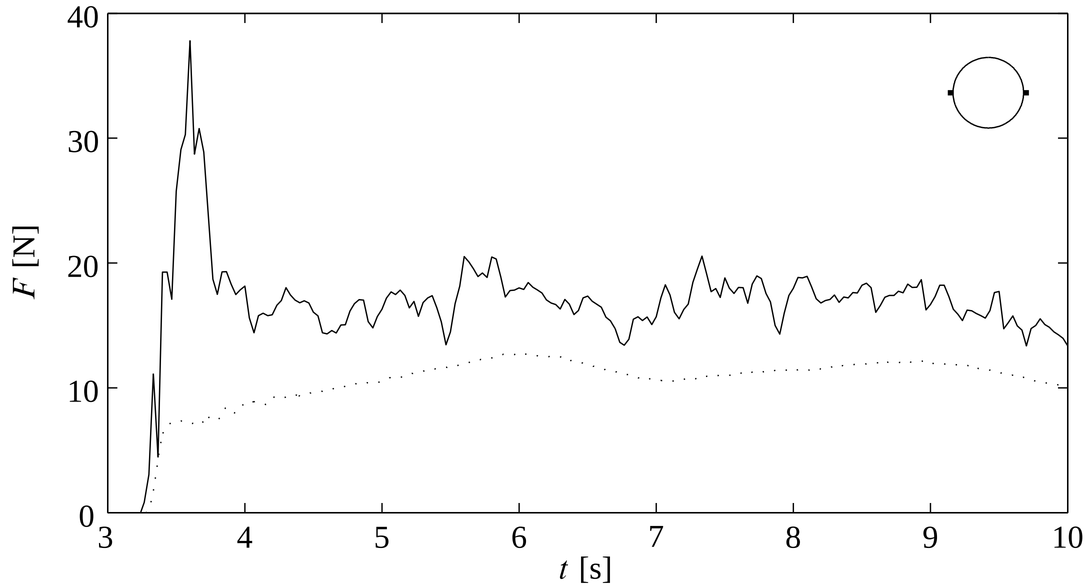

Figure 5.91: Hydrostatic force (solid lines) using the water level at the upstream (x = 0 mm) and downstream (x = 140 mm) sides of the large circular column compared to the measured force (dotted line) for h_1 = 250 mm

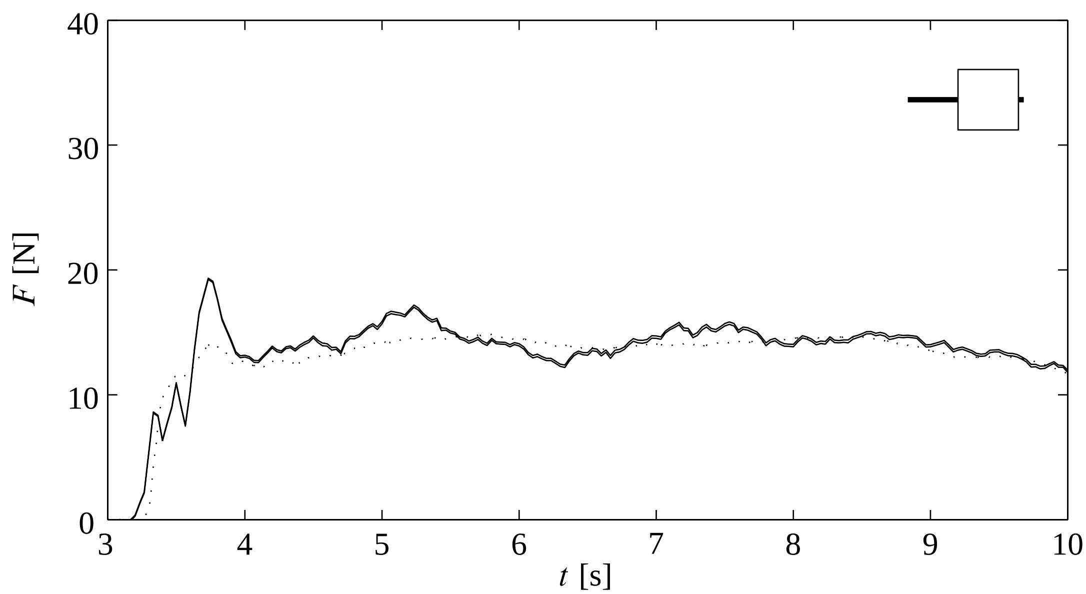

Figure 5.92: Hydrostatic force using upstream water level over the interval -100 mm $< x <$ 0 mm and the downstream water level at x = 120 mm for the square column, h_1 = 250 mm

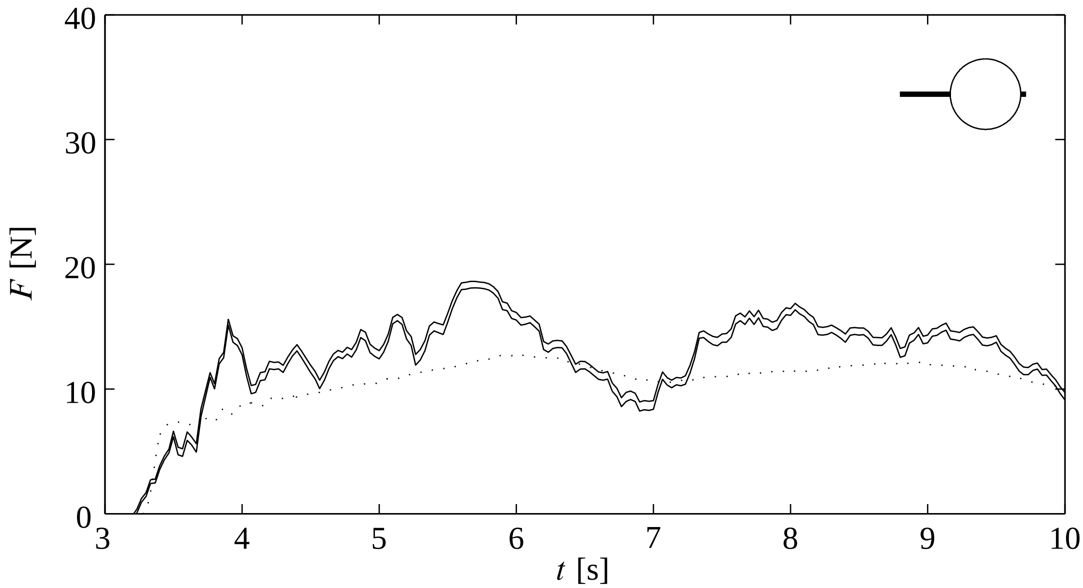

Figure 5.93: Hydrostatic force using upstream water level over the interval -100 mm $<$ $x < 0$ mm and the downstream water level at $x = 140$ mm for the large circular column, $h_1 = 250$ mm

the height difference, again assuming the same range for the camera angle. The logos in the top right corner of each figure indicate the column shape and location of the water level measurements. It is clear from the figure that the uncertainty in the angle does not affect the force estimate to any appreciable degree. In the case of the square column, there is a fairly good correspondence between the calculated hydrostatic force and the measured force on the column, with the exception of the initial impact. This is not the case for the circular column as can be seen in Figure 5.91. There the difference is considerable. The hydrostatic force estimate is solely built on the water level on the centerline, upstream and downstream, and does not take into account the continuous changes in between. The hydrostatic force estimate is therefore less accurate for a circular column than a square one where pressure on the sides does not yield any force in the x-direction. Figure 5.92 shows the same kind of force comparison as Figure 5.90, except rather than using upstream water level right at the column, an average of the water level for the first 100 mm upstream of the column (see Fig-

Table 5.4: Impact force on the square column for each bore size

h_1	F_I	$\frac{F_\mathrm{I}}{F_\mathrm{R}}$	$\frac{F_\mathrm{I}}{F'_\mathrm{I}}$
[mm]	[N]	—	—
300	19.91	1.02	1.10
275	17.41	1.04	1.23
250	14.12	1.01	1.13
225	11.42	0.99	1.24
200	8.85	0.99	1.22
175	7.18	1.07	1.24
150	5.25	1.17	1.49
125	3.65	1.24	1.48
100	2.27	1.34	1.47

ure 5.85). This gives a more even representation of the upstream water level and therefore also the force estimate. Figure 5.92 shows the hydrostatic force on the large circular column calculated using the averaged water level upstream as shown in Figure 5.87. Although the fit with the measured force is still less accurate than for the square column, this approach gives a better result than just using the upstream water level at a single point right at the column.

5.3.3 Initial impact

The values of the maximum force during the initial impact, F_I, for the square column and various impoundments can be seen in Table 5.4. It also shows the ratio between F_I and the resistance force F_R, i.e. the average force after the bore impact, calculated using the same time interval as used for the calculations of C_R, i.e.

$$F_\mathrm{R} = \frac{1}{t^* - 1.2t_0} \int_{1.2t_0}^{t^*} F_x \, \mathrm{d}t, \tag{5.40}$$

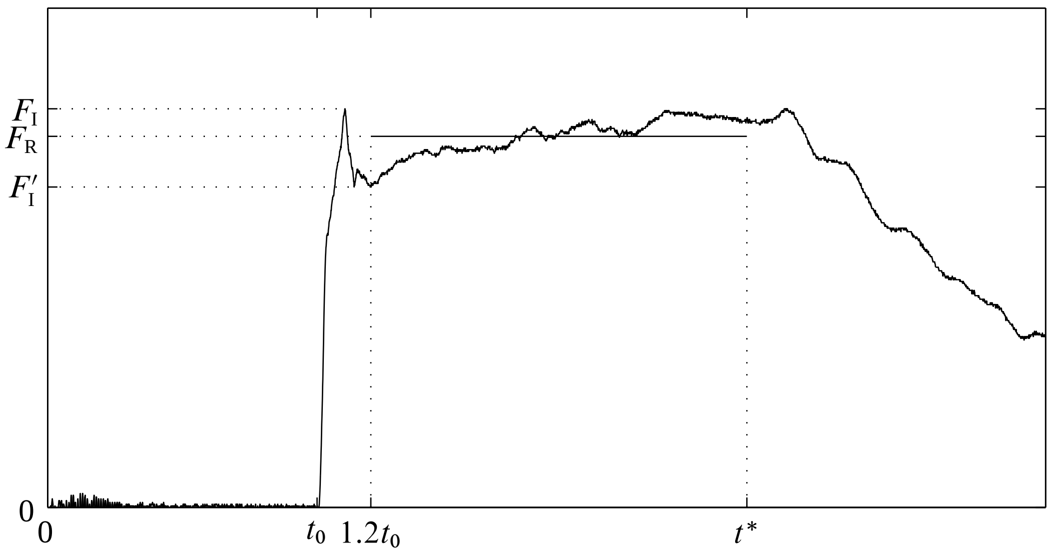

Figure 5.94: The definitions of F_I, F_I' and F_R, using the example of $h_1 = 175$ mm

where t_0 is the arrival time of the bore and t^* is the time when the effects of the flow depletion from the tank's upstream boundary are expected to arrive. For all but the smallest bores this ratio is very close to 1. This is because the load continues to increase during the bore passing and the peak during the impact does not always represent the maximum force applied to the structure. We can also compare the impact force to the force immediately after the initial peak has subsided F_I'. This yields the fourth column in Table 5.4. Figure 5.94 shows the definitions of the different force values. For the smaller bores the force on the square column during the impact is about 50 % higher than the force after the initial impact. This corresponds well with the results of Nakamura and Tsuchiya (1973).

5.3.4 Effects of orientation of the square column

Figures 5.95 through 5.97 show the histories of force for both orientations of the square column for different bore heights. The time t is measured from the removal of the gate. In every case the bore causes a larger load, for nearly the duration of passing, on the column when it has its diagonal in the main flow direction. Only during the initial impact is the

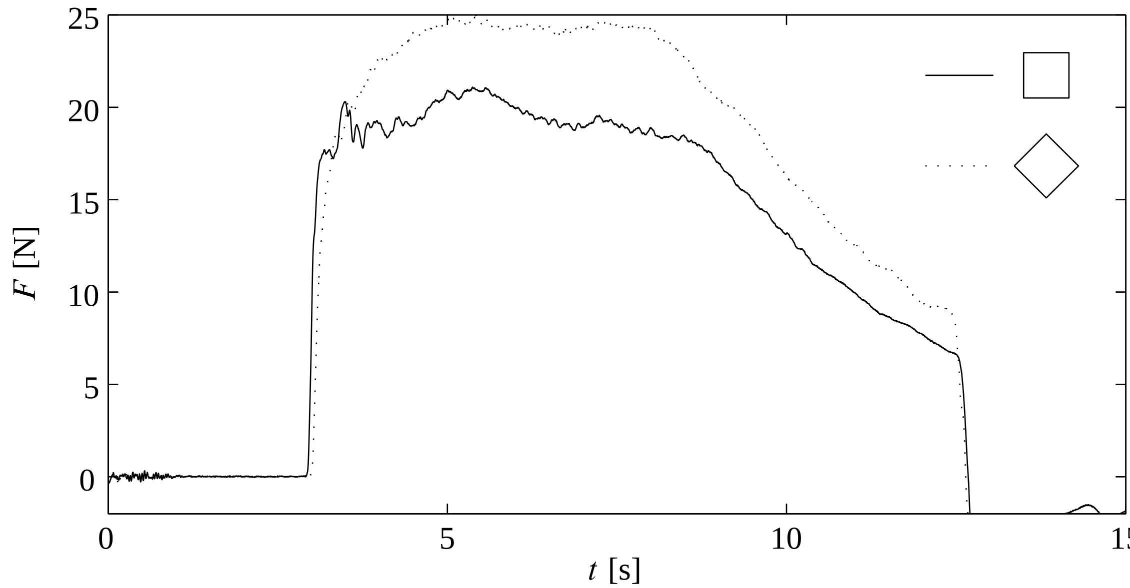

Figure 5.95: Comparison of force time history for the two orientations of the square column, $h_1 = 300$ mm

load higher on the one parallel to the flow, for some, but not all cases. The initial peak is however never higher than the maximum load for the diagonal setup. The relative difference of forces between the two orientations is less than width ratio ($\sqrt{2}$), so force divided by column width is smaller for diagonal orientation.

Figure 5.98 shows a comparison of the water surface history at the upstream edge of the obstacle and Figures 5.99 through 5.101 show the same kind of comparisons at points 100, 200 and 300 mm upstream of the edge respectively. For comparison, the water surface history without any obstacle in the tank at $x = 0$ can be seen in Figure 5.57. The data in Figures 5.98 through 5.101 are taken from video whereas the data in Figure 5.57 are from a wave gauge. Apart from very close to the impact, the profiles for the two different orientations are quite similar, indicating that the difference in load is not caused by a significantly different amount of water being held back by each orientation.

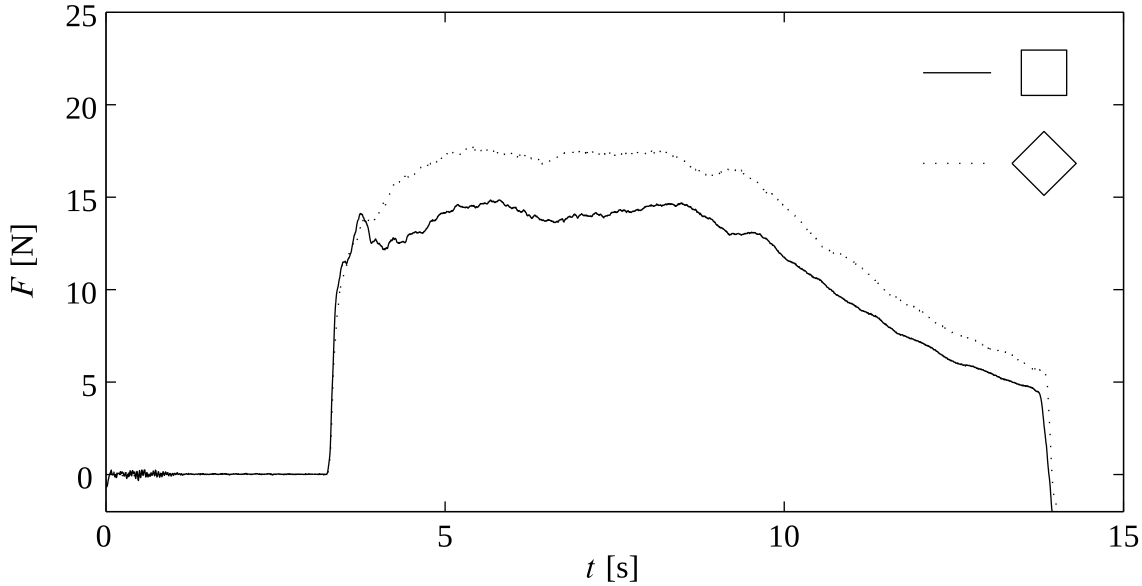

Figure 5.96: Comparison of force time history for the two orientations of the square column, $h_1 = 250$ mm

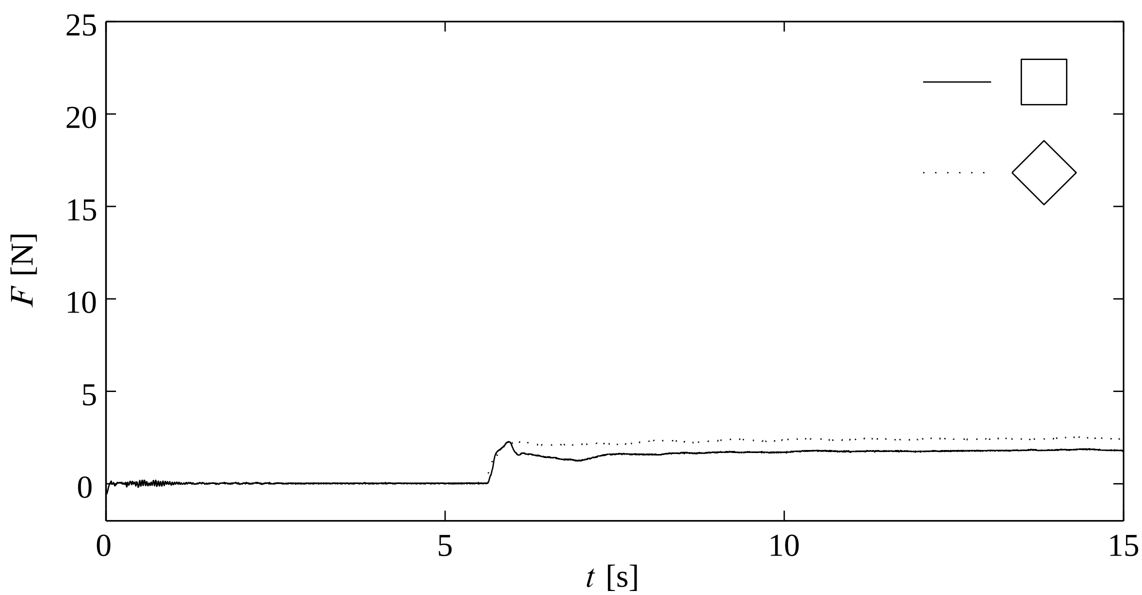

Figure 5.97: Comparison of force time history for the two orientations of the square column, $h_1 = 100$ mm

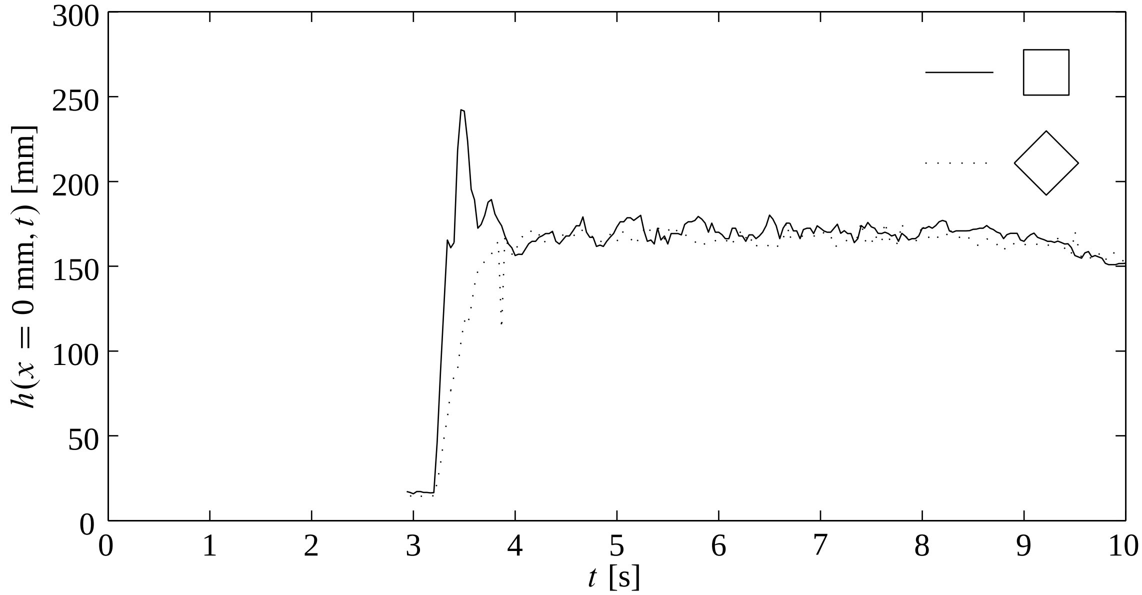

Figure 5.98: Comparison of the water surface profile on the centerline at the upstream edge of the obstacles, $h_1 = 250$ mm

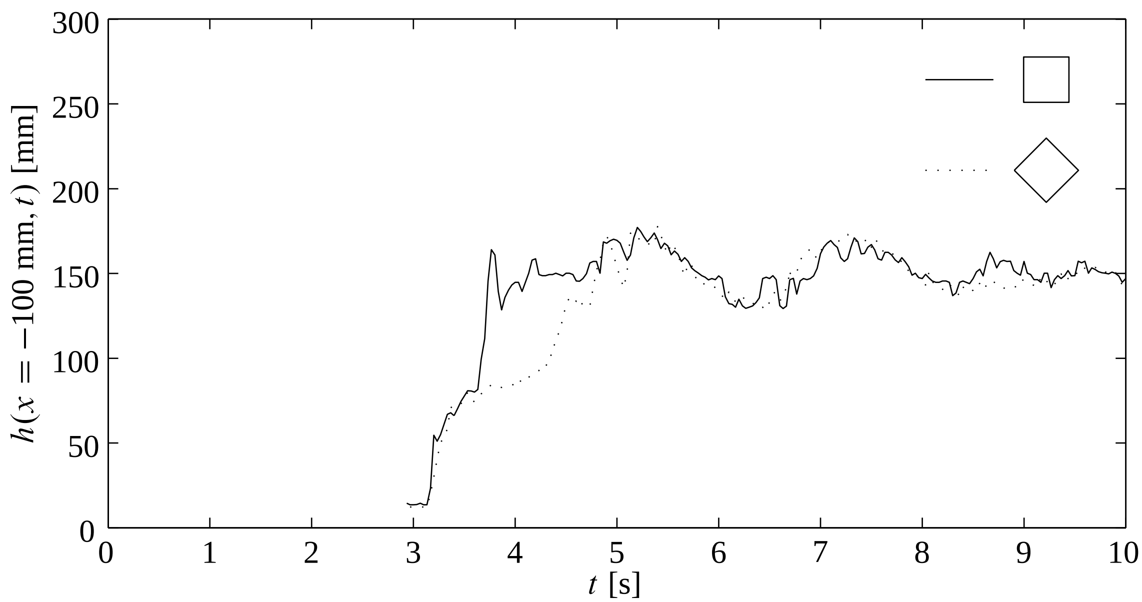

Figure 5.99: Comparison of the water surface profile on the centerline 100 mm upstream of the obstacles, $h_1 = 250$ mm

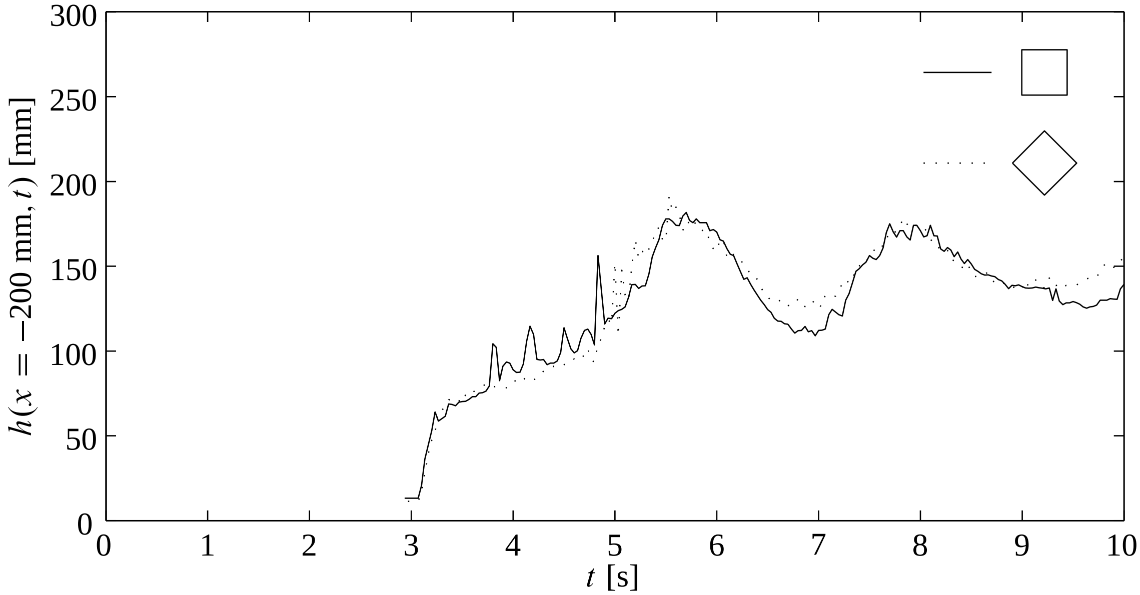

Figure 5.100: Comparison of the water surface profile on the centerline 200 mm upstream of the obstacles, $h_1 = 250$ mm

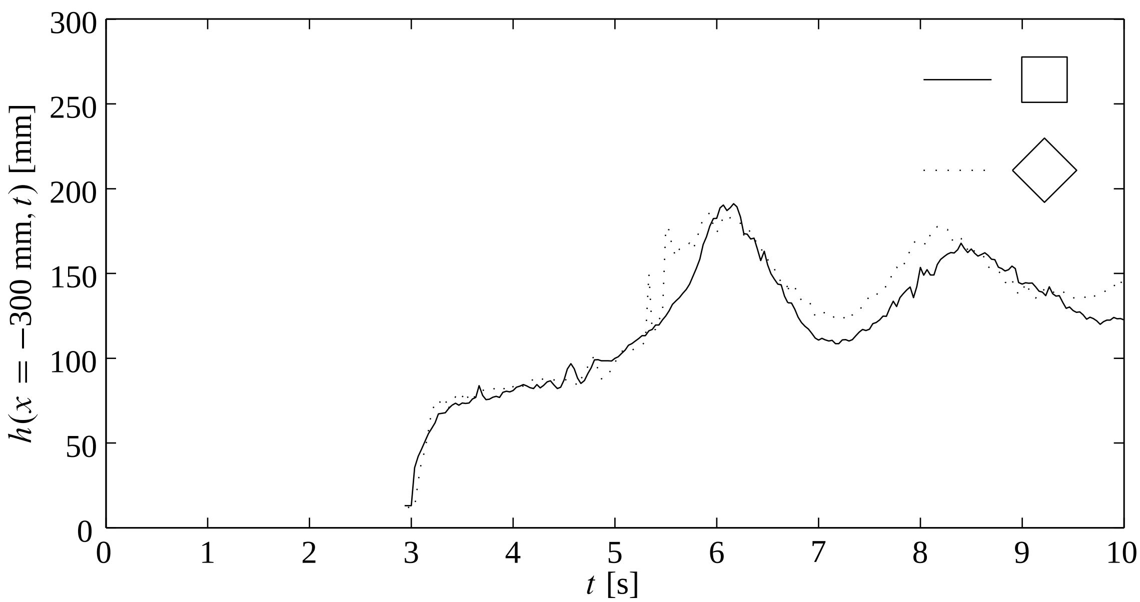

Figure 5.101: Comparison of the water surface profile on the centerline 300 mm upstream of the obstacles, $h_1 = 250$ mm

Chapter 6

CONCLUSIONS

6.1 Qualitative observations

The bore propagates towards the column and upon impact runs up onto it, causing a buildup of water on the upstream face of the column. It is highest in an area, extending a distance about equal to the bore depth, upstream of the large columns with blockage ratio b/B of about 0.2 and higher, but evens out at a lower level further upstream. For the case of the large circular column and higher bores, two prominent waves travel upstream from the column. In comparison, for the square column both aligned and set diagonally to the flow, the two waves travelling upstream are still prominent though the second one is not quite as pronounced, particularly for the diagonal case. These waves are attributable not only to the effects of flow being redirected around the obstacle in the presence of a free surface but also to the presence of the tank sidewalls, effectively making a series of columns upon which the bore impinges. In the wake of the obstacles, the convergence of the split flow at the back of the obstacle results in a turbulent rooster tail that extends downstream. The rooster tail is highly three-dimensional and unsteady. It is usually asymmetric in the transverse direction and fluctuates from side to side. The wake behind the obstacle shows larger wake angles and more transverse velocity components for the smaller bores, while larger bores maintain more of their downstream directed momentum.

The effects of the smallest cylinder, $b/B = 0.05$, on the water surface level are minimal. There is a small runup directly on the cylinder but only minor signs of it affecting the surface further away. That would indicate minimal effects of blockage for this setup. The effects of the intermediate cylinder, $b/B = 0.10$, do reach across the tank, but it does not cause the large water level difference between the upstream and downstream side that are seen for the large cylinder.

6.2 Energy and momentum

The energy and momentum around a circular cylindrical column are examined by calculating the mean and fluctuating components of the flow velocity. The turbulent kinetic energy is estimated by using velocity deviations about a mean flow. In order to avoid the limitations that occur when averaging the velocity, temporally or spatially, around the abrupt velocity change at bore-obstacle impact, a special base velocity is found using path averaging. The energy budget in the wake is then estimated to find the potential energy, the mean flow kinetic energy, and the turbulent kinetic energy.

In the wake of the obstacle, the turbulent kinetic energy is found to be about 0.5–10 % of the total energy in the wake. The highest turbulent kinetic energy values (10 % of total kinetic energy) are observed in the rooster tail directly behind the obstacle. The average value over the entire cross section is roughly 2 % of the total kinetic energy. The contribution of the potential energy is found to be approximately equal to that of the kinetic energy, both for the flow without any obstacle and for the flow in the wake of the column. The energy loss passed to the column is about 7 % compared to the flow without any obstacle.

The specific momentum of the flow is calculated at a single cross-section upstream and at two cross-sections downstream using the same data as are used for the energy calculations. The dynamics of the bore interaction with the structures and tank side walls yield highly unsteady momentum flux in the region of the structures. Using the momentum flux to estimate the force acting on the columns was therefore found to be non-productive. The large scale fluctuations in the upstream momentum correspond closely to the build-up and upstream propagation of breaking wave on the front face of the obstacles. Although the conclusions regarding the energy and momentum are not unexpected, they demonstrate the ability to obtain quantitative values for these attributes in the laboratory using careful water surface and velocity measurements.

6.3 Forces

The total resistance coefficient C_{R} is observed to be in the range 1–2, dependent on shape, object spacing and relative depth. For the circular columns C_{R} is found to be a function of the Froude number Fr, relative depth h/b and blockage b/B. The resistance decreases with increasing Froude number and relative bore height. The variation of the resistance coefficients with bore height is much less pronounced for the square column than for the circular ones. For the square column, although C_{R} decreases as Fr and h/b increase, that decrease is small and considering C_{R} to be a constant for either orientation of the square column is quite reasonable. With one side facing the flow $C_{\mathrm{R}} = 2.1 \pm 0.1$ and with one corner into the flow $C_{\mathrm{R}} = 1.8 \pm 0.2$. The invariant C_{R} for the square column can be explained by the fixed flow separation points at the corners of the column.

The values of C_{R} observed in these experiments are somewhat higher than what can be found in standard hydraulics texts (see for example Roberson and Crowe (1995) and Daugherty et al. (1985)) for drag coefficients, C_{D}, for infinite cylinders in submerged steady flow and for comparable Reynolds numbers.

The measured forces compare relatively well with hydrostatic forces calculated from water level on either side of the square column. The relatively large size of the columns compared to the impinging bore as well as the existence of a free surface are the primary causes for the piling up of water on the upstream face of the obstacle and the low water depth on the downstream face. The redirection of flow towards the tank sidewalls and subsequent reflections are also important. These flow changes are more variable for the large circular column than for the square column because of flow separation on the square column always occurs at the corners.

For the smaller bores, the force during the initial impact is about 50 % higher than the resistance force during the bore passing. For the larger bores, the force increases during the bore due to blockage effects, so the maximum resistance force can be as large or even larger than the force during the initial impact.

BIBLIOGRAPHY

Afzal, N. and Bushra, A. (2002). Structur of the turbulent hydraulic jump in a trapezoidal channel, *Journal of Hydraulic Research* **40**(2): 205–214.

Bradley, J. N. and Peterka, A. J. (1957). The hydraulic design of stilling basin: Hydraulic jumps on a horizontal apron, *Journal of the Hydraulic Division, ASCE* **83**(5): 1–24.

Cross, R. H. (1967). Tsunami surge forces, *Journal of Waterways and Harbor Division, ASCE* **93**(4): 201–231.

Cumberbatch, E. (1960). The impact of a water wedge on a wall, *Journal of Fluid Mechanics* **7**: 353–374.

Daugherty, R. L., Franzini, J. B. and Finnemore, E. J. (1985). *Fluid Mechanics with Engineering Applications*, eighth edition, McGraw-Hill Book Company, New York.

Davletshin, V. K. and Lappo, D. D. (1986). Tsunami forces exerted on vertical cylindrical barriers, *Fluid Mechanics – Soviet Research* **15**(3): 137–147.

Dressler, R. F. (1952). Hydraulic resistance effect upon the dam-break functions, *Journal of Research of the National Bureau of Standards* **49**(3): 217–225.

Dudley, W. C. and Lee, M. (1988). *Tsunami!*, University of Hawai‘i Press, Honolulu.

Eaton, J. P., Richter, D. H. and Ault, W. U. (1961). The tsunami of May 23, 1960 on the Island of Hawaii, *Bulletin of the Seismological Society of America* **51**(2): 135–157.

Fujima, K. and Shuto, N. (1990). Formulation of friction laws for long waves on a smooth dry bed, *Coastal Engineering*, Vol. 33, pp. 25–47.

Fukui, Y., Nakamura, M., Shiraishi, H. and Sasaki, Y. (1963a). Hydraulic study on tsunami, *Coastal Engineering, Japan* **6**: 67–82.

Fukui, Y., Nakamura, M., Shiraishi, H. and Sasaki, Y. (1963b). Hydraulic study on tsunami acting on dikes and their preservation, *Transactions of the Agricultural Engineering Society of Japan* (5): 31–48.

Gardarsson, S. M. (1997). *Shallow-Water Sloshing*, Ph.D. dissertation, University of Washington.

Gupta, V. P. and Goyal, S. C. (1975). Hydrodynamic forces on bridge piers, *Journal of the Institution of Engineers (India), Civil Engineering Division* **56**: 12–16.

Miller, D. J. (1960). Giant waves in Lituya Bay, Alaska, *Technical Report Geological Survey Professional Paper 354-C*, Unites States Government Printing Office, Washington.

Moore, A. L. (1999). *Combined use of clast-size measurements and wave-tank experiments to estimate Pleistocene tsunami size at Molokai, Hawaii*, Ph.D. dissertation, University of Washington.

Nakamura, S. and Tsuchiya, Y. (1973). On shock pressure of surge on a wall, *Bulletin [of the] Disaster Prevention Research Institute* **23**(12): 47–58.

Ramsden, J. D. (1993). *Tsunamis: Forces on a Vertical Wall Caused by Long Waves, Bores, and Surges on a Dry Bed*, Ph.D. dissertation, California Institute of Technology.

Ritter, A. (1892). Die Fortpflanzung der Wasserwellen, *Zeitschrift des Vereines Deutscher Ingenieure* **36**(24): 947–954.

Roberson, J. A. and Crowe, C. T. (1995). *Engineering Fluid Mechanics*, fifth edition, John Wiley & Sons, New York.

Schlichting, H. (1979). *Boundary-Layer Theory*, McGraw Hill Book Co., New York.

Stoker, J. J. (1948). The formation of breaker and bores, the theory of nonlinear wave propagation in shallow water and open channels, *Communications on Applied Mathematics* **1**(1): 1–87.

Sumer, B. M. and Fredsøe, J. (1997). *Hydrodynamics around cylindrical structures*, World Scientific Publishing Company, Singapore.

Wang, J. D. and Ansari, H. R. (1986). Dynamics of surge run-up on dry bed, *Internal report*, Division of Applied Marine Physics, Rosentiel School of Marine and Atmospheric Science, University of Miami.

Wang, K. H. and Chwang, A. T. (1984). Nonlinear impulsive force on a vertical cylinder, *in* A. P. Boresi and K. P. Chong (eds), *Engineering Mechanics in Civil Engineering*, pp. 859–862.

Wang, K.-H. and Chwang, A. T. (1986). Flow around an impulsively starting vertical cylinder, *in* H. G. S. et al. (ed.), *Advancements in Aerodynamics, Fluid Mechanics and Hydraulics*, pp. 322–328.

Wang, K.-H. and Chwang, A. T. (1989). Free–surface flow produced by accelerating vertical cylinder, *Journal of Engineering Mechanics* **115**(7): 1559–1566.

Warton, W. J. L. and Evans, F. J. (1888). On the seismic sea waves caused by the eruption at Krakatoa, August 26th & 27th 1883, part III of eruption of Krakatoa and subsequent phenomena, *in* G. L. Symonds (ed.), *Report of the Krakatoa Committee of the Royal Society*.

Whitham, G. B. (1955). The effects of hydraulic resistance on the dam-break problem, *Proceedings of the Royal Society, series A* **227**: 399–407.

Appendix A

VELOCITY FIELD DATA

A.1 Introduction

This is a compilation showing the evolution of velocity fields in a bore flowing past a cylinder. There are three different cases, §A.2 shows data taken at $z = 15$ mm, where z represents height above the floor, for an initial impoundment of $h_1 = 250$ mm, §A.3 shows data for $z = 35$ mm and $h_1 = 250$ mm and §A.4 for $z = 15$ mm and $h_1 = 300$ mm. Each figure is compiled from PIV measurements from 11 different views, mapped out in Figure 4.17. The length of the arrows is scaled so that it equals the distance a particle would travel between consecutive frames, were it to travel at that velocity. The time t indicated at the bottom of each figure is the time passed since the gate was lifted. The extreme upstream point of the cylinder is 5.2 m from the upstream side of the gate.

A.2 Velocity field 15 mm above the floor for 250 mm impoundment

Figures A.1 through A.9 show the compilation of PIV velocity measurements for $h_1 = 250$ mm and $z = 15$ mm

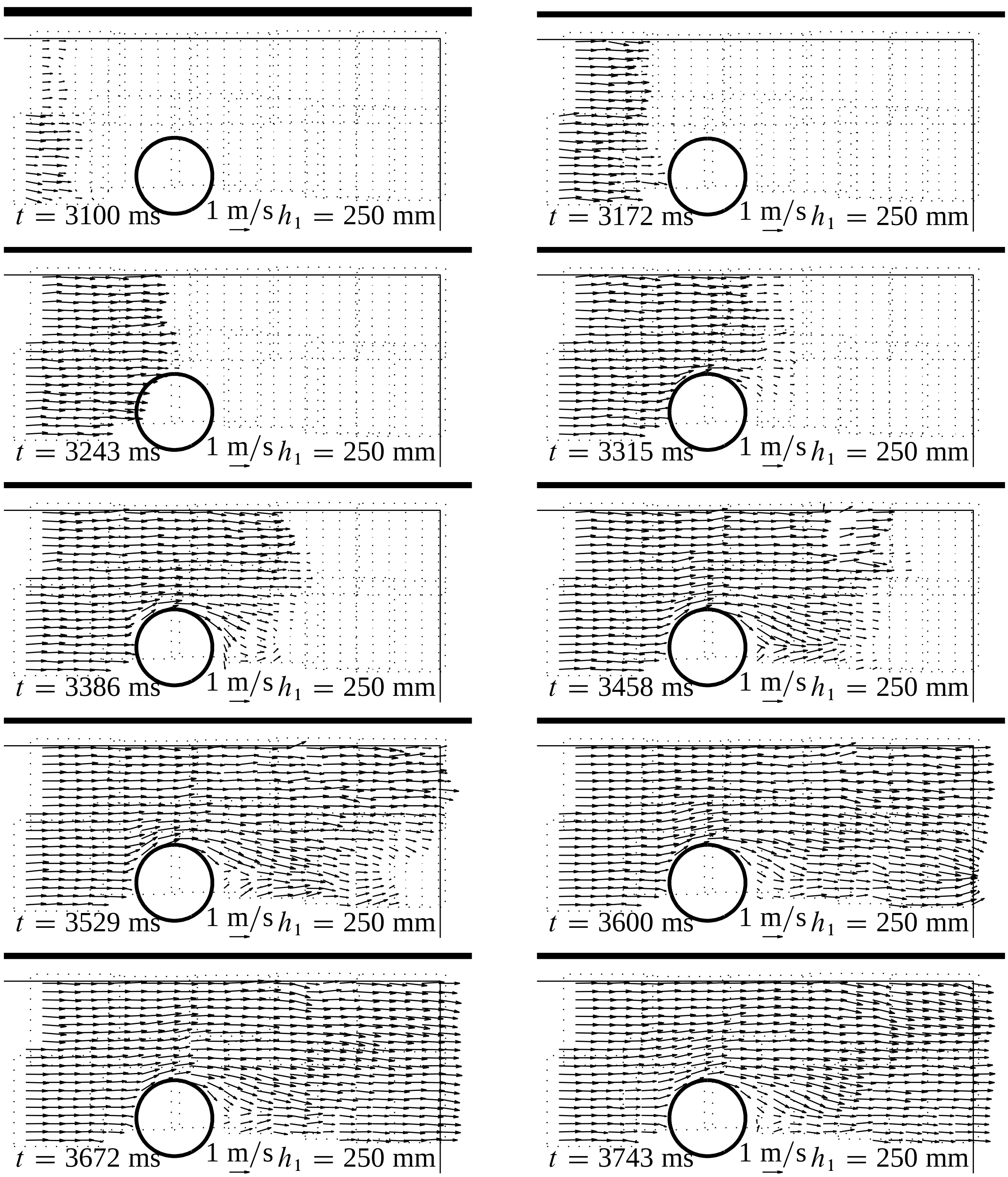

Figure A.1: Horizontal velocity field at $t = 3100$ through 3743 ms for $h_1 = 250$ mm and $z = 15$ mm.

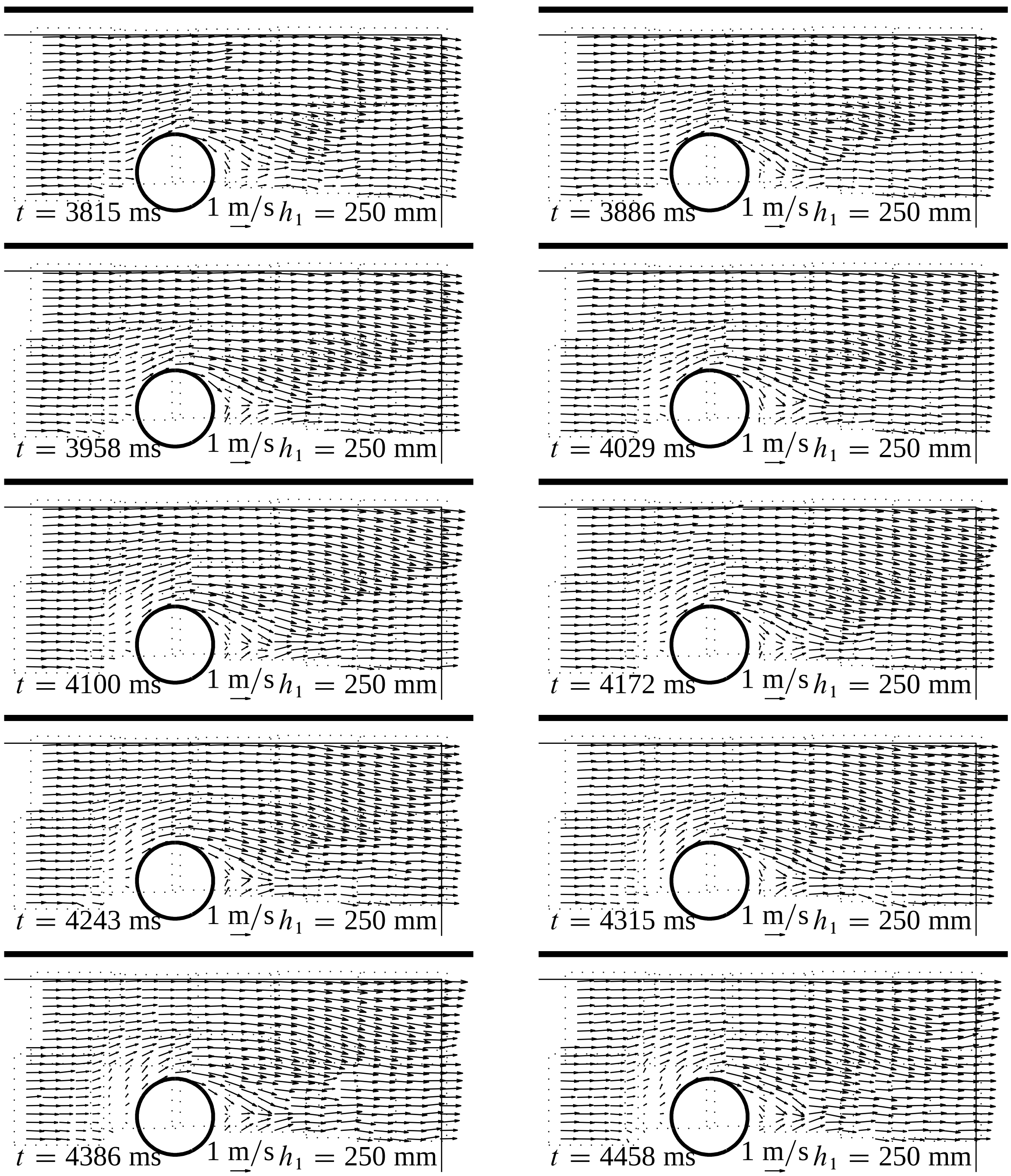

Figure A.2: Horizontal velocity field at $t = 3815$ through 4458 ms for $h_1 = 250$ mm and $z = 15$ mm.

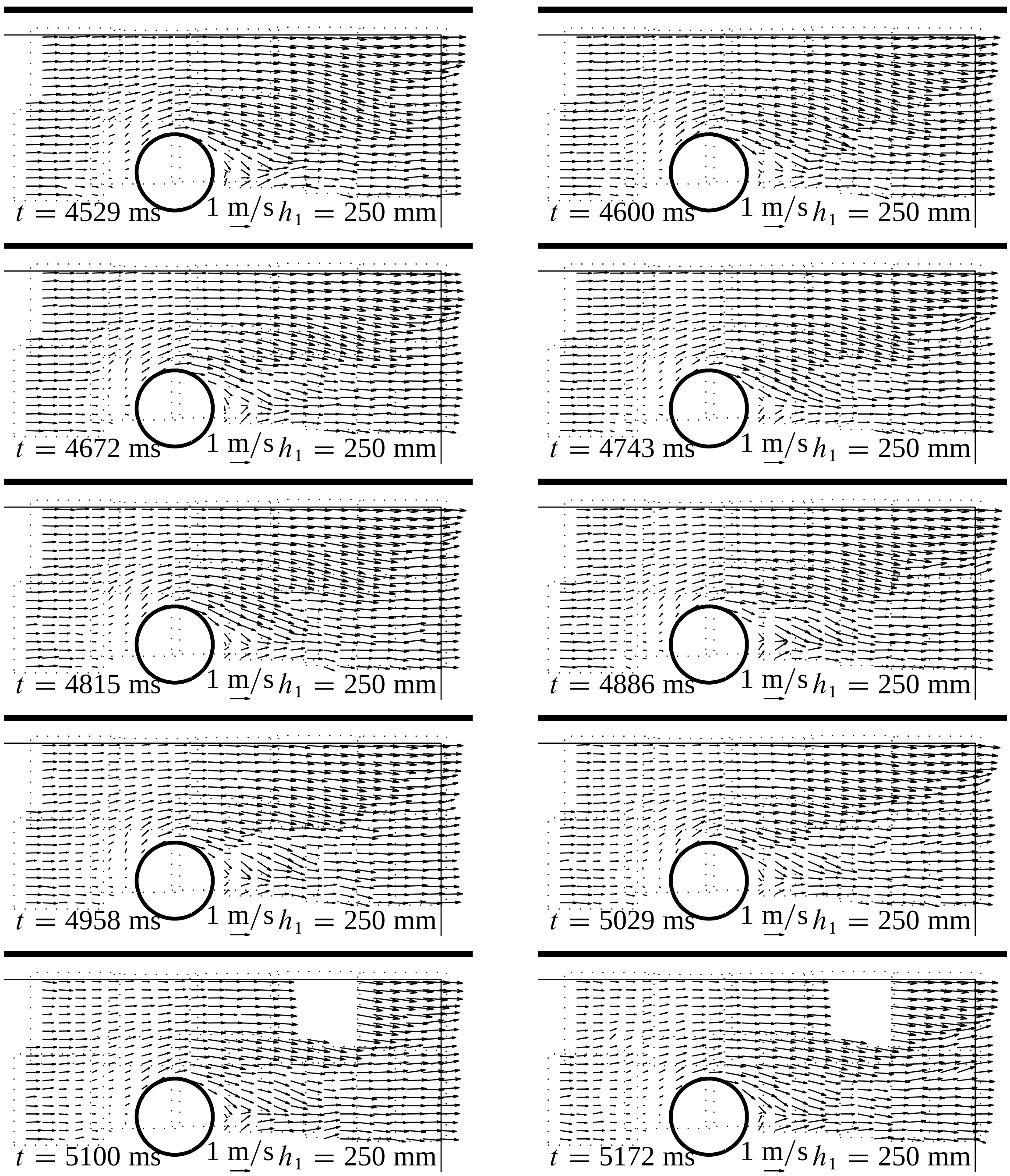

Figure A.3: Horizontal velocity field at $t = 4529$ through 5172 ms for $h_1 = 250$ mm and $z = 15$ mm.

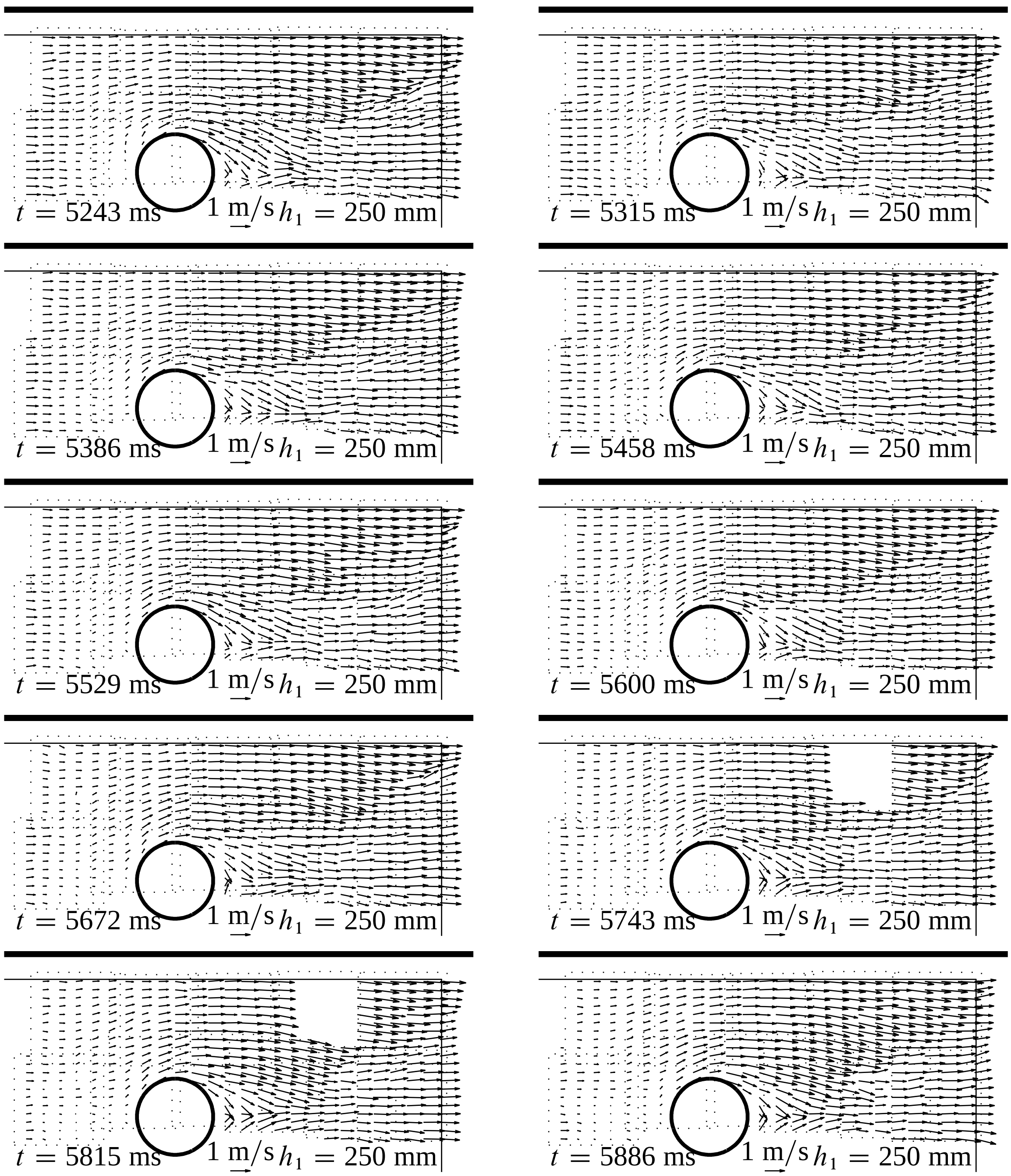

Figure A.4: Horizontal velocity field at $t = 5243$ through 5886 ms for $h_1 = 250$ mm and $z = 15$ mm.

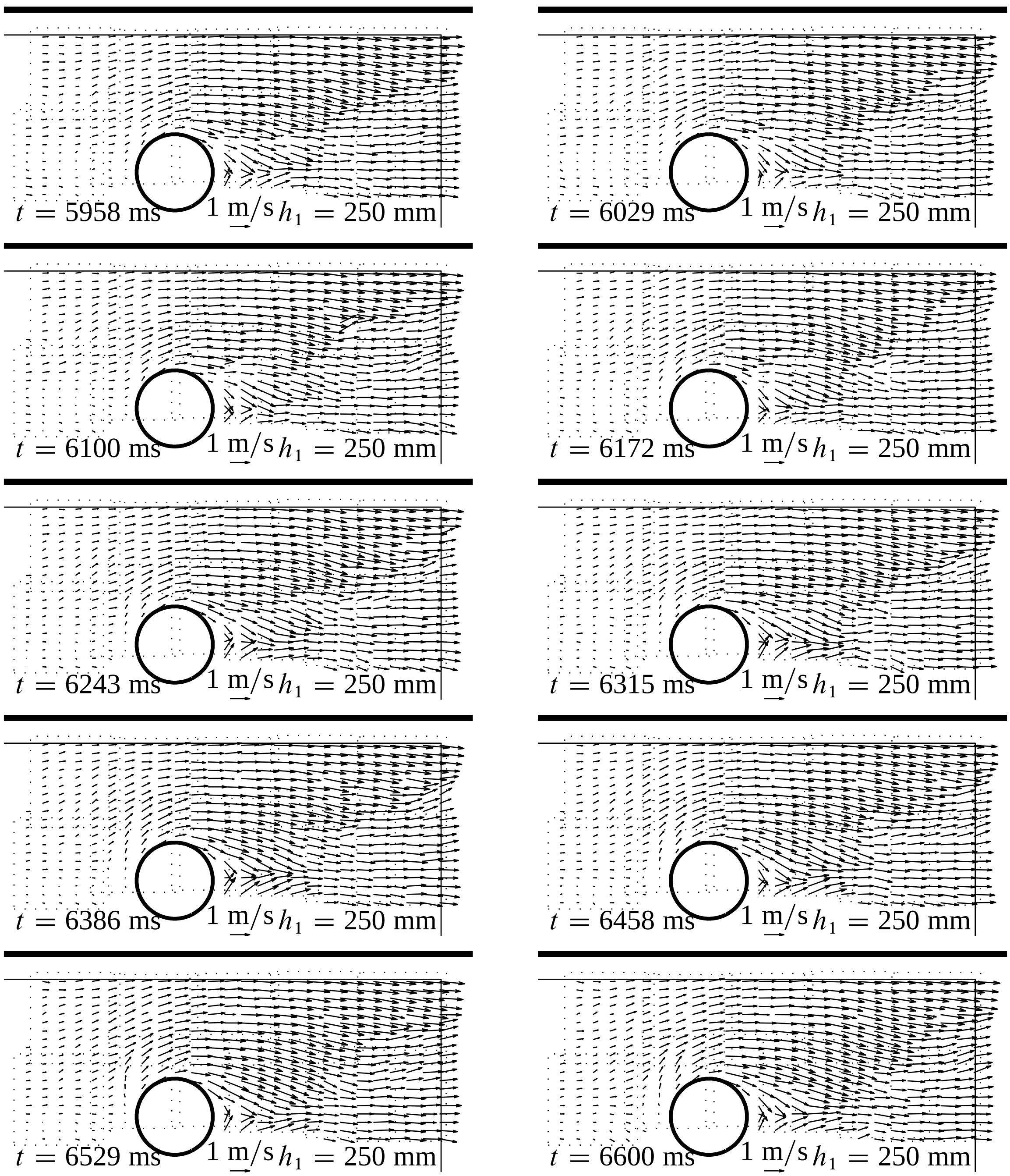

Figure A.5: Horizontal velocity field at $t = 5958$ through 6600 ms for $h_1 = 250$ mm and $z = 15$ mm.

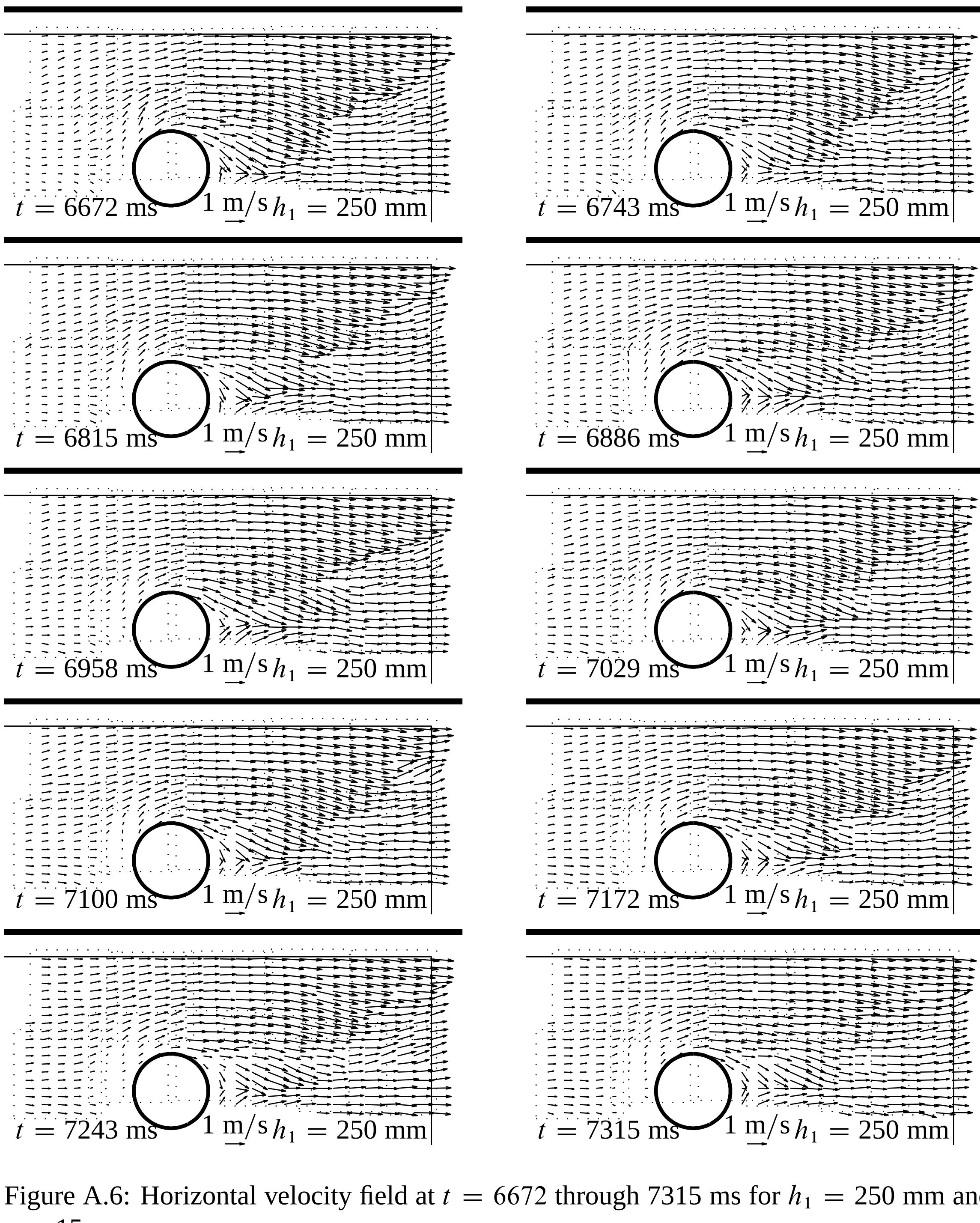

Figure A.6: Horizontal velocity field at $t = 6672$ through 7315 ms for $h_1 = 250$ mm and $z = 15$ mm.

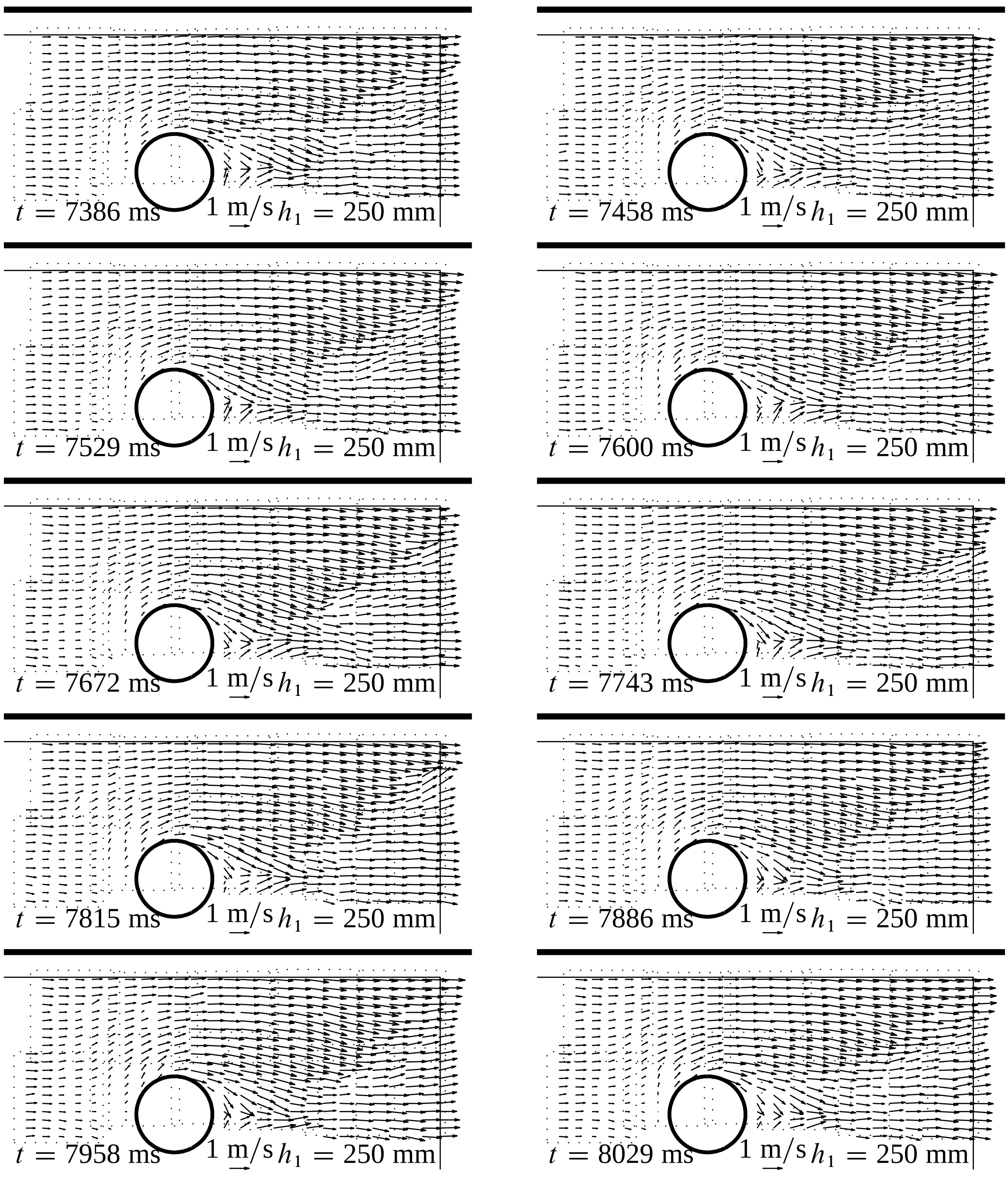

Figure A.7: Horizontal velocity field at $t = 7386$ through 8029 ms for $h_1 = 250$ mm and $z = 15$ mm.

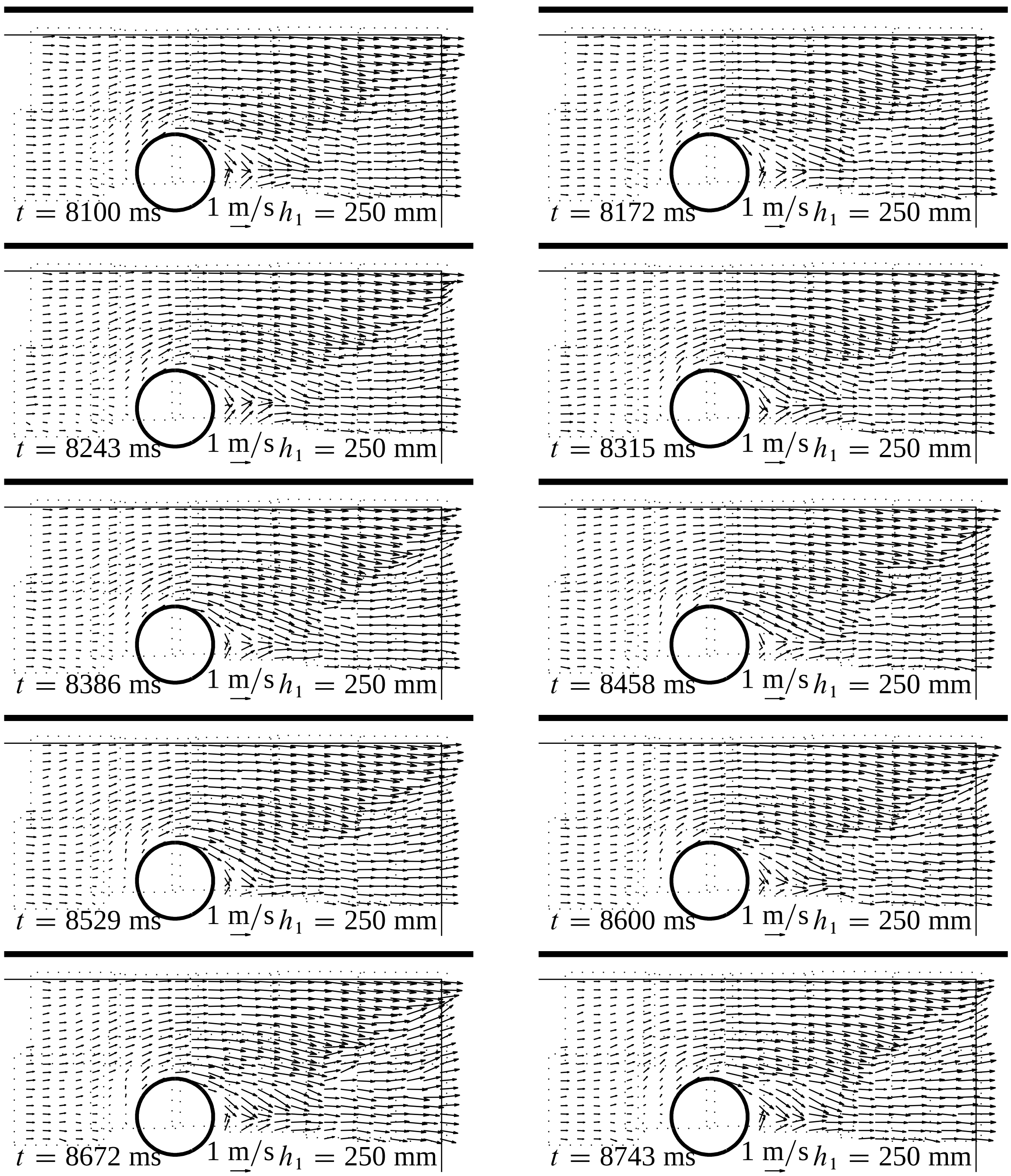

Figure A.8: Horizontal velocity field at $t = 8100$ through 8743 ms for $h_1 = 250$ mm and $z = 15$ mm.

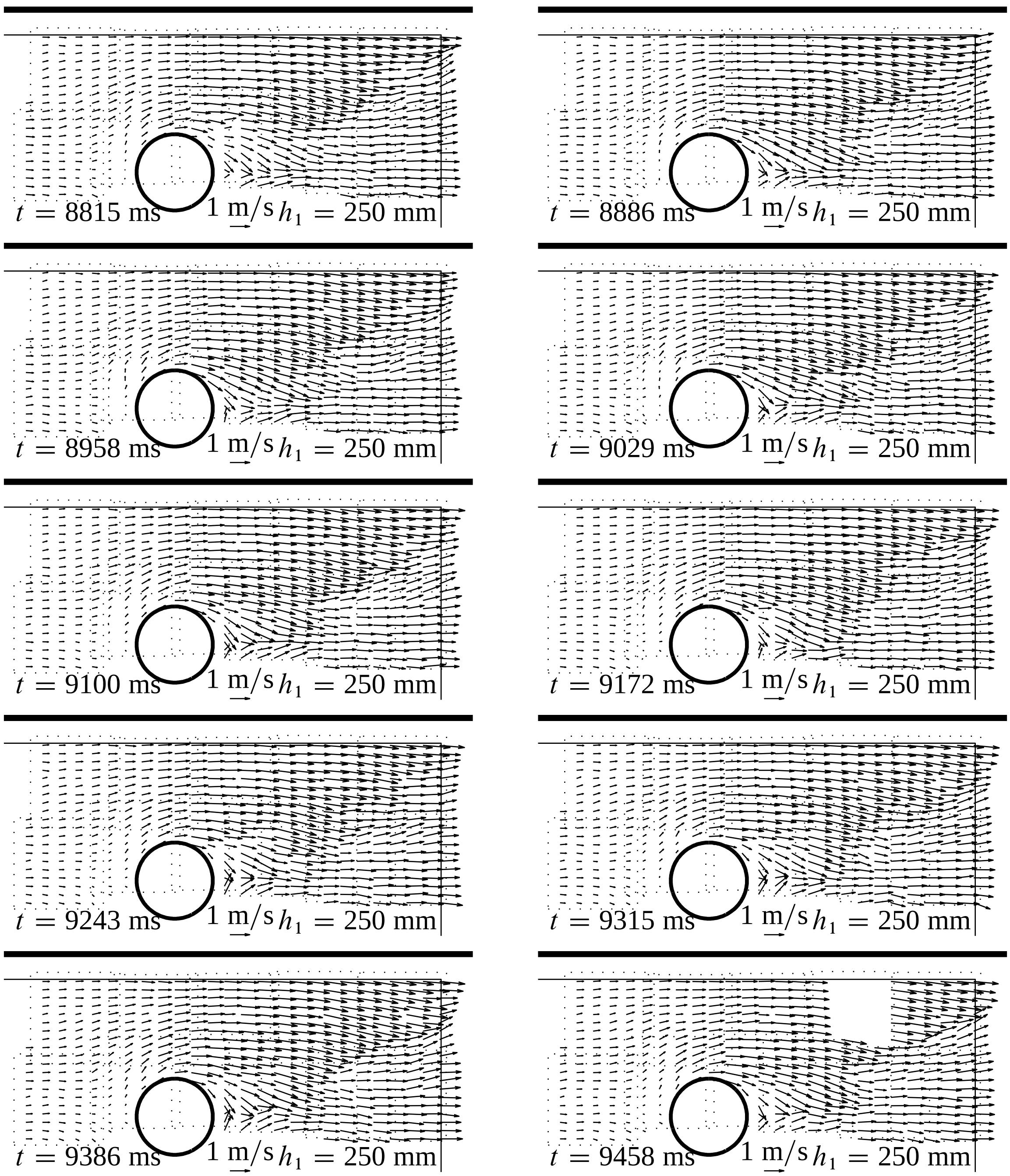

Figure A.9: Horizontal velocity field at $t = 8815$ through 9458 ms for $h_1 = 250$ mm and $z = 15$ mm.

A.3 Velocity field 35 mm above the floor for 250 mm impoundment

Figures A.10 through A.19 show the compilation of PIV velocity measurements for $h_1 = 250$ mm and $z = 35$ mm

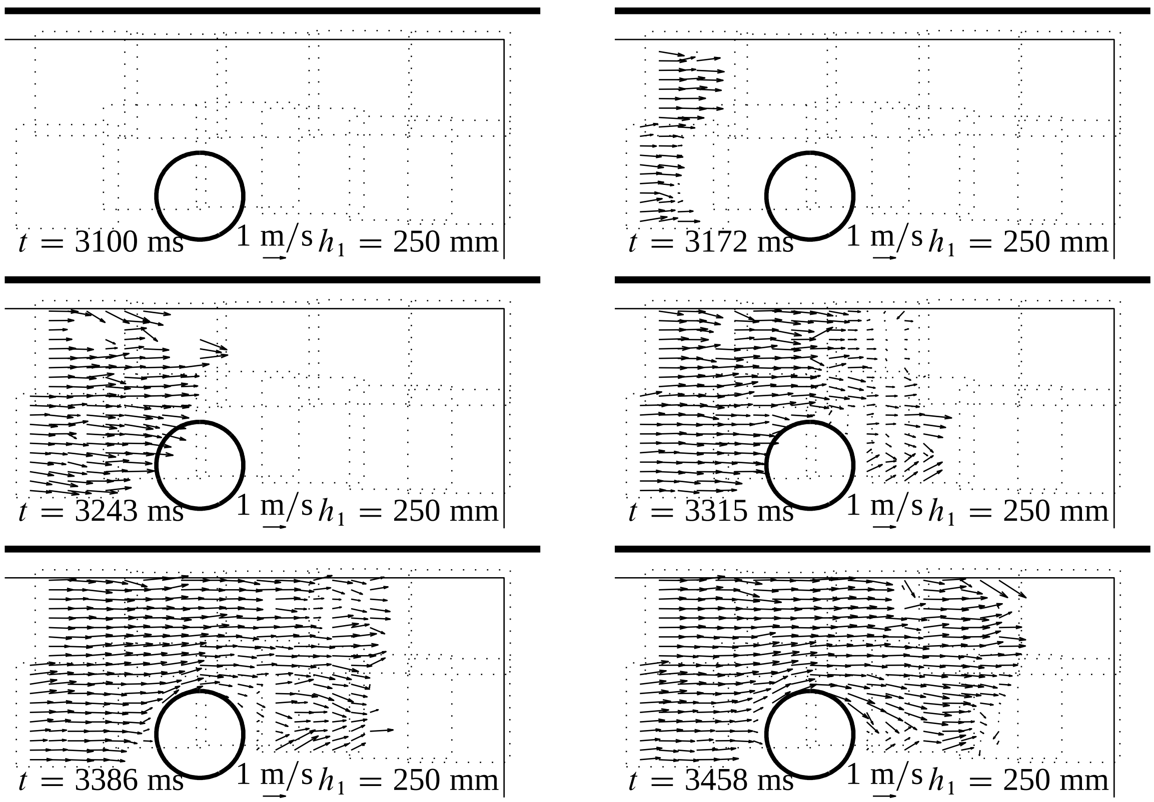

Figure A.10: Horizontal velocity field at $t = 3100$ through 3458 ms for $h_1 = 250$ mm and $z = 35$ mm.

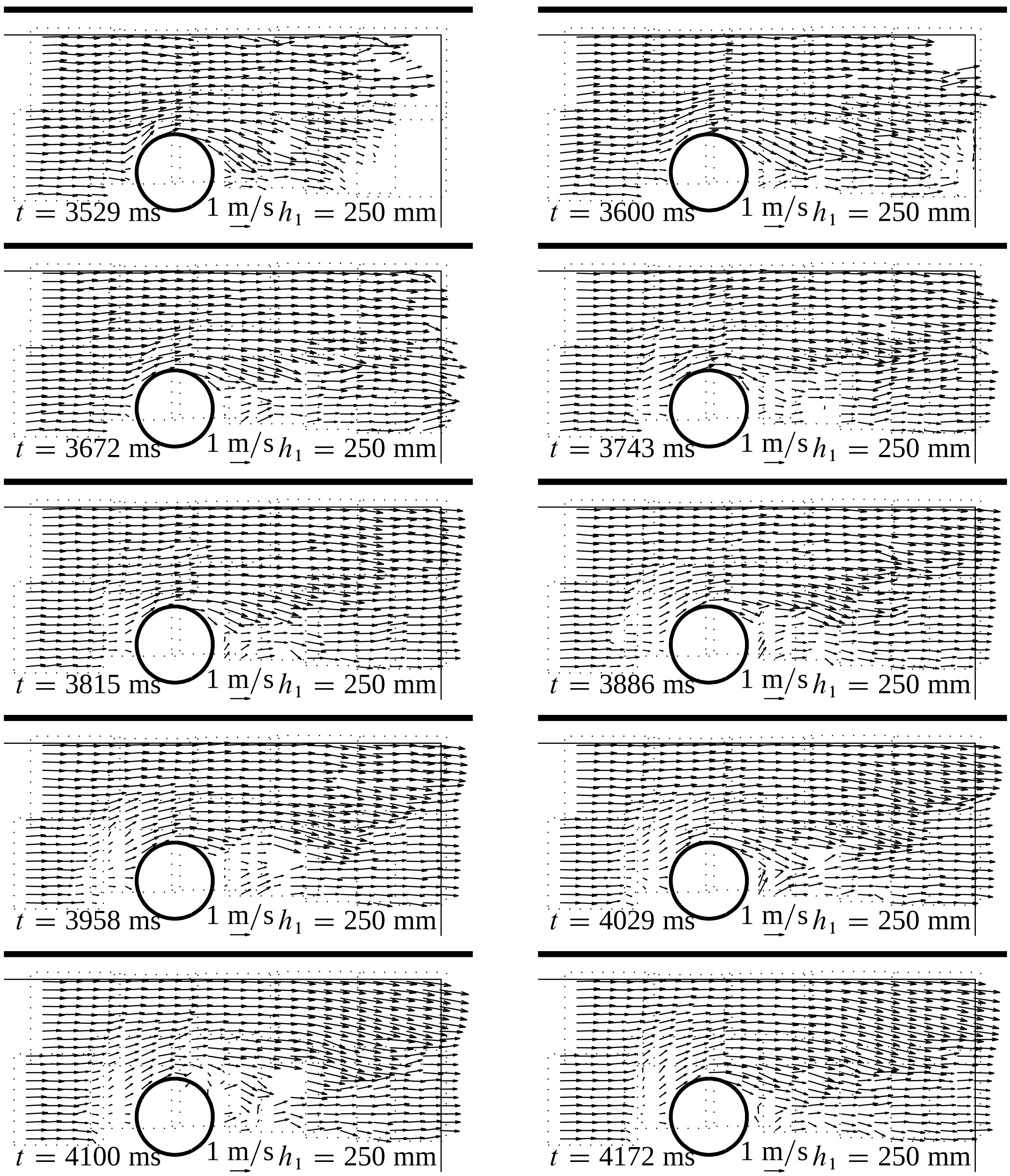

Figure A.11: Horizontal velocity field at $t = 3529$ through 4172 ms for $h_1 = 250$ mm and $z = 35$ mm.

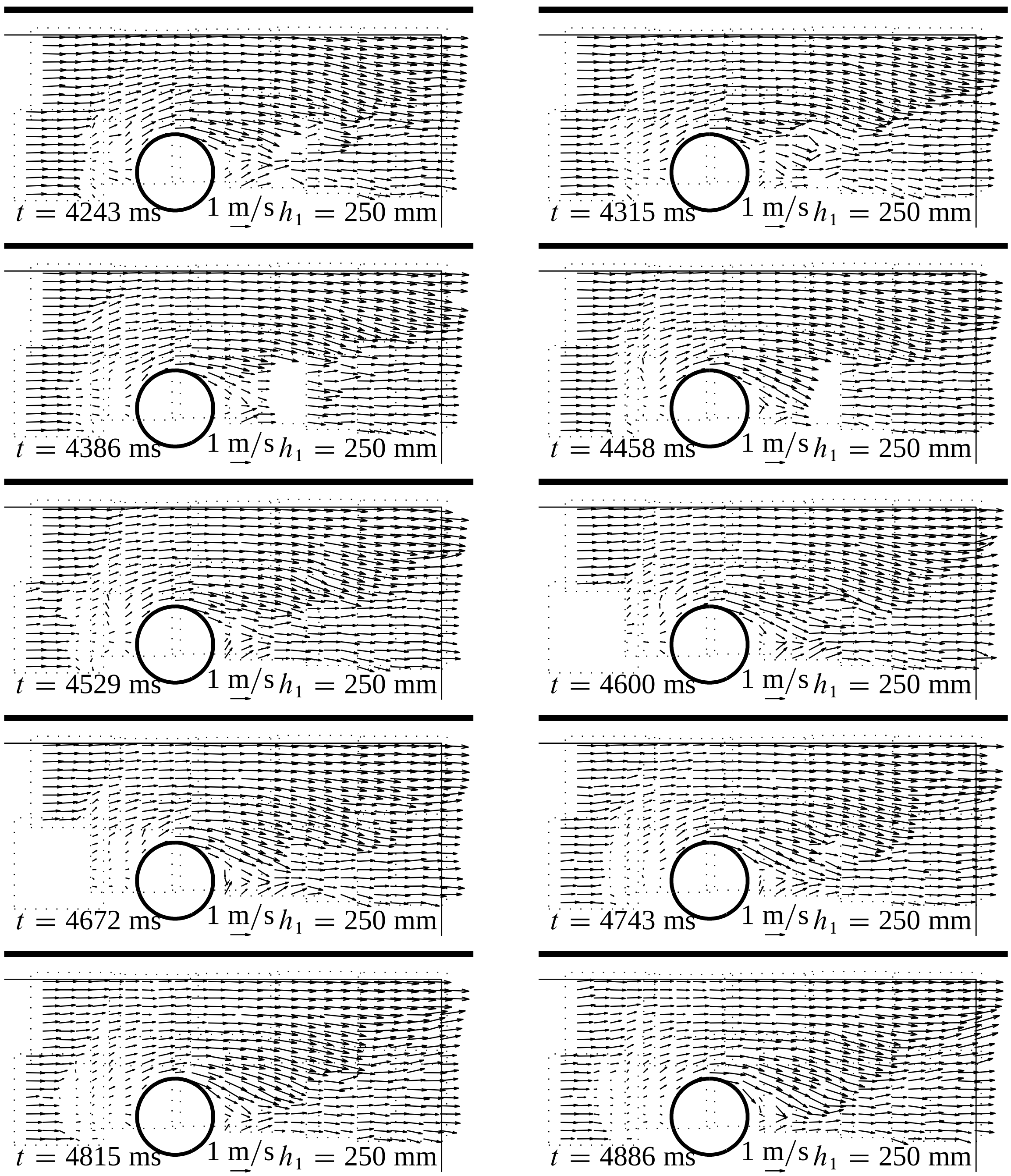

Figure A.12: Horizontal velocity field at $t = 4243$ through 4886 ms for $h_1 = 250$ mm and $z = 35$ mm.

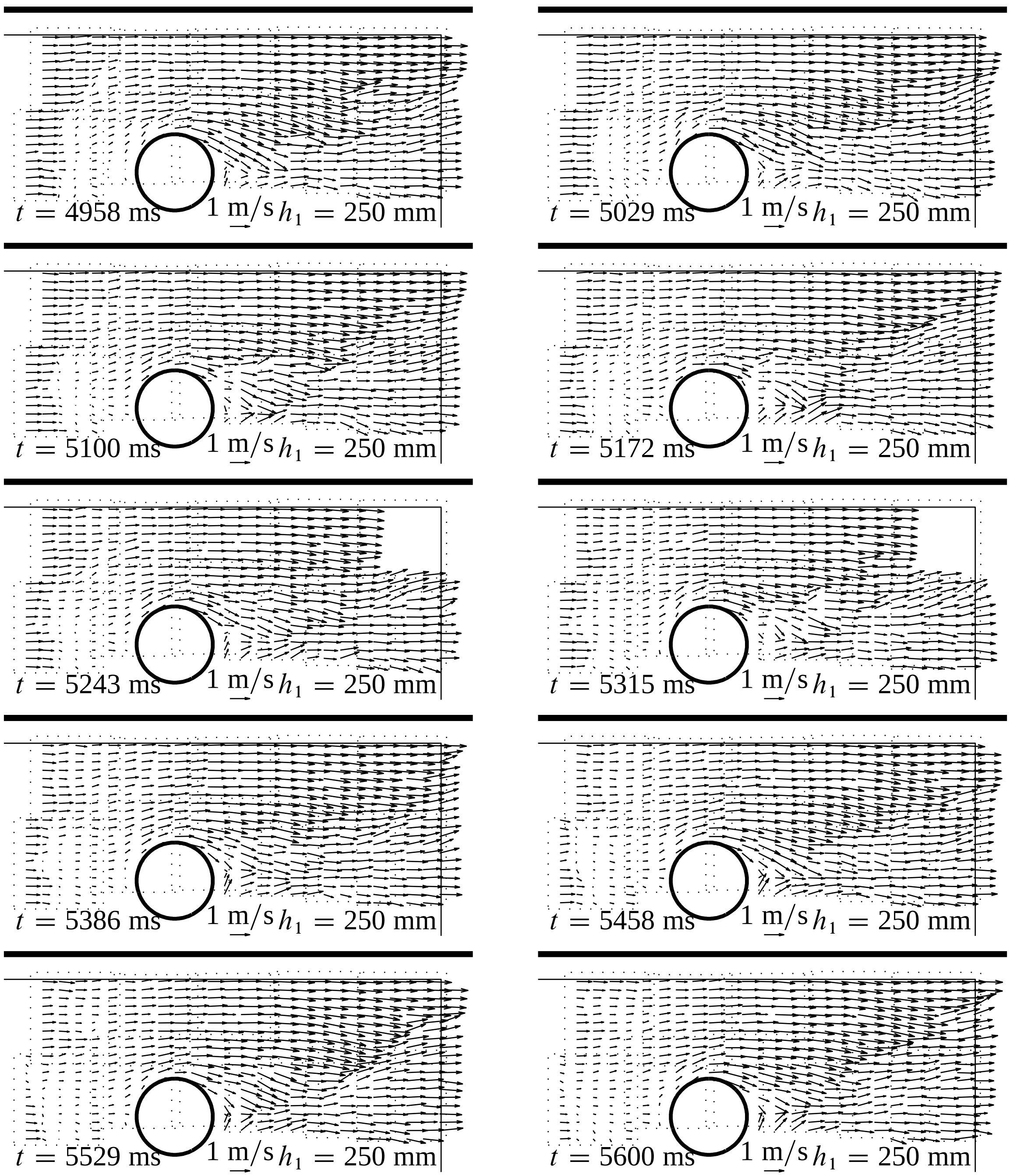

Figure A.13: Horizontal velocity field at $t = 4958$ through 5600 ms for $h_1 = 250$ mm and $z = 35$ mm.

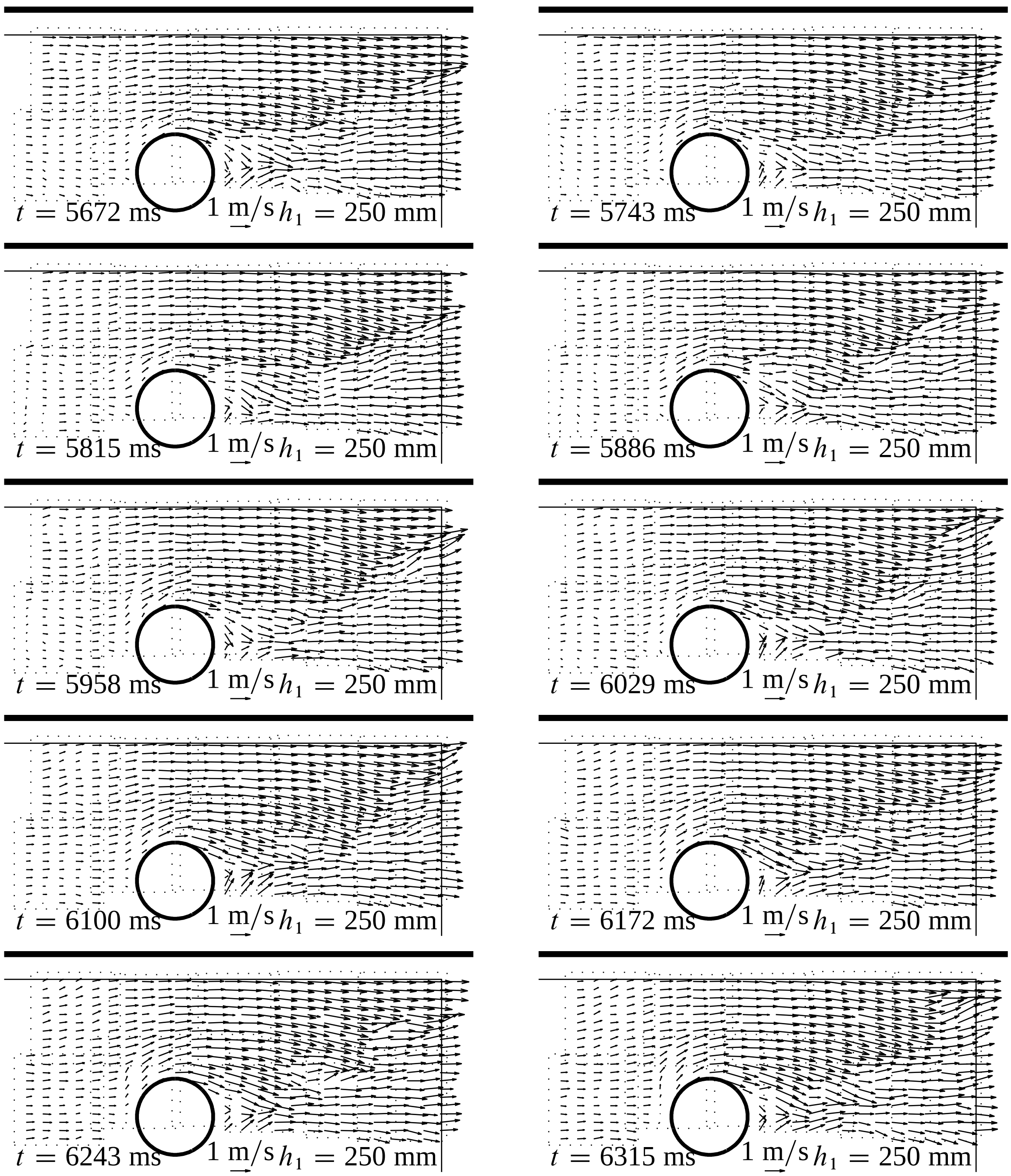

Figure A.14: Horizontal velocity field at $t = 5672$ through 6315 ms for $h_1 = 250$ mm and $z = 35$ mm.

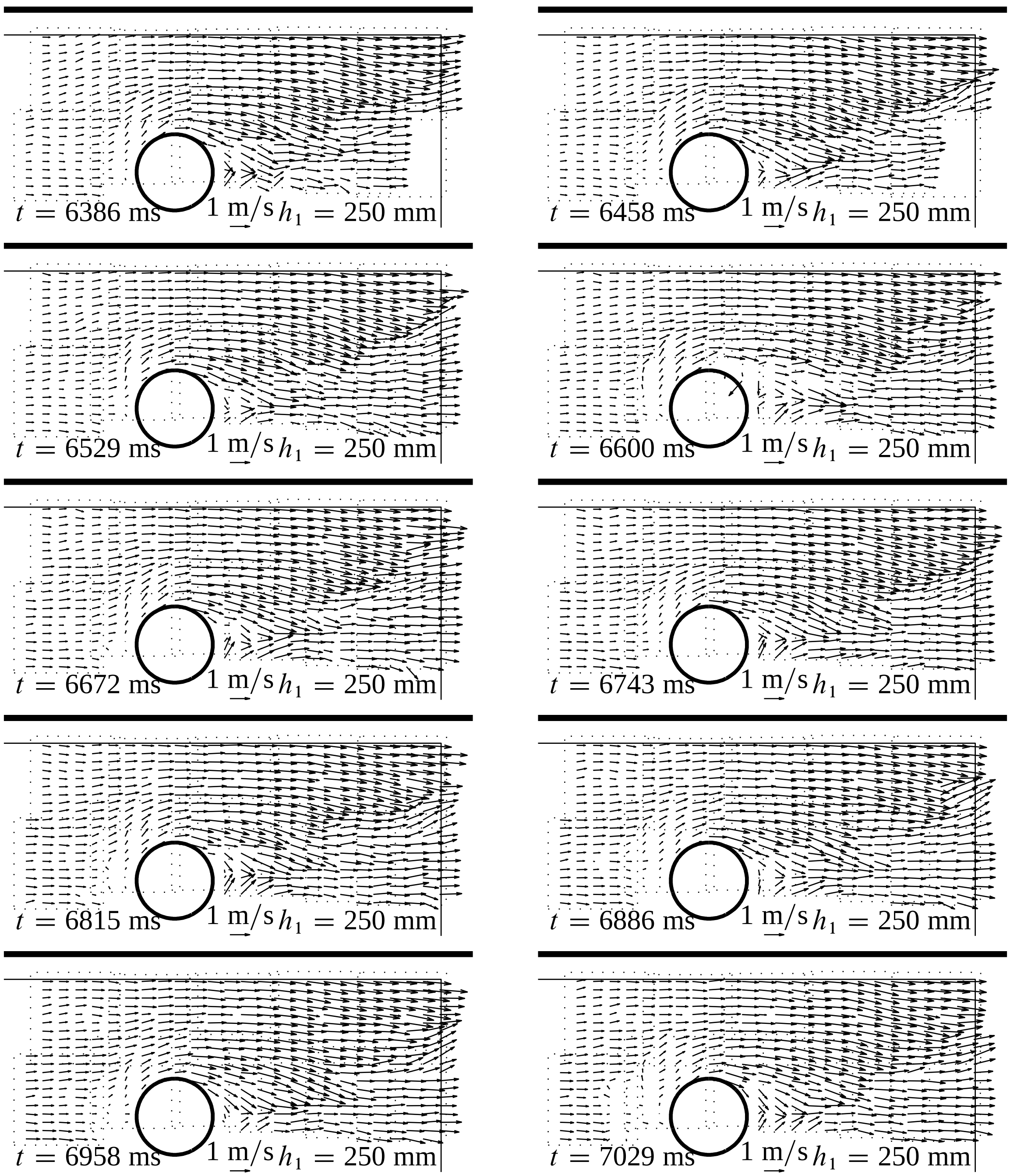

Figure A.15: Horizontal velocity field at $t = 6386$ through 7029 ms for $h_1 = 250$ mm and $z = 35$ mm.

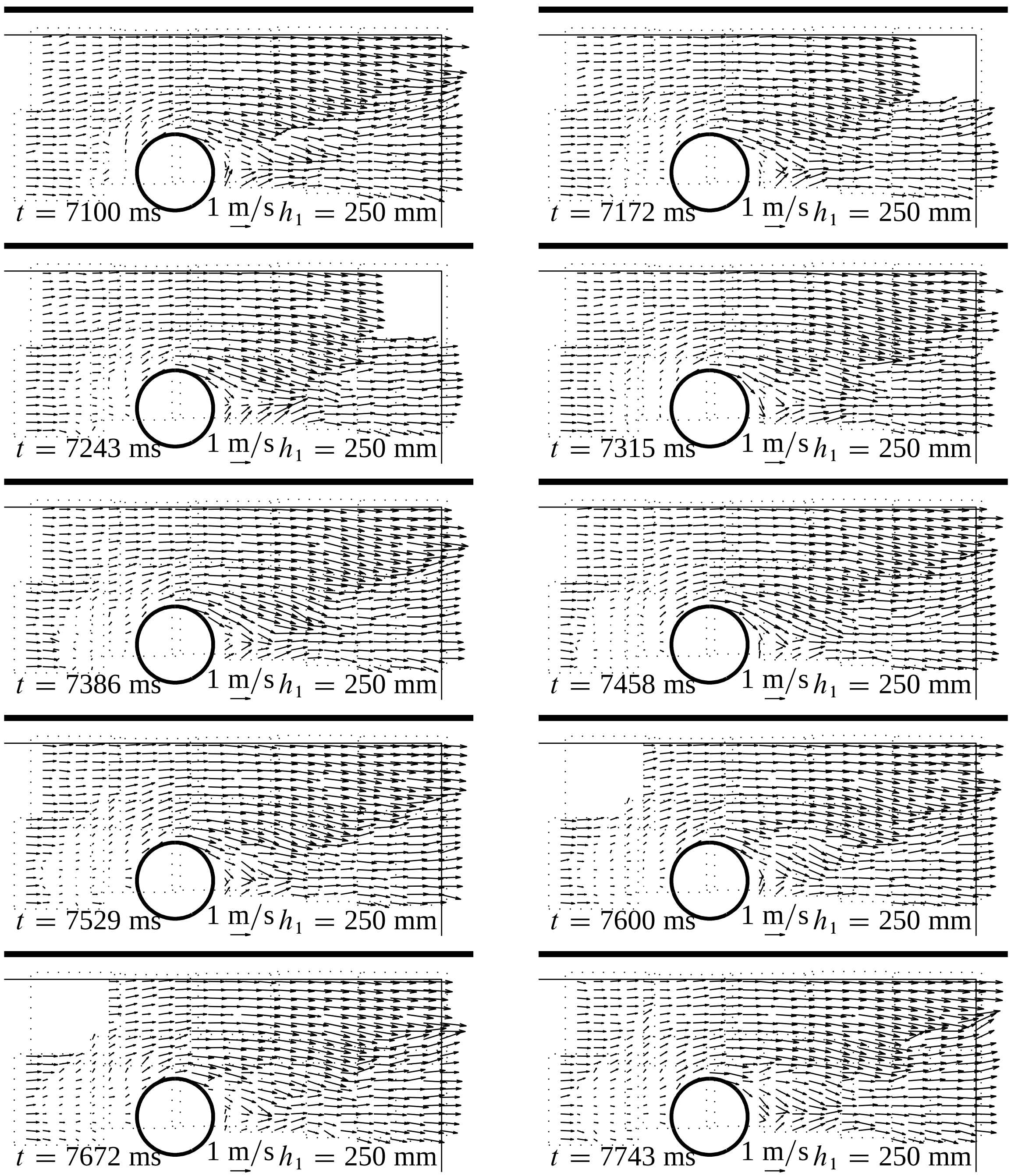

Figure A.16: Horizontal velocity field at $t = 7100$ through 7743 ms for $h_1 = 250$ mm and $z = 35$ mm.

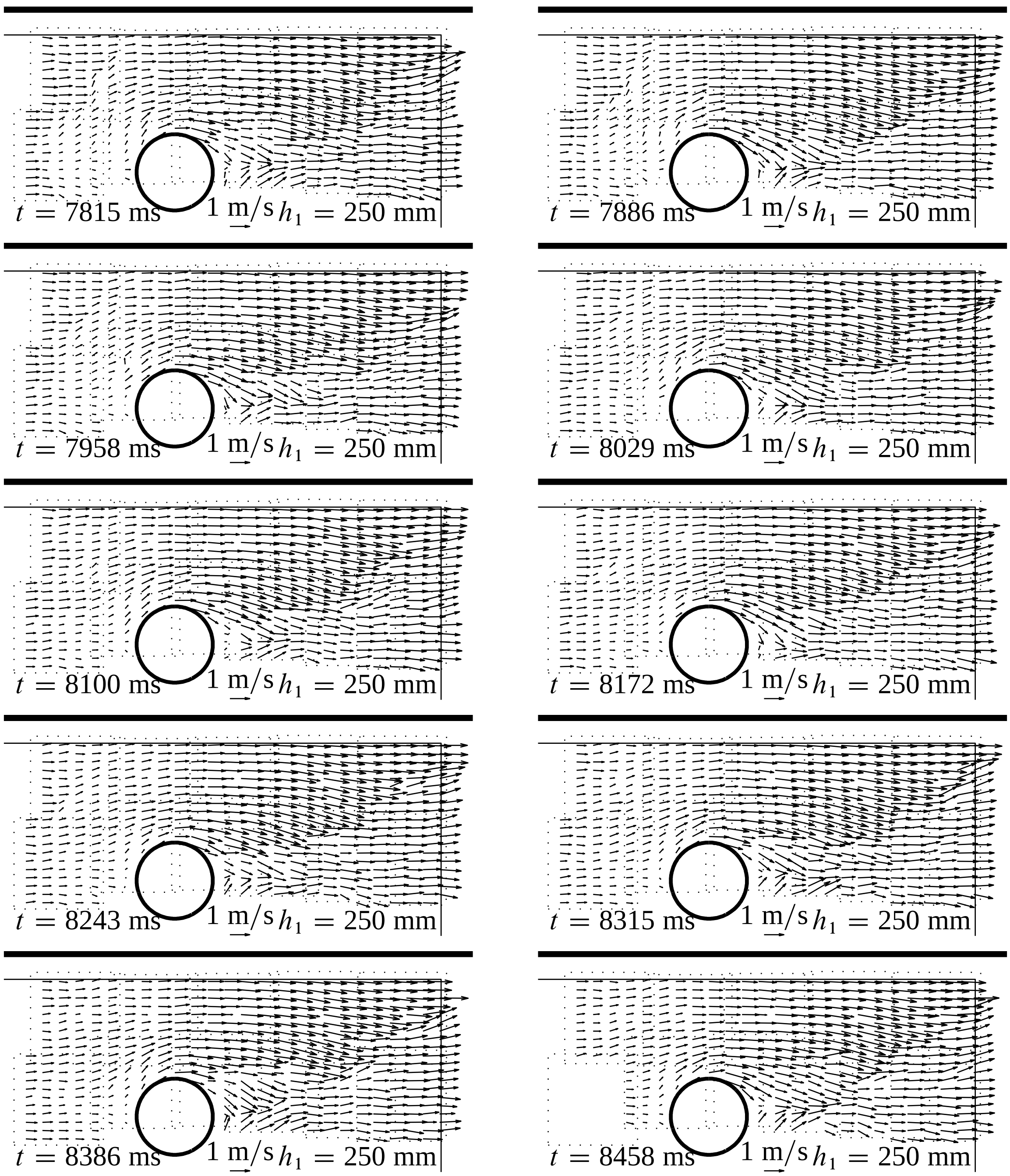

Figure A.17: Horizontal velocity field at $t = 7815$ through 8458 ms for $h_1 = 250$ mm and $z = 35$ mm.

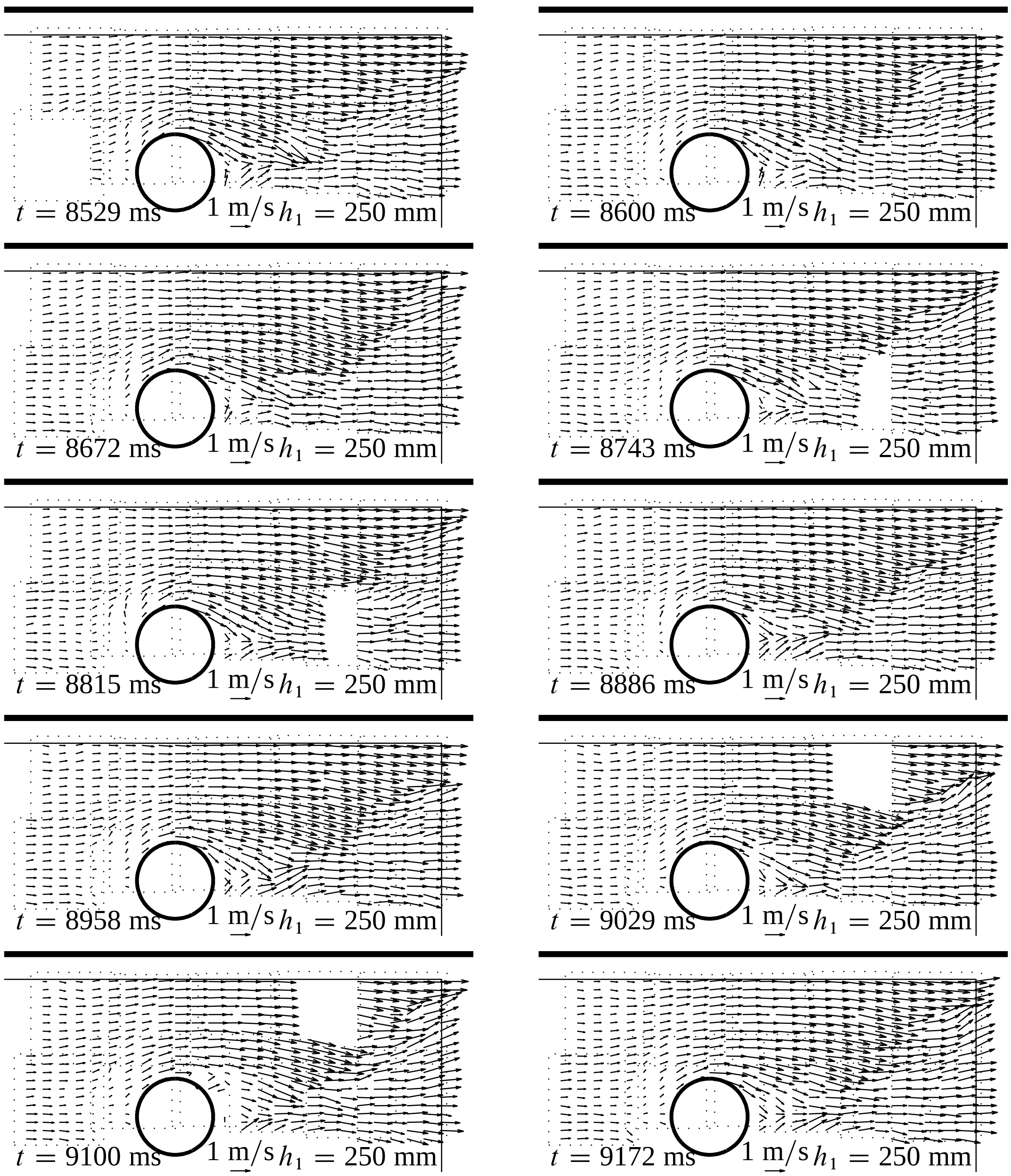

Figure A.18: Horizontal velocity field at $t = 8529$ through 9172 ms for $h_1 = 250$ mm and $z = 35$ mm.

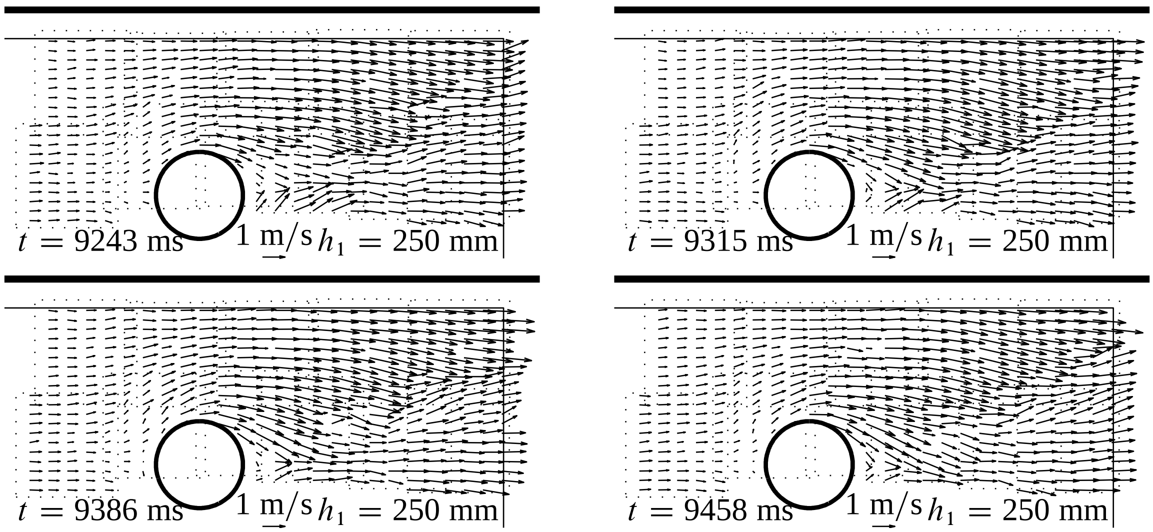

Figure A.19: Horizontal velocity field at $t = 9243$ through 9458 ms for $h_1 = 250$ mm and $z = 35$ mm.

A.4 Velocity field 15 mm above the floor for 300 mm impoundment

Figures A.20 through A.29 show the compilation of PIV velocity measurements for $h_1 = 300$ mm and $z = 15$ mm

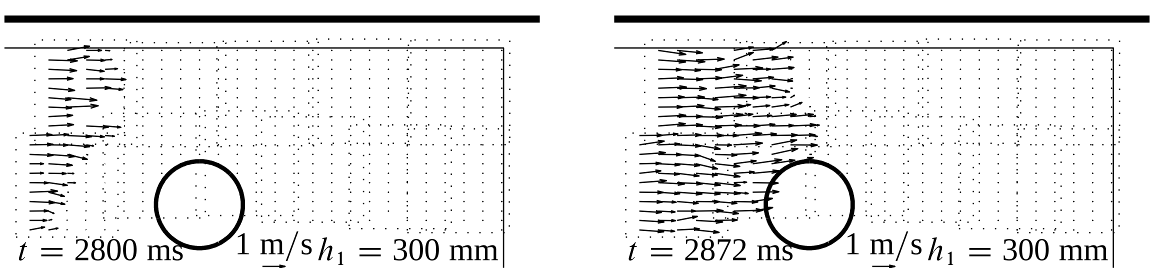

Figure A.20: Horizontal velocity field at $t = 2800$ through 2872 ms for $h_1 = 300$ mm and $z = 15$ mm.

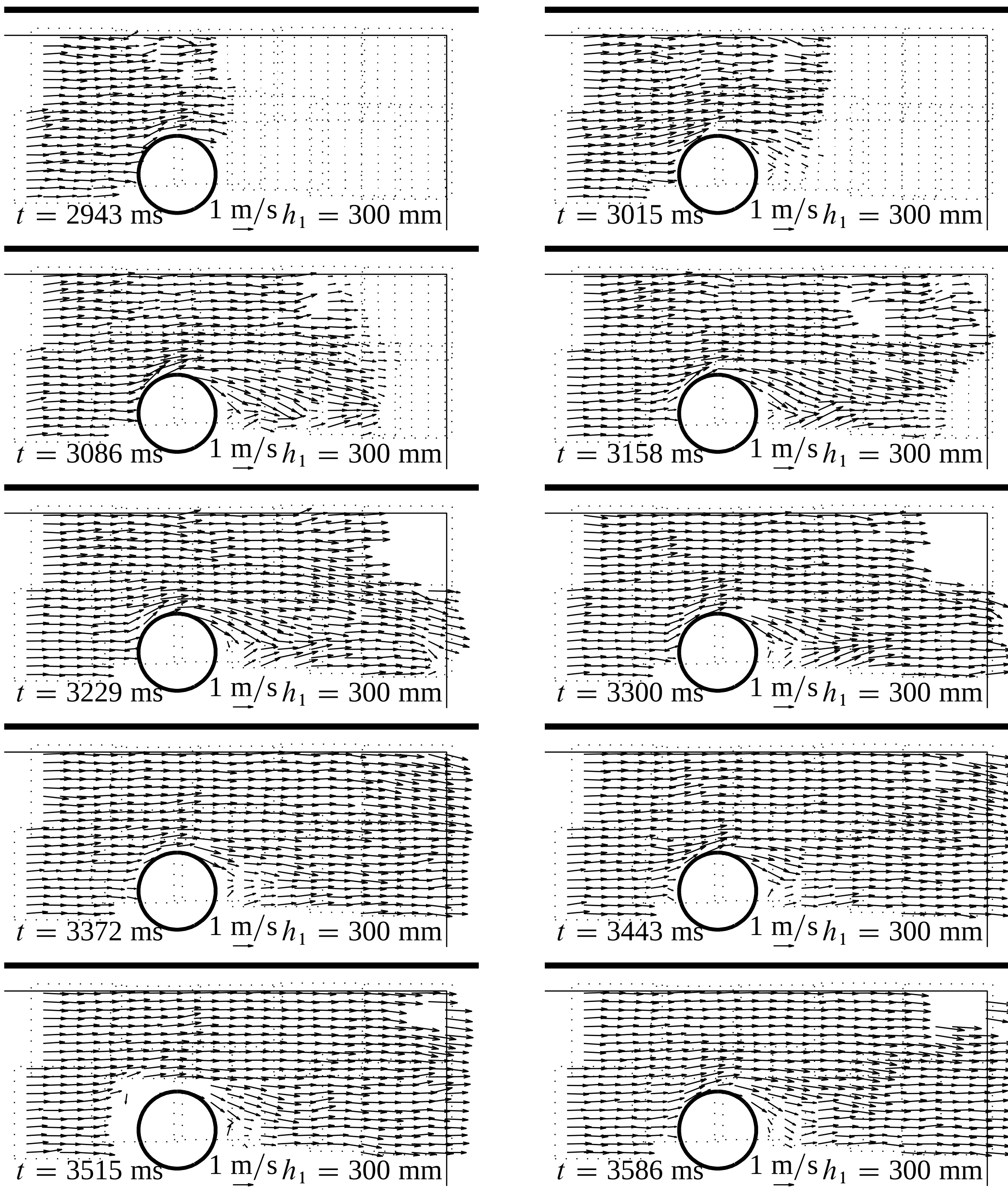

Figure A.21: Horizontal velocity field at $t = 2943$ through 3586 ms for $h_1 = 300$ mm and $z = 15$ mm.

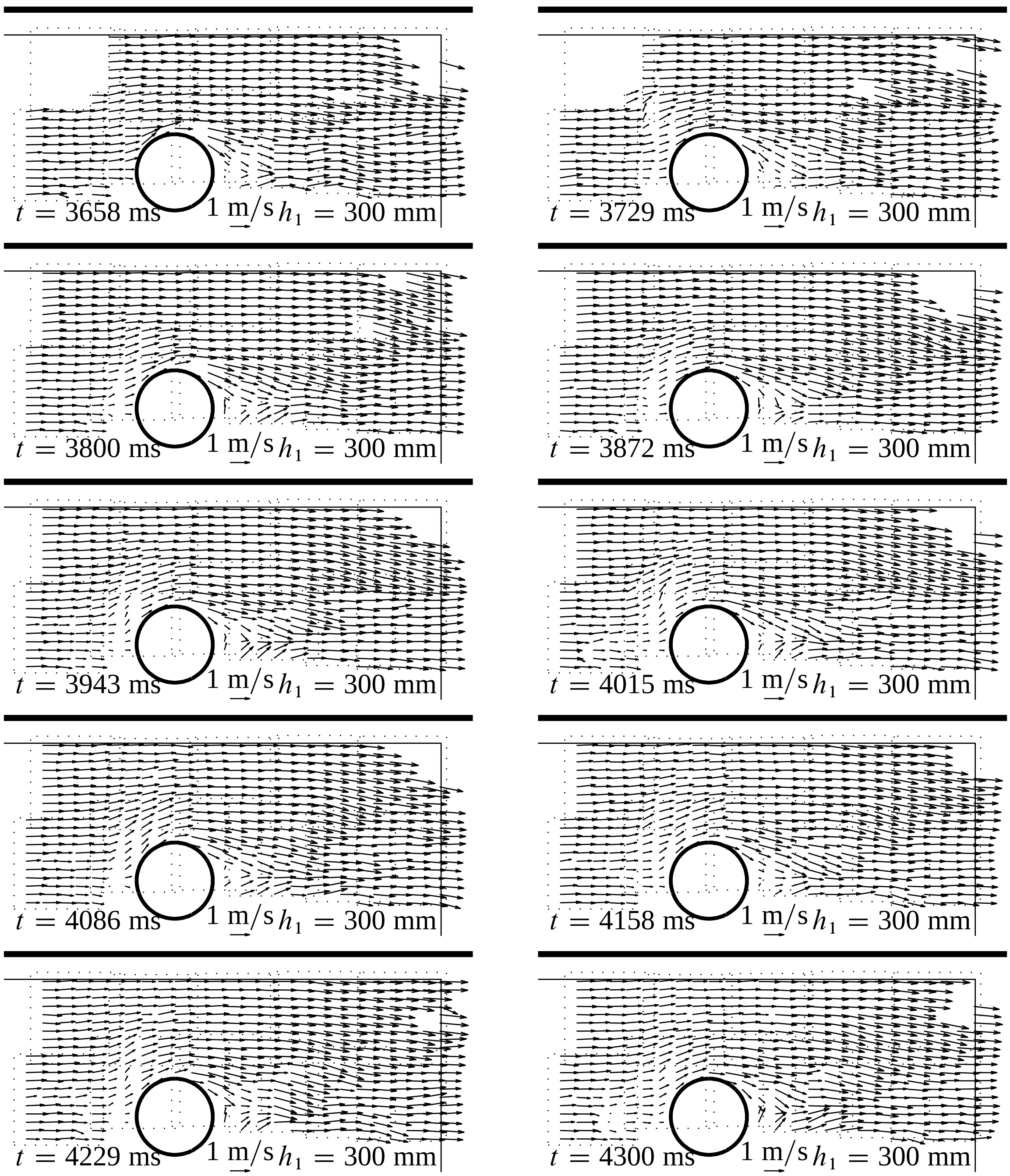

Figure A.22: Horizontal velocity field at $t = 3658$ through 4300 ms for $h_1 = 300$ mm and $z = 15$ mm.

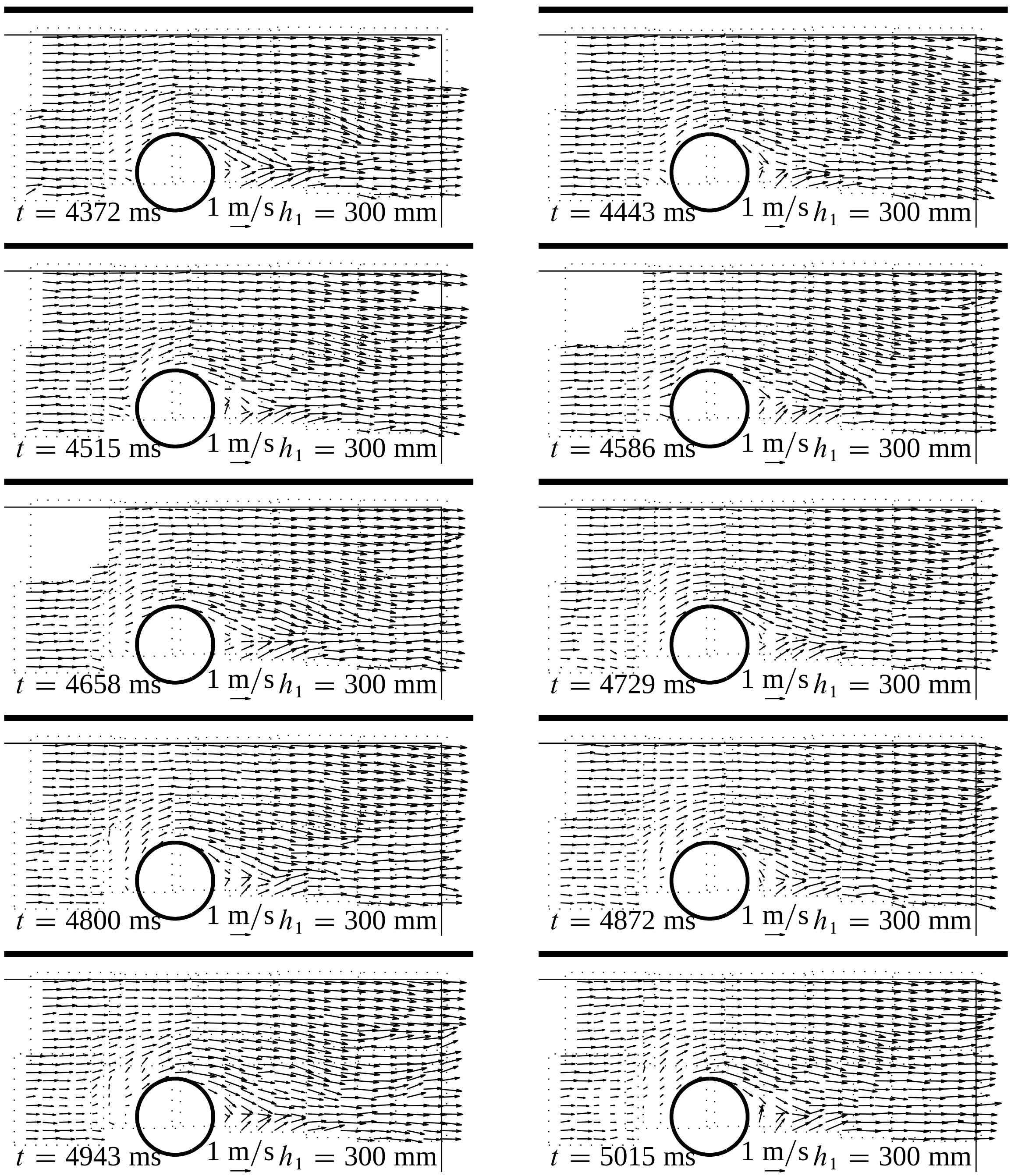

Figure A.23: Horizontal velocity field at $t = 4372$ through 5015 ms for $h_1 = 300$ mm and $z = 15$ mm.

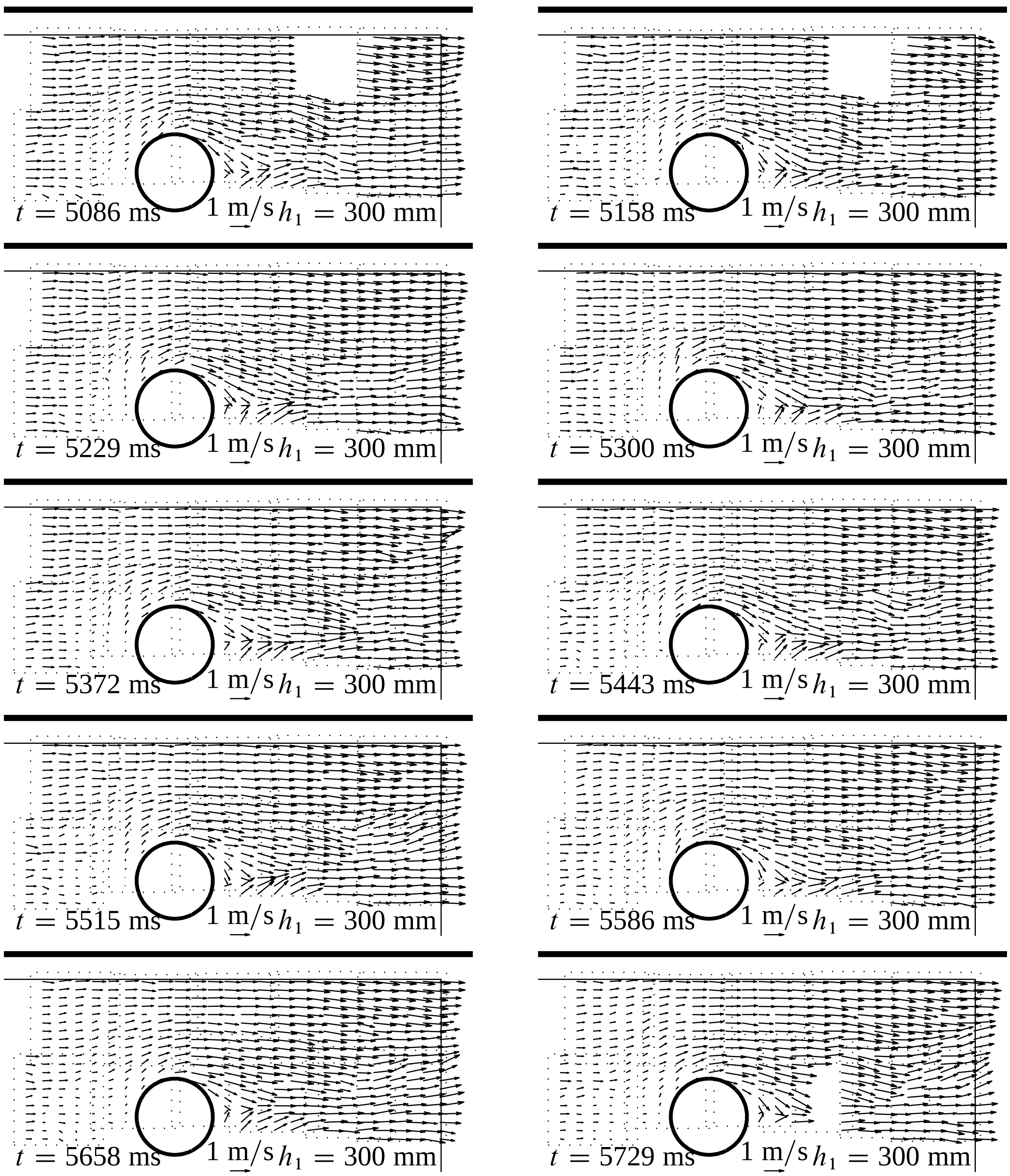

Figure A.24: Horizontal velocity field at $t = 5086$ through 5729 ms for $h_1 = 300$ mm and $z = 15$ mm.

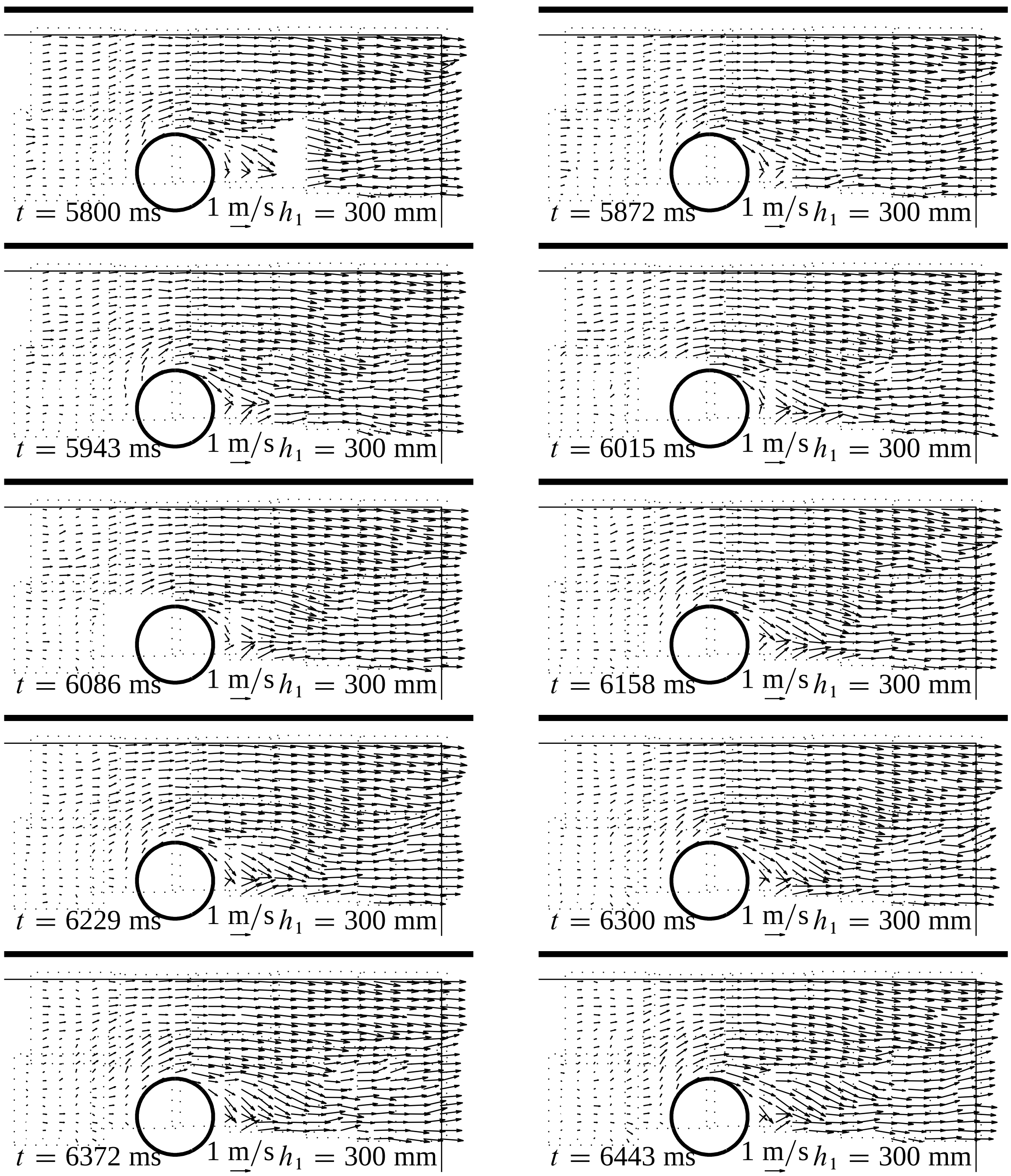

Figure A.25: Horizontal velocity field at $t = 5800$ through 6443 ms for $h_1 = 300$ mm and $z = 15$ mm.

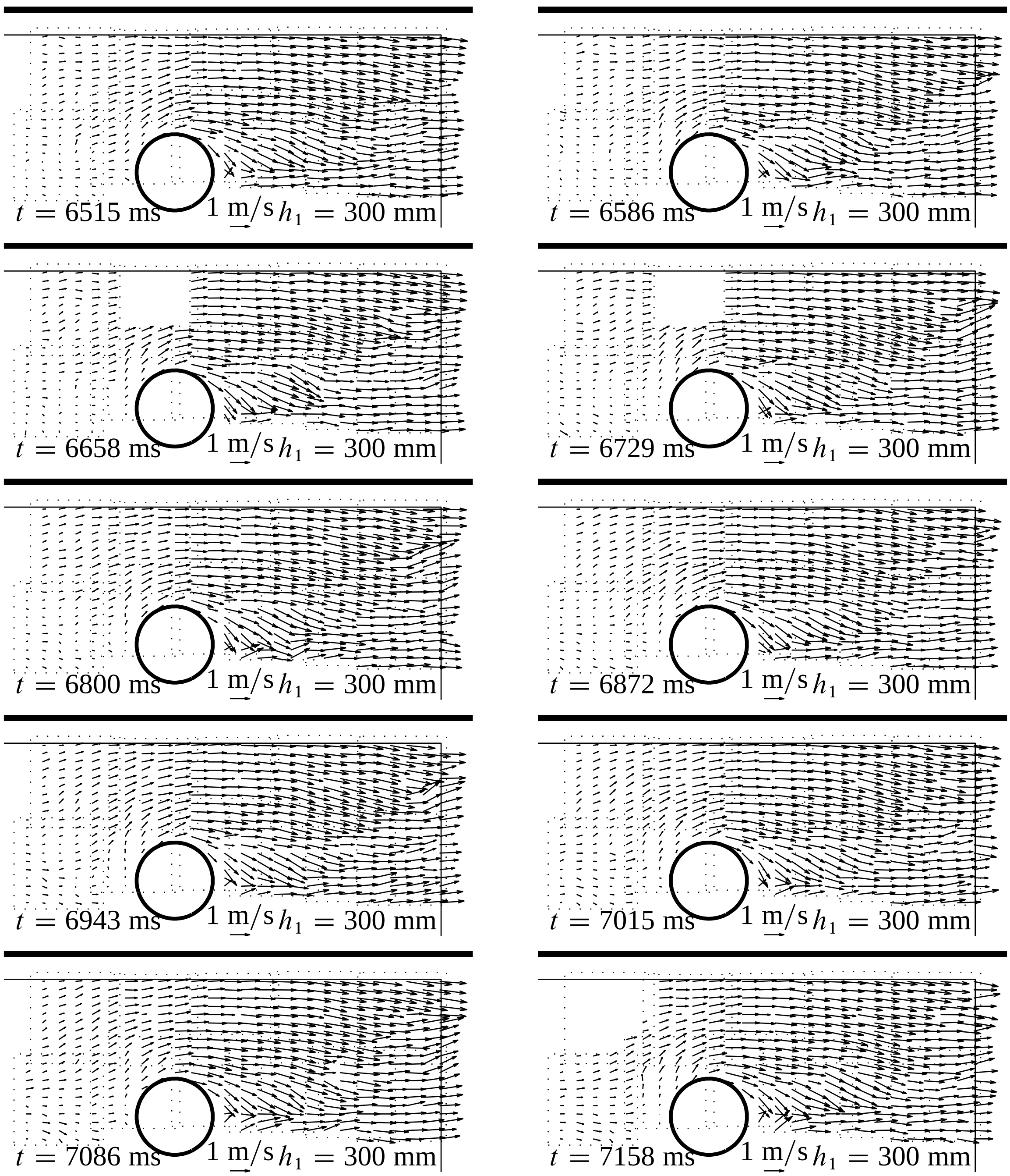

Figure A.26: Horizontal velocity field at $t = 6515$ through 7158 ms for $h_1 = 300$ mm and $z = 15$ mm.

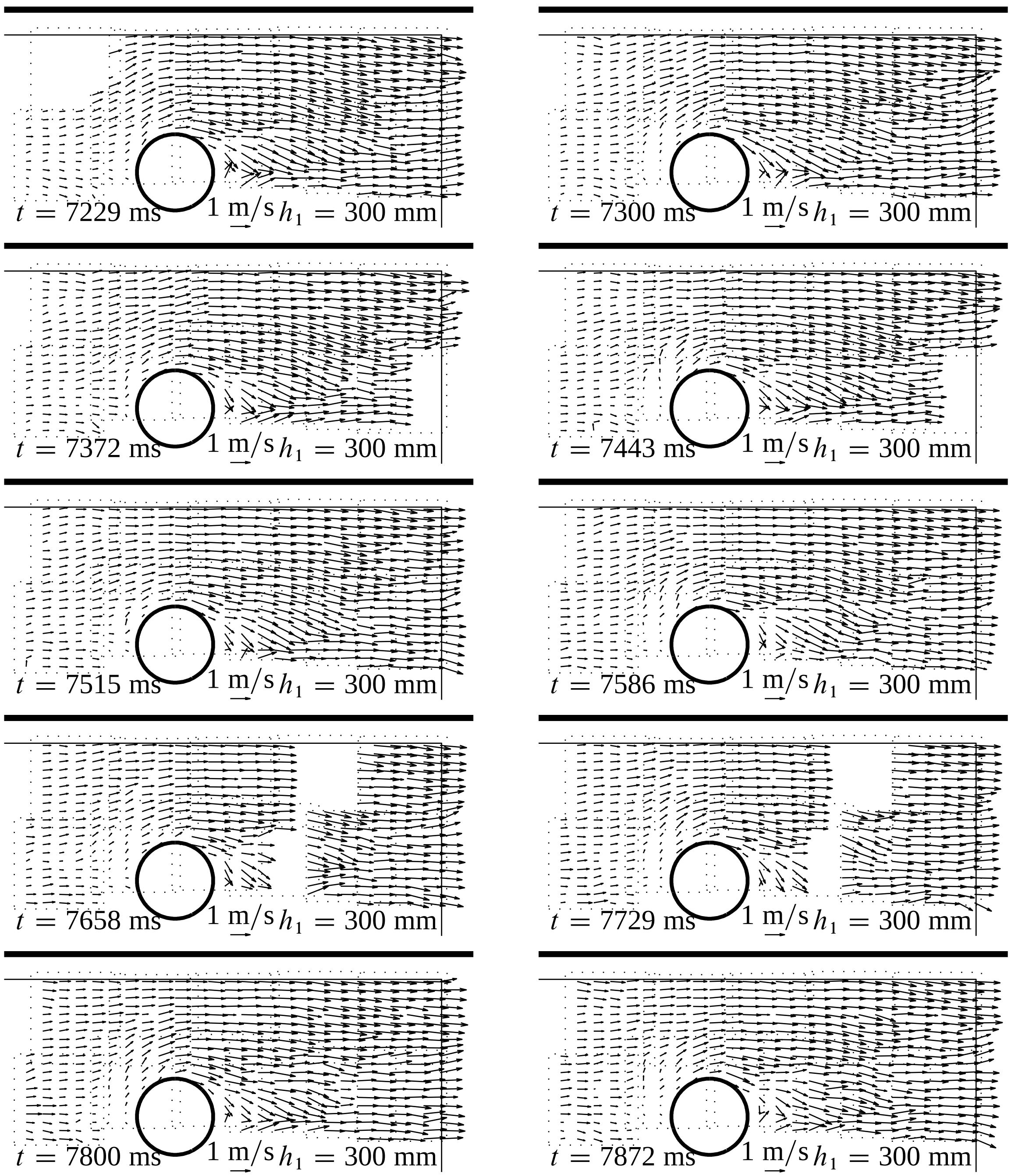

Figure A.27: Horizontal velocity field at $t = 7229$ through 7872 ms for $h_1 = 300$ mm and $z = 15$ mm.

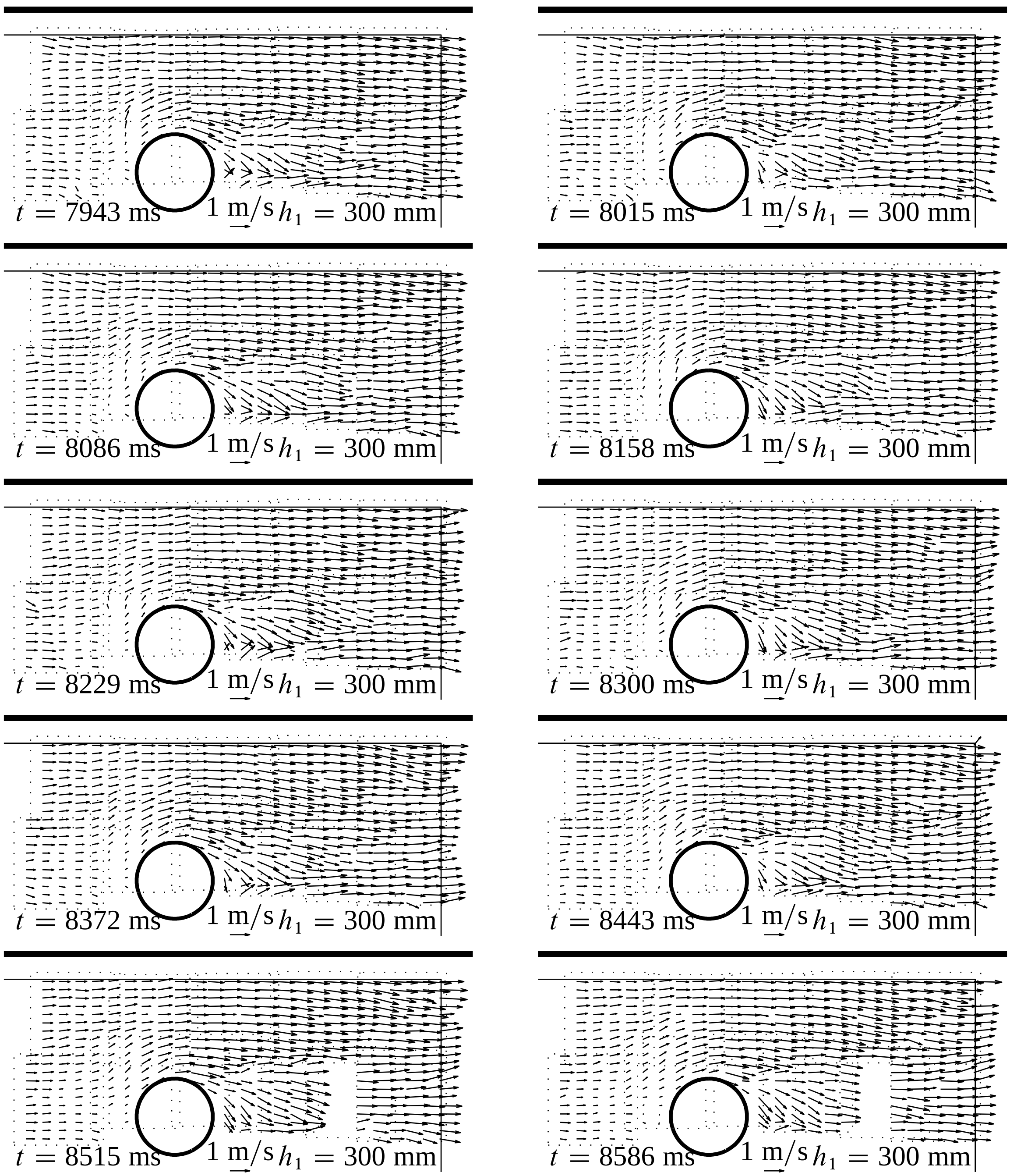

Figure A.28: Horizontal velocity field at $t = 7943$ through 8586 ms for $h_1 = 300$ mm and $z = 15$ mm.

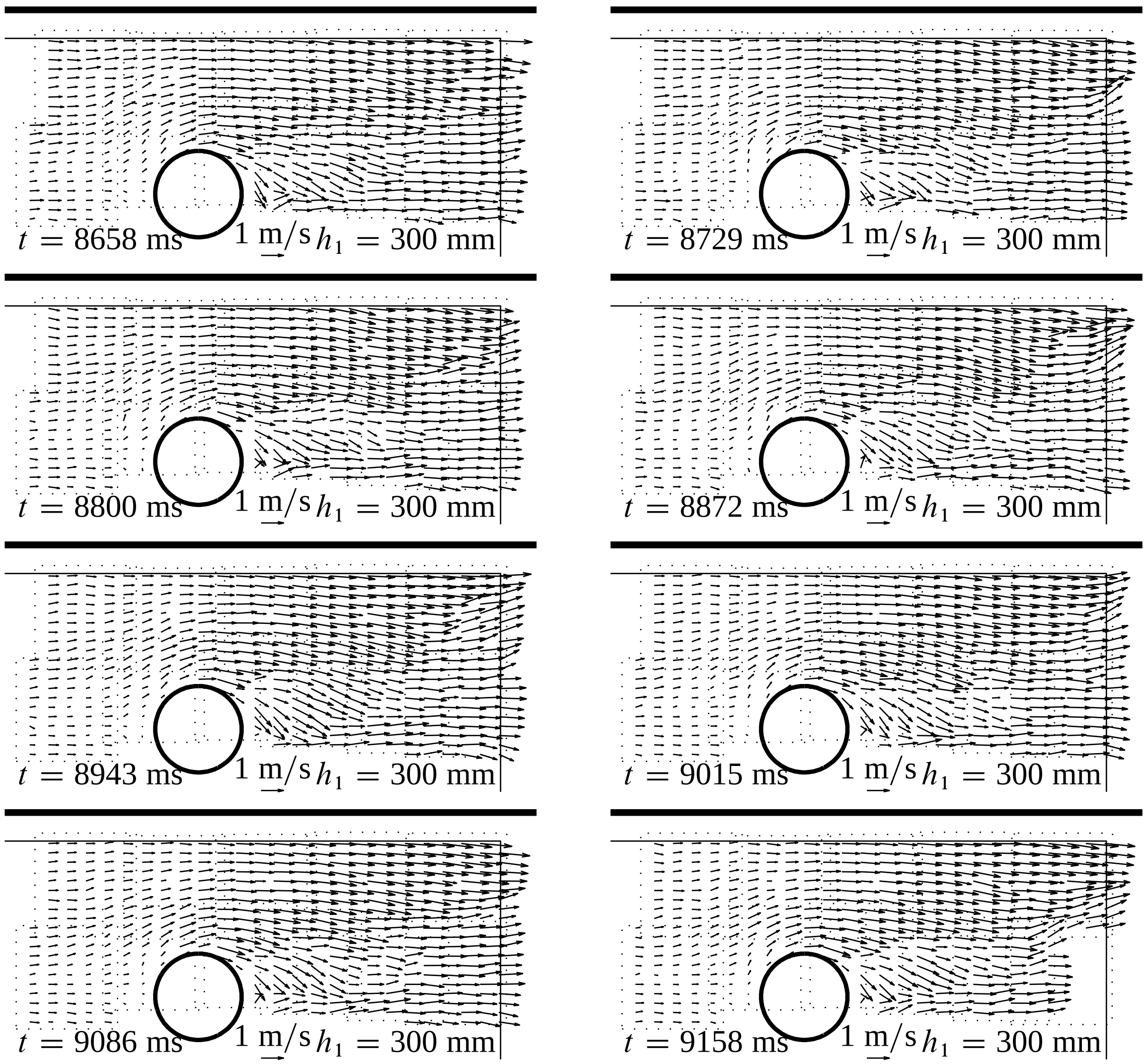

Figure A.29: Horizontal velocity field at $t = 8658$ through 9158 ms for $h_1 = 300$ mm and $z = 15$ mm.

VITA

Halldór Árnason was born in Reykjavík, Iceland on January 29th 1970. He received a Cand. Sci. degree in Civil Engineering from the University of Iceland (Háskóli Íslands) in 1993 and a Master of Science in Civil Engineering degree from the University of Washington in 1995.